ESRF
The European Synchrotron

ESRF HIGHLIGHTS 2015

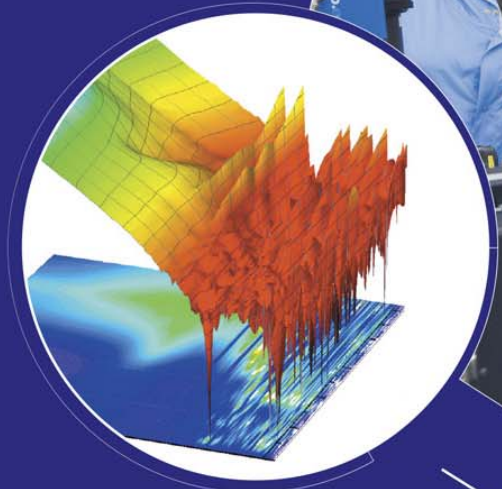

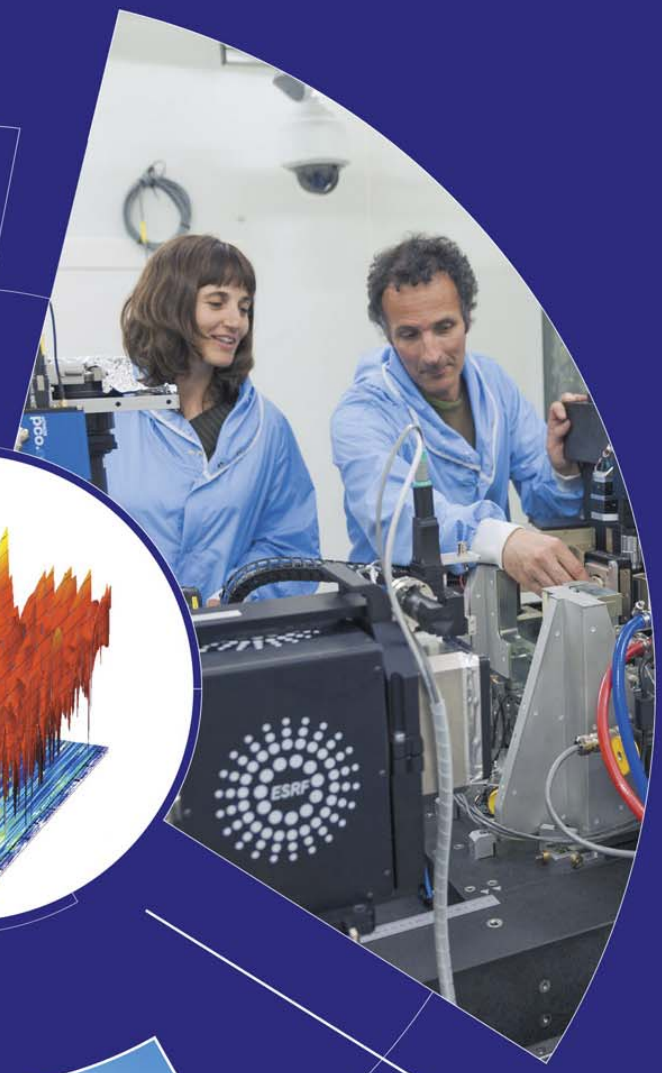

ESRF
The European Synchrotron

ESRF HIGHLIGHTS 2015

EUROPEAN SYNCHROTRON RADIATION FACILITY

Francesco Sette

DEAR READER

I am proud to present to you the 2015 issue of the ESRF Highlights.

2015 has been a very special year for the ESRF.

The ESRF launched its new and final development phase of the Upgrade Programme: the ESRF Extremely Brilliant Source Programme, or ESRF-EBS. This new phase is supported enthusiastically by the ESRF's 21 partner nations and by the European Commission, notably through a contract signed recently with the European Investment Bank. This new programme is revolutionary, and is centred on the construction of a new storage ring that will adopt an all-new hybrid multi-bend achromat lattice design. It will have a normalised horizontal emittance at least a factor of 10 better than any other synchrotron source constructed or presently under construction, and its performances will be a factor of 40 better than the present ESRF storage ring. This new X-ray source is expected to deliver X-ray beams to ESRF beamlines with an increase of approximately 100 times in brilliance and coherence. The EBS programme also includes the construction of new state-of-the-art beamlines, a scientific instrumentation programme with ambitious detector projects and a data management and analysis strategy. An instrumentation upgrade is also planned for several beamlines, including the "national beamlines" operated by Collaborating Research Groups.

During this last year, the ESRF has made tremendous progress in the EBS programme by finalising the engineering of the new storage ring, reviewing the project costs and spending profile, preparing and launching the pre-procurement and procurement phases, defining the master plan, scheduling the work during the assembly and commissioning phases, and establishing the procedures and planning for the restart of the beamlines.

The EBS accelerator project schedule includes a long shutdown period, required for the dismantling of the existing storage ring, for the assembly and commissioning of the new one, and for the adaptation of the ESRF beamline portfolio to the new source. The present plan foresees normal User Operation until end 2018, a long shutdown in 2019 and 2020, and restart of User Operation at the end of August 2020 with a maximum number of operational beamlines. Adaptation of the beamlines, their refurbishment and construction schedule are key items on the agenda of the new ESRF Science Advisory Committee (SAC), and the

Management is presently working on the beamline implementation master plan.

In 2015, the ESRF also completed the Upgrade Programme Phase I, on time and within budget. The ESRF Council, at its last plenary meeting, on 30 November and 1 December 2015, praised the delivery of Phase I through the following message: "*The Council celebrates the delivery of the ESRF Upgrade Programme Phase I, which has been completed on time, within budget and with minimal impact on the operation of the facility and the ongoing user programme. It recognises that the skills, competence and dedication of the ESRF staff have been the key to this successful delivery. The Council warmly thanks and congratulates all the staff for their outstanding work and for their efforts over the last few years, which consolidates the ESRF's pioneering role in the development of cutting-edge synchrotron X-ray science and techniques*." I wish to echo the Council's words, and thank and congratulate ESRF staff and users who, during these last seven years, have contributed with dedication and enthusiasm to this outstanding accomplishment!

The launch of ESRF-EBS and the delivery of ESRF UP Phase I, two critical steps for the ESRF's future, have been carried out while maintaining optimum conditions for user operation: excellent operation of the accelerator complex and outstanding beamline performances with record values in terms of submitted proposals and operation statistics. This is presented within this latest issue of the Highlights, where the quality and breadth of the scientific research carried out at the ESRF, and the relevance of the knowledge being generated by our users is clearly evident.

Of significance for the user programme, in 2015, the ESRF completed a long, multiannual process which led to the drafting of the ESRF "Data Policy". For the first time since construction, the ESRF has finally adopted a comprehensive "Data Policy" document that deals with key aspects of the ESRF's core activity such as data ownership, long-term storage, access, curation, documentation, etc. This document was endorsed by the Council at its last meeting in December 2015.

In terms of daily operation of the facility, we have seen our site logistics improving steadily during 2015, with the completion of the relocation of staff offices, the new contract for the management of our restaurant and guest house, and the availability of green spaces for all on the EPN Science Campus.

Over the year, the ESRF has also continued to strengthen its international visibility and attractiveness with outreach activities that are increasingly gaining recognition. Notable examples include supporting the HERCULES school in close collaboration with the Université Joseph Fourier (now part of the Université Grenoble Alpes) and the ILL, organising the second edition of the ESRF-ILL International Undergraduate Student Programme, supporting the Synchrotron@school programme in partnership with the Académie de Grenoble, hosting the First Conference and Workshop for an African Light Source in the context of the International Year of Light, participating in numerous H2020 programmes, actively contributing to renowned science fairs, and welcoming an increasing number of visitors from academia and from the general public.

All this has been possible thanks to the engagement of ESRF staff, to the enthusiastic support of our partner nations and to the trust of our science community, allowing us to imagine and construct the ESRF's future for the benefit of all, for new generations of researchers as well as for society in general.

I am convinced that now, more so than ever before, the ESRF is not only an excellent place to carry out science, but it is also a prime example of international collaboration and cooperation. Therefore, we have the duty and responsibility to share our passion for science and technology with the widest possible community, to contribute to the advancement of knowledge across borders, and to inspire the new generations to perpetuate the ESRF's legacy for many years to come. Science is an inescapable driver to peaceful relations among cultures and nations, a force for sustainability and a necessity in confronting the major challenges facing our world today. This vision should guide us daily and in our long-term activities and initiatives.

I wish to end by thanking the ESRF users, to whom this new issue of the ESRF Highlights is dedicated, for their support and congratulating them for the excellent science that they carry out at the ESRF.

FRANCESCO SETTE
Director General,
ESRF

2015 at the ESRF

Ribbon cutting in 2015: ID01, ID31, ID30B, CAL

In 2015 the ESRF inaugurated three new beamlines (ID01, ID31 and ID30B) and one ultra-high-tech crystal analyser laboratory.

ID30B is the latest of the new Macromolecular Crystallography beamlines to be inaugurated. It is an energy-tuneable beamline operated by the ESRF-EMBL Joint Structural Biology Group.

ID01 is a nanodiffraction beamline which produces extremely small beams (100 nm) for the study of nanostructures.

ID31 is a high-energy beamline for buried interface structure and materials processing.

May 2015
A new generation of synchrotrons

The ESRF officially launched the second phase of its extensive upgrade programme which includes the construction of a new storage ring with boosted performances: the ESRF- Extremely Brilliant Source (ESRF-EBS) project.

June 2015: Great success for Synchrotron@School

Since its launch in 2013 in partnership with the French "Académie de Grenoble", the education programme, Synchrotron@School, has welcomed 26 classes and 800 high-school students. In 2016 the programme will be reinforced with 30 classes, 5 of which are located outside France.

August 2015
International Student Summer Programme

For the second year running, the ESRF and ILL organised a joint International Student Summer Programme for undergraduates from all over Europe. 15 students, originating from 9 different countries were offered four weeks of immersion into the world of X-ray and neutron science.

September 2015
Unequalled beam stability

Beam stability at the ESRF is unequalled among synchrotrons the world over.

In September, 427.5 hours of beam were delivered without a failure, the equivalent of three weeks of uninterrupted beamtime. During operation, 224 beam position monitors analyse the position of the beam and a feedback system adjusts the trajectory. With an electron beam just the width of a human hair and covering a distance of 26 billion kilometres every day, this system is precise to less than 1 µm.

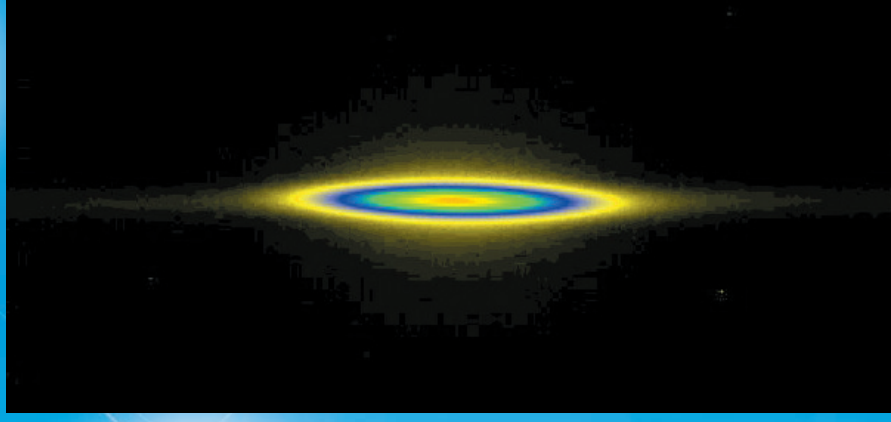

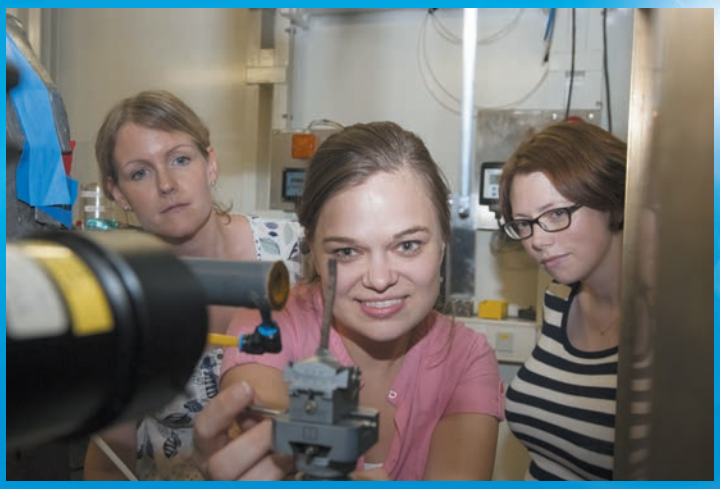

September 2015
Thank you, Users!

1135 proposals were received for the September applications session. This is the highest number ever received for the September deadline and the second highest ever, especially with two beamlines not yet in operation.

November 2015
ESRF hosts the First African Light Source Workshop and Conference

In the context of the 2015 UNESCO International Year of Light, nearly 100 scientists from across the world and government officials met to draft resolutions and a roadmap to initiate the process towards the construction of the first light source in Africa. For the AFLS organising committee, "the Grenoble resolutions will lay strong foundations for a future Light Source in Africa".

December 2015
EIB backs the ESRF for 65 M€

As part of the Horizon 2020 programme, the European Investment Bank (EIB) has decided to support the project ESRF-EBS to the level of 65 million euros. The signing of this contract with the EIB is a mark of strong recognition for the ESRF and decisive support for the ESRF-EBS project.

Status of the Upgrade Programme

2015 has been a challenging year for the ESRF with ongoing user operation, the final year of Phase I of the Upgrade Programme and the first year of the ESRF-EBS project. We are proud to report that the staff in all ESRF divisions has mastered this challenge and achieved tremendous progress for the facility and its users. In the following, we have summarised a selection of the major activities that took place at the ESRF in 2015.

The upgrade of the beamline portfolio with 19 new or fully refurbished beamlines has been completed in 2015. The key performance indicators have all been reached and most beamlines are back in full user operation. The following list provides a summary on the upgrades of the beamline portfolio implemented in Phase I of the Upgrade Programme.

ID01 – X-ray nano diffraction:
Beamline ID01 has been reconstructed in 2014 and returned to partial user operation in early 2015. The last remaining items were installed by the end of 2015 and commissioning of these shall be finished by mid 2016.

ID02 – X-ray ultra-small and small angle scattering:
The time-resolved ultra-small angle scattering beamline ID02 returned to user operation in July 2014. The key performance indicators have been reached and a large number of successful academic and industrial user experiments have been carried out already.

ID06 – Hard X-ray Microscopy prototype:
The development of the Hard X-ray Microscope (HXRM) continues and will be finished in spring 2016. The design of the challenging high precision positioning unit for the optics and sample is nearly completed.

ID09 – Time-resolved X-ray diffraction and scattering:
The time-resolved scattering beamline ID09 has undergone a gradual upgrade without a shutdown since 2010. The key elements such as the high speed chopper have been installed and the new large area detector received. The mirror as the last remaining element will be installed in spring 2016.

ID10 – X-ray photo correlation spectroscopy and X-ray scattering from liquid surfaces:
The reconstructed beamline ID10 has been in routine user operation since 2012 after having reached all key performance indicators. The last remaining item, the new diffractometer for liquid samples, was installed during the winter shutdown.

ID15 – High energy X-ray diffraction and scattering:
The last large-scale project within Phase I started with the decommissioning of beamlines ID15A and ID15B in December 2014. The new hutch complex with its infrastructure has been constructed. The design and procurement of beamline components is progressing. The beamline should receive first users in autumn 2016.

ID16 – X-ray nano-imaging and nano-analysis:
The ID16A – nano-imaging beamline has resumed user operation (**Figure 1**). Cryo-cooling for the sample stage was ready for installation at the end of 2015. The ID16B – nano-analysis beamline is operational with XANES spectroscopy and *in situ* holo-tomography, including a furnace reaching 800°C.

ID17 – Paleontology project at the medical beamline:
The paleontology project at beamline ID17 has been successfully finished with the installation of a dedicated microtomography station.

ID19 – High energy X-ray imaging:
The beam expander has been installed in the summer shutdown 2015 and is currently under commissioning. The upgrade of the beamline was completed with the delivery of three new detectors for fast and ultrafast imaging down to the time scale of a single X-ray pulse.

ID20 – X-ray resonant and non-resonant inelastic scattering:
The inelastic scattering beamline ID20 resumed full user operation. The installation of the phase plate setup for polarisation control will be finished in spring 2016.

ID22 – X-ray powder diffraction:
ID22 is in full user operation with a new transfocator and a new Perkin Elmer flat panel large area detector. The delivery of the new high resolution diffractometer has been delayed. The installation is now planned in spring 2016.

ID24 – Time-resolved and extreme conditions X-ray absorption spectroscopy:
The two XAS beamlines ID24 and BM23 returned to user operation in 2012 and 2013, respectively. The chemistry programme at ID24 has resumed operation after commissioning of the infrared spectrometer.

ID30 – MASSIF – Macromolecular crystallography and scattering:
The complex of structural biology beamlines BM29, ID30A-1, ID30A-3 and ID30B has been completed in 2015 and is in full user operation. ID30A-1 is the only fully-automated hands-off user beamline worldwide. A new prototype versatile sample changer is in operation on ID30B together with a high capacity dewar.

ID31 – High energy X-ray diffraction and scattering:
Beamline commissioning with the HEMD instrument has started and first user experiments were performed at the end of 2015. The remaining optical elements and part of the experimental hutch facilities will be installed in 2016 (see **Figure 2**).

ID32 – Soft X-ray dichroism and resonant inelastic scattering:
The soft X-ray spectroscopy beamline ID32 features two branches. The XMCD branch has returned to user operation. The RIXS branch has received first users employing medium resolution. The final version of the sample cooling stage and the high resolution grating have been installed.

During 2015, several upgrades to parts of the accelerator system were completed within Phase I of the Upgrade Programme. The radio frequency (RF) system has been renewed with the addition of solid state amplifiers and HOM-damped cavities. All the planned straight sections have been lengthened from 5 m to 6 m, with one 7 m-long section in cell 23, enabling the installation of the RF cavities. Following the construction of ID32, a new helical undulator was put into place in its straight section in 2015. Canted straight sections have also been installed at ID15, ID16 and ID30. An improved electron beam position monitoring system and a fast orbit feedback system have been successfully developed and installed. The new bunch cleaning system in the booster will greatly aid top-up operation, scheduled for 2016.

Last year also marked the beginning of the execution phase of the EBS project. A fruitful year followed, in which 90% of the design work was completed and calls for tender were sent out for all of the magnets as well as the stainless

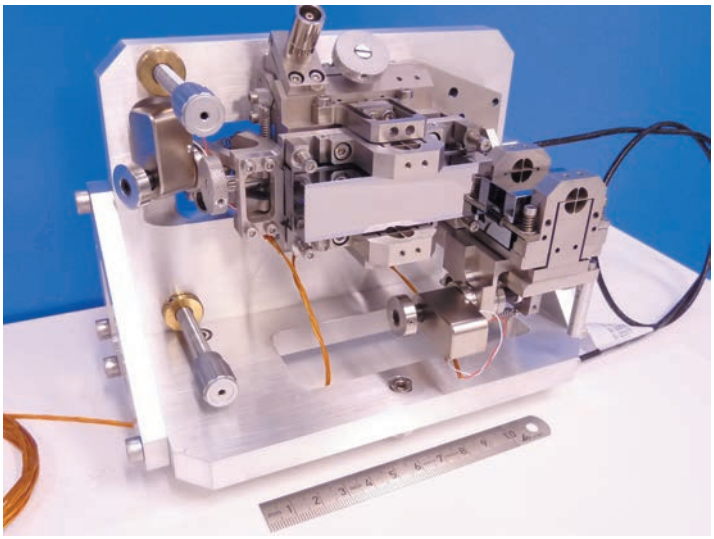

Fig. 1: Nanofocusing KB system for beamline ID16A.

Fig. 2: ID31 experimental hutch during construction of the beamline.

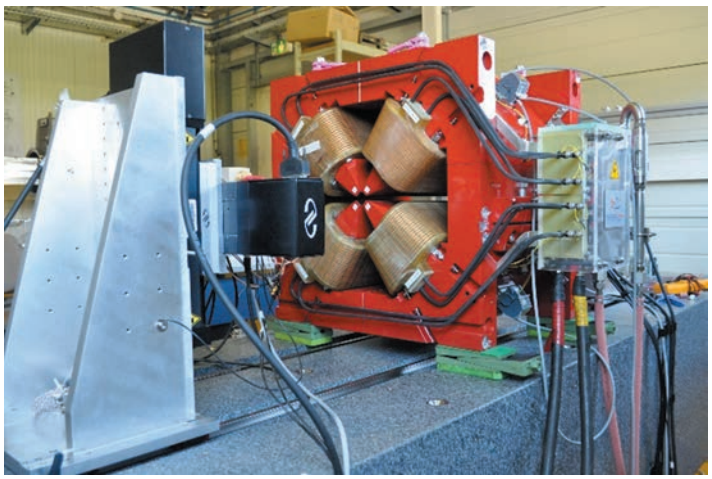

Fig. 3: High gradient, 87 T/m quadrupole magnet under test on a magnetic measurement bench.

steel and aluminium vacuum chambers. Significant effort was put into optimising the design of the ESRF–EBS lattice. While evolution of the standard cell is now minor, work has progressed on the design of the injection section, on chromaticity tuning and on the optimisation of lifetime and injection efficiency. Different solutions for the sources for the bending magnet beamlines have been studied. The requirements for a back-up solution in case of a magnet power supply failure have been specified. The study of collective effects is also progressing with a first longitudinal impedance budget. Bunch lengthening and Touschek lifetime estimates have been correspondingly updated. The benefits of a third-harmonic RF cavity have also been explored.

More than one thousand magnets will be built for and installed in the ESRF-EBS storage ring. Large-scale procurement has started and the first two contracts were signed at the end of 2015. The dipole magnet assembly zone is being prepared in the Chartreuse Hall including benches for full magnetic characterisation (**Figure 3**).

The prototype girder for the new machine has been put through a series of motion tests (**Figure 4**) to check the alignment of the attached dummy magnets. It could be concluded that the magnets move less than 50 micrometres out of place during transportation, thus ensuring that the girders for the EBS project can be completely pre-assembled before transportation into the storage ring.

Fig. 4: Transportation of the prototype girder during stability testing.

The RF system design for the new storage ring has also been finalised. Two of the existing three klystron transmitters will be kept to power (with redundancy) 10 HOM-damped single-cell cavities in cells 5 and 7 of the new ring. Three existing 150 kW solid state amplifiers will be moved to cell 25 where they will power one cavity each. Optionally, a fourteenth cavity will be fed by the in-house-developed solid state amplifier. The procurement is making good progress with twelve single-cell HOM-damped cavities in fabrication and almost all other major RF components having been ordered if not yet delivered.

In 2015, resources had to be carefully balanced in order to finalise the Upgrade Phase I beamline projects, keep pace with the tight schedule for the ongoing upgrade of the accelerator complex, and initiate the ESRF-EBS programme, without neglecting to provide efficient operational support for the functioning accelerator complex and experimental facilities. Project management played a key role and our project management practices will be consolidated by modernising tools and methods, and by fostering the dissemination of best practices to all project managers. This will include a regularly updated, multi-annual resource schedule.

Strategic developments for future scientific instrumentation as presented in the *Orange Book* have been initiated. The first objective is the development of new instrumentation, which will be crucial in exploiting the new source properties to the full extent; the second objective is the consolidation of major ongoing instrumentation programmes initiated during Upgrade Phase I. In the context of ESRF-EBS, four main development lines centered around beamline control and data management, X-ray detectors (**Figure 5**), X-ray optics, and high-precision engineering have been identified.

In line with the worldwide trend towards an open data policy to enhance the dissemination of knowledge, the ESRF has developed a data policy which was presented and discussed by SAC and approved by Council in December 2015. A data manager was recruited and the metadata capture on several beamlines has started. As part of the data analysis strategy, work progressed on a new data analysis platform, comprising common software routines for analysing synchrotron data, a

Fig. 5: ESRF-built imaging cameras - more than 25 are in operation at the beamlines.

set of generic applications and a catalogue of software. This work is supported with advances in the implementation of identity management to allow for the persistent authentication of users, major extensions to our disk storage and tape archive systems, and investigations of the usage of cloud technologies. A task force has been set up to coordinate the efforts required to implement the open data policy, with the aim of its full implementation for all beamlines by mid 2020.

The creation of a Precision, Dynamics and Mechatronics Unit in spring 2015 will strengthen our expertise in real-time instrument control and provide the basis for the development of mechatronics concepts, combining mechanical design with on-line metrology and fast-feedback closed-loop control.

The Crystal Analyser Laboratory (CAL), dedicated to the development and production of curved crystal analysers for spectroscopy applications, was officially inaugurated at the occasion of the autumn SAC meeting. The facility has so far produced more than 70 analysers for instruments at the ESRF and other facilities in Europe and the United States.

The development of a generic double crystal monochromator (DCM) for X-ray spectroscopy with ultra-high stability is progressing well. Design studies for the rotation axis and the crystal cage were concluded, and a prototype version of these components will be built and tested in 2016.

The ESRF strategy also relies on international collaboration to foster synergies with many other European research infrastructures. As part of the European Union's research and innovation programme, Horizon 2020, the ESRF is involved in several major projects that were launched in autumn 2015.

R. DIMPER, M. KRISCH, P. RAIMONDI, H. REICHERT and J. SUSINI

X-ray nanoprobe

In this year's highlight selection, the ESRF's nanoprobe tools show their impact in fields ranging from bio-composites and semiconductor technology to extraterrestrial and environmental sciences and to cultural heritage studies. This is representative of the broad impact and the rapid development of the user community. Three upgraded beamlines (ID16A, ID16B and ID01) entered full user operation in 2015 marking a considerable step forward in the availability of nano-imaging methods. These beamlines join the already operational micro and nanodiffraction beamline ID13 and the X-ray microscopy beamline ID21 with its long standing tradition in spectromicroscopy. Gathering these five beamlines together to form the X-ray Nanoprobe Group (XNP-group) will generate a synergy that assures efficient development of world leading nanoprobe tools that will be made available to ESRF users.

This year's article selection reflects both the fostering of established techniques making them available to non-expert users and the pioneering of new techniques of worldwide uniqueness. This demonstrates the variety and complementarity of our methods and experiments and also the necessary investment of our staff in the permanent evolution of our nanoprobes.

During this final phase of the ESRF's Upgrade Phase I, ID01 started partial user operation interlaced with commissioning periods. The nanodiffraction endstation is routinely being used for the study of nanostructures and devices. Bragg coherent diffraction imaging, as presented in ref. [1], is one of the main techniques to benefit from the new endstation. This developing technique starts to show its full potential by shedding light on the displacement fields between two inversion domains in polar GaN. Along with this, a more flexible compromise between flux and beamsize should open the facility to more operando experiments examining structure-function relationships as presented by Bussone *et al.* [2].

ID13 has started operation of an Eiger 4M Pixel detector, highlighting the ESRF's recent drive to invest in the most recent detector technology. The first experiments on time-resolved *in situ* nanocalorimetry of polymer-crystallisation have been successfully carried out with a 250 Hz framerate and a 10 µs readout time. Close to one millisecond resolution was achieved during the test phase of this device.

ID16A started full user operation in 2015, opening for users with nanotomography, including fluorescence tomography and ptychography, at two fixed energies, 17 and 33.6 keV. ID16B has been fully operational since 2014 and has recently started offering X-ray absorption nanospectroscopy with spatial resolution in the 50-100 nm range. A few user experiments have already been performed successfully. The beamline is also currently developing *in situ* devices for both high and low temperature studies. Together the ID16A/B tandem offers the ultimate resolution of a hard X-ray nanoprobe with beams in the 20-50 nm range and imaging methods typically applicable to heterogeneous structures such as biomaterials and fuel cells.

ID21 has opened a new side-branch for microdiffraction and microfluorescence 2D mapping that combines chemical and structural mapping within one instrument. This is further extending the micro-spectroscopy capabilities already offered in the tender X-ray range (2-9 keV) and the mid-infrared domain making ID21 best suited for investigating cultural heritage, geological, environmental and biological materials. As exemplified in the recent study of bioresorbable Mg implants, users are increasingly taking advantage of the combination of various micro and nano probes (here µXRF and µXANES at ID21 and µSAXS and µXRD at ID13). By offering complementary techniques, whether on a unique beamline or at several beamlines, a problem can be tackled with different views, and a full picture of the complex and interlaced physical, chemical or biological mechanisms can be obtained [3].

Extending the nanoprobes to the white beam regime, BM32 is routinely investigating poly- and monocrystalline samples. Its rainbow filtering technique [4], a new feature made available to users this year, allows determination of the full strain tensor, locally, without movement of the sample. Strain determination has become a necessity for materials such as highly strained semiconductors nanostructures that may represent new electronic properties in established materials. Guilloy *et al.* have demonstrated a material's transformation by strain [5].

These examples draw a detailed picture of the structure and chemistry of samples from many different fields of applications, imaging parameters with a level of detail which

often relied before on model calculations. The experimental findings presented here partially show the limits of such models and hence underline the importance of progress in experimental physics and new imaging methods in these fields. The coming years will see an increased effort in the development of user friendly software for our scanning probe microscopes as well as for the coherent reconstruction methods.

T.U. SCHÜLLI

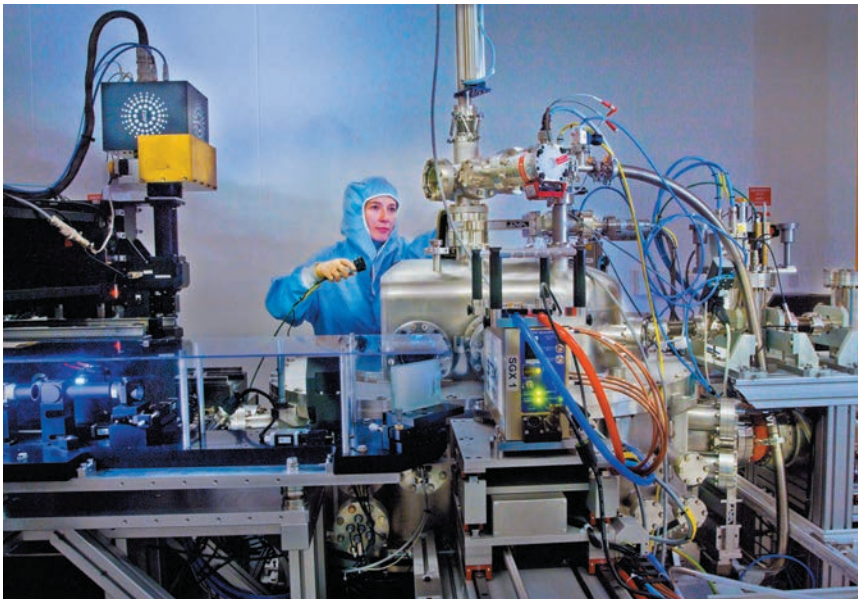

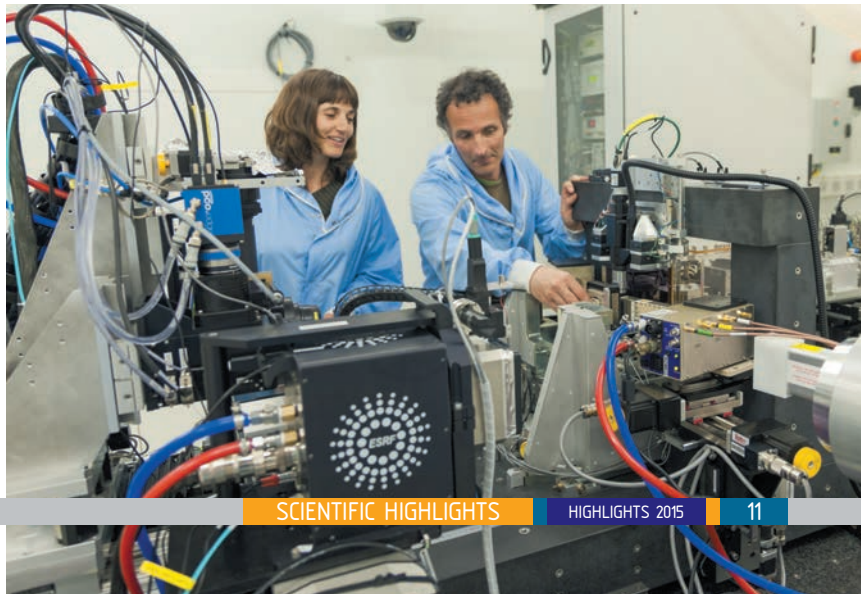

REFERENCES

[1] S. Labat *et al.*, *ACS Nano* **9**, 9210 (2015); doi: 10.1021/acsnano.5b03857.
[2] G. Bussone *et al.*, *Nano Lett.* **15**, 981-989 (2015); doi: 10.1021/nl5037879.
[3] T.A. Grünewald *et al.*., *Biomaterials* **76**, 250 (2016); doi: 10.1016/j.biomaterials.2015.10.054.
[4] O. Robach *et al.*, *Acta Cryst. A* **69**, 164 (2013); doi: 10.1107/S0108767313000172.
[5] K. Guilloy *et al.*, *Nano Lett.* **15**, 2429 (2015); doi: 10.1021/nl5048219.

COHERENT DIFFRACTION IMAGING OF INVERSION DOMAIN BOUNDARIES

The first study of the displacement field induced by several inversion domain boundaries in gallium nitride (GaN) wires is reported here. A spatial resolution better than 10 nm and a displacement accuracy of a few picometres was achieved.

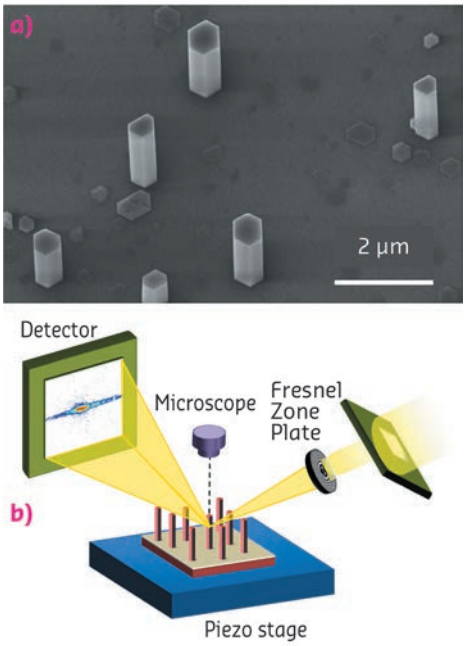

Fig. 6: (a) Scanning electron microscopy images of GaN wires. (b) Experimental setup at beamline ID01.

Nitride materials have been studied intensively and mastering their growth has opened the way to blue-light emission [1] and applications in power devices. Since defects in GaN wires are a key issue, their study can give new insight into the optoelectronic properties of nitride semiconductors.

GaN wires were grown by metal organic vapour phase epitaxy on a *c*-oriented sapphire substrate (**Figure 6a**). They have their *c*-axis parallel or antiparallel to the growth axis and smooth lateral $\{1\bar{1}0\}m$-plane facets. The coherent Bragg imaging (CBI) technique was used to investigate the arrangement of the inversion domain boundaries inside the GaN wires and the displacement field generated by these defects (**Figure 6b**).

When a crystal is fully illuminated by a coherent X-ray beam, the scattered waves from all parts of the sample interfere in the diffraction pattern. The intensity scattered by the sample is measured in the far field and a real space image of the sample may be reconstructed from the intensity pattern thanks to phase retrieval algorithms [2]. The modulus M(r) and the phase $\phi(\mathbf{r})$ of the reconstructed objects will be displayed in two separate images. M(r) is related to the electron density and ϕ(r) includes the effects of the structure factors and the displacement field. Each Bragg peak is sensitive to the displacement field U(r) projected onto the scattering vector G, *i.e.* G.U(r). In this work, X-ray measurements were performed at beamline **ID01**. We measured five Bragg peaks: 004, 014, 104, 112 and 203. In all three-dimensional diffraction patterns, the measured intensity is concentrated in a (*h*,*k*)-plane perpendicular to the *l*-axis. This means that the inner structure of the measured slab is constant along the wire axis. 2D intensity maps were thus extracted from the 3D data sets in order to reconstruct a 2D image of the sample (**Figure 7**).

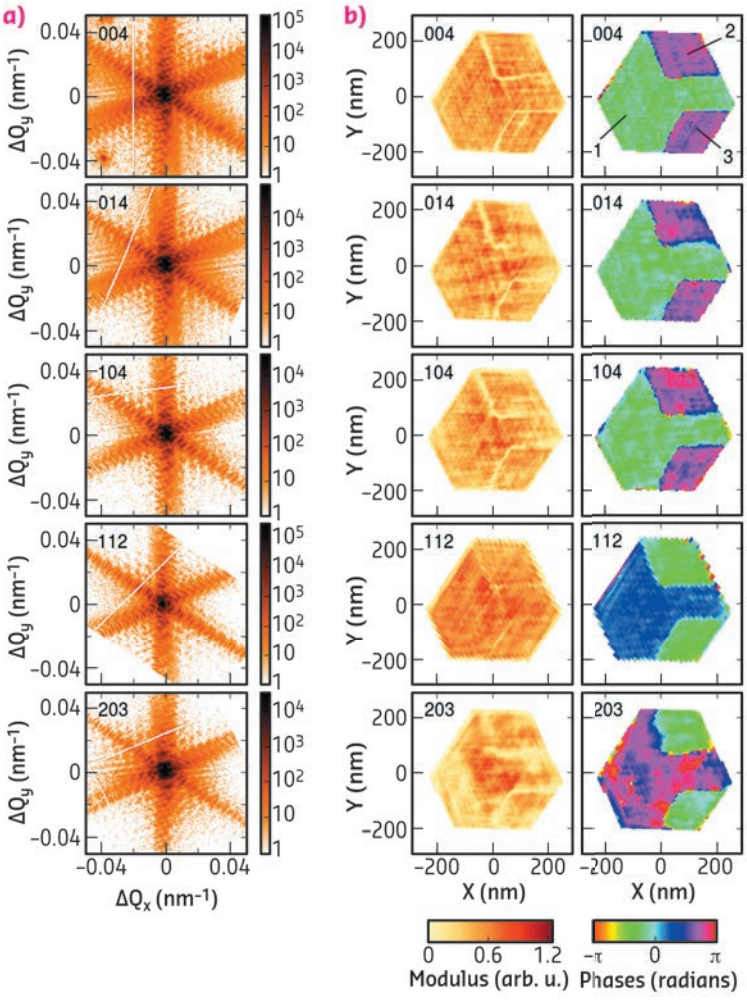

Fig. 7: Coherent X-ray diffraction measurements of five Bragg reflections (a) and the corresponding real space reconstructions (b).

The reconstructions (**Figure 7b**) clearly provide evidence of three domains: one large (1) and two small ones (2-3). The phase values are constant inside the domains and the two small domains show the same phase value for all reconstructions.

The homogeneity of the phase inside the domains denotes the absence of significant strain

variation. The phase difference between the domains originates in the phase difference of the structure factor between Ga and N-terminated GaN domains and a homogeneous displacement of the domains between each other. One has to introduce a rigid displacement of the atomic lattice in the z direction of (c/2+8) pm of the *+c* with respect to the -c domains to match the experimental values. The error bar of this value is estimated to be 1 pm from the accuracy of the phase shift. It is possible to assert that the largest domain is *-c* (N-terminated) and the two small domains are *+c* (Ga-terminated), in agreement with the usual tendency of this type of wire growth.No displacement is needed to fit the experimental phase values in the (x,y)-plane. Nevertheless, the accuracy of the displacement in this plane is lower than the one along the z axis. It is estimated as 4 pm.

These values differ from those calculated for an isolated defect in an infinite media by Northrup *et al.* [3]. Interestingly, our molecular statics calculations with Tersoff-Brenner potential failed to reproduce the displacement field found experimentally, even though the complex configuration of domains had been taken into account.

In conclusion, this study demonstrates that the CBI technique offers a very precise inner view of the microstructure of small crystals in the presence of interacting defects. This technique can be also applied in a straightforward manner to materials under complex environment or *operando* as found in microelectronics and optoelectronics devices.

PRINCIPAL PUBLICATION AND AUTHORS

Inversion domain boundaries in GaN wires revealed by coherent Bragg imaging, S. Labat (a), M.-I. Richard (a,b), M. Dupraz (c,d), M. Gailhanou (a), G. Beutier (c,d), M. Verdier (c,d), F. Mastropietro (a), T.W. Cornelius (a), T.U. Schülli (b), J. Eymery (e,f) and O. Thomas (a), *ACS Nano* **9**, 9210–9216 (2015); doi: 10.1021/acsnano.5b03857.
(a) Aix Marseille Univ., CNRS, Univ. Toulon, IM2NP UMR 7334, Marseille (France)
(b) ESRF
(c) Univ. Grenoble Alpes, SIMAP (France)
(d) CNRS, SIMAP, Grenoble (France)
(e) Univ. Grenoble Alpes (France)
(f) CEA, INAC-SP2M, "Nanophysique et semiconducteurs" group, Grenoble (France)

REFERENCES

[1] S. Nakamura *et al.*, *Jpn. J. Appl. Phys.* **34**, L797-L799 (1995).
[2] M.A. Pfeifer *et al.*, *Nature* **442**,63-66 (2006).
[3] J.E. Northrup *et al.*, *Phys Rev. Lett.* **77**,103-106 (1996).

INDIVIDUAL GaAs NANOWIRES: A CORRELATION OF ELECTRICAL AND STRUCTURAL PROPERTIES

The electrical response of individual as-grown GaAs nanowires on the original silicon substrate has been correlated with their structural quality. The electrical characteristics of single nanowires were measured in a focused ion beam chamber and their polytype composition determined using X-ray nano-diffraction.

Semiconductor nanowires in as-grown geometry on their substrate are promising building blocks for novel electronic, photonic and optoelectronic devices. The electronic band structure and functionality of those devices can be strongly influenced by the crystalline purity of the constituent materials and the presence of different polytypes, such as zinc-blende, twinned zinc-blende and wurtzite. The nanowires under investigation were grown on a Si substrate along the (111) direction with diameter of 100 nm and height of about 1 µm by means of self-assisted molecular beam epitaxy (MBE). Before growth, periodic openings were fabricated through the SiO_2 thermal oxide layer by electron beam lithography with a pitch distance of 2 µm. This allowed the nanowires to be grown only at pre-defined positions across the substrate surface.

Individual free-standing GaAs nanowires were electrically investigated in a dual-focused ion beam (FIB) system. Nanometre-sized tungsten needles with a mean radius of 30 nm were used to contact the top of a selected nanowire. A second contact was made onto the conducting substrate. Subsequently, voltage-current (V-I) characteristics (**Figure 8**) with a voltage varying between -10 V and +10 V were measured using a semiconductor analyser. The inset in **Figure 8** shows the contacting needle close to the top of a single nanowire. Two different electrical regimes were identified in the electrical characteristics: a back-to-back Schottky diode regime, complying

with the thermoionic emission theory, and a space charge limited current regime. Effective mobility and resistance values were extracted for different nanowires, having 10 cm^2/Vs and 10^2 MΩ respective orders of magnitude. To check the reproducibility of the measurements, each nanowire was contacted several times by approaching the W tip to the top and applying different pressures. The current-voltage curves collected were compared to quantify the influence of the contacting procedure, and this constitutes the uncertainty in our measurements.

To determine the origin of the differences detected, the structure of the same individual nanowires was investigated using nanofocused X-ray Bragg diffraction [1,2] at beamline **ID01**. To identify the very same nanowires previously characterised in the FIB chamber, Pt-markers (easily detectable with an optical microscope) were deposited simultaneously in the FIB chamber by a gas injector system close to the position of interest. The X-ray beam used had a photon energy of 7.8 keV, and was focused with a Fresnel Zone Plate (FZP) down to a focal size of 400 x 700 nm^2 providing the spatial resolution required to achieve single nanowire inspection. During the X-ray exposure, a constant nitrogen flux was blown over the sample to protect the nanowires from possible radiation-induced oxidation. To identify the nanowire to be measured, X-ray nano-diffraction maps of large areas on the sample surface were collected under Bragg conditions using the K-map method [3]. For accurate structural characterisation, intensity maps were collected as a function of the three components of the wave vector transfer, *i.e.* reciprocal space maps, at the structurally sensitive [4] asymmetric (331), (422) and (10$\bar{1}$5) reflections. The structural investigation revealed the presence of several zinc-blende and twinned zinc-blende segments, stacked above each other and most likely separated by multiple stacking faults. A correlation was found between the number of these units and the extracted electrical parameters (**Figure 9**). A monotonic increase of the resistive behaviour with the number of segments, and therefore phase boundaries, was observed. The origin of this specific structural configuration may be related to the pressure exerted onto the nanowire during the electrical characterisation. The role played by the contacting procedure acquires therefore great importance. A small plastic deformation may lead to the simultaneous activation of several secant {111} glide planes, and change the nature of the phase boundaries by enhancing the number of stacking faults.

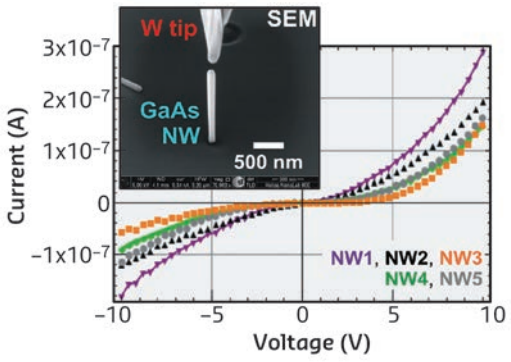

Fig. 8: Voltage–current characteristics of several nanowires (NWs). Inset: Scanning electron microscope (SEM) image of a tungsten contacting needle close to the top of an individual nanowire inside the FIB chamber.

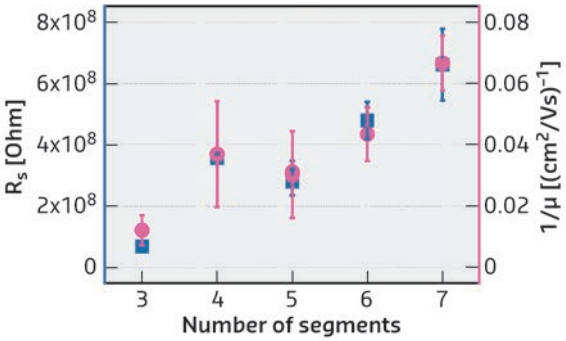

Fig. 9: Total extracted resistance (R_s) and inverse effective mobility (1/μ) as functions of the number of segments (interfaces) within the nanowires.

In conclusion, a method for correlating the differences in the V–I characteristics with the number of intrinsic interfaces within the same individual nanowire was demonstrated. It is suitable for the collection of valuable data for the improvement of growth and contacting techniques, towards tuneable electrical properties.

PRINCIPAL PUBLICATION AND AUTHORS

Correlation of Electrical and Structural Properties of Single As-Grown GaAs Nanowires on Si (111) Substrates, G. Bussone (a,b), H. Schäfer-Eberwein (c), E. Dimakis (d,e), A. Biermanns (b), D. Carbone (a), A. Tahraoui (d), L. Geelhaar (d), P. Haring Bolívar (c), T.U. Schülli (a) and U. Pietsch (b), *Nano Lett.* **15**, 981-989 (2015); doi: 10.1021/nl5037879.

(a) ESRF
(b) Festkörperphysik, Universität Siegen (Germany)
(c) Hochfrequenztechnik and Quantenelektronik, Universität Siegen (Germany)
(d) Paul-Drude-Institut für Festkörperelektronik, Berlin (Germany)
(e) Helmholtz-Zentrum Dresden-Rossendorf, Institute of Ion Beam Physics and Materials Research, Dresden (Germany)

REFERENCES

[1] A. Biermanns *et al.*, *J. Synchrotron Rad.* **16**, 796-802 (2009).
[2] G. Bussone *et al.*, *J. Appl. Crystallogr.* **46**, 887-892 (2013).
[3] G.A. Chahine *et al.*, *J. Appl. Crystallogr.* **47**, 762-769 (2014).
[4] A. Biermanns *et al.*, *J. Appl. Crystallogr.* **45**, 239-244 (2012).

INTRINSIC INHOMOGENEITY OF CHARGE DENSITY WAVE ORDER IN CUPRATES AND SUPERCONDUCTIVITY AT 95 K

The emergence of non-Euclidean geometry at the mesoscale for superconductivity has been shown in a cuprate superconductor at optimum doping, using scanning micro X-ray diffraction. Direct evidence was found for the intrinsic inhomogeneity of the superconducting CuO_2 plane. This experiment provided the imaging of the spatial distribution of charge density wave (CDW) puddles with a power law distribution of the CDW puddle size. The power law exponent of the distribution points toward a hyperbolic space for superconductivity.

A state of matter that allows a macroscopic quantum coherent condensate to resist the decoherence effect of high temperature is of interest for material science and other fields ranging from the physics of life, quantum biology and new quantum technologies such as quantum computing.

Standard BCS superconductors must be cooled to temperatures close to absolute zero to operate. A couple of decades ago, a ceramic material, La_2CuO_{4+y} doped by oxygen interstitials (O-i), was discovered to exhibit superconductivity around 40 K. This was followed by the discovery of other superconducting cuprate perovskites made of a CuO_2 atomic layer intercalated with different spacer layers. The maximum superconducting critical temperature in a single layer of cuprate, T_c = 95 K, was achieved in $HgBa_2CuO_{4+y}$, by optimisation of the misfit strain between the CuO_2 layer and the spacer layers. Following joint EXAFS and diffraction experiments, it was proposed that a new phase of matter, called superstripes, appears at optimum microstrain of the CuO_2 plane and at optimum doping [1]. The superstripes phase is generated by the spontaneous breaking of both translational symmetry (CDW electronic crystalline phase) and gauge symmetry (superconductivity).

We have used an approach based on scanning synchrotron radiation diffraction measurements, carried out at beamline **ID13** using a focussed microbeam. The CDW size distribution and their spatial arrangement has been determined at the nanoscale and the mesoscale. We studied the tetragonal $HgBa_2CuO_{4+y}$ doped by oxygen interstitials with T_c = 95 K.

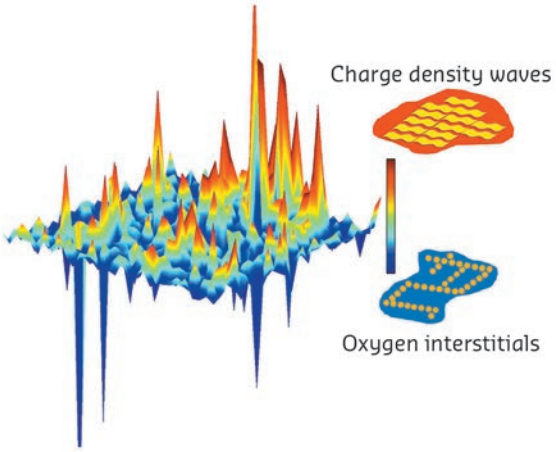

Fig. 10: Spatial anti-correlation of charge density wave order (CDW puddle rich regions in green to-red) and oxygen interstitial stripes density (green to blue) on a 30 x 30 μm² area of $HgBa_2CuO_{4+y}$.

We visualised the oxygen interstitials (O-i) in the spacer layers $HgBa_2O_{2+y}$, already observed in other cuprates [2-4]. The oxygen interstitials introduced as dopants form atomic stripes of defects that are anti-correlated with electronic CDW puddles forming inhomogeneous patterns as shown in **Figure 10**. We found that electrons form short range CDW puddles, as reported recently for many cuprates [5], at temperatures lower than 240 K. At 100 K, near the onset of superconductivity, the size of the CDW puddles in the CuO_2 plane shows a power law distribution as shown in **Figure 11**.

Therefore, the CDW puddles introduce a significant topological change in the available space for the free electrons that do not crystallise,

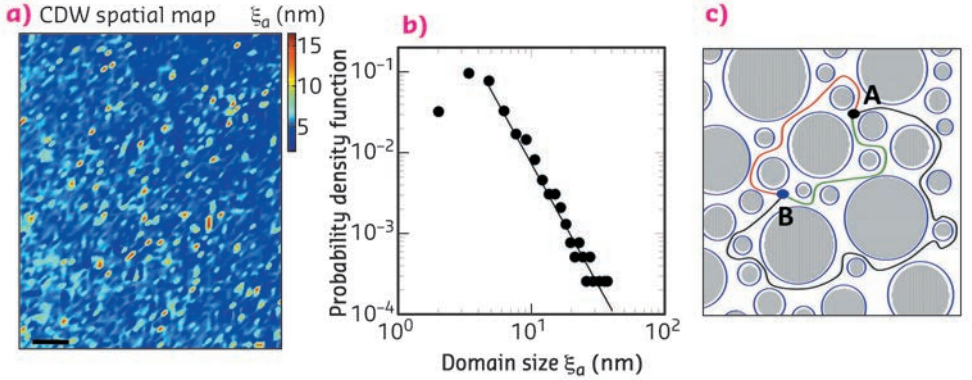

Fig. 11: (a) Spatial map of the CDW puddles size (scale bar 10 μm) and (b) Probability density function (PDF) of the CDW puddles size. c) Pictorial view of the superconducting current running in the interface space between CDW puddles.

making Cooper pairs flow in the interstitial space outside of the CDW puddles at low temperatures. In this landscape, electrons that go from a point A to a point B can take different paths that cannot be topologically deformed one into the other. Figure 11 shows possible paths taken by electrons at the Fermi level running in the interfacial space outside of the CDW puddles. These paths go around the CDW puddles in different ways creating non-trivial paths for electrons which are mapped into a hyperbolic space for a system of puddles with power law distribution.

In conclusion, we have found an intrinsic inhomogeneity in a tetragonal cuprate perovskite with a very high critical temperature, T_c = 95 K, both in the spacer and in the active superconducting layers. It is known that *random* disorder suppresses the critical temperature, but here the oxygen interstitials form a *correlated* quenched disorder of atomic wires in the spacer layers. The O-i rich zones are anti-correlated with CDW nanopuddles in the CuO_2 plane showing a power law distribution, as has already been found in La_2CuO_{4+y} [4]. The emerging complex phase separation at the mesoscale shows a spatial charge distribution resulting from competition between O-i rich domains and CDW puddles where the interface space between CDW puddles (loci of superconductivity) shows an emergent non-Euclidean hyperbolic geometry favouring superconductivity.

PRINCIPAL PUBLICATION AND AUTHORS

Inhomogeneity of charge density wave order and quenched disorder in a high Tc superconductor, G. Campi (a,b), A. Bianconi (a,b), N. Poccia (b,c), G. Bianconi (d), L. Barba (e), G. Arrighetti (e), D. Innocenti (b,f), J. Karpinski (f,g), N.D. Zhigadlo (g), S.M. Kazakov (g,h), M. Burghammer (i,j), M. v. Zimmermann (k), M. Sprung (k) and A. Ricci (b,k), *Nature* **525**, 359 (2015); doi: 10.1038/nature14987.
(a) Institute of Crystallography, CNR, Monterotondo Roma (Italy)
(b) Rome International Center for Materials Science, Superstripes, RICMASS, Roma (Italy)
(c) MESA+ Institute for Nanotechnology, University of Twente, Enschede (Netherlands)
(d) School of Mathematics, Queen Mary University of London (UK)
(e) Institute of Crystallography, Sincrotrone Elettra UOS Trieste (Italy)
(f) EPFL, Institute of Condensed Matter Physics, Lausanne (Switzerland)
(g) ETH, Swiss Federal Institute of Technology Zurich Laboratory for Solid state Physics (Switzerland)
(h) Department of Chemistry, M.V. Lomonosov Moscow State University (Russia)
(i) ESRF
(j) Department of Analytical Chemistry, Ghent University (Belgium)
(k) Deutsches Elektronen-Synchrotron DESY, Hamburg (Germany)

REFERENCES

[1] A. Bianconi, *Int. J. Mod. Phys. B*, **14**, 3289 (2000).
[2] N. Poccia, *et al.*, PNAS (USA) **109**, 15685-15690 (2012).
[3] G. Campi *et al.*, *Phys. Rev. B*, **87**, 014517 (2013).
[4] M. Fratini *et al.*, *Nature* **466**, 841-844 (2010).
[5] E.W. Carlson, *Nature* **525**, 329–330 (2015).

RESIDUAL STRAIN IN THE MINERAL NANOPARTICLES OF HUMAN TOOTH DENTINE MAKES TEETH STRONGER

Human teeth operate in the mouth for many decades where they are subjected to huge forces and much wear and tear. The main tooth bulk material is dentine, which supports enamel externally, and is very tough and damage resistant. Evidence was found for the role of a previously overlooked toughening mechanism, arising from residual strain in the nanocomposite ultrastructure of dentine.

Dentine is a bone like biological nanocomposite, built of crystalline mineral particles, collagen fibres, and water [1]. This nanocomposite contains tubules, channels formed by odontoblast cells that produce dentine during tooth genesis. These cells typically reside in the pulp of normal 'living' teeth, sending out long 'finger like' extensions into the tubules. The tubules traverse the entire dentine tissue thickness, and they course through the mineralised collagen layers where they are surrounded by thick micrometre-sized 'peritubular' mineral sheaths (Figure 12). Mineralised collagen fibres are arranged in layers perpendicular to the tubules, and form a fibrous mass of inter-tubular dentine. Just how these different mineralised structures 'work' together to help dentine survive the excessive cyclic loading is still a mystery. This is particularly curious considering the lack of a self-healing biological mechanism such as remodelling, which is known to exist in bone.

To shed additional light on the link between the micro-architecture of dentine and its remarkable structural integrity, we combined synchrotron-based diffraction methods at different length

scales: a micrometre-sized beam in MySpot at BESSY, Germany and a nanofocused X-ray beam at the former **ID22NI** beamline (now ID16A/B) for diffraction nanotomography. We revealed important differences in the spatial arrangement of the nanometre-sized mineral crystallites. Diffraction nanotomography (see **Figure 13**) showed that crystallite alignment with the collagen fibres in the inter-tubular dentine differs from crystallite alignment in the peritubular dentine. The c-lattice parameters of apatite in differently treated samples of human tooth dentine were analysed along various azimuthal orientations of the radii of the apatite (002) Debye rings. The analysis, performed using XRDUA [2], showed that mineralised particles attached to dry collagen are under compression, and that compressive stresses vary as a function of humidity. Compression is no longer apparent when the collagen is destroyed by heating.

We conclude that in the native tissue there is strong interaction of the mineral particles with the organic matrix that leads to significant compression of the mineral-particles, and we propose that this interaction is important for energy dissipation and damage resistance in teeth. This conclusion is corroborated by the observation that crystallites that are co-aligned with collagen fibres become more compressed than mineral particles of the tubules. The residual strains are completely eliminated by mild annealing at 250°C, *i.e.* when the organic component is destroyed [3]. The compressive strain and corresponding mineral-particle deformation correlate with the collagen layered arrangement, and presumably work against crack propagation from outside the tooth towards the pulp, across the layers, thus increasing resistance of the biostructure as a whole.

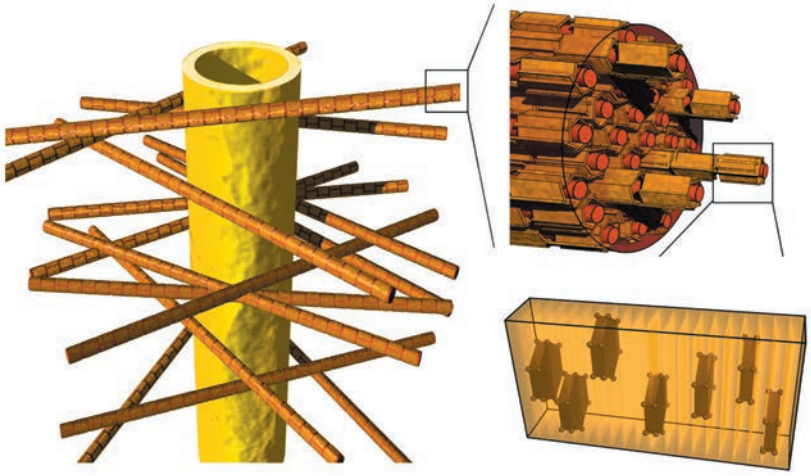

Fig. 12: Schematic representation of the dentine nanocomposite structure made of collagen fibres embedded in mineral, oriented orthogonally to dental tubules that lead to the pulp. The c-axis of the mineral particles in the fibres is aligned with the collagen axis.

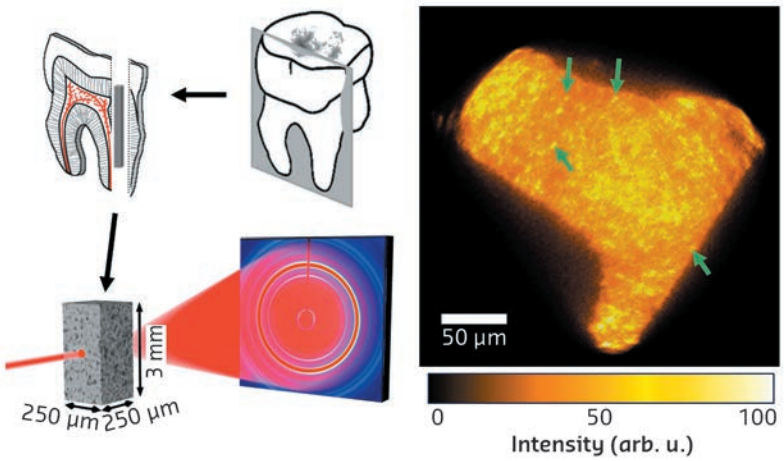

Fig. 13: Slices cut from human teeth were used to create small pin-like bars which were mounted for diffraction-tomography at ID22NI. More than 15,000 diffraction images were analysed and the intensity distribution of the apatite 002 peak was mapped across the dentine microstructure. High intensity spots are distributed throughout the structure (green arrows) and correspond mainly to dentine tubules, with distinctly different mean orientation of the mineral particles, as compared to the general collagen-rich mineralised matrix, surrounding the tubules.

Engineers use internal stresses to strengthen materials for specific technical purposes, for example in concrete. Evolution has presumably 'known' about this trick for a long time, and has incorporated it into our natural teeth. Our findings suggest that residual stress and mineral compression mediated by the collagen/mineral interactions contribute significantly to the strengthening and toughening of teeth, complementing other toughening mechanisms and well-known structural strategies, acting in all similar bony biocomposites at larger length scales (*e.g.* microcracking). We believe that the balance of stresses between the nanoparticles and collagen and, especially, mineral compression initiated by the collagen/mineral bond, are important for the extended survival of teeth in the mouth.

PRINCIPAL PUBLICATION AND AUTHORS

Compressive residual strains in mineral nanoparticles as a possible origin of enhanced crack resistance in human tooth dentin, J.-B. Forien (a), C. Fleck (b), P. Cloetens (c), G. Duda (a), P. Fratzl (d), E. Zolotoyabko (e) and P. Zaslansky (a), *Nanoletters* **15**, 3729–3734 (2015); doi: 10.1021/acs.nanolett.5b00143.

(a) Julius Wolff Institute, Charité – Universitätsmedizin, Berlin (Germany)
(b) Materials Engineering, Berlin Institute of Technology, Berlin (Germany)
(c) ESRF
(d) Department of Biomaterials, Max-Planck-Institute of Colloids and Interfaces, Potsdam (Germany)
(e) Department of Materials Science and Engineering, Technion – Israel Institute of Technology, Haifa (Israel)

REFERENCES

[1] P. Zaslansky, 'Dentine' in P. Fratzl (Ed.), Collagen: structure and mechanics, Springer, New York (2008), pp. 421–442.
[2] W. De Nolf *et al.*, *Appl. Crystallogr.* **47**, 1107–1117 (2014).
[3] S.R. Armstrong *et al.*, *J. Endod.* **32**, 638–641 (2006).

ANALYSIS OF SOLID OXIDE CELL PERFORMANCE AND DEGRADATION BY X-RAY PHASE NANOTOMOGRAPHY

Efficiency and durability of solid oxide cells are important for the development of high temperature electrochemical converters. By analysing three-dimensional reconstructions of the electrodes obtained with X-ray phase nanotomography, a better understanding has been gained of the basic local phenomena that govern the macroscopic cell behaviour in terms of performance and degradation.

Solid oxide cells (SOCs) have potential for use as electrochemical converters operating at high temperatures. Their advantages include a high flexibility in terms of technological applications. For example, the same object can be alternatively used in fuel cell and steam electrolysis modes. In addition, high efficiency for hydrogen production and electrical power generation can be reached without the use of expensive electrocatalysts. Nevertheless, SOCs will become a competitive technology only if durability issues are solved.

SOCs consist of a ceramic multilayer cell, composed of a dense electrolyte sandwiched between two porous electrodes. The electrode microstructure plays a major role in the global electrolyser efficiency by controlling the rates of the electrochemical reactions. Moreover, evolution of the electrode microstructure in operation is widely correlated with cell degradation, even if the basic mechanisms are still not understood.

The global SOCs response is complex and depends on local electrode properties. Therefore, models describing the global SOC operation coupled to local visualisation of the fine electrode microstructure could help to unravel the SOCs operating mechanisms. An in-house multi-scale and multi-physics model has been developed at the CEA in collaboration with the ESRF [1-4]. Three dimensional reconstructions of electrodes are required in order to determine key model parameters for an accurate description of the electrode microstructure. To obtain both a large field of view and a high spatial resolution, X-ray phase nanotomography, or magnified holotomography, was selected for this study, using the former ESRF beamline ID22NI, now ID16A/B.

The methodology has been applied to different commercial cells composed of the typical SOCs materials. Hydrogen electrodes were made of a cermet of nickel and yttria stabilised zirconia (Ni-YSZ). The setup and data processing have been specifically adapted to handle such strongly absorbing ceramic materials by using harder X-rays and optimising the phase retrieval procedure. X-ray phase nanotomography was performed at an energy of 30 keV and electrode reconstructions were obtained with a field of view of 50 µm and a spatial resolution of about 75 nm (25 nm voxel size) [5].

The reconstruction of a Ni-YSZ electrode bilayer (**Figure 14**) has been analysed numerically to compute all its morphological properties. Thanks to the large field of view of the reconstructions, all the microstructure properties have been successfully quantified with a high level of confidence [6,7]. These microstructural parameters were used to simulate the electrode overpotential at the microscopic scale as a function of temperature [6]. A deconvolution between the thermally activated processes has been proposed. This allows basic degradation mechanisms to be investigated.

A major degradation phenomenon occurring in electrolysis mode corresponds to nickel agglomeration in the Ni-YSZ cathode. The Ni particle coarsening was observed by X-ray phase

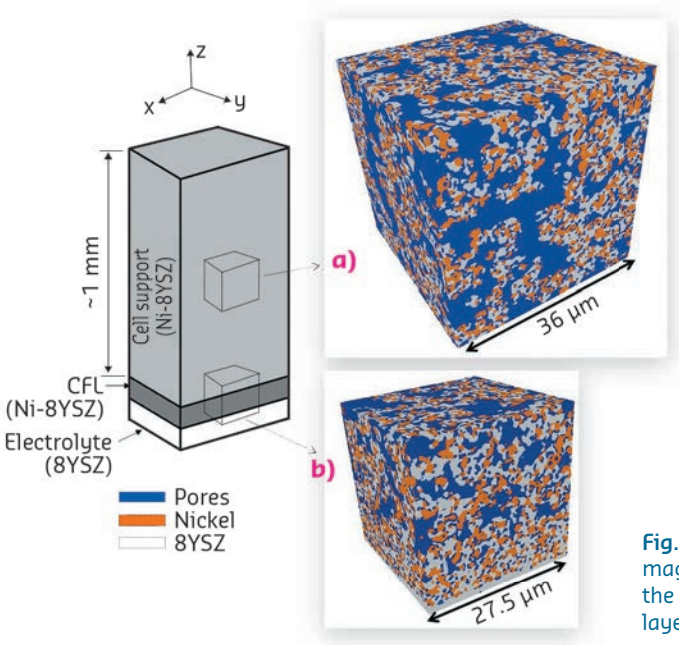

Fig. 14: 3D volume renderings of Ni-YSZ cermet obtained by magnified holotomography [5,6]. (a) Reconstruction taken in the cell support. (b) Reconstruction of the cathode functional layer (with a part of the support and the electrolyte).

nanotomography. Microstructural properties extracted from the 3D reconstructions, such as the Ni/YSZ/gas triple phase boundary (TPB) lengths, exhibit a remarkable evolution during the long term tests (**Figure 15**). The evolution of morphological parameters was introduced in the micro and macro models to evaluate their impact on the cell response. It has been found that the decrease in density of TPB length results in a significant cell voltage increase, which explains the main part of the degradation rates.

To enhance the predictive power of the simulation tools, physical models of Ni coarsening need to be calibrated. Therefore, a next step will be to obtain reconstructions of Ni particles before and after coarsening with improved spatial resolution at the new beamline ID16A.

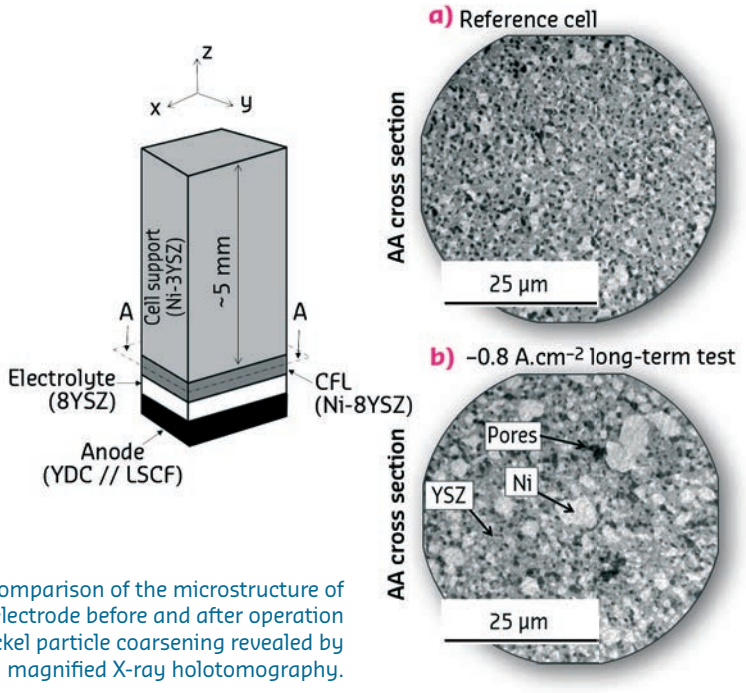

Fig. 15: Comparison of the microstructure of the Ni-YSZ electrode before and after operation showing nickel particle coarsening revealed by magnified X-ray holotomography.

PRINCIPAL PUBLICATION AND AUTHORS

Degradation study by 3D reconstruction of a nickel–yttria stabilised zirconia cathode after high temperature steam electrolysis operation, E. Lay-Grindler (a), J. Laurencin (a), J. Villanova (b), P. Cloetens (b), P. Bleuet (a), A. Mansuy (a), J. Mougin (a) and G. Delette (a), *Journal of Power Sources* **269,** 927-936 (2014); doi: 10.1016/j.jpowsour.2014.07.066.

(a) CEA-LITEN, Grenoble (France)
(b) ESRF

REFERENCES

[1] J. Laurencin *et al.*, *J. Euro. Ceram. Soc.* **28**, 1857-1869 (2008).
[2] J. Laurencin *et al.*, *J. Power Sources* **196**, 2080–2093 (2011).
[3] G. Delette *et al.*, *Inter. J. Hydrogen Energy* **38**, 12379-12391 (2013).
[4] E. Lay-Grindler *et al.*, *Int. J. of Hydrogen Energy* **38** 6917-6929 (2013).
[5] J. Villanova *et al.*, *J. Power Sources* **243**, 841-849 (2013).
[6] F. Usseglio-Viretta *et al.*, *J. Power Sources* **256**, 394-403 (2014).
[7] J. Laurencin *et al.*, *J. Power Sources* **198**, 182-189 (2012).

NANOSCOPIC X-RAY FLUORESCENCE IMAGING OF METEORITIC PARTICLES AND DIAMOND INCLUSIONS

The elemental composition of geological samples represents key-information for identifying the component phases. In particular, when dealing with extra-terrestrial samples such as meteorite fragments, the precise elemental signature can shed light on the origin of the material. Here, fragments from the achronditic meteorite NWA 6693 and diamond inclusions have been studied at the new ESRF ID16B nano-analysis beamline.

Unlike most achondrites, which can usually be classified according to a common origin, NWA 6693 does not belong to a specific group. Several bubble-like tracks are present inside this meteorite, some of which consist of various mineral phases. Our study at ID16B aimed to gather high-resolution elemental information on these structures, allowing a further expansion of our knowledge on the origin, formation and history of the meteorite.

An overview scan of 100 x 100 µm^2 was made to locate the bubble stream inside the fragment of NWA 6693, using a fast-scanning procedure (50 ms dwell time, 100 nm step size). Significant amounts of Ca, Ti, Cr, Mn, Fe, Ni and As were detected within the investigated area. Using the chromium elemental map, several regions of interest (ROI) were selected for detailed, high-resolution analysis (25-40 nm steps) with longer measurement time (1 s per point). **Figure 16** shows the Cr overview map, combined with an RGB composite image from the respective Fe, Cr and Ni elemental distributions obtained from one of the high-resolution scans. As observed, the matrix of the meteorite fragment is mainly

composed of Fe-rich phases (*i.e.* pyroxene and olivine), while most inclusions are rich in Cr with trace amounts of Ti and Mn, a minor fraction of the inclusions consists of Ni combined with As and Ca. The mere size of the inclusions demonstrates the need for nanoscopic analysis techniques in the study of this kind of samples.

Nano-XRF spectroscopy was also used in the study of diamond inclusions. During the formation and growth of diamonds, fluids, rock fragments and minerals can be trapped within, thus being shielded from the environment when the diamond is transported to the surface of the Earth. By conserving materials which are unattainable by other means, diamond inclusions give a unique insight into the interior of our planet. Recently, scientists identified a diamond inclusion as ringwoodite (*i.e.* a hydrous Fe phase), which was its first discovery in natural, terrestrial material. The presence of this hydrous phase in the interior of the Earth might play an important role in terrestrial magnetism and plate tectonics. Preliminary studies using Raman spectroscopy indicated the possible presence of ringwoodite in diamond SL05. Nano-XRF spectroscopy was employed to image the inclusions in SL05 at higher resolution to gain insights into the elemental distributions in a non-destructive manner allowing for future studies using multiple analytical methods.

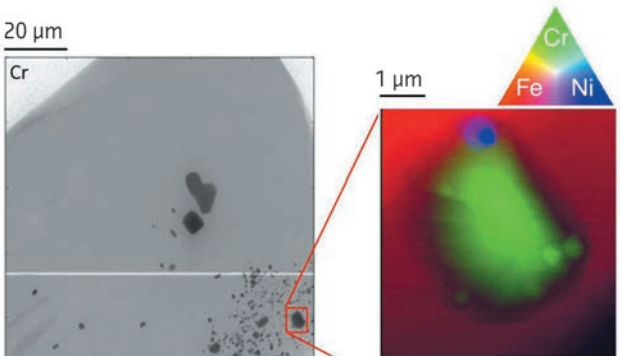

Fig. 16: XRF overview map (Cr) of NWA 6693 fragment (100 x 100 µm^2, 100 nm step size, 50 ms per point) and Fe/Cr/Ni RGB image of indicated ROI (7 x 6 µm^2, 40 nm step size, 1 s per point) beam dimensions for both scans: 46 nm (v) x 50 nm (h), excitation energy 17.5 keV.

The analysis of the diamond inclusions followed the same pattern as the study of the meteorite fragments. A 100 x 100 µm^2 overview map (**Figure 17**) of the region where preliminary studies indicated the possible presence of ringwoodite was used to select a ROI for detailed investigation. As observed, significant amounts of Ca, Ti, Cr, Fe, Ni, Cu, Zn and As were found to be present within the area investigated. The distribution of some of these elements is represented in **Figure 17**, revealing a localised aggregation of Cu and Zn, representing elements that are not usually linked to materials stemming from deep Earth. Detailed analysis using PCA and K-means clustering indicated these elements are present in a single, relatively large particle. This could have been a secondary phase that adhered to the diamond during its voyage to the surface of the Earth. In contrast, the presence of Fe-rich particles is an important observation with respect to the hypothesised presence of a ringwoodite inclusion in SL05.

The study of these rare geological samples has clearly proven the potential and importance of nanoscopic XRF analysis as a non-destructive imaging tool yielding valuable and otherwise unreachable information to add to our knowledge of the planet and even the universe.

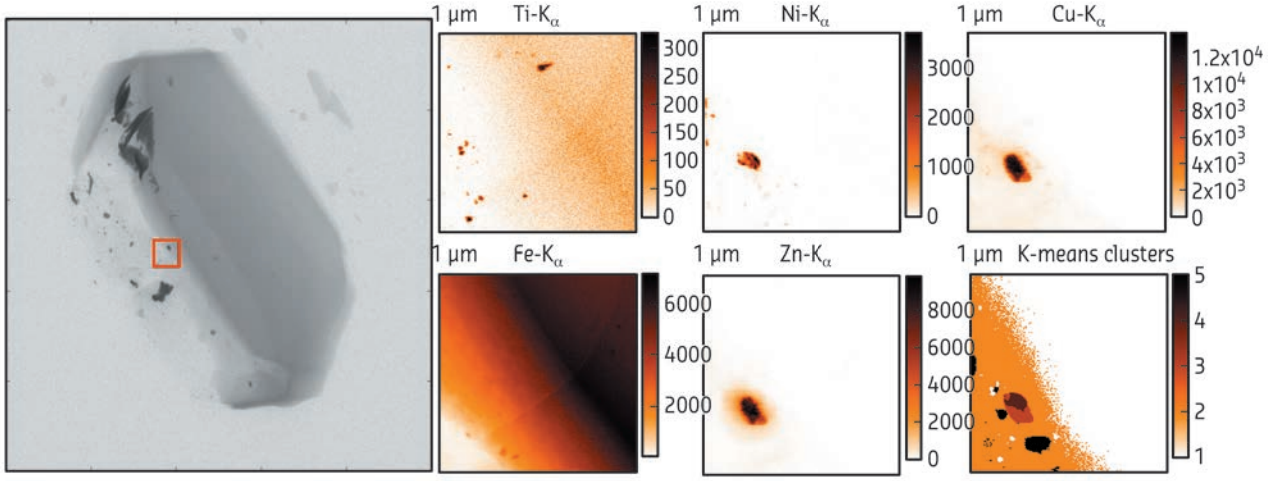

Fig. 17: XRF overview map (Fe) of diamond SL05 (100 x 100 µm^2, 100 nm step size, 50 ms per point) with element distributions of Ti, Fe, Ni, Cu and Zn in indicated ROI (7 x 6 µm^2, 40 nm step size, 1 s per point) beam dimensions for both scans: 46 nm (v) x 50 nm (h), excitation energy 17.5 keV.

PRINCIPAL PUBLICATION AND AUTHORS

Nanoscopic X-ray fluorescence imaging of meteoritic particles and diamond inclusions, B. Laforce (a), S. Schmitz (b), B. Vekemans (a), J. Rudloff (b), J. Garrevoet (a), R. Tucoulou (c), F.E. Brenker (b), G. Martinez-Criado (c) and L. Vincze (a), *Analytical Chemistry* **86**, 12369-12374 (2015), doi: 10.1021/ac503764h.

(a) X-ray Microspectroscopy and Imaging Group (XMI), Ghent University (Belgium)
(b) GeoScience Institute, JWG University (Germany)
(c) ESRF

PROBING NANOWIRES IN THE SPATIAL AND TIME DOMAINS

An imaging tool to investigate nanowires with site, optical and chemical sensitivity has been developed using pulsed hard X-ray nanobeams. Its unprecedented temporal and spatial resolution provided a deeper understanding of geometrical size-dependent phenomena. The approach opens new avenues for further imaging studies in nanoscience.

Interest in semiconductor nanowires for nanoscale devices has been greatly driven by their simultaneous capability of optical guiding and electrical driving, and large surface to volume ratio, which is crucial for sensitive and selective sensors. Although it is rather difficult to find single analytical tools covering simultaneously several properties in the length and time scales, most nanowire applications rely on the ability not only to grow, but also to fully characterise individual and collections of nanowires. Accordingly, synchrotron based nanoprobes in the multi-keV energy range have great potential in terms of surface/deep information depths, element-, site-, and orbital-selectivity, structural and chemical trace sensitivity, as well as temporal effects.

Examples of the use of hard X-ray nanobeams at beamline ID22 in the determination of spatially-resolved properties of nanowires by concurrent X-ray fluorescence (XRF), X-ray absorption, and/or X-ray diffraction include the investigation of the ion implantation process in a possible formation of magnetic precipitates in single ZnO nanowires [1], the spontaneous phase segregation in single $In_xGa_{1-x}N$ nanowires [2], local order in crossed Ga_2O_3/SnO_2 wires [3], as well as the controlled epitaxy of core-multishell InGaN/GaN multiquantum well wires [4].

As an illustration, here we show how a hard X-ray nanoprobe was used for the first time to examine geometrical quantum confinement within a single coaxial nanowire based light emitting diode. Owing to its central role in limiting carrier dynamics, the specific use of the X-ray excited optical luminescence (XEOL) technique allows the optical imaging of nanosized-dependent dynamics in core-multishell nanowires.

Figure 18 shows a schematic of the ID22 nanoprobe (now at ID16B) that provides simultaneous compositional, structural, and optical information with high spatio-temporal resolution. Apart from the emission of characteristic secondary X-rays collected with a Si drift detector, while raster-scanning the sample, the X-ray diffraction patterns can be recorded with a FReLoN camera, and the emitted photons detected by a far-field optical system. As a proof of concept, the XEOL approach has been applied to hexagonal

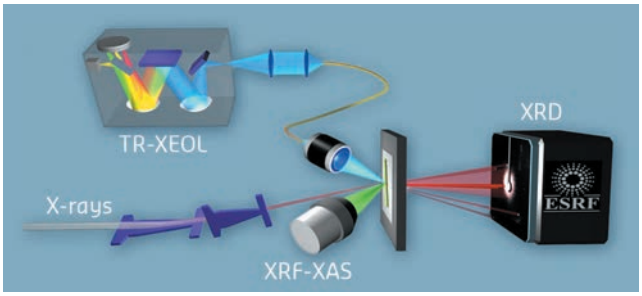

Fig. 18: Multimodal setup at the former nanoprobe beamline ID22 (now at ID16B).

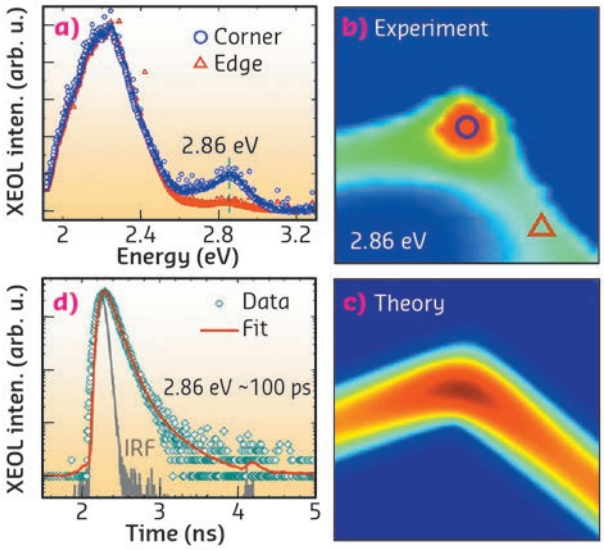

Fig. 19: (a) XEOL spectra acquired at the corner and at the edge of the hexagonal core-multishell nanowire. (b) XEOL intensity map of the emission at 2.86 eV (1.8 x 1.8 μm^2). (c) Electron probability density calculated for the same structure. (d) Time-resolved XEOL decay curve recorded for the 2.86 eV band at the hexagon corner.

n-GaN/$In_xGa_{1-x}N$/n-GaN nanowire based light emitting diodes. XRF analyses (not shown) revealed that the radial chemical composition is consistent with the targeted heterostructure design. After the X-ray absorption process, an electron is promoted to a high energy state above the Fermi level, leaving behind a hole in the core shell. Both carriers relax their energy mostly by emission of photons (XRF), electrons, and lower energy phonons until they find their corresponding band minima near the semiconductor band gap energy (typically 0.5-3 eV). The XEOL signal arises from the radiative recombination of these thermalised electron hole pairs that have a characteristic decay time ranging from a few tens picoseconds to a few tens of nanoseconds depending on their spatial overlap.

Figure 19 displays different results for an $In_xGa_{1-x}N$/GaN core-multishell nanowire by

scanning a 60 x 60 nm^2 X-ray spot across its radial direction. The spectra shown in **Figure 19a** have been taken at the edge and the corner of the hexagon, respectively. In both cases, two emission bands can be identified: a broad band at 2.21 eV attributed to the common yellow band, which has the largest excited volume, and a narrower band at 2.86 eV attributed to the transitions from the InGaN/GaN multiquantum wells. **Figure 19b** displays the spatial projection of the luminescence intensity at 2.86 eV. The multiquantum wells signal appears confined to the edges of the nanowire, revealing intensity maxima at the hexagon corners. Theoretical calculations indicate that geometrical quantum confinement might be responsible for this effect.

The square of the electron wave function in its ground state is depicted in **Figure 19c**. The wave function for the electrons in its lowest energy state, and similarly for the holes (not shown), is localised at the corner, decaying towards the edges of the hexagon. **Figure 19d** shows the fast luminescence decay curve of the multiquantum wells emission measured at the hexagon corner. Using the 16-bunch filling mode of the storage ring [5.68 MHz repetition frequency and 50 ps pulse duration], time-resolved-XEOL data could also be simultaneously collected with the X-ray nanoprobe. The decay time of 100 ps clearly supports the ultrafast recombination processes related to the intriguing quantum confinement size effects as well.

PRINCIPAL PUBLICATION AND AUTHORS

Exploring single semiconductor nanowires with a multimodal hard X-ray nanoprobe, G. Martínez-Criado (a), J. Segura-Ruiz (a), B. Alén (b), J. Eymery (c), A. Rogalev (a), R. Tucoulou (a) and A. Homs (a), *Advanced Materials* **26**, 7873-7879 (2014); doi: 10.1002/adma.201304345.
(a) ESRF
(b) IMM-Instituto de Microelectrónica de Madrid (CNM-CSIC), Tres Cantos (Spain)
(c) Equipe mixte CEA-CNRS-UJF "Nanophysique et semiconducteurs", SP2M, UMR-E CEA/UJF-Grenoble 1, INAC, Grenoble (France)

REFERENCES

[1] J. Segura-Ruíz *et al.*, *Nano Letters* **11**, 5322 (2011).
[2] J. Segura-Ruíz *et al.*, *Nano Letters* **14**, 1300 (2014).
[3] G. Martínez-Criado *et al.*, *Nano Letters* **14**, 5479 (2014).
[4] G. Martínez-Criado *et al.*, *Nano Letters* **12**, 5829 (2012).

VAN GOGH'S SUNFLOWERS: EVIDENCE OF DEGRADATION OF THE CHROME YELLOWS

The darkening of the yellow colours in Van Gogh's *Sunflowers* (Van Gogh Museum, Amsterdam) has been strongly debated over the past few decades. This study presents firm evidence of the chemical alteration of chrome yellows in this iconic painting, outlining the regions with the highest risk of colour change due to the instability of the pigment used.

The fourth version of *Sunflowers*, painted by Vincent van Gogh in Arles in 1888-1889, comprises three similar paintings that are now on display at the National Gallery in London, the Seji Togo Memorial Sompo Japan Nipponkoa Museum of Art (Tokyo) and the Van Gogh Museum (Amsterdam), respectively. The vibrancy of these artworks was made possible by the use of chrome yellows (CYs), an early 19th century pigment class of which the hues ranged from lemon-yellow to orange-yellow. Despite their strong similarities, the three paintings feature different yellow tonalities with subtle variations in contrast among the sunflower petals, the background and the table area.

The extent to which different yellow shades are ascribable to Van Gogh's stylistic choices (via the use of paint mixtures) and/or to unintended effects of colour changes (due to the degradation of original materials) has been questioned.

Earlier Cr K-edge μ-XRF/μ-XANES investigations at **ID21** proved that the darkening of different CY types ($PbCr_{1-x}S_xO_4$, with $0 \leq x \leq 0.8$) in artificially aged paint models and microsamples taken from several Van Gogh paintings is due to a photo-redox process [1-4]. The formation of reduced Cr is more favoured for sulfate-rich, lemon-yellow, orthorhombic $PbCr_{1-x}S_xO_4$ varieties of the pigment (with $x > 0.4$) than for the orange-yellow, monoclinic $PbCrO_4$ that is the most lightfast of these materials [1,2].

In this study, non-invasive *in situ* spectroscopic investigations of the painting combined with synchrotron-based X-ray analysis of two microsamples were performed to assess the extent to which the *Sunflowers* version of the Van Gogh Museum (**Figure 20a**) contains lightfast $PbCrO_4$ (denoted as LF-CY) and light sensitive S-rich $PbCr_{1-x}S_xO_4$ ($x > 0.4$) (LS-CY), as well as to determine whether or not these

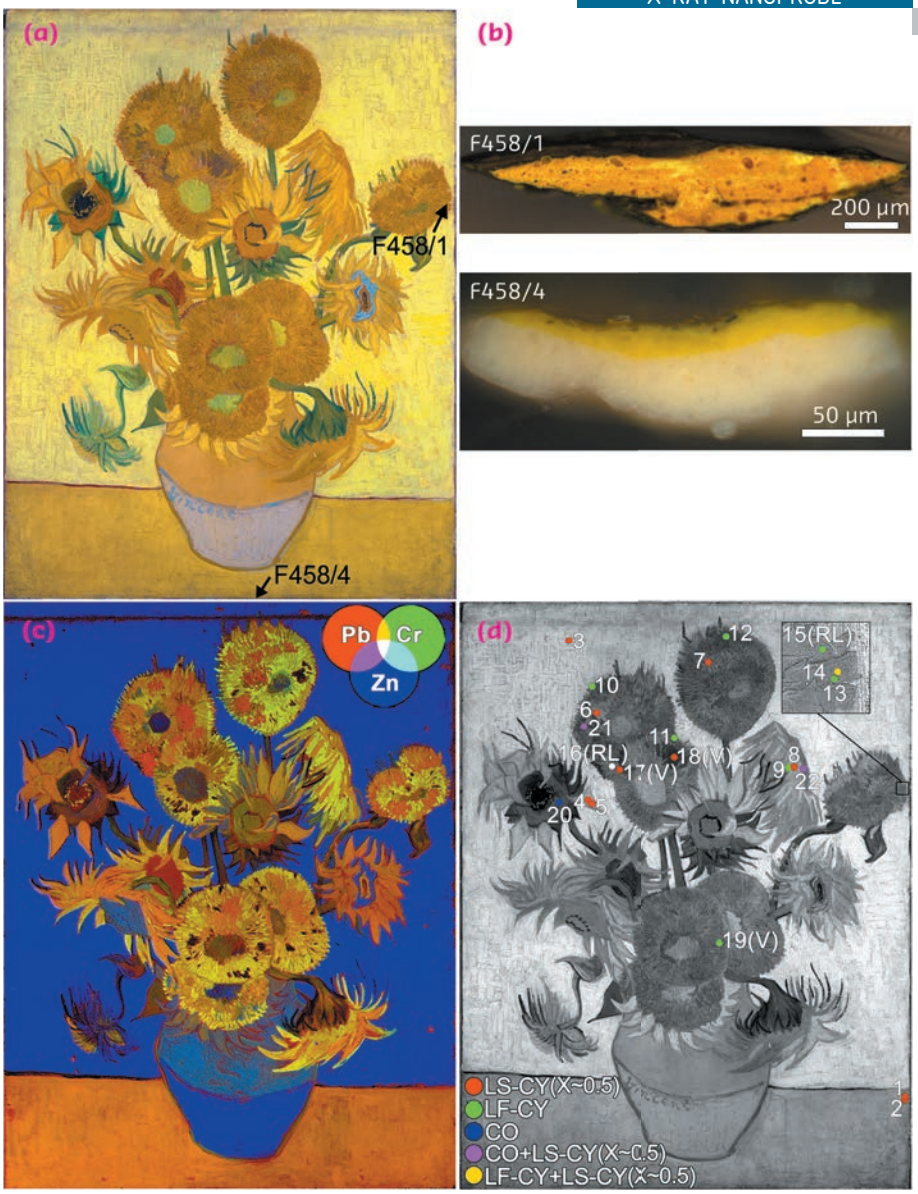

Fig. 20: (a) Photograph of Van Gogh's *Sunflowers* (Van Gogh Museum, Amsterdam) and (b) corresponding analysed micro-samples. (c) RGB composite MA-XRF maps of Pb/Cr/Zn. (d) Raman distribution of different CY types [LS-CY: light sensitive chrome yellow-$PbCr_{1-x}S_xO_4$ (x~0.5); LF-CY: lightfast chrome yellow-$PbCrO_4$; CO: chrome orange-$(1-x)PbCrO_4{\cdot}xPbO$)]. "V" and "RL" indicate spots containing also vermilion and red lead, while the white circle shows the location where only red lead was identified.

pigments have been subject to a reduction process.

Non-invasive MA-XRF scanning combined with vibrational spectroscopic analysis (**Figure 20c-d**) revealed the use of different CYs, including the LF-CY and the LS-CY (x~0.5). Since these compounds were found in mixtures with other pigments (*e.g.* vermilion, zinc white, emerald green, red lead) as well as in unmixed form, the visual assessment of any colour change due to photo-reduction of the chromate is not straightforward.

The degradation state of the CY paint was evaluated by determining the Cr-oxidation state *via* Cr K-edge µ-XANES/µ-XRF analysis of two microsamples (**Figure 20b**) at **ID21**.

Clear indications of the presence of reduced Cr were found inside the varnish layer and at the varnish/paint interface of both these materials. At one location of sample F458/4 (from the light-yellow table; **Figure 21a-b**), a Cr-rich particle is completely reduced to the Cr^{III}-state and the corresponding µ-XANES spectrum (**Figure 21d**: pt $01_{4\text{-I}}$) resembles that of Cr_2O_3. In the area surrounding this particle, the relative abundance of Cr^{III} was around 50% (pt $02_{4\text{-I}}$). In another region (**Figure 21c**), about 35% of Cr^{III}-species are present as a 2-3 µm thick layer right at the varnish/paint interface, while only Cr^{VI}-compounds constitute the yellow paint underneath (**Figure 21d**: pts $01_{4\text{-II}}$-$02_{4\text{-II}}$). This pattern is very similar to that observed earlier in photochemically aged LS-CY (x > 0.4) paint models [2], suggesting that a colour change arising from CY reduction has occurred.

In conclusion, the results provide evidence of the chemical alteration of CYs in Van Gogh's *Sunflowers*. Selected locations of the painting with the highest probability of colour change because of

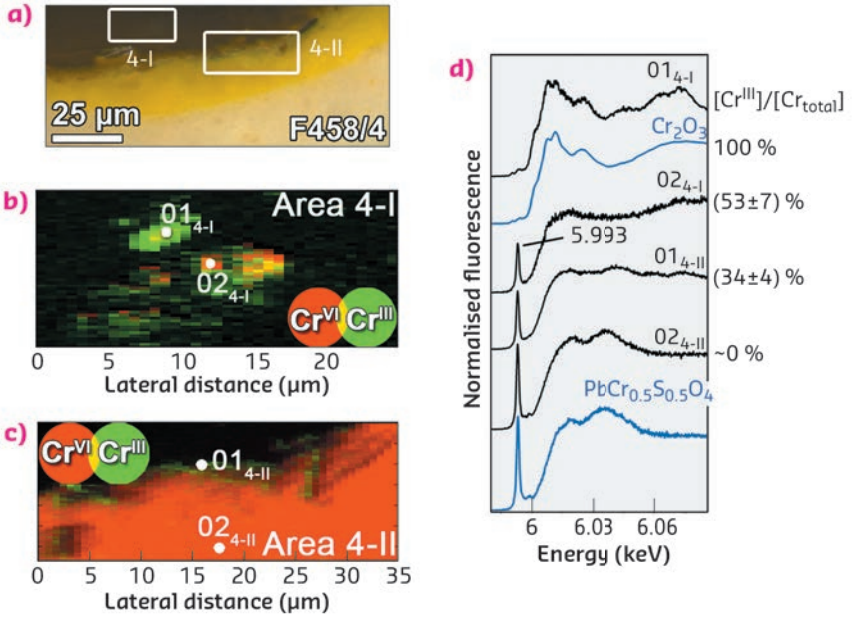

Fig. 21: (a) Photomicrograph detail of sample F458/4 and corresponding (b-c) RG composite Cr^{VI}/Cr^{III} chemical state maps. (d) µ-XANES spectra collected from areas indicated in (b-c).

Cr^{VI}-reduction were identified, thus calling for careful monitoring in the future. The findings of this study, supported by those of our earlier work [1,2], open up the way to the elaboration of safer strategies for the light exposure of the painting.

PRINCIPAL PUBLICATION AND AUTHORS

Evidence for degradation of the chrome yellows in Van Gogh's Sunflowers: a study using noninvasive *in situ* methods and synchrotron-radiation-based X-ray techniques, L. Monico (a, b), K. Janssens (b), E. Hendriks (c), F. Vanmeert (b), G. Van der Snickt (b), M. Cotte (d), G. Falkenberg (e), B. G. Brunetti (a) and C. Miliani (a), *Angewandte Chemie International Edition* **127**, 14129-14133 (2015) doi: 10.1002/anie.201505840.
(a) CNR-ISTM and Perugia University (Italy)
(b) Antwerp University (Belgium)
(c) Van Gogh Museum, Amsterdam (The Netherlands)
(d) ESRF
(e) DESY (Germany)

REFERENCES

[1] L. Monico *et al.*, *Analytical Chemistry* **85**, 860-867 (2013).
[2] L. Monico *et al.*, *Journal of Analytical Atomic Spectrometry* **30**, 1500-1510 (2015).
[3] L. Monico *et al.*, *Analytical Chemistry* **83**, 1224-1231 (2011).
[4] L. Monico *et al.*, *Analytical Chemistry* **86**, 10804-10811 (2014).

SPECIATION OF PHOSPHORUS BEARING INORGANIC PHASES IN SURFACE SLUDGE DEPOSIT OF A VERTICAL FLOW CONSTRUCTED WETLAND

In order to better describe P species within a sludge deposit from a constructed wetland, four complementary methods were performed: sequential P extractions, ^{31}P solution RMN, X-ray fluorescence (XRF) mapping and X-ray absorption near edge structure (XANES) spectroscopy at P and Fe K-edge. XRF mapping and XANES spectroscopy allowed the different P-bearing Fe- and Ca-species to be distinguished, contributing to our understanding and crucial for the prediction of the potential reversibility of phosphorus capture within the complex organic environmental samples under study.

Phosphorus (P) may be considered both as a beneficial fertilising element and a pollutant since its release into surface aquatic ecosystems may induce eutrophication. P treatment from domestic wastewaters has therefore received increasing attention in recent years. A particular combined wetland treatment process has been developed [1] for the treatment of domestic wastewaters. The process includes a biological trickling filter followed by dephosphatation with ferric chloride dosing. The coagulated suspended solids are then separated from effluent and progressively accumulate at the constructed wetland surface to form a P-rich sludge deposit (above 2% w/w of P in dry matter [2]).

Several complementary analytical techniques were used for qualitative and quantitative descriptions of P species within sludge samples taken from a real municipal wastewater treatment plant. Sequential extractions provided quantitative information on the distribution of

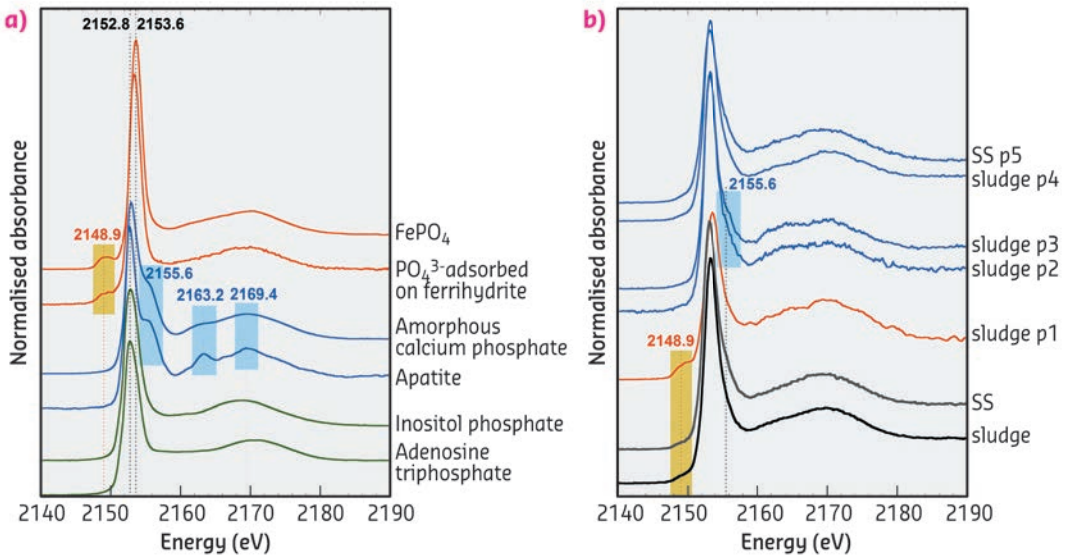

Fig 22: P K-edge XANES spectra of (a) a selection of reference P minerals (blue and red lines) and organic P species (green lines) and (b) the sludge and suspended solids (SS) samples, collected using an unfocused beam (bottom) and on selected points of interest (p1 to p5) using a µ-beam (top).

P in organic and inorganic fractions. Solution ^{31}P NMR spectroscopy showed the presence of orthophosphates monoesters, diesters and phosphonates. Inorganic P species were identified using a combination of X-ray fluorescence (XRF) mapping and X-ray absorption near edge structure (XANES) spectroscopy at P and Fe K-edge at beamline **ID21** to accurately locate the different types of P-bearing phases and determine their status.

The spectra collected on suspended solids and sludge pellets were found to be very similar to each other (**Figure 22b**). The pre-edge around 2148.9 eV attested to the presence of phosphates-Fe^{III} bonds (see $FePO_4$ and PO_4^{3-} sorbed onto ferrihydrite, **Figure 22a**). Moreover, the broad enlargement of the white line around 2155.6 eV attested also for the presence of phosphates-Ca bonds (see the post-edge shoulder and oscillations at 2163.2 and 2169.4 eV for calcium phosphate in **Figure 22a**). Spectra collected with the µ-beam on P-rich points of Interest (POIs; p1 to p5) confirmed the presence of Fe^{III}-species (p1 spectrum). Comparison with collected and literature reference spectra [3,4] showed that p2 to p5 were close to amorphous calcium phosphate, phosphate sorbed onto calcite or dicalcium phosphate. The oscillation around 2163.2 eV remained however systematically less pronounced in the spectra collected on suspended solids and sludge samples than in reference spectra.

The discrimination between $FePO_4$ and phosphates sorbed onto ferrihydrite remained difficult from spectra collected at P K-edge. However, their corresponding XANES spectra at Fe K-edge evidenced distinct features with an additional peak at 7137.6 eV for $FePO_4$ in comparison to phosphates adsorbed onto ferrihydrite, and an additional peak at 7147.3 eV for ferrihydrite in comparison with $FePO_4$ (**Figure 23a**). The shape of XANES spectra and elemental compositions of POIs obtained from Fe K-edge µ-XRF maps (**Figure 23b**) evidenced that P was predominantly bound to iron in forms of ferric phosphate, rather than sorbed onto ferric oxyhydroxide. In addition, the Fe K-edge bulk spectrum collected from sludge sample was well-fitted by a linear combination of $FePO_4$, ferrihydrite and Fe_3O_4 spectra (with respective contribution of 52, 30 and 19 %), confirming the predominance of $FePO_4$ among Fe-bearing species.

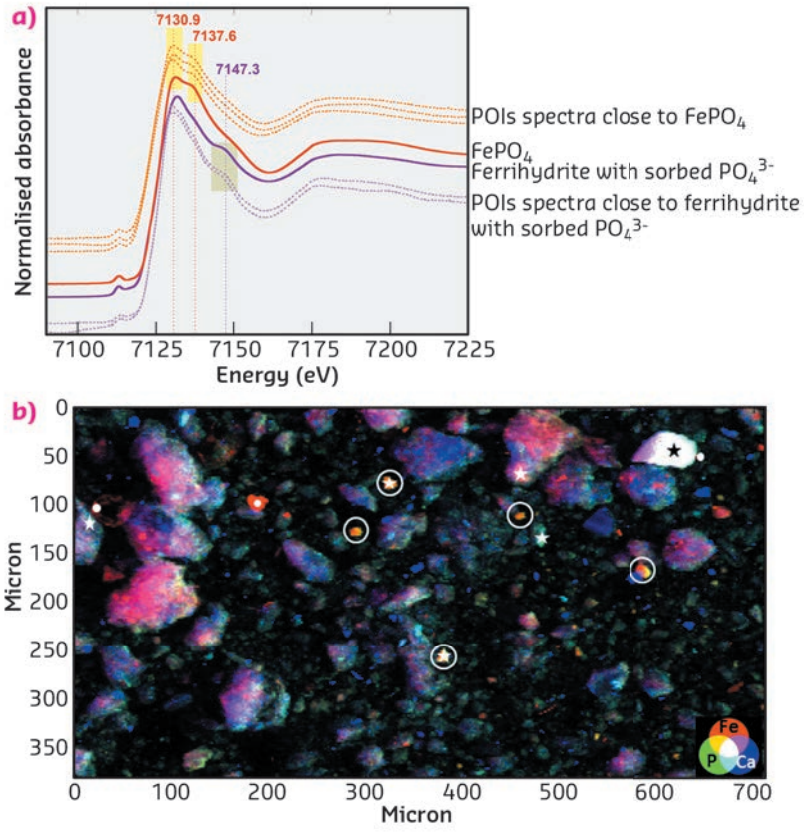

Fig. 23: (a) Fe K-edge XANES spectra of $FePO_4$ and phosphates sorbed onto ferrihydrite (references, bold lines) compared with µ-XANES spectra on POIs of sludge sample (dotted lines). (b) µ-XRF map collected above Fe K-edge with points of interest (POIs) having corresponding spectra close to $FePO_4$ (stars) and ferrihydrite with sorbed phosphates (filled circles).

By combining sequential P extractions, ^{31}P solution RMN and XANES spectroscopy, the present study provided good descriptions of P species within organic environmental complex samples. XRF mapping and XANES spectroscopy allowed us to distinguish the different P-bearing Fe- and Ca-species, contributing to a better understanding of the P retention mechanisms. The generated knowledge was thus crucial to predict the potential reversibility of P capture within the surface sludge deposit.

PRINCIPAL PUBLICATION AND AUTHORS

Effect of aging on phosphorus speciation in surface deposit of a vertical flow constructed wetland, B. Kim (a,b), M. Gautier (a), C. Rivard (c), C. Sanglar (d), P. Michel (b) and R. Gourdon (a), *Environmental science and technology.* **49**, 4903-4910 (2015); doi: 10.1021/es506164v.
(a) INSA Lyon, University of Lyon, LGCIE-DEEP, Villeurbanne (France)
(b) SCIRPE, Sainte-Foy-Lès-Lyon (France)
(c) ESRF
(d) Université de Lyon, CNRS, Institut des Sciences Analytiques, Villeurbanne (France)

REFERENCES

[1] B. Kim *et al.*, *Ecological Engineering* **71**, 41-47 (2014).
[2] B. Kim *et al.*, *Water Science and Technology* **68**, 2257-2263 (2013).
[3] C. Giguet-Covex *et al.*, *Geochimica et Cosmochimica Acta.* **118**, 129-147 (2013).
[4] J. Rajendran *et al.*, *Materials science and engineering C,* **33**, 3968–3979 (2013).

PROBING THE STRAIN IN GERMANIUM NANOWIRES BY LAUE MICRODIFFRACTION

The band structure of germanium can be tuned by application of very large stresses, which is only possible at the microscale. Probing both the strain state and the electro-optical properties on the same nano-object is a difficult challenge tackled here using synchrotron radiation.

Silicon and germanium are the most commonly employed materials in electronics. However, they are not key players in the world of emitter photonics materials since they are poor light emitters due to the indirect nature of their bandgaps – as compared to group III-V semiconductors which are not CMOS compatible. Yet germanium possesses a direct bandgap that is slightly (140 meV) above its fundamental (and indirect) bandgap. This peculiar feature, compared to silicon, has recently generated a great interest in the band diagram tailoring of germanium by application of very large strains. Indeed, tensile strain reduces the difference between the indirect and direct bandgaps [1] and can be used as a way to activate direct optical transition, a prerequisite to get a germanium based laser. It is thus necessary to correlate the strain state and the band diagram properties for the same microsized object. The latter has motivated this study on the effect of longitudinal stresses on the position of the direct bandgaps in germanium nanowires, which give the unique opportunity to probe the influence of stresses along the <111> crystallographic axis. Laue X-ray diffraction at beamline **BM32** appeared to be the technique of choice to measure the deviatoric strain tensor in our nanowires.

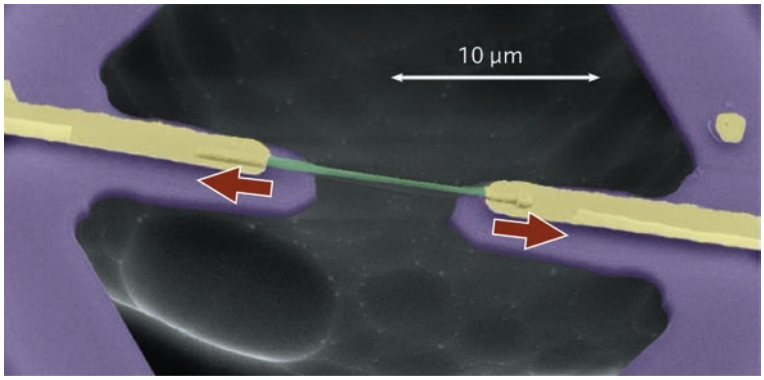

Fig. 24: SEM image of a stressed germanium nanowire (in green). The silicon nitride is in purple and the gold contacts in yellow.

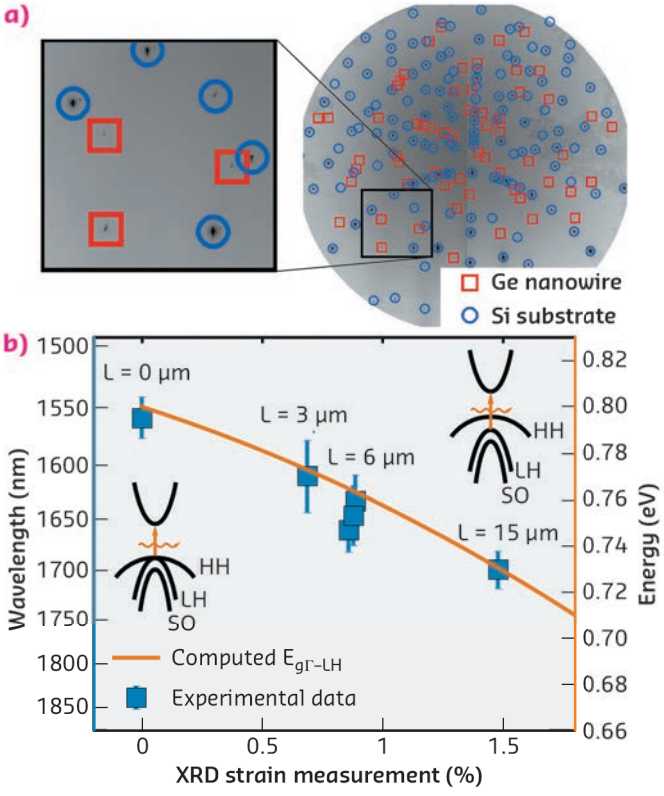

Fig. 25: (a) X-ray diffraction pattern of a single nanowire (b) Strain measurements compared with photocurrent spectroscopy bandgap measurements.

We grew the nanowires in a chemical vapor deposition (CVD) reactor using the vapor-liquid-solid mechanism [2]. The nanowires were then transferred by sonication onto a silicon nitride stressed layer on a silicon substrate. They were then encapsulated in a silicon oxide layer in order to mechanically anchor them on the nitride layer. We patterned the shape of two arms by lithography by aligning the lithographic mask on a nanowire. Finally, the nanowires were mechanically stretched by etching the silicon substrate underneath. The stretching arms retracted upon release, transmitting their elongation to the nanowire. **Figure 24** shows a SEM image of such a stressed nanowire.

We accessed the strain components of such a system by Laue micro-diffraction. The white X-ray beam resulting from the bending magnet was focused onto a 300 nm x 300 nm spot and aligned at the centre of the nanowire. The resulting diffraction pattern was collected on a 2D detector at 90° from the incident beam, the sample being at 40°. **Figure 25a** shows a diffraction pattern from a strained germanium nanowire. Both nanowire and substrate X-ray diffraction patterns were measured. By removing

the silicon background, we were able to obtain the orientation and the deviatoric strain tensor of the germanium nanowire – all strain components except the hydrostatic part. Assuming no stress on surfaces perpendicular to the axis of the nanowire, we were able to calculate a longitudinal strain up to 1.48% in the most stressed nanowire.

We finally measured the value of the light-hole band to Γ conduction band optical transition – one of the two direct bandgaps – by photocurrent spectroscopy. We excited the nanowire at different wavelengths using a Xe arc lamp and a monochromator. The generated electrical current – of about 200 fA – was probed using a lock-in amplifier. The obtained bandgaps were plotted as a function of strain measured by X-ray diffraction and compared to theoretical models from the literature [3], as shown in **Figure 25b**. A good agreement was observed.

In conclusion, we propose a novel approach to stress individual nano-objects (such as semiconducting nanowires, quantum dots in nanowires, nanotubes, etc.), using standard microfabrication processes. For the same single object, we have correlated the strain state and the band structure properties by using a combination of X-ray microdiffraction and microphotocurrent spectroscopy.

PRINCIPAL PUBLICATION AND AUTHORS

Tensile strained germanium nanowires measured by photocurrent spectroscopy and X-ray microdiffraction, K. Guilloy (a), N. Pauc (a), A. Gassenq (a), P. Gentile (a), S. Tardif (b), F. Rieutord (b) and V. Calvo (a), *Nano Lett.* **15**, 2429 (2015); doi: 10.1021/nl5048219.
(a) SINAPS, INAC-SP2M, Université Grenoble Alpes and CEA, Grenoble (France)
(b) NRS, INAC-SP2M, Université Grenoble Alpes and CEA, Grenoble (France)

REFERENCES

[1] P. Boucaud *et al.*, *Photon. Res.* **1**, 102 (2013).
[2] R.S. Wagner and W.C. Ellis, *Appl. Phys. Lett.* **4**, 89 (1964).
[3] C.G. Van de Walle, *Phys. Rev. B* **39**, 1871 (1989).

Structure of materials

Through the reorganisation of the Experiments Division in July 2015, the high energy beamlines have been brought together within the Structure of Materials Group. The Microtomography Beamline, ID19, has joined the group, while beamlines ID01 and ID03 now belong to the X-ray Nanoprobe Group and Complex Systems and Biomedical Sciences Group, respectively. This new portfolio of high-energy X-ray techniques strengthens our capability to study complex heterogeneous devices and new advanced materials such as rechargeable batteries, catalytic materials, as well as serving complementary scientific communities including palaeontology, environmental research and cultural heritage.

From the Materials Science Beamline, ID11, in addition to the articles selected for this chapter, there is also an article on full-field X-ray orientation microscopy in the Enabling Technologies chapter, describing the recently developed six-dimensional framework for diffraction contrast tomography that allows the combined reconstruction of the shape and local orientation of single grains inside the sample. This year, ID11 took over several experiments which would normally have been performed at ID15, for example some XRD-CT and a high-energy experiment on the POLAR detector [1]. The 3DXRD station continues to run well with a full suite of detectors for near-field and far-field diffraction where it is possible to carry out simultaneous diffraction and imaging studies with micrometre scale spatial resolution. The installation of a new end-station for nano-focussing experiments is currently taking place allowing for the mapping of materials with around 100 nm resolution.

The refurbishment of ID15 began in December 2014 and the beamline will be reopened for users in the spring 2016 proposal round. The canted straight section houses the Engineering Materials Science and Materials Chemistry branch ID15A as well as the High Pressure Diffraction branch ID15B, relocated from ID09A, part of the Matter at Extremes Group. ID15A will offer two new end-stations, which have been developed for stress/strain measurements in the field of metallurgy and high speed tomography, and for time and space resolved materials chemistry. Both experimental hutches will share the main optical components. The Engineering Materials Science instrument will benefit from an improved flux of collimated X-rays in the range 50–150 keV. An additional high-energy monochromator inside the experimental hutch can deliver energies up to 750 keV. The improved instrument will provide an optimised setup for combined diffraction and micro tomography studies, offering both polychromatic and monochromatic beam conditions. Various sample environments (cryostats, high temperature ovens, stress rigs) are available to emulate real service conditions of advanced materials used today in high-end technological appliances. The end-station focussed on Materials Chemistry will feature a variety of sample environments and ancillary probes (mass, infra-red and fluorescence spectroscopy) in addition to a much more intense focal spot down to 1x1 μm^2, delivered by the completely redesigned primary and secondary optics. The station is to be equipped with a photon counting Pilatus3 X CdTe pixel detector that will be shared with ID31. This detector is optimised for high-energy X-ray diffraction and features a maximum frame rate of 500 fps. Coupling more intense focused beams with this high-speed, high-efficiency and low-noise detector will make it possible to carry out non-spatially resolved diffraction studies of irreversible chemical processes on the timescale of milliseconds, and two and three dimensionally spatially resolved studies (XRD-CT, PDF-CT) on the timescale of seconds and minutes, respectively.

The users of the Microtomography Beamline, ID19, will benefit from many developments completed during 2015: the monochromator is now operational in both Bragg-Bragg and Laue-Laue geometries giving access to photon energies up to 200 keV; the accumulation mode is implemented for PCO-edge and FReLoN detectors for high dynamical range tomography of highly absorbing samples; new optical configurations based on Hasselblad photographic lenses are available for medium and high resolution tomography; the implementation of *jpeg2000* data compression for radiographs and reconstructed data provides a 10-fold reduction in the final data size with negligible loss in quality; larger usable beams up to 75 mm are available. Furthermore, a Shimadzu HPV-X high speed camera was purchased for acquisition speeds up to single bunch imaging as well as an image-intensified camera PIMAX4 by Princeton Instruments for shock and impact studies. In addition to the selected articles, one should note the paper by Babel *et al.* [2] about the characterisation of dendrite morphologies in rapidly solidified droplets and the paper by Smith *et al.* [3] about the advances in virtual dental histology on early hominids.

The high resolution Powder Diffraction Beamline, ID22, has now commissioned its Perkin Elmer large area detector for complementary studies to the standard high-resolution configuration. The implementation of this detector was accompanied by the installation of a monochromatic-beam

transfocator equipped with 185 aluminium refractive lenses manufactured in house. This detector can be used for checking for preferred orientation and graininess, for faster measurements on weakly scattering samples, and for one-shot PDF analysis, which is much quicker than the high resolution scanning mode that remains an option for highest quality data. Thanks to this 2D detector, ID22 and ID11 were able to help cover experiments that might normally be performed at ID15, unavailable to users during its refurbishment, such as looking at the behaviour of bio-alcohol reforming catalysts under reaction conditions.

The High-energy Beamline for Buried-interface Structures and Materials Processing, ID31, was known as upgrade beamline project UPBL2 during the Upgrade Phase I Programme. Beamline components were installed during spring 2015, and after commissioning, the beamline was ready to take first users in autumn 2015, as foreseen. ID31 offers a portfolio of hard X-ray characterisation techniques including reflectivity, wide-angle diffraction both in transmission and grazing incidence geometry, small-angle X-ray scattering, imaging methods, and auxiliary techniques coupled with a great versatility in choice of beam size and detectors optimised for high energy X-rays. The first large area, high-energy single-photon counting detector, Pilatus3 2M CdTe, was commissioned just before the winter break. This detector, to be shared with ID15A, allows measurements of weak signals next to strong ones with best possible signal-to-noise ratio for photon energies up to 100 keV. Currently, this long beamline is working with a multilayer monochromator with 0.36% bandpass in the energy range 20-70 keV. A bent Laue-Laue monochromator with adjustable bandpass over the energy range 50 to 150 keV will be installed during spring 2016. The installation of a new small gap and short period undulator, U14, and a new instrument with extended nanofocusing capabilities at high photon energies is scheduled later in 2016.

These improvements together with better detectors and sample environments constitute a revolutionary enhancement in performance for an ever increasing community of users from academia and industry. The highlights from ESRF and CRG beamlines selected for 2015 demonstrate how synchrotron X-ray characterisation techniques have been applied for the study of both real devices under operating conditions and idealised model systems under precisely controlled environments.

V. HONKIMÄKI

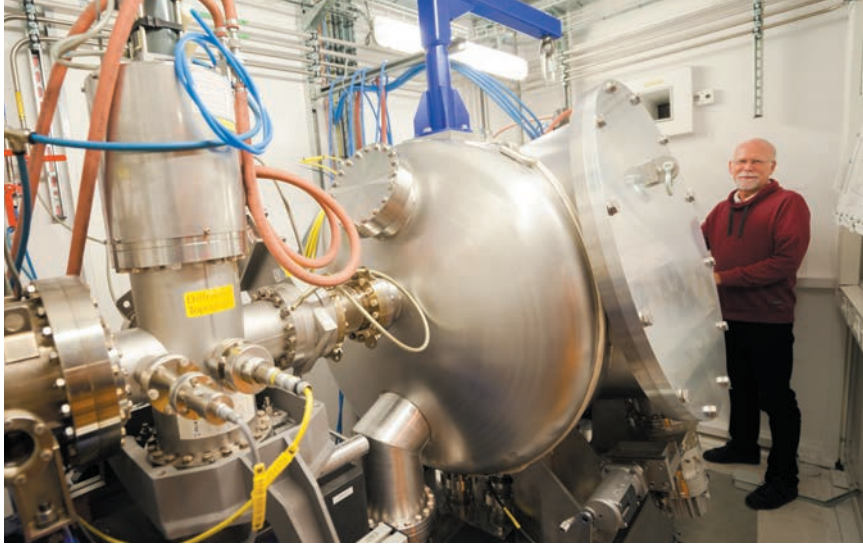

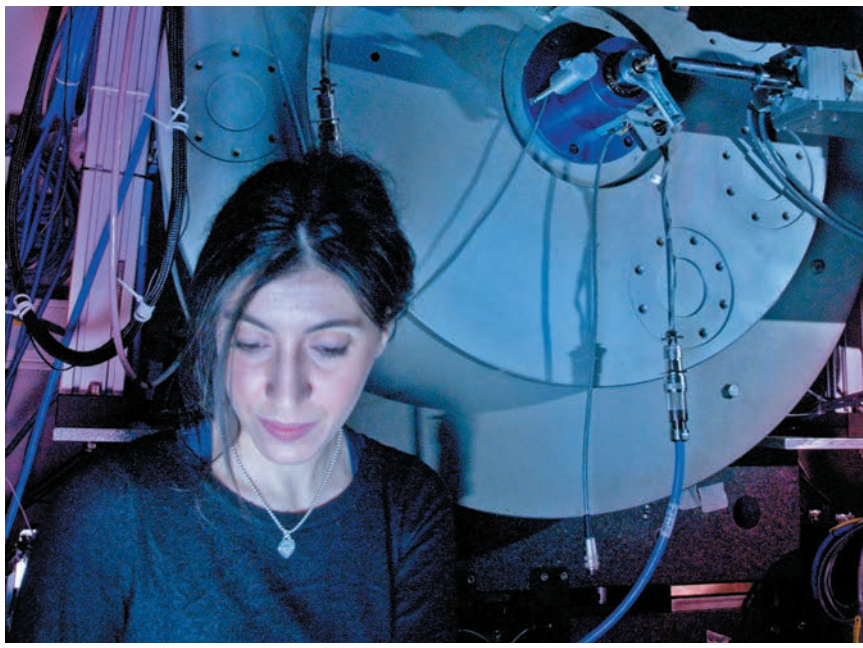

REFERENCES

[1] H.L. Xiao *et al.*, *Calibration of gamma-ray burst polarimeter POLAR,* arXiv:1512.02784v1 [astro-ph.IM] 9 Dec 2015.
[2] M. Bedel *et al.*, *Characterization of dendrite morphologies in rapidly solidified Al–4.5 wt.%Cu droplets, Acta Materialia* **89**, 234–246 (2015).
[3] T.M. Smith *et al.*, *Dental ontogeny in pliocene and early pleistocene hominins,* PLoS ONE 10(2): e0118118 (2015).

MICROBEAM DIFFRACTION GIVES NEW INSIGHTS INTO THE WORKING OF LITHIUM-ION BATTERY ELECTRODES

This work aimed at revealing the local structural changes in Li-ion electrodes during charge and discharge, which are decisive for battery performance as they limit fast charging and play a crucial role in the restricted cycle life of Li-ion batteries.

The overall phase transformation behaviour of Li-ion battery electrode materials is well known. However, even for well-studied electrode materials such as $LiFePO_4$, it is unknown how the transformation proceeds within individual grains and how it is distributed over the many grains present in an electrode, mainly due to the difficulty to probe the phase nucleation and growth within individual grains. This is crucial information for future battery improvement because the local conditions, such as the local current density, govern the Li-ion battery cycle life and rate performance. Using the microbeam at **ID11**, operando X-ray diffraction was employed to monitor the transformation of many individual $LiFePO_4$ particles inside an Li-ion battery electrode from slow to fast battery (dis)charging rates, as shown schematically in **Figure 26a**. The diffraction results revealed the cycling-rate dependent phase transition mechanism, shown in **Figure 27**, within individual electrode grains. Measuring the transformation process of individual $LiFePO_4$ particles allowed the first quantification of local current densities, *i.e.* the current per surface area of individual grains.

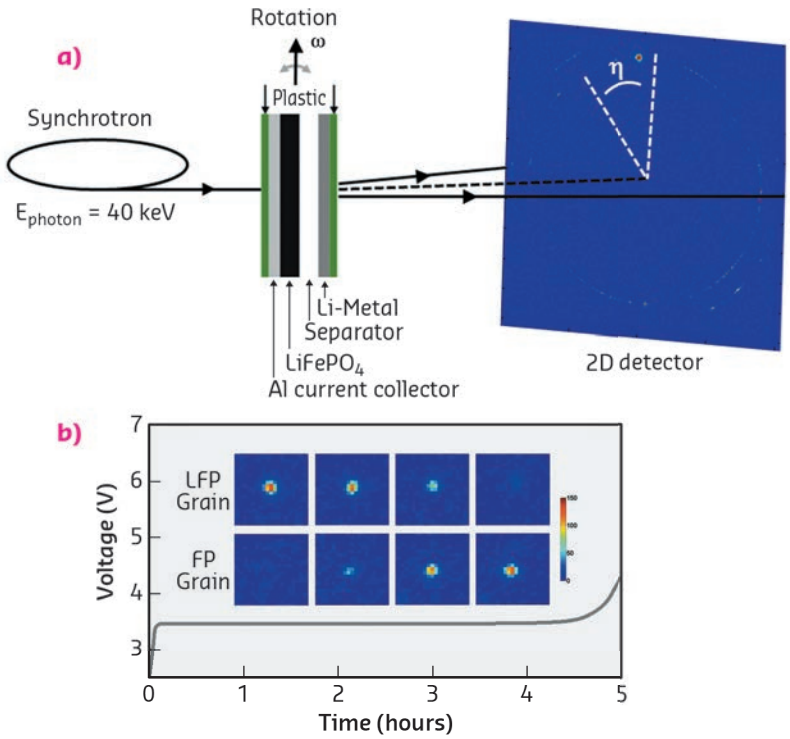

Fig. 26: (a) Schematic representation of the *in situ* synchrotron X-ray diffraction experiment. (b) Charging voltage curve including the evolution of a 2D (200) $LiFePO_4$ (LFP) and (200) $FePO_4$ (FP) peak showing the progressive FP formation and LFP disappearance.

Due to the sub-micrometre sized and intense X-ray beam, the diffraction rings that are observed from powder diffraction break up into individual spots, each representing an individual nanosized $LiFePO_4$ grain. This allowed the evolution of the (200) reflection to be monitored for individual $LiFePO_4$ particles during charge and discharge, as shown in **Figure 26**. The gradual disappearance of the (200) $LiFePO_4$ and appearance of the (200) $FePO_4$ diffraction peaks reflect the first-order phase transition when Li-ions are removed from the $LiFePO_4$ electrode.

A surprising observation is that a significant fraction of the reflections during slow charge and discharge appear as streaks as illustrated by the reflections in **Figure 27a**, rather than symmetric peaks as shown in **Figure 26b**. The considerable one dimensional broadening implies platelet-shaped domains of both $FePO_4$ and $LiFePO_4$ as shown in **Figure 27a**, where the plate thickness is inversely proportional to the length of the streaks.

When the charge and discharge rate is increased, the streaked reflections narrow and disappear, translating into a decrease in number of platelet domains and an average increase in platelet domain thickness. At fast charging, a double peaked reflection appears, **Figure 27b**, where the appreciable intensity between the $LiFePO_4$ (200) and $FePO_4$ (200) end-member indicates a continuous distribution of intermediate compositions, reflecting a diffuse interface over the full length scale of the 140 nm grain. This proves that the recently observed bypassing of the first-order phase transition [1] occurs within a single grain, rationalising the excellent battery performance of this electrode material.

Measuring the transformation process of individual $LiFePO_4$ particles allowed the first quantification of local current densities in Li-ion battery electrodes under realistic charge and discharge conditions, as shown in **Figure 27c**. The local current densities are larger than expected

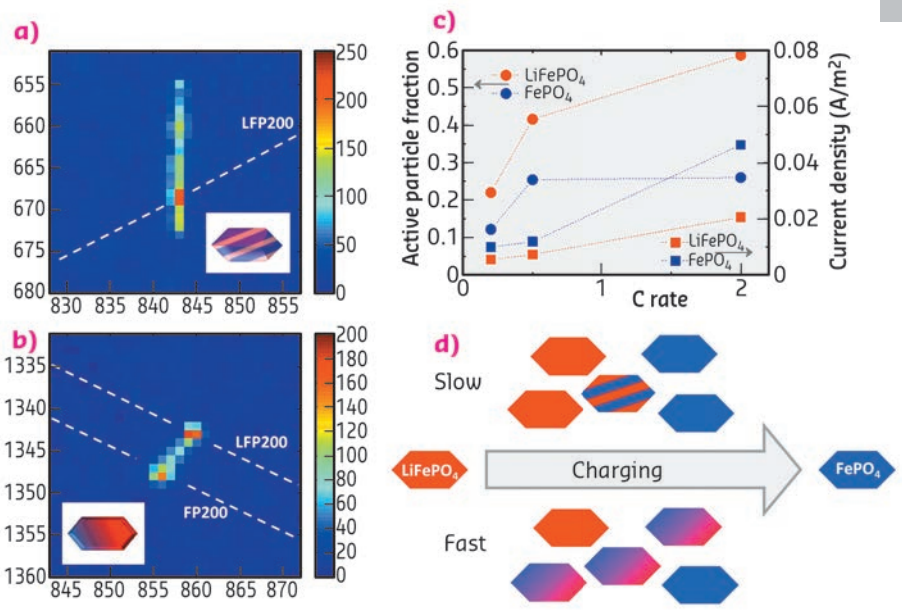

Fig. 27: Phase transformation mechanism slow and fast cycling rates: (a) For a slow charge rate vertical (200) streaks are observed for both $LiFePO_4$ (LFP) and $FePO_4$ (FP) phases. The broadening in the z-direction gives the thickness of the platelet domains in this case leading to 10 nm in 140 nm particles. This leads to the shown internal two phase FP/LFP morphology. (b) (200) reflection at a high charging rate showing coexistence of the LFP and FP phases within a single grain. The dashed lines indicate the powder rings for the (200) reflections of the LFP and FP phases, indicated as LFP200 and FP200, respectively. For both phases the *a*-axis is closely aligned indicating a diffuse coherent interface. (c) Active fraction and current density of the particles resulting from the average transformation times where C/*n* denotes the rate at which a full charge or discharge takes *n* hours. (d) Sketch of the rate-dependent transformation upon charge as follows from the microbeam diffraction experiments (similar upon discharge only with a smaller active particle fraction, see (c)).

if all electrode active material is assumed to participate but smaller than that expected from the established particle-by-particle mosaic transformation. The derived charge and discharge rate dependence of the local current density is a crucial parameter for electrode design that can help to prevent the occurrence of hotspots and fractures in electrodes.

PRINCIPAL PUBLICATION AND AUTHORS

Direct view on the phase evolution in individual $LiFePO_4$ nanoparticles during Li-ion battery cycling, X. Zhang (a), M. van Hulzen (a), D.P. Singh (a), A. Brownrigg (b), J.P. Wright (b), N.H. van Dijk (a) and M. Wagemaker (a), *Nature Communications* **6** (2015); doi: 10.1038/ncomms9333.
(a) Department of Radiation Science and Technology, Delft University of Technology (The Netherlands)
(b) ESRF

REFERENCES

[1] X. Zhang *et al.*, *Nano Letters* **14**, 2279-2285 (2014).

BRILLIANT SYNCHROTRON RADIATION AND ELECTRON MICROSCOPY – A POWERFUL COMBINATION FOR CHALLENGING STRUCTURE ANALYSES

Extremely brilliant microfocused synchrotron radiation enables the extension of "standard" single-crystal structure determination to samples smaller than one micrometre. In combination with transmission electron microscopy, novel compounds in inhomogeneous reaction products can be discovered and accurately characterised. Taking this information into account allows one to develop efficient syntheses.

Structure analyses of compounds present in heterogeneous samples can be demanding, especially if metastable phases or the products of precursor reactions do not exhibit crystals with sizes required for conventional structure analysis. Powder X-ray diffraction is, in many cases, insufficient for the precise and accurate characterisation of such materials with unknown structure types. Despite recent advances to overcome the problem of dynamical diffraction, electron crystallography still cannot compete with the accuracy of single-crystal structure analyses.

The very stable beam at beamline **ID11** can be focused to diameters of less than one micrometre by refractive lenses. This enables precise X-ray structure analyses of microcrystals which can be centred by detecting their characteristic X-ray emission while moving the sample in the beam (fluorescence scans, **Figure 28**). However, it would be extremely tedious to identify a good crystallite of a new compound that occurs as a side phase in heterogeneous materials. Transmission electron microscopy (TEM), on the other hand, is a reliable tool for the discovery of such new phases and the determination of their

unit-cell metrics by electron diffraction and their chemical composition by energy-dispersive X-ray spectroscopy. TEM and microdiffraction were efficiently combined by using microcrystalline samples on carbon-coated copper grids. Crystallites were pre-characterised by TEM and re-located at the beamline by fluorescence scans so that diffraction data could be acquired.

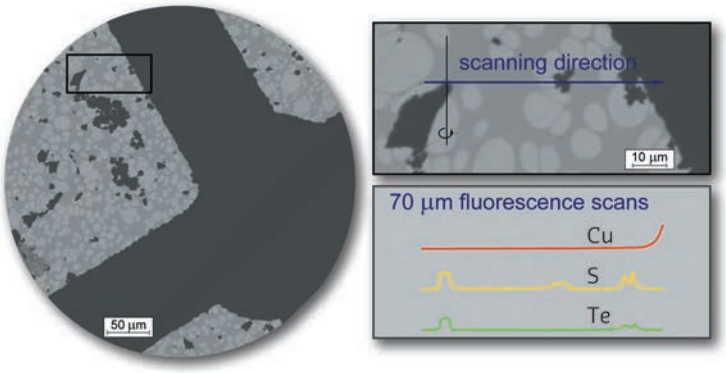

Fig. 28: TEM image of the selected crystallite on a copper grid (left, scanned region marked by black box) and an enlarged image of the measured tip of the crystallite (0.3 × 0.5 × 1 µm³) with centre of rotation (top right), and a schematic representation of fluorescence line scans of Cu, Te and S (bottom right). The copper crossbar functions as a "landmark"; a side-phase visible in the centre of the scan contains no Te, whereas the crystals on the right side of the scans are located too close to the copper bar to be measured independently.

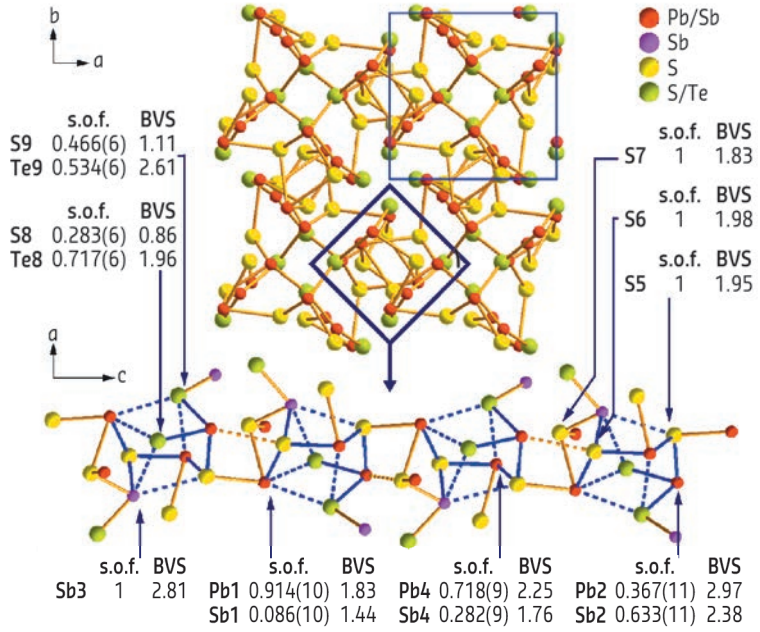

Fig. 29: Crystal structure of $Pb_8Sb_8S_{15}Te_5$ as obtained by microfocus diffraction with bond valence sums and site occupancies; characteristic chain-like unit with heterocubane-like building blocks (bottom).

As an example, the very unusual compound $Pb_8Sb_8S_{15}Te_5$ was found in quenched samples with the nominal composition "$Pb_5Sb_4S_6Te_5$" that contained a mixture of PbTe, Sb_2Te, and an unknown quaternary phase. The latter's metrics and approximate composition as determined by TEM methods revealed the presence of a new sulfide telluride. The lack of single crystals and strongly overlapping broadened reflections in powder diffraction patterns impeded further characterisation. The tip of a pre-characterised quaternary crystallite (ca. 0.3 x 0.5 x 1 mm³) in a suitable and accessible position on the grid was analysed at **ID11**. The resulting dataset turned out to be precise enough for a detailed description of the structure, which was refined including twinning around [110] and additional inversion twinning. Mixed site occupancies as well as anisotropic displacement parameters could be elucidated as in any high-quality X-ray analysis of macroscopic single crystals. $Pb_8Sb_8S_{15}Te_5$ crystallises in space group $P4_1$ (a = 8.0034(4) Å, c = 15.0216(5) Å) and exhibits an intriguing structure with chain-like fragments in combination with heterocubane-like entities (**Figure 29**). The structure model was further confirmed by the excellent match of simulated and experimental high-resolution TEM images of the very crystallite. Furthermore, the detailed knowledge of the structure and exact composition led to the subsequent synthesis, optimisation and thermoelectric characterisation of phase-pure material.

This combined TEM and microdiffraction approach avoids the once tedious and time-consuming "trial and error" structure analysis of microcrystalline heterogeneous samples and opens new perspectives in solid-state synthesis, which can now follow the full structural characterisation instead of being a requirement for it. Selecting specimens for X-ray diffraction by TEM can also be applied to intergrown domains in composite materials and other fields of materials science (for further examples, see refs. [1,2]). In addition, this strategy might also be applied to the study of reaction pathways and intermediates.

PRINCIPAL PUBLICATION AND AUTHORS

Discovery and structure determination of an unusual sulfide telluride through an effective combination of TEM and synchrotron microdiffraction, F. Fahrnbauer (a), T. Rosenthal (b), T. Schmutzler (a), G. Wagner (a), G.B.M. Vaughan (c), J.P. Wright (c) and O. Oeckler (a), *Angew. Chem. Int. Ed.* **54**, 10020-10023 (2015); doi: 10.1002/anie.201503657.
(a) Faculty of Chemistry and Mineralogy, Leipzig University (Germany)
(b) Department of Chemistry, LMU Munich (Germany)
(c) ESRF

REFERENCES

[1] F. Fahrnbauer *et al., J. Mater. Chem. C* **3**, 10525 (2015).
[2] D. Durach *et al., Inorg. Chem.* **54**, 8727 (2015).

CAPTURING RAPID FAILURE MECHANISMS OF LITHIUM-ION BATTERIES BY HIGH SPEED TOMOGRAPHY

Improving the safety of lithium-ion batteries is imperative for their success in a range of applications from consumer electronics to automotive power trains. Here high speed tomography was used to image the rapid structural changes occurring within batteries during failure giving rise to an improved understanding of failure mechanisms and highlighting the importance of safety devices.

Li-ion batteries have become the technology of choice for consumer electronics, and in the future will find a diverse range of uses from mW to MW applications. The advancement of electric and hybrid electric vehicles requires high energy density batteries to operate under a wide range of demanding conditions where the safety of Li-ion batteries is of utmost importance. Recent high profile battery failures have highlighted the need for improved safety devices in commercial cell designs [1,2]. When a critical temperature is reached, the active electrode materials within a Li-ion battery begin to break down exothermically, generating large quantities of heat and causing a runaway reaction, known as thermal runaway. Safety devices such as pressure relief vents and positive temperature coefficient (PTC) devices are incorporated into commercial cells to help mitigate the risks associated with thermal runaway but little is understood about the dynamic mechanisms associated with thermally induced failures.

X-ray tomography has become a widely used technique for 3D structural analyses of electrochemical materials [3]. The exceptional photon flux density and brilliance at **ID15A** allowed acquisition of tomograms over very short periods of time providing unprecedented temporal resolution for 4D (time lapse) tomography whereby fast morphological changes were tracked in 3D over time. For the first time we have been able to image the nucleation and propagation of failure within working cells in real time. Simultaneous thermal imaging provided detailed information on the temperature of the cell during failure which was enabled by *in situ* containment apparatus (**Figure 30**) to protect beamline equipment from energy intensive failures.

Two commercial Li-ion batteries (18650 NMC cells) with different mechanical designs were imaged using high speed radiography and tomography during failure, to evaluate and compare the effectiveness of different cell safety devices. For example, it was found that an internal cylindrical support (**Figure 31a**) played an important role in improving the safety of a cell by providing structural support for the tightly wound electrode layer, and acting as a channel for gases to flow uninterrupted from the base of the cell to the vent during failure. Without the cylindrical support the internal architecture collapsed after venting, the consequences of which include increased risk of thermal runaway due to exposure of cell material to air.

One of the major safety concerns for battery manufacturers is the occurrence of pressure relief vent clogging during failure which occurs due to the re-distribution of failed material within the cell housing. High speed radiography at 1250 fps captured the rapid propagation of thermal runaway (**Figure 31c**) in both cells and highlighted the cause of clogging by identifying the shift of the bulk material towards the vent; clogging led to an uncontrolled ejection of the cell contents.

As well as thermal imaging which determined skin temperature for the cell, critical internal temperatures were estimated by pinpointing regions where aluminium and copper current collectors began to melt. During the rapid thermal runaway process, extreme temperature gradients

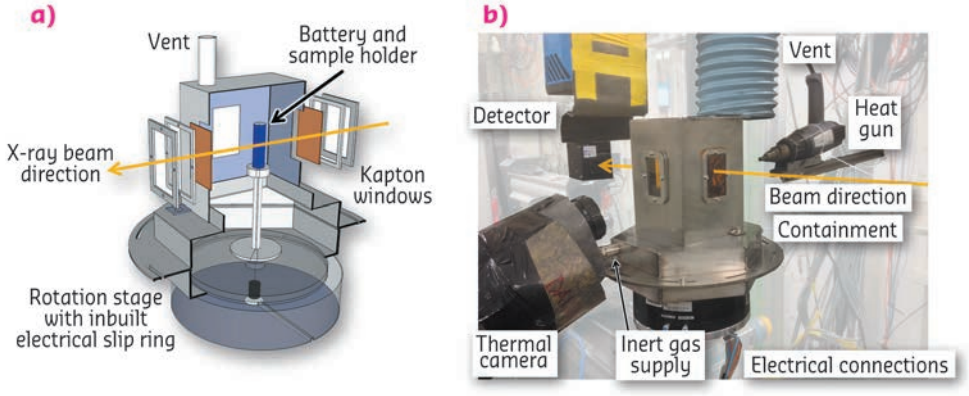

Fig. 30: (a) Illustrative representation of the containment system; (b) photograph of the mounted containment system with labelled apparatus.

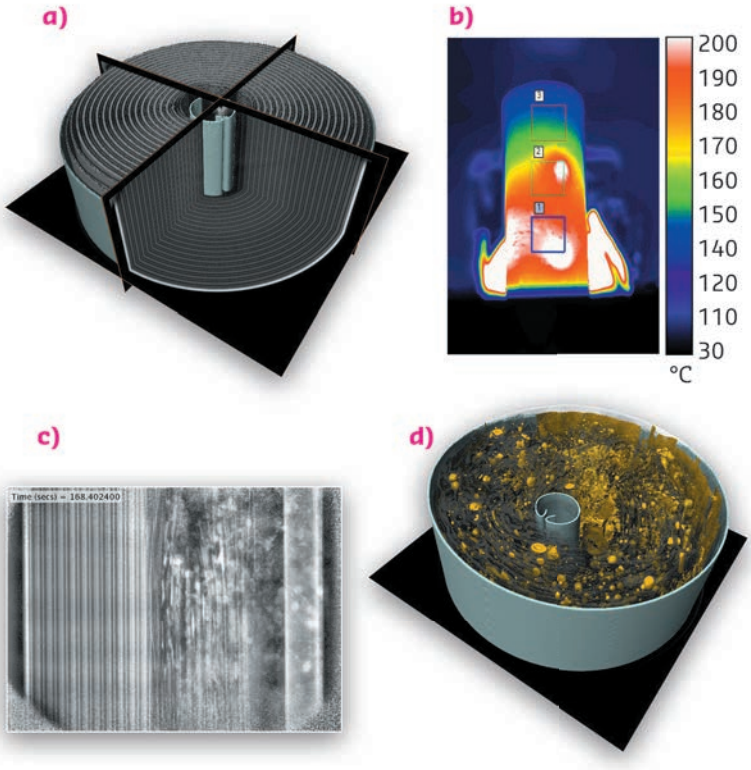

of > 700°C were observed across the cells. **Figure 31d** shows a *post-mortem* reconstruction where the majority of the copper current collector within the cell has melted.

As well as enhancing our understanding of the role of safety devices and intelligent engineering designs in mitigating battery failure, this work has also demonstrated the use of high speed radiography, tomography and thermal imaging in concert, as a powerful diagnostic tool for understanding rapid failure mechanisms.

Fig. 31: (a) 3D reconstruction of a fresh cell with internal cylindrical support, (b) thermal image of a failing cell, (c) radiograph showing the propagation of thermal runaway and (d) *post-mortem* 3D reconstruction.

PRINCIPAL PUBLICATION AND AUTHORS

In-operando high-speed tomography of lithium-ion batteries during thermal runaway, D.P. Finegan (a), M. Scheel (b,c), J.B. Robinson (a), B. Tjaden (a), I. Hunt (d), T.J. Mason (a), J. Millichamp (a), M. Di Michiel (b), G.J. Offer (d), G. Hinds (e), D.J.L. Brett (a) and P.R. Shearing (a), *Nature Communications* **6**, 6924 (2015).
(a) Electrochemical Innovation Lab, Chemical Engineering Dept., UCL, London (UK)
(b) ESRF
(c) Synchrotron Soleil, Saint-Aubin (France)
(d) Mechanical Engineering Dept., Imperial College London (UK)
(e) National Physical Laboratory, Teddington (UK)

REFERENCES

[1] AAIB, Air accident report: 2/2015 (2015).
[2] K. Bullis, Are Electric Vehicles a Fire Hazard?, MIT Tech Review (2013).
[3] M. Ebner *et al.*, *Science* **342**, 716-720 (2013).

EVIDENCE OF THE IMPACT OF SOLVATED NANOPARTICLES UPON THEIR SURROUNDINGS

Colloidal nanoparticles are widely used in dispersed form for consumer and industrial goods. However, little is known about the chemical environment near the particle surface. Using high-energy X-ray scattering, it has now been shown that nanoparticles subtly influence the local solvent density. Each nanoparticle induces a nanoscopic solvation shell, reaching out as far as 2 nm from the particle surface. This effect is expected to strongly influence the chemistry and rheology of these important materials.

The properties of matter at the nanoscale can differ wildly from that of bulk materials. For example, pronounced increases in chemical reactivity, or changes in optical properties are commonplace. In recent years, nanoparticles with a typical size of 1-100 nm have therefore been used in a wide diversity of applications. In many real world applications, for example in sun screen, a liquid or gel carrier is used. To prevent agglomeration and so prolong the lifetime of the product, it is important to know how the solvent interacts with the nanoparticles. Likewise, in homogeneous catalysis, where chemical reactions occur at the particle surface, it is important to know whether the local chemical environment is different from that of the bulk solvent.

The reorganisation of solvent molecules around isolated cations has been recognised for many years [1]. Pioneering experiments with synchrotron radiation have shown how bulk planar surfaces can induce surface ordering in fluids [2]. However, no definitive proof previously existed for the formation of a nanoscale solvation

shell around colloidal nanoparticles. Nevertheless, such effects have been reported in simulations of solvated nanoparticles [3]. In real systems, this would influence properties including diffusion coefficients and particle growth, which influence the applications described above.

The influence of solvated nanoparticles upon their surroundings has been addressed experimentally using high-energy X-ray scattering at beamline ID15B, in particular using the pair distribution function (PDF) technique. This technique makes use of area detectors to collect scattering data up to a very high resolution in reciprocal space. Fourier transformation then yields the PDF, which is a histogram of all the interatomic distances in the material. Well-defined species, such as the ZnO nanoparticles studied here, yield sharp peaks whereas the isotropic density variations found in liquids at medium distances are reflected in a damped oscillation reflecting the average molecular correlations.

We discovered that the PDF of dry nanoparticles could be well explained by a simple crystal structure model. However, when the nanoparticles were dispersed in a range of solvents, an additional signal appeared. This takes the form of a damped oscillation like that seen in the bulk solvent (**Figure 32**). However, it is out of phase and cannot be subtracted as if it were a background contribution. After exhaustive experiments, we were able to show that this signal does not depend strongly on particle size, shape, nor the capping agent used. Supplementary measurement on metallic, polar and non-polar oxides showed that the formation of a solvation shell is apparently universal for colloidal nanoparticles.

The signal is extremely weak, reflecting both the very low solubility of our nanoparticles (ca. 30-40 millimolar in ethanol), and the proportion of solvent in proximity to the particles. However, we were able to parameterise it using a simple model. The fitting shows that solvent restructuring extends as far as 2 nm into the bulk solvent. We also found that the signal shifts with alkyl chain length, so the alcohol molecules are likely to arrange perpendicular to the surface (**Figure 33**). Profound changes in the chemical properties of the solvent in this region are thus supported by our analysis.

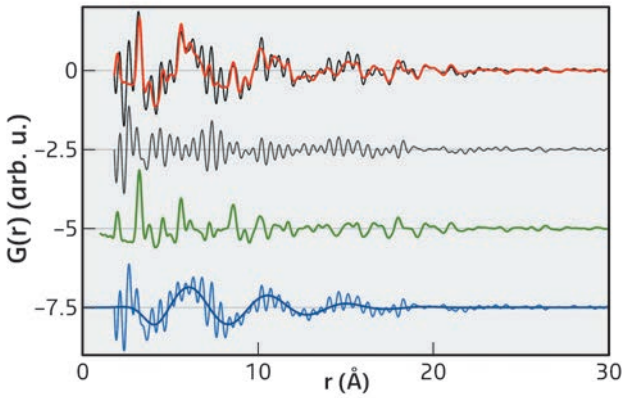

Fig. 32: Fit to the PDF of redispersed ZnO nanoparticles with citrate ligands in propanol. Experimental PDF of ZnO nanoparticles (black) and their fit (red), showing the overall difference of the fit (grey), the contribution of the nanoparticle (green), and the contribution and fit of the restructured solvent (blue), offset for clarity. The contribution of the restructured solvent (blue) is the difference-PDF of the experimental, background-corrected PDF (black) and the nanoparticles (green).

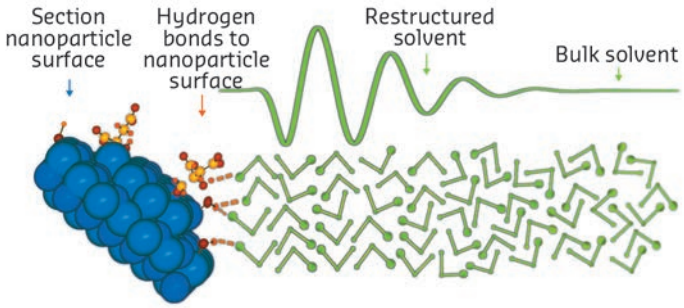

Fig. 33: Enhanced short-range order of solvent molecules at ZnO nanoparticle surfaces. The ethanol molecules (hydrogen atoms omitted) form hydrogen bonds with surface hydroxyl groups and citrate molecules. The surface coverage of these groups is reduced for clarity. The enhanced short-range order extends a few molecular layers into the bulk liquid.

In summary, we have been able to detect the formation of a nanoscopic solvation shell around colloidal nanoparticles using high energy X-rays. Although the tiny solvent density changes reported here are at the very limit of detectability, when the ESRF-EBS lattice upgrade is complete, we should be able to detect changes in nanoparticle size, shape and chemistry, as well as the influence of the solvation shell in real time. This will open the door to a more complete understanding of the chemical and rheological properties of solvated colloidal nanoparticles.

PRINCIPAL PUBLICATION AND AUTHORS

Universal solvent restructuring induced by colloidal nanoparticles, M. Zobel (a), R.B. Neder (a) and S.A.J. Kimber (b), *Science* **347**, 292-294 (2015); doi: 10.1126/science.1261412.

(a) Department of Physics, Institute of Crystallography and Structural Physics, Friedrich-Alexander University Erlangen-Nuremberg (Germany)

(b) ESRF

REFERENCES

[1] D.T. Bowron, S. Diaz-Moreno, *J. Phys. Chem. B*, **113**, 11858 (2009).
[2] O.M. Magnussen *et al.*, *Phys. Rev. Lett.*, **74**, 4444 (1995).
[3] D. Spagnoli *et al.*, *Langmuir*, **27**, 1821 (2001).

METAL-ORGANIC FRAMEWORK WITH NOVEL TOPOLOGY DISCOVERED THROUGH *IN SITU* MONITORING OF A MECHANOCHEMICAL REACTION

A mechanochemical reaction environment has provided the conditions for the formation of an unusual new metal-organic framework possessing new network topology. This discovery was enabled by *in situ* reaction monitoring via powder X-ray diffraction since the new MOF is a transient intermediate in a multi-step reaction.

The monitoring of mechanochemical milling reactions by X-ray powder diffraction, first developed at the **ID15B** high-energy beamline of the ESRF [1], has provided a major breakthrough in the understanding of milling reactions [2], themselves becoming central to solvent- and waste-free chemical transformations. Before the introduction of this technique, *in situ* monitoring of milling transformations was virtually impossible since such reactions are conducted by rapid oscillation of closed reaction vessels, with the reaction mixture under persistent impact of agitated steel balls and with vessel walls usually made from several millimetres thick steel or tungsten carbide. Application of high-energy X-ray diffraction at ID15B, in combination with reaction vessels manufactured from amorphous and light-atom plastic, now enables *in situ* monitoring of the evolution of crystalline phases during milling, with time resolution in seconds. The technique has also proven applicable to purely organic materials and the formation of pharmaceutical cocrystals, demonstrating its generality for monitoring a wide range of milling transformations [3].

Most recently, we have studied the mechanochemical transformations of the commercially important zeolitic imidazolate framework (ZIF) ZIF-8. *In situ* monitoring was crucial for the discovery of a new metal-organic framework (MOF), which also revealed a previously unknown tetrahedral framework topology, named katsenite (kat) after A.D. Katsenis, the first author of the article. The discovery of a new ZIF material in a system that was the subject of hundreds of earlier

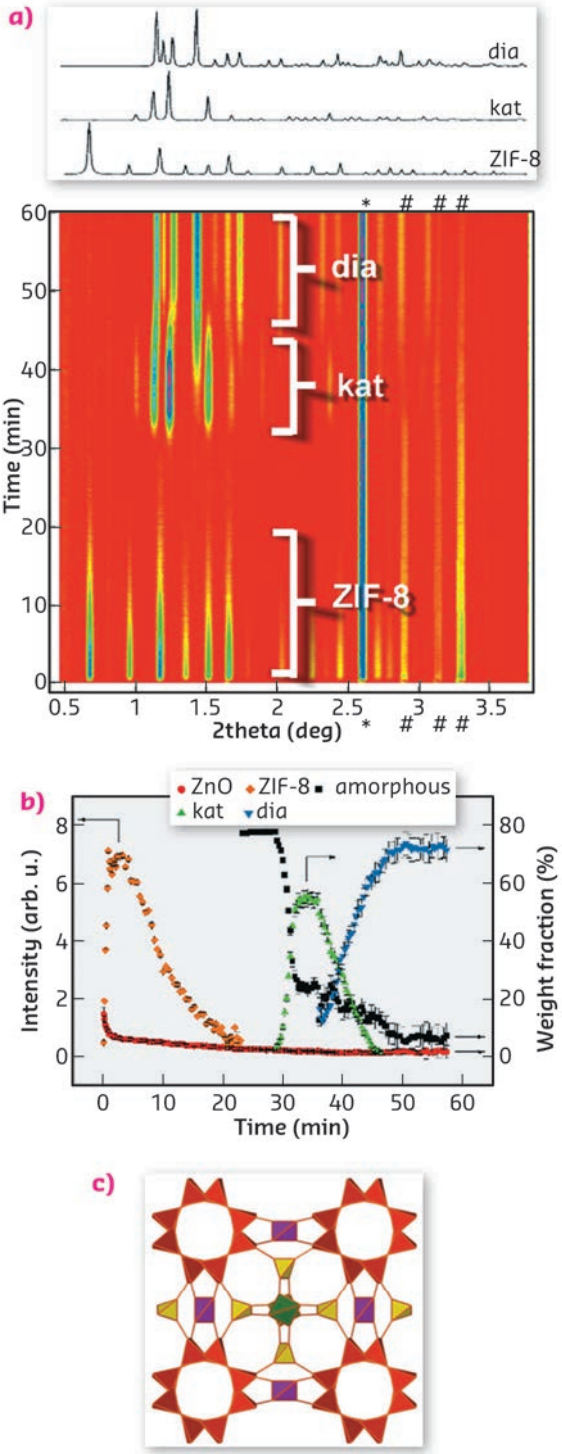

Fig. 34: (a) Time-resolved *in situ* diffraction experiment exhibiting initial formation of ZIF-8, its amorphisation is evident from the diminishing diffraction signal and subsequent recrystallisation of the amorphous matrix first into the katsenite framework and finally into the diamondoid-topology framework. (b) Time evolution of phases during milling as obtained from Rietveld refinement. (c) Katsenite framework represented by its vertex figure with different colouring for each type of vertex.

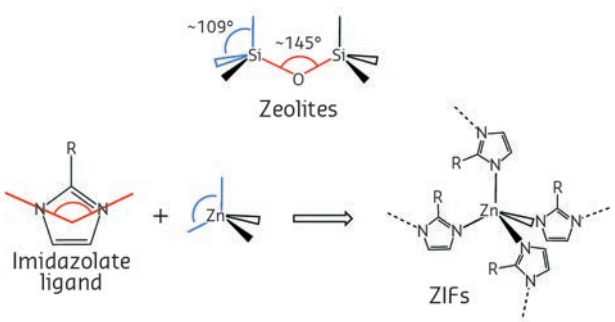

Fig. 35: Similar geometries of valence angles are the reason for coinciding topologies of zeolites and ZIFs. Similar valence angles in zeolites and ZIFs are colour-coded.

studies revealed, for the first time, that a mechanochemical environment can create conditions for the formation of new phases and structural motifs that cannot be obtained by other conventional methods. Katsenite, itself a polymorph of ZIF-8, was of limited stability under milling conditions and would finally transform to the non-porous diamondoid-topology polymorph of ZIF-8 (Figure 34).

Topologies of most ZIFs can be matched to those of known zeolites. The reasons for this are geometrical, as the tetrahedral metal cation (*e.g.* Zn^{2+}) mimics the tetrahedral silicon centre of zeolites while the arrangement of nitrogen atoms of coordinating imidazolate linkers mimic the Si-O-Si valence angle characteristic for zeolites (Figure 35) [4,5]. Surprisingly, however, katsenite exhibits a novel topology, never previously seen for zeolites. Its crystal structure was determined from powder X-ray diffraction data to reveal its tetragonal symmetry with four zinc atoms and four imidazolate linkers in the asymmetric unit. The underlying kat-net is unique due to its four non-equivalent 4-c nodes, each adopting a different coordination sequence and point symbol, overall leading to a quadrinodal network based on tetrahedral nodes with transitivity 4463.

A captivating aspect of katsenite is its formation as an intermediate phase in a multi-step process that involves the initial formation of the ZIF-8 sodalite framework by liquid-assisted grinding (LAG) of ZnO and 2-methylimidazole. Its structural collapse into an amorphous material that crystallises into the katsenite structure upon further milling and which, subsequently, arranges into the more stable and completely non-porous diamondoid topology framework during milling. This unusual sequence of events, which is the first example of structural degradation and recrystallisation upon mechanical milling, is highly dependent on using dilute aqueous acetic acid as a catalytic milling liquid additive. While using other additives such as N,N-dimethylformamide (DMF) results in highly crystalline and stable ZIF-8, aqueous acetic acid first catalyses the formation of open ZIF-8 which, surprisingly, collapsed over 20-30 minutes of milling. Importantly, the thus formed amorphous matrix would not always result in the formation of katsenite but would sometimes directly yield the non-porous diamondoid-topology product, serving as the first direct evidence of stochastic, nucleation-related behaviour in mechanochemical synthesis.

PRINCIPAL PUBLICATION AND AUTHORS

In situ X-ray diffraction monitoring of a mechanochemical reaction reveals a unique topology metal-organic framework, A.D. Katsenis (a), A. Puškarić (b), V. Štrukil (a,b), C. Mottillo (a), P.A. Julien (a), K. Užarević (b), M.-H. Pham (c), T.-O. Do (c), S.A.J. Kimber (d), P. Lazić (b), O. Magdysyuk (e), R.E. Dinnebier (e), I. Halasz (b) and T. Friščić (a), *Nat. Commun.* **6**, 6662 (2015); doi: 10.1038/ncomms7662.
(a) Department of Chemistry, McGill University, Montreal (Canada)
(b) Ruđer Bošković Institute, Zagreb (Croatia)
(c) Department of Chemical Engineering, Université Laval (Canada)
(d) ESRF
(e) Max Planck Institute for Solid State Research, Stuttgart (Germany)

REFERENCES

[1] T. Friščić *et al.*, *Nature Chem.* **5**, 66-73 (2013).
[2] K. Užarević *et al.*, *J. Phys. Chem. Lett.* **6**, 4129–4140 (2015)
[3] I. Halasz *et al.*, *Angew. Chem. Int. Ed.* **52**, 11538-11541 (2013)
[4] X.-C. Huang *et al.*, Chen, *Angew. Chem. Int. Ed.* **45**, 1557 –1559 (2006).
[5] A. Phan *et al.*, *Acc. Chem. Res.* **43**, 58-67 (2010).

THE COELACANTH OUT OF BREATH

Although it has been studied extensively, the extant coelacanth *Latimeria* still has some anatomical features that are not well understood. Based on propagation phase contrast X-ray microtomography performed at beamline ID19 as well as conventional tomography techniques, the development and evolutionary history of the coelacanth lung has been recently studied. The presence of a lung in *Latimeria*, its allometric growth through the ontogeny and the development of a fatty organ as an adaptation to deep-waters has been confirmed.

Coelacanths are a group of sarcopterygian fishes known since the Devonian, 410 million years (Ma) ago. Due to their absence from the record during the Cenozoic Era (65 Ma ago to present), they were thought to be extinct until the first specimen of the extant species *Latimeria chalumnae* [1] was caught in deep-waters of the Indian Ocean in 1938. This discovery has been the subject of many articles [1-4], thereby making the coelacanth one of the most famous large marine vertebrates. Among these studies, some [2, 4] have mentioned the presence of a vestigial lung apparatus in *L. chalumnae,* which merited further investigation.

The adult, juvenile and embryonic *Latimeria* specimens studied here belong to different institutional collections: South African Institute for Aquatic Biodiversity (Grahamstown, South Africa), Zoologische Staatssammlung (München, Germany) and Muséum National d'Histoire Naturelle (Paris, France). Direct observations on partial dissections and on histological material were made in the Collection of Comparative Anatomy of the MNHN.

The X-ray imaging study was mostly conducted at beamline **ID19**. Three embryos and a juvenile individual were scanned using long propagation (up to 13 metres) phase-contrast synchrotron X-ray microtomography. Two adult specimens were scanned in a hospital in Paris and on the AST-RX Platform of the MNHN, Paris, respectively.

This study allowed us to confirm the presence of a non functional lung in extant coelacanths, and demonstrate an allometric growth of the lung relative to the adjacent correlated organs (digestive tract, fatty organ) during ontogenetic development (**Figure 36**). Although the growth of the fatty organ is correlated to the total length of the animal through the different ontogenetic stages, the lung presents a decreasing growth, exhibiting a vestigial shape at late ontogenetic stages. Due to the small number of invaluable coelacanth specimens housed in collections worldwide, and especially of embryos, access to high quality tomography facilities was necessary to study the fine anatomy of individuals of a unique ontogenetic series, without damage on these rare specimens. In this respect, the use of long propagation phase contrast made it possible to obtain high levels of contrast for soft tissues.

Considering the structures of the coelacanth pulmonary apparatus through time, we postulate that adaptation to deep water led to the reduction of the lung, the complete loss of its respiratory function and the development of the fatty organ for buoyancy control. We also proposed that this adaptation - probably initiated by the end of the Mesozoic (100-65 Ma ago) - may have allowed the survival of deep-water living coelacanths during the Cretaceous/Paleogene extinction event.

In *Latimeria*, the fatty organ has a buoyancy function [5], possibly analogous to that of the liver of some sharks, which store lipids as a reserve, the fat-invested string of tissue of some deep-water actinopterygians fishes, and the spermaceti of some cetaceans, whose function is to maintain neutral buoyancy both at the surface and at depth.

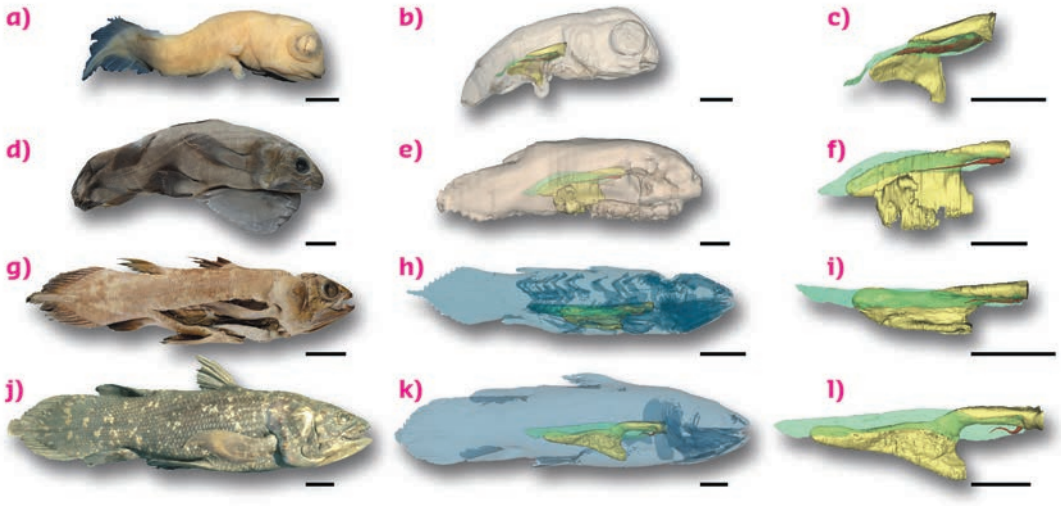

Fig. 36: Photos and three-dimensional reconstructions of the lung and the fatty organ, in relation to the digestive tract, in a unique ontogenetic series of *Latimeria chalumnae* in right lateral views. (a, b, c) Early embryo CCC 202.1. (d, e, f) Late embryo with yolk sac CCC 29.5. (g, h, i) Juvenile CCC 94. (j, k, l) Adult CCC 22. Yellow, oesophagus and stomach; green, fatty organ; red, lung. Scale bar, 0.5 cm (a, b, c); 2.5 cm (d, e, f); 5 cm (g, h, i); 10 cm (j, k, l).

PRINCIPAL PUBLICATION AND AUTHORS

Allometric growth in the extant coelacanth lung during ontogenetic development, C. Cupello (a), P.M. Brito (a), M. Herbin (b), F.J. Meunier (c), P. Janvier (d), H. Dutel (e) and G. Clément (d), *Nature Communications* **6**, 8222 (2015); doi:10.1038/ncomms9222.

(a) Departamento de Zoologia, Universidade do Estado do Rio de Janeiro (Brazil)
(b) Département Écologie et Gestion de la Biodiversité, UMR 7179 CNRS-MNHN, Muséum National d'Histoire Naturelle, Paris (France)
(c) Département des Milieux et Peuplements Aquatiques, UMR 7208 (CNRS-IRD-MNHN-UPMC), Muséum National d'Histoire Naturelle, Paris (France)
(d) Centre de Recherche sur la Paléobiodiversité et les Paléoenvironnements (CR2P, UMR 7207), Sorbonne Universités, MNHN, CNRS, UPMC-Paris6, Muséum National d'Histoire Naturelle, Paris (France)
(e) Laboratory for Evolutionary Morphology, RIKEN, Kobe (Japan)

REFERENCES

[1] J.L. B Smith, *Nature* **143**, 455–456 (1939).
[2] J. Millot, J. Anthony, D. Robineau, in *Anatomie de Latimeria chalumnae III* (CNRS, 1978).
[3] C.T. Amemiya *et al.*, *Nature* **496**, 311–316 (2013).
[4] D. Robineau, *Ann. Sci. Nat. Zool.* **8**, 43–60 (1986).
[5] P.M. Brito *et al.*, *Palaeontology* **53**, 1281–1290 (2010).

IN SITU FATIGUE ANALYSIS OF DENTAL IMPLANTS WITH X-RAY TOMOGRAPHY

Prior studies revealed that conical titanium implants develop a microscopic gap at the implant-abutment connection (IAC). This microgap widens when the implant is subject to extra axial load. Since masticatory forces may cause mechanical fatigue of the implant, we use the IAC microgap as a marker for early cyclic deformation in fatigue experiments. To carry out the latter, an *in situ* setup was designed for synchrotron radiography and computed tomography, both of which can be recorded while the fatigue experiment is running.

Dental titanium implants play an important role in oral maxillofacial surgery. To prolong the lifetime of dental implants it is mandatory to investigate all aspects of possible failure. Recent studies reveal that a gap forms under load at the implant-abutment connection (IAC). This microgap is observed well below the yield of 600-1000 N and is thus believed to be the early onset of plastic deformation which first occurs at the IAC. In addition, the long-time reliability remains a very important issue mostly for clinical reasons. We have already studied the high cycle fatigue (HCF) for over 1 million load cycles by means of high-resolution synchrotron computed tomography (CT) [1]. Now we turn our attention to the cyclic deformation processes which need to be studied *in situ* in order to develop more durable implants. Similar to the HCF study, we propose to use the IAC microgap as a marker for early cyclic deformation, which is most likely to occur at the implant shoulder, hence at the IAC. Presuming that cyclic deformation might – by formation of a permanent microgap - cause the IAC to remain "open", the IAC can be prone to bacterial colonisation and infection.

Synchrotron CT in combination with inline phase contrast was employed to examine the inner structure of the implant system. Through the analysis of interference fringes we detected small material interfaces which are enhanced. We showed that even for 2D radiography this technique can detect and measure microgap sizes down to 0.1 µm, which is well below the resolution of the X-ray images [2]. Thereby, in order to match the interference to simulations, prior knowledge of the sample such as the geometry and the refracting index of the material were used. Furthermore, propagation and tomographic projection can be considered two exchangeable linear operators; hence the technique of analysing the IAC microgap readily applies for 3D CT images as well. Moreover, since we investigate fatigue processes *in situ*, keeping the exposure time of the X-ray images short, *i.e.* of the order of milliseconds, is critical. The polychromatic "pink beam" (wiggler spectrum around 60 keV) at ID19 was best suited for this purpose.

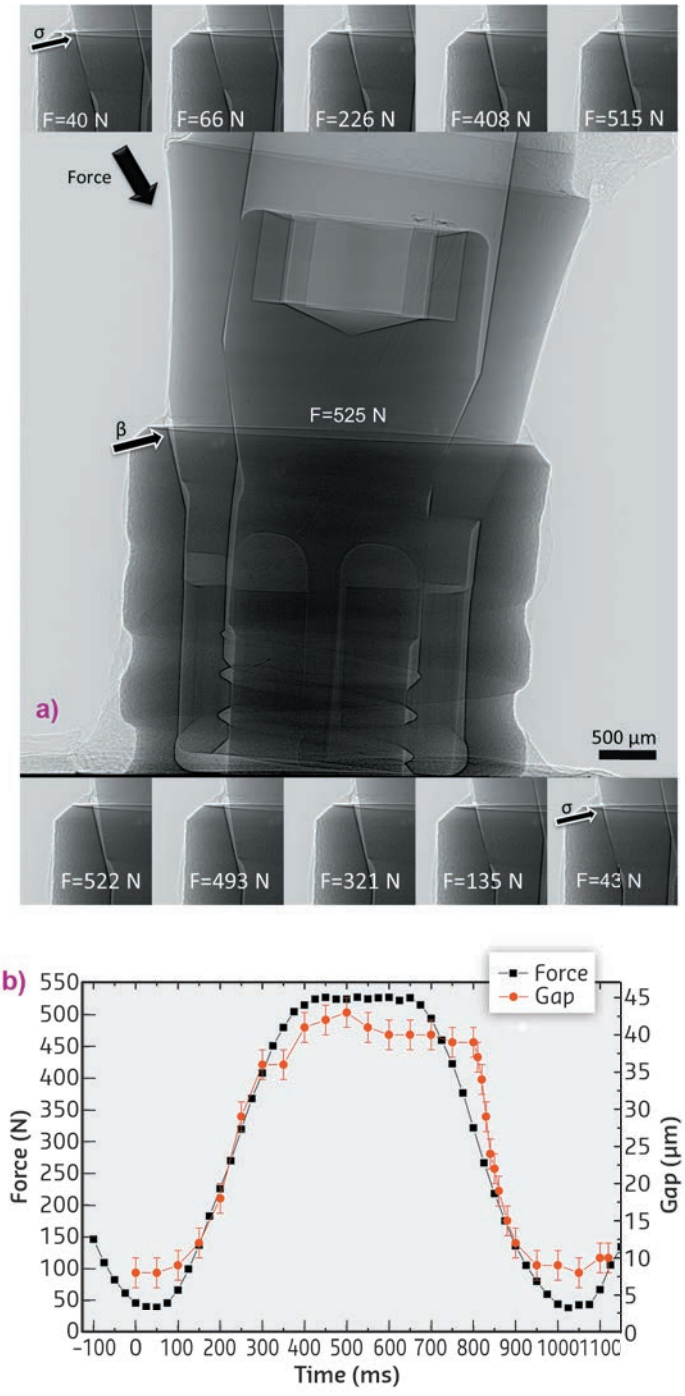

Fig. 37: (a) Representative frames from the real-time radioscopy experiment (middle maximum force). The gap opening at the implant shoulder is labelled with arrows, β indicates a big gap and σ indicates a small gap. The loaded implant was a BoneLevel (Straumann AG, Switzerland). (b) Measured force vector and calculated microgap for each time point for one cyclic deformation cycle (approx. 1 Hz repeat). The error for the gap size is ± 2 µm and the error for the measured force is an estimation of ± 4 N.

2D and 3D images were recorded with a pixel sampling of 2.75 µm. A thick crystalline scintillator screen (250 µm GGG) allowed for a good signal to noise ratio even at exposure times of 10 ms (100 fps). In this mode we were able to record real-time radioscopy movies of the cyclic implant deformation (f = 2 Hz). For recording *in situ* 3D CT images during fatigue (f = 10 Hz), a single radiographic projection was recorded at the force peak of each load cycle while sample and fatigue machine rotate continuously. Hence, 1000 fatigue cycles were used for one scan assuming quasi stationary conditions during the loading. Altogether 10 scans (10 000 cycles) were recorded for one experiment, then the sample was replaced or the force was increased. This strategy represents a compromise between available beam time, the achievable number of fatigue cycles and the norm testing of dental implants.

The apparatus for *in situ* testing comprised a direct drive motor (LinMot, Switzerland) and a DC force sensor (Burster, Germany) for either constant-strain or constant-stress fatigue. For synchronising cyclic load, sample position and the trigger for image acquisition, the essential parts were controlled by a FPGA system (National Instruments, USA).

An example for real time radioscopy of a dental implant during fatigue is shown in **Figure 37a**. For each image the microgap was determined by the abovementioned method, the results of which are shown along with the measured forces in **Figure 37b**. The gap size was found to correlate well with the force, the latter changes from 40 N to 525 N peak (force ratio R ~ 0.1 was required), causing the microgap to open up to 43 µm. The sample was a BoneLevel Implant (Straumann AG, Switzerland).

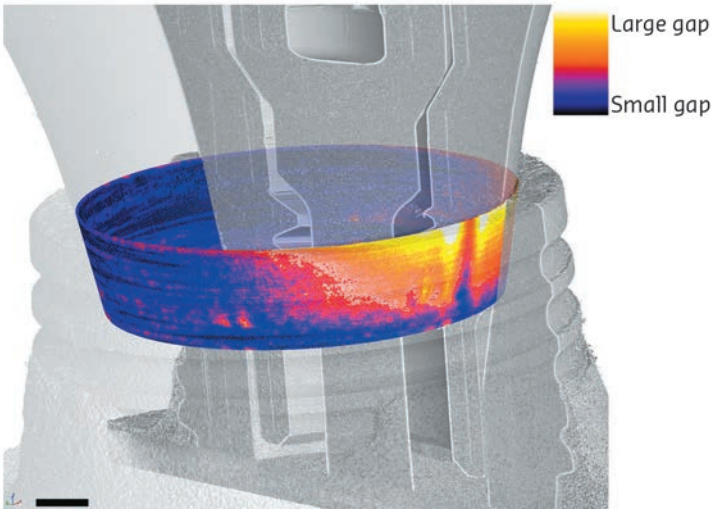

Fig. 38: Exemplary three-dimensional visualisation of an IAC microgap map (coloured) superimposed on the CT scan of the dental implant, indicating the orientation of the latter. Here the implant is a NobelActive (Nobel Biocare, Switzerland) under 333 N cyclic load. The look-up table is only a quantitative classification of the gap size.

An example of 3D *in situ* CT of a NobelActive (Nobel Biocare, Switzerland) implant which was subject to mechanical fatigue during the scan is shown in **Figure 38**, peak force was 333 N. **Figure 38** displays a composite view of the IAC gap (coloured conical surface) and the implant, which allows a qualitative appreciation of the gap size and location [3]. Through the observation of such cylinder projection maps of the microgap one can investigate the formation and the changes in the IAC-gap as a function of the number of cycles or as a function of peak-force.

Real time radioscopy clearly is a powerful qualitative and quantitative tool for *in situ* observation of fatigue in dental implants or other similar metallic joints. The observed deformation was mainly elastic, when observed after short time offset and even at 525 N peak force. This preliminary result implies quasi-stationary conditions which are needed for recording tomographic images, as illustrated in **Figure 38**. By means of synchrotron *in situ* CT, complete 3D analysis of the IAC can be carried out. No changes were observed to occur from 1000 to 10,000 cycles. Yet, when load is increased, changes in gap size and lateral extension were detected. Surprisingly, the IAC became narrower during application of cyclic load.

In our study we have demonstrated a setup for real *in situ* investigation that does not require interruption of testing for CT scans to be recorded, but presumes quasi-stationary conditions over 1000 cycles and scans the sample during the cyclic loading. This mode is particularly important for fatigue studies which require a low or a negative force ratio. More generally, our setup is not limited to synchrotron X-ray sources, however, the photon flux has to be high to reach a sufficient signal to noise ratio at short exposure times.

PRINCIPAL PUBLICATION AND AUTHORS

In situ microradioscopy and microtomography of fatigue-loaded dental two-piece implants, W. Wiest (a), S. Zabler (a), A. Rack (b), C. Fella (a), A. Balles (a), K. Nelson (c), R. Schmelzeisen (c) and R. Hanke (a,d), *Journal of Synchrotron Radiation* **22**, 1492-1497 (2015); doi: 10.1107/S1600577515015763.
(a) Institute of Physics, University of Würzburg (Germany)
(b) ESRF
(c) Department of Oral and Maxillofacial Surgery, Medical Centre – University of Freiburg (Germany)
(d) Fraunhofer EZRT, Fürth (German)

REFERENCES

[1] K. Blum *et al.*, *Dent. Mat.* **31**, 1415-1426 (2015).
[2] S. Zabler *et al.*, *Rev. Sci. Instr.* **81**, 103703 (2010).
[3] S. Zabler *et al.*, *Int. J. Mat. Res.* **103**, 207-216 (2012).

UNRAVELLING THE STRUCTURAL CODING OF A COMPLEX ZEOLITE FAMILY

A new approach that combines structure solution with structure prediction, and inspires the targeted synthesis of new super-complex zeolites has been developed. High-resolution powder X-ray diffraction (PXRD) combined with rotation electron diffraction was key to the determination of complex zeolite structures ZSM-25 and PST-20, which have shown very attractive CO_2 adsorption properties.

Zeolites are widely used in industry for gas separation, catalysis and ion-exchange because of their well-defined pore structures. Until recently, zeolites were mainly discovered using a trial-and-error synthesis approach whereby it was difficult to know in advance exactly which new zeolite structure the synthesis may produce. Furthermore, zeolites are synthesised as polycrystalline crystals, too small or too complex to be solved by X-ray diffraction. One such example is the aluminosilicate zeolite ZSM-25, first reported in 1981 [1], but the structure remained unknown.

We have developed the rotation electron diffraction (RED) method for collecting 3D single crystal electron diffraction data from micro- and nano-sized crystals [2]. RED data of ZSM-25 was collected from a crystal of 250 nm in size (**Figure 39a**), which revealed that ZSM-25 has a cubic space group *Im*-3*m* with $a \sim 42.3$ Å. However, the low data resolution (~2.5 Å) caused by electron beam damage prevented structure solution using direct methods. By searching in the Database of Zeolite Structures, we found that zeolite RHO and PAU have the same space group as ZSM-25, and the distribution of the strong reflections of ZSM-25 is the same as those calculated for RHO (a = 15.0 Å) and PAU (a = 35.0 Å) (**Figure 39b**), indicating the RHO, PAU and ZSM-25 structures are related. Strong reflections represent the main structure features of a crystal and can be used for structure solution. We chose the 21 strongest reflections from RED data and assigned their phases to be those of PAU. All 16 symmetry-independent T-atoms (T = Si, Al) were located from the 3D electron density map calculated from the 21 reflections (**Figure 39c**). A rough structural model with oxygen atoms placed between the T-atoms was built (**Figure 39d**). To obtain accurate atomic positions and locate the guest species in the pores, high-resolution PXRD data of ZSM-25 was collected at beamline ID31 (now **ID22**), which gives narrow peaks with accurate peak positions and intensities. Four TEA^+, 13 Na^+, and 24 water molecules were located in the asymmetric unit by Rietveld refinement combined with modelling (**Figure 39e**).

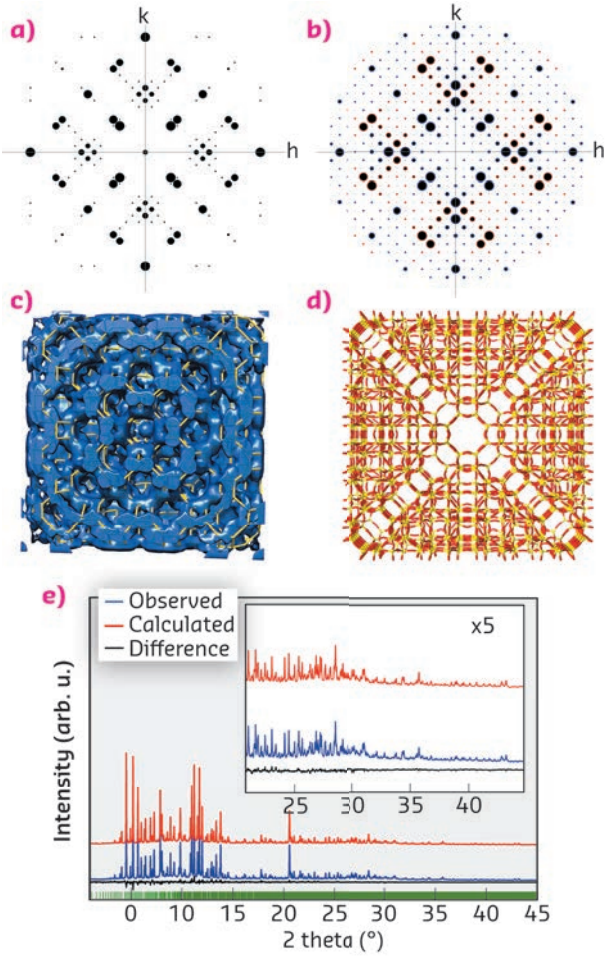

Fig. 39: (a) The 2D slice of (*hk*0) cut from the reconstructed 3D reciprocal lattice from the RED data. (b) Simulated (*hk*0) diffraction patterns of PAU, with the structure factor phases marked in blue (180°) and red (0°). (c) 3D electrostatic potential map generated by using amplitudes from RED of ZSM-25 and phases from PAU. (d) The framework structure of ZSM-25. (e) Rietveld refinement of as-made ZSM-25.

PAU and ZSM-25 can be considered as expanded versions of RHO by adding extra pairs of *pau* and *d8r* cages (~10 Å) along each unit cell edge (**Figure 40**). We call this the RHO-family, and denote RHO to be the first generation (RHO-G1), PAU the third (RHO-G3) and ZSM-25 the fourth (RHO-G4) generation. We anticipated that the structural relationship (structural coding) of the members would also be reflected in reciprocal space, and that this could be exploited for structure prediction. We found that the framework of ZSM-25 could be predicted from the PAU framework by only using the intensities and phases from the strong reflections of PAU. Similarly, higher generations of zeolite members were predicted, from RHO-G4 (ZSM-25) to RHO-G5 and from RHO-G5 to RHO-G6 (**Figure 40**). All the members are related by hitherto unrecognised structural principles; we call these embedded isoreticular zeolite structures.

The structures of RHO-G3 to RHO-G6 are all built of seven cage types, and certain cage

types increase more rapidly with the generations. To promote the formation of such cage types, Sr^{2+} and Ca^{2+} cations were introduced. RHO-G5 and RHO-G6 could be successfully obtained (denoted PST-20 and PST-25 with a = 55.0664 and 65.0436 Å, respectively), which are the most complex zeolites discovered so far. The structure of PST-20 was confirmed by high-resolution PXRD data collected at ID22 and accurate atomic positions obtained, and the structural model confirmed by Rietveld refinement. *In situ* studies of the structural changes upon CO_2 sorption are now in progress, where high-resolution PXRD is crucial.

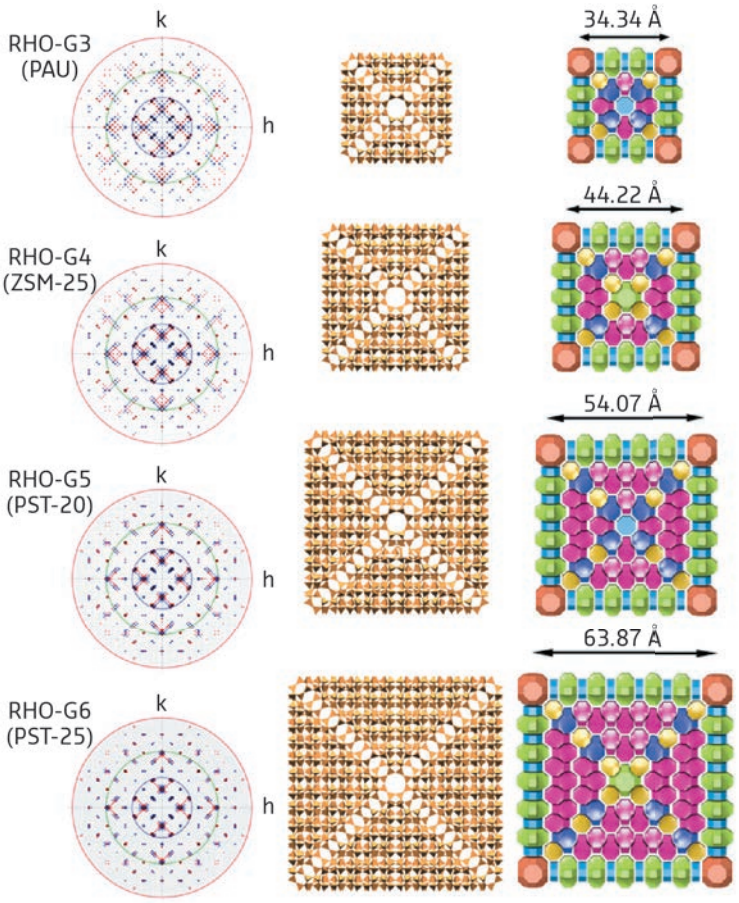

Fig. 40: Comparison of the reflection distributions and framework structures of RHO-G3 to RHO-G6. The (*hk*0) reciprocal plane (left), polyhedral (middle) and tiling (right) representations of cross-sections (about 12 Å thick).

PRINCIPAL PUBLICATION AND AUTHORS

A zeolite family with expanding structural complexity and embedded isoreticular structures, P. Guo (a), J. Shin (b), A. G. Greenaway (c), J.G. Min (b), J. Su (a), H.J. Choi (b), L.F. Liu (a), P.A. Cox (d), S.B. Hong (b), P.A. Wright (c) and X.D. Zou (a), *Nature* **524**, 74-78 (2015); doi: 10.1038/nature14575.
(a) Department of Materials and Environmental Chemistry, Stockholm University (Sweden)
(b) School of Environmental Science and Engineering, POSTECH, Pohang (Korea)
(c) EaStCHEM School of Chemistry, University of St. Andrews (UK)
(d) School of Pharmacy and Biomedical Sciences, University of Portsmouth (UK)

REFERENCES

[1] H.G. Doherty *et al.*, *US Patent* 4247416 (1981).
[2] W. Wan *et al.*, *J. Appl. Crystallogr.* **46**, 1863-1873 (2013).

FORMATION OF QUASI-SOLID STRUCTURE BY ADSORBED NOBLE GAS ATOMS IN PORES OF METAL-ORGANIC FRAMEWORK

***In situ* high-resolution synchrotron powder diffraction measurements of noble gas adsorption in metal-organic framework Cu^{I}-MFU-4*l* revealed a stepwise filling of adsorption sites: 10 crystallographically different positions for Xe and 8 for Kr. Formation of a quasi-solid structure with very dense packing of adsorbed noble gas atoms was observed above the boiling temperature of the corresponding noble gases.**

The development of porous materials for selective adsorption of the heavier noble gases has attracted much attention over last few years, being driven by the technological requests for noble gas-storage, separation, and sensing [1]. Xenon, in particular, is an expensive gas that has a lot of potential applications such as in lighting, thermal insulation, excimer lasers, ionisation chambers, general anaesthesia, and NMR probes. The very low concentration of Xe in the atmosphere requires energy-intensive cryogenic distillation of large volumes of air, and gives a mixture of Xe and Kr. The cryogenic separation of Xe/Kr mixtures in rare gas production remains a critical step that could be improved by sorption-based separation technologies. Other applications include Xe recovery from spent nuclear fuel and storage of radioactive Kr.

We have studied the unique noble gas adsorption and storage properties in the exceptional thermally and chemically stable metal-organic framework

Cu^{I}-MFU-4*l*, which contains alternating large and small voids [2]. Measurements at various pressures and temperatures revealed very high volumetric uptake of Xe and Kr as well as a unique quasi-solid noble gas structure in the pores of Cu^{I}-MFU-4*l*, which was formed above the boiling temperature of the corresponding gases.

The high-resolution powder diffraction data collected at beamline **ID22** allowed precise localisation of crystallographically different adsorption positions, 10 for Xe atoms and 8 for Kr atoms. Surprisingly, the main adsorption site for both Xe and Kr is not located near an open metal site in the small void, rather it is located in the corner of the large void and interacts with the largest part of the framework. For both Xe and Kr atoms, the coordinatively unsaturated Cu^{I} sites are not the first occupied adsorption sites, and their filling starts only after the major adsorption site near the framework in the large void has been filled.

The formation of the first adsorption layer by noble gas atoms in Cu^{I}-MFU-4*l* is complete after filling 4 different adsorption sites in the large pores and one adsorption site in the small pores. Further increase of pressure (or decrease of temperature) results in the formation of a second adsorption layer in the large pores, which consists of 3 positions. The formation of the second adsorption layer in the small pores (2 positions) was observed only for Xe atoms, showing that small and large pores are not equivalent for noble gas adsorption.

The filling of accessible voids in the small pores is responsible for the inflection in the Xe adsorption isotherms (**Figure 41**, top). It can be seen that the main adsorption step for Xe adsorption is unusually steep and reflects highly-selective filling of the large pores (approx. 85% of total pore volume).

In contrast to Xe adsorption, Kr shows only one adsorption step with a rather usual shape. In the case of Kr adsorption at 130 K, the small pore remains empty even at high pressure (100 kPa, corresponding to 0.5 relative pressure, **Figure 41**, bottom). This fact looks more surprising taking into account the smaller kinetic radius of Kr atoms and can only be explained by the larger difference between the actual temperature of the measurement (130 K) and the boiling temperature of Kr (120 K) in contrast to Xe (170 K measurement temperature and 165 K boiling temperature).

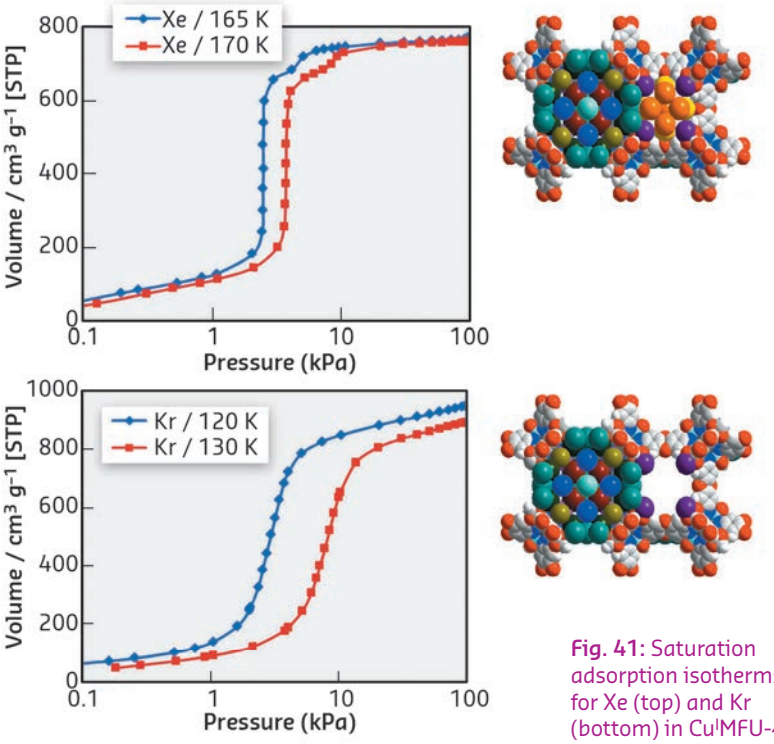

Fig. 41: Saturation adsorption isotherms for Xe (top) and Kr (bottom) in Cu^{I}MFU-4*l* in semilogarithmic scale (left), and corresponding position for Xe (at 170 K) and Kr (at 130 K) atoms in the large and small pores of Cu^{I}MFU-4 (right).

At the highest loadings in this experiment, the large voids adsorb ca. 55 atoms of Xe and ca. 70 atoms of Kr in 83 available positions, providing a very dense packing of adsorbed noble gas atoms. Strong van der Waals interaction of adsorbed noble gas atoms with framework atoms and also between adsorbed Xe and Kr atoms lead to an apparent increase of the freezing point for Xe and Kr and the formation of a quasi-solid structure of noble gas atoms inside the voids above their boiling temperature – a phenomenon to the best of our knowledge has not been reported before.

The detailed crystallographic study of this quite complicated gas adsorption phenomenon was only possible by using high-resolution synchrotron powder diffraction. Precise determination of crystal structures at different pressures and temperatures allowed accurate interpretation of adsorption isotherms, which is very important for unusual and very rare type of isotherms observed for Xe adsorption.

PRINCIPAL PUBLICATION AND AUTHORS

Formation of a quasi-solid structure by intercalated noble gas atoms in pores of Cu^{I}-MFU-4*l* metal–organic framework, O.V. Magdysyuk (a), D. Denysenko (b), I. Weinrauch (c), D. Volkmer (b), M. Hirscher (c) and R.E. Dinnebier (a), *Chem. Commun.* **51**, 714-717 (2015); doi: 10.1039/C4CC07554D.
(a) Max Planck Institute for Solid State Research, Stuttgart (Germany)
(b) Augsburg University, Augsburg (Germany)
(c) Max Planck Institute for Intelligent Systems, Stuttgart (Germany)

REFERENCES

[1] A.U. Czaja *et al.*, *Chem. Soc. Rev.* 38, 1284 (2009).
[2] D. Denysenko *et al.*, *Angew. Chem.* **126**, 5942 (2014).

MIXED-ANION METAL BORANES FOR SOLID STATE Na AND Li ELECTROLYTES

Na-based materials are becoming competitive alternatives to Li-ion batteries. For all-solid battery systems, electrode and electrolyte materials need to be developed and tested. Simple packed compounds have been discovered based on the tetrahydroborate $[BH_4]^-$ (borohydride) and the dodecahydroborate $[B_{12}H_{12}]^{2-}$ (*closo*borane) anions with very high conductivities for Li^+ and Na^+ cations comparable to NASICON-type materials, sulphide-glasses and rivalling even superionic β-alumina.

Much battery research is currently oriented towards the development of all-solid state concepts, where the liquid electrolyte, usually based on an organic solvent that dissolves the mobile species, *e.g.* Li^+ in Li-ion batteries, is replaced by a polymer or solid electrolyte. The aim is to avoid the safety issues arising with conventional, flammable liquid electrolytes. While such modifications eliminate the risk of dendritic growth or failure due to bad electrochemical and thermal stability of the cell, they pose a challenge with respect to the mobility of charge carriers, commonly orders of magnitude lower in the solid state than in the liquid.

Li-ion batteries are currently considered the benchmark technology for mobile applications. However, tremendous efforts are being invested on a global scale to take both mobile and stationary applications beyond lithium. These targets include large-scale implementations such as grid energy storage, where low power density can be compensated for by quantity or size. Hence, Na-based materials could become competitive alternatives. For all-solid battery systems, electrode and electrolyte materials need to be developed and tested.

This study deals with the solid-state electrolyte. Electrochemically stable materials with a large operating voltage window and a high conductivity at room temperature (RT) are required, potentially allowing a battery-design that employs metallic Na as anode-material, thus providing high capacity. Ionic conduction in a solid-state electrolyte is promoted by vacancy-driven mechanisms as well as structural dynamics. In particular, the *bcc* anion lattice has been found to favour ionic mobility. Novel materials that contain poly-anions $[AB_y]^{n-}$, where the structure is rationalised as a salt, are also promising. In such compounds the energy barrier for ionic conduction is lowered due to the rotational mobility of the poly-anion, which acts as a "paddle wheel" on the mobile ionic species, loosely bound in the host framework.

A number of solid state boranes are available to materials scientists exploring the conductive properties of complex hydrides. The present

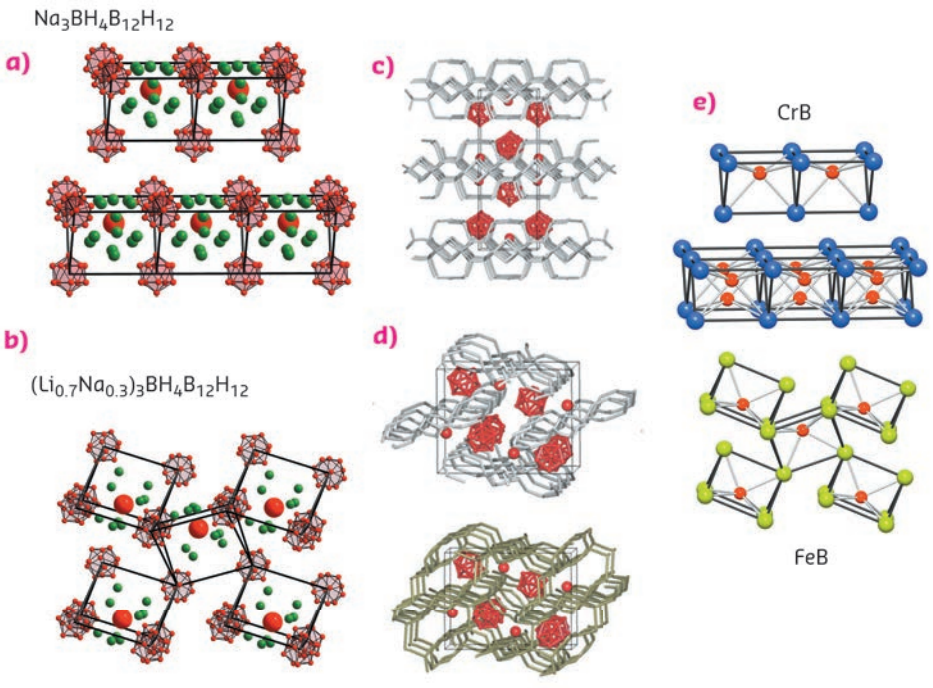

Fig. 42: (a) Crystal structure of $Na_3BH_4B_{12}H_{12}$ and (b) $(Li_{0.7}Na_{0.3})_3BH_4B_{12}H_{12}$; mobile species ($Li^+$,$Na^+$) in green, boron as red spheres, $[B_{12}H_{12}]^{2-}$ as molecule. (c) and (d) Conduction pathways for Na (grey) and Li (brown). (e) Comparison with the prototypical relationship between CrB and FeB; boron in red.

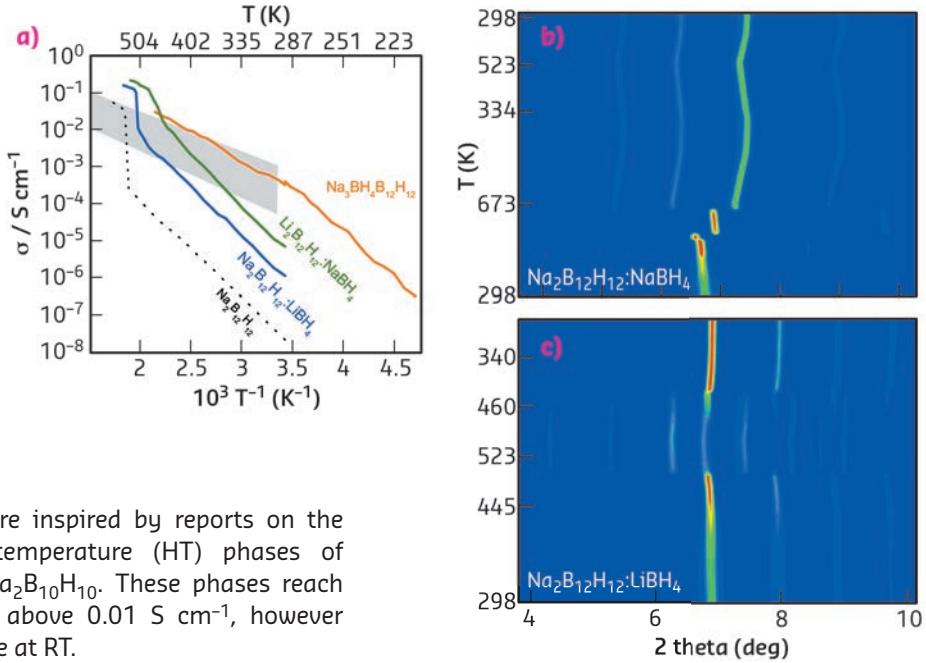

Fig. 43: (a) Ionic conductivities obtained from impedance spectroscopy. Typical NASICON and β-alumina materials in the shaded field. (b) *In situ* temperature-dependent diffraction data for the reaction forming $Na_3BH_4B_{12}H_{12}$ and (c) $(Li_{0.7}Na_{0.3})_3BH_4B_{12}H_{12}$.

investigations were inspired by reports on the superionic high-temperature (HT) phases of $Na_2B_{12}H_{12}$ and $Na_2B_{10}H_{10}$. These phases reach HT-conductivities above 0.01 S cm^{-1}, however they are not stable at RT.

Here, we explore anion-mixing of the tetrahydroborate $[BH_4]^-$ (borohydride) and the dodecahydroborate $[B_{12}H_{12}]^{2-}$ (*closo*borane) anions, attempting to build stable anion-sublattices of high crystal symmetry using the larger *closo*borane, while implementing additional rotational mobility with the borohydride anion. We discovered simple packed compounds and provide a roadmap based on crystal chemistry arguments to explore the phase diagram $Na_3BH_4B_{12}H_{12}$ – $Li_3BH_4B_{12}H_{12}$ in a search for further anion-mixed single- and double-cation conductors.

$Na_3BH_4B_{12}H_{12}$ and $(Li_{0.7}Na_{0.3})_3BH_4B_{12}H_{12}$ show very high conductivities of close to, and above, 10^{-1} S cm^{-1} at 500 K (**Figure 42**). To monitor HT reactions forming the solid electrolytes, we chose to work with the 2D Dectris Pilatus detector at **BM01A**, which allows very high counting statistics to be acquired at a fast rate (**Figure 43**). The crystal structures of the novel materials (**Figure 42**) provide evidence of localisation of the mobile species, Na^+ and Na^+/Li^+, respectively, in the structural fragments containing the borohydride anion, supporting the concept of anion-engineering, one of the initial aims of this project.

Topologically, a 1-dimensional conduction path is accessible to the Na-species in $(Li_{0.7}Na_{0.3})_3BH_4B_{12}H_{12}$, while a 2-dimensional path is available to Li (**Figure 42**), theoretically both species can conduct. However, the material is subject to a reversal chemical reaction upon cooling, and dissociates to its precursors. Upon heating, it again forms the superionic phase at 500 K (**Figure 43**).

$Na_3BH_4B_{12}H_{12}$, on the other hand, is formed by a reaction between $Na_2B_{12}H_{12}$ and $NaBH_4$ at 673 K, and is stable at RT. The 2D conduction pathways allow this phase to reach RT-conductivity values close to 10^{-2} S cm^{-1}, comparable to NASICON-type materials, sulphide-glasses and rivalling even superionic β-alumina. Next to the electrochemical stability of $Na_3BH_4B_{12}H_{12}$ (up to 10 V) and the favourable mechanical properties due to the material softness, the high RT-conductivity implies the potential use of Na-metal as anode. Furthermore, the reducing nature of the material minimises the risk of surface reactions on the electrode.

Our structural analyses have revealed a most striking similarity to the relationship between different stacking variants of metal-borides, which points towards the existence of further electrolytes in the $Na_3BH_4B_{12}H_{12}$ – $Li_3BH_4B_{12}H_{12}$ diagram, simply related by polytypism.

PRINCIPAL PUBLICATION AND AUTHORS

Superionic conduction of sodium and lithium in anion-mixed hydroborates $Na_3BH_4B_{12}H_{12}$ and $(Li_{0.7}Na_{0.3})_3BH_4B_{12}H_{12}$, Y. Sadikin, M. Brighi, P. Schouwink and R. Černý, *Adv. Energ. Mater.* 1501016 (2015); doi: 10.1002/aenm.201501016.

Laboratory of Crystallography, Department of Quantum Matter Physics, University of Geneva (Switzerland)

STRUCTURE AND PROPERTIES OF COMPLEX HYDRIDE PEROVSKITE MATERIALS

Borohydride perovskites pave the way to functional design in complex hydride materials for energy-applications. A novel mechanism is suggested for symmetry-design in perovskites, arising from the hydridic nature of hydrogen and inverting the temperature-dependency of lattice instabilities.

Perovskite materials are ubiquitous in materials science because of their distinct adjustability of physical properties and the readiness to incorporate most chemical elements from the periodic table. Slight alterations of the crystal structure can induce dramatic changes in the physical properties. Widely known as reducing agents in organic chemistry, the high hydrogen content per unit mass/volume and the rich structural dynamics of metal borohydrides have triggered vast investigations on their energy-related implementation as materials for solid-state hydrogen storage and all-solid batteries. Initially this was driven by the potential to develop $LiBH_4$ into a storage medium for on-board automobile applications. The motivation behind metal borohydrides in the materials science community hence directly targets a prime issue of modern consumer societies.

Due to the hydridic nature of hydrogen in the BH_4-molecule, borohydrides are somewhat an outsider, chemically speaking. The covalently bound hydrogen in molecular chemistry commonly carries a positive formal charge (protic hydrogen).

Despite the application-oriented search for novel complex hydrides, the rational structure-property design of metal borohydrides is still in its infancy. The principal objective of this study was to provide an extensive characterisation of a host material capable of meeting the requirements of genuine functional design, in order to take borohydrides beyond hydrogen storage applications in the future. Ideally, such a host material is of reduced complexity and superior stability.

Motivated by our previous discovery of a double-cation borohydride $KMn(BH_4)_3$ crystallising in the perovskite lattice, this structure type was systematically explored leading to the discovery of over 45 different materials whose formability criteria were evaluated based on the commonly used Goldschmidt tolerance factor (**Figure 44**).

We began to study this field on powder samples prepared by mechanochemistry using the Dectris Pilatus M2 detector at **BM01A**, systematically heating the sample to its decomposition (detection of thermal stability). With the resulting materials, we have managed to produce metal borohydrides with unforeseen

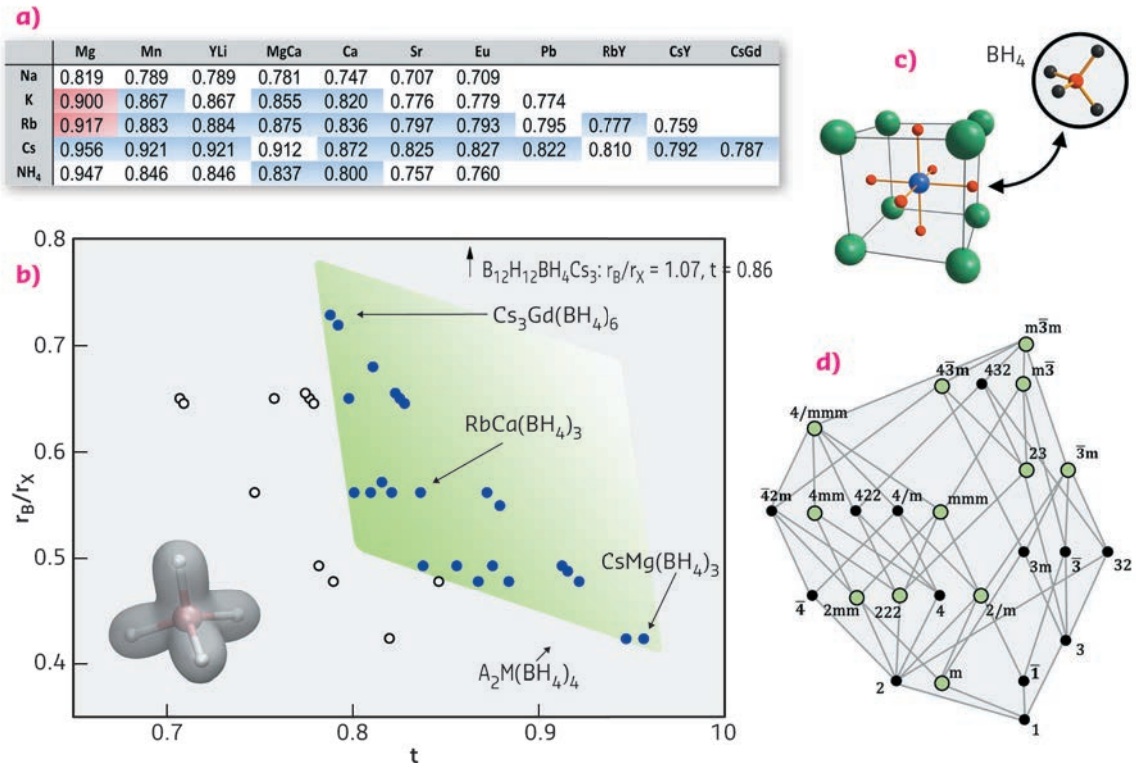

	Mg	Mn	YLi	MgCa	Ca	Sr	Eu	Pb	RbY	CsY	CsGd
Na	0.819	0.789	0.789	0.781	0.747	0.707	0.709				
K	0.900	0.867	0.867	0.855	0.820	0.776	0.779	0.774			
Rb	0.917	0.883	0.884	0.875	0.836	0.797	0.793	0.795	0.777	0.759	
Cs	0.956	0.921	0.921	0.912	0.872	0.825	0.827	0.822	0.810	0.792	0.787
NH_4	0.947	0.846	0.846	0.837	0.800	0.757	0.760				

Fig. 44: (a-b) Formability field (green) of borohydride perovskites based on octahedral vs. tolerance factor *t* (listed in table (a). The $AM(BH_4)_3$ structure is shown in (c). (d) Sub-groups of the cubic aristotype, green circles correspond to crystal symmetries of discovered borohydrides.

physical properties such as photoluminescence, magnetic refrigeration, semiconductivity, and proton-hydride interactions between cations NH_4^+ and anions BH_4^- which facilitate H_2-formation. Simple concepts such as the tolerance factor and ionic substitution were applied in order to obtain a desired property, following the established approaches for metal-oxide perovskites.

An unexpected structural trend was revealed for metal-borohydride perovskites. For perovskites in general, both the rotation (tilt) of MO_6 octahedra and atomic displacements tend to vanish upon heating due to an increase in crystal symmetry, likewise for polar physical properties, such as an electric dipole moment. But for $AM(BH_4)_3$ (A: alkali metal, M: bivalent metal), we often find this trend to be reversed, hence stabilising low crystal symmetry at high temperature, and providing the structural requirements for polar properties. Our working hypothesis assigns the origin of this behaviour to interactions between molecular B-H vibrations and lattice vibrations and hence proposes a novel mechanism useful for tailoring perovskite symmetries [1]. For instance, a prominent lattice instability (*R*-point) of symmetry *Pnma* is activated upon heating $KCa(BH_4)_3$ into the HT-phase (**Figure 45**). A discrete step in the bandwidth of the Raman B-H stretching signature concurs with the structural transition, suggesting that internal modes of the BH_4 molecule and lattice modes stabilising the crystal symmetry communicate with each other.

Theoretical solid state calculations provided further insight into the transformation mechanism, pointing towards the crucial role of close homopolar repulsive di-hydrogen for the structural behaviour of $AM(BH_4)_3$ (**Figure 45**). As well as providing a stable host for functional design, the borohydride perovskite hence incorporates weak interactions, which define structure and packing in molecular and supramolecular chemistry, into a structural behaviour otherwise controlled by lattice vibrations. Meanwhile, the role of these interactions in $AM(BH_4)_3$ has been verified by quasielastic neutron scattering studies of BH_4 reorientations [2] and single crystal X-ray diffraction performed at **BM01A** on the first double-cation metal-borohydride single crystal [3].

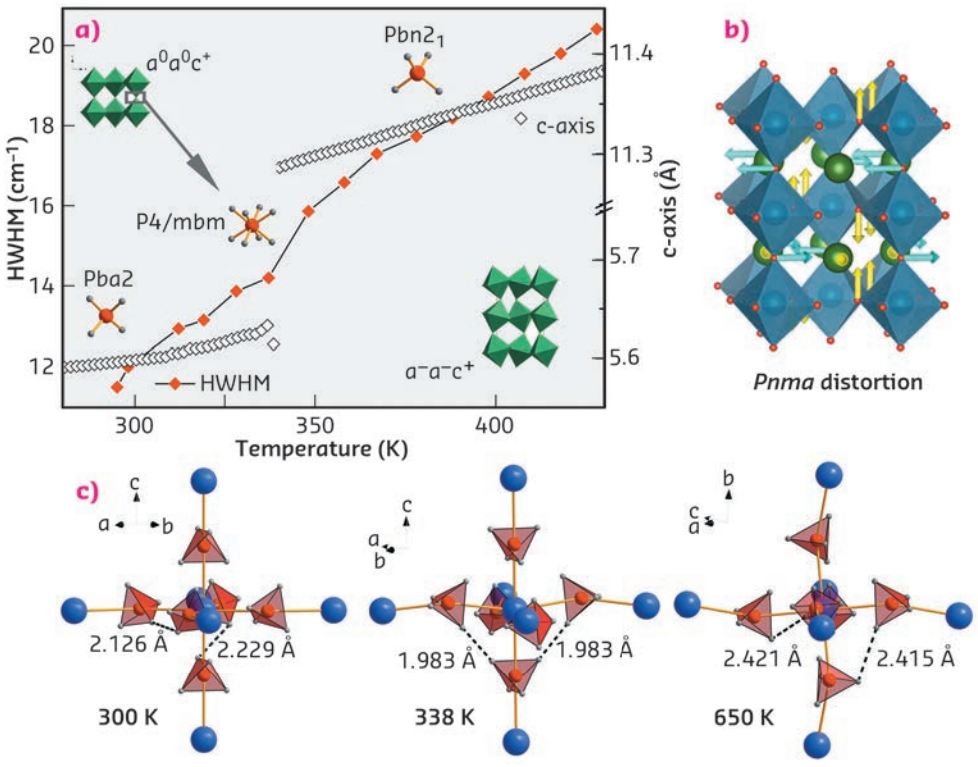

Fig. 45: (a) Changes in structure during the high-temperature phase transition of $KCa(BH_4)_3$, followed by *in situ* powder diffraction and Raman spectroscopy; (b) The corresponding apolar parent distortion; (c) relevant short H···H contacts within the $Ca(BH_4)_6$-octahedron.

PRINCIPAL PUBLICATION AND AUTHORS

P. Schouwink (a), M.B. Ley (b), A. Tissot (c), H. Hagemann (c), T.R. Jensen (b), L. Smrčok (d) and R. Černý (a), *Nature Comm.* **5**, 5706 (2014).
(a) Laboratory of Crystallography, Department of Quantum Matter Physics, University of Geneva (Switzerland)
(b) Interdisciplinary Nanoscience Center (iNANO), Department of Chemistry, University of Aarhus (Denmark)
(c) Department of Physical Chemistry, University of Geneva (Switzerland)
(d) *Institute of Inorganic Chemistry, Slovak Academy of Sciences, Bratislava, (Slovak Republic)*

REFERENCES

[1] J.M. Rondinelli and C.J. Fennie, in *Adv. Mater.* **24**, 1961-1968 (2012).
[2] P. Schouwink *et al.*, in *J. Phys. Condens. Matt.*, **27**, 265403 (2015).
[3] P. Schouwink *et al.*, in *CrystEngComm*, **17**, 2682-2689 (2015).

FORMATION AND EVOLUTION OF A HIGH CATALYTIC PERFORMANCE CARBON SUPPORTED Pd SULFIDE NANO-PHASE

The combination of high-energy X-ray diffraction (HEXRD) and mass spectroscopy (MS) measurements reveals that the reduction under hydrogen of the carbon supported palladium sulphate precursor provides a Pd_4S based catalyst with significant activity and superior selectivity to partial hydrogenation of dialkenes, and high stability under reaction conditions.

Partial hydrogenation of alkynes and alkadienes in the presence of alkenes is one of the most important processes in the chemical industry and its selectivity is a relevant issue. Supported palladium catalysts are currently used for the hydrogenation of 1,3-butadiene (Bd), but because they lack selectivity for the desired n-butenes when the ratio of monoalkenes to dienes is high, promoters (Ag, Au, Ga or Cu) or modifiers (CO or sulfur) are needed to enhance the yield of partially hydrogenated products [1]. These alternatives suppose complex preparation methods or continuous feeding of a modifier compound to maintain the catalyst properties during reaction [1, 2].

We present here a new procedure for the preparation of palladium sulfide nanoparticles, which are deposited-anchored over highly graphitised carbon nanofibres. The preparation method is based on the use of $PdSO_4$ as metal precursor or alternatively in the previous functionalisation of the carbon surfaces with sulfonic groups by treatment with fuming sulfuric acid. Using "*in situ*" high-energy X-ray diffraction coupled with mass spectroscopy at the **ID15A** beamline, for both cases it was demonstrated that the initially present palladium hydride is transformed into a palladium sulfide (Pd_4S) during the reduction treatment. **Figure 46** shows the structural evolution of the sample prepared with palladium sulfate as measured with HEXRD. When the sample is exposed to hydrogen/helium at room temperature the HERXD pattern reveals the formation of the β phase of Pd hydride (peak (111) at 2.70 $Å^{-1}$) which is transformed into metallic Pd at 90°C (2.80 $Å^{-1}$). As the temperature approaches 150°C, a second transformation occurs, resulting in the formation of the Pd_4S phase ((210) and (112) peaks at 2.74 and 2.83 $Å^{-1}$, respectively). The formation of the Pd sulfide phase is further described with the help of MS. From the MS analysis (inset, lower panel), we observe the evolution of H_2S (m/z = 34) and SO_2 (m/z = 64). Both products stem as main gas residues coming from the decomposition/reduction of the sulfate anions of the metal precursor deposited on the support and appear with a constant level from 100 to 160°C. At this latter temperature, Pd is completely transformed to the single well crystallised Pd_4S structure.

Subsequently, we studied the evolution of Pd phases under butadiene hydrogenation reaction atmosphere at different temperatures and during $H_2/(H_2+Bd)/H_2$ alternate exposure. Once the catalysts were treated in hydrogen at 250°C, the temperature was reduced to the corresponding reaction temperatures. **Figure 47** shows an HEXRD study carried out on the sample prepared with palladium sulfate.

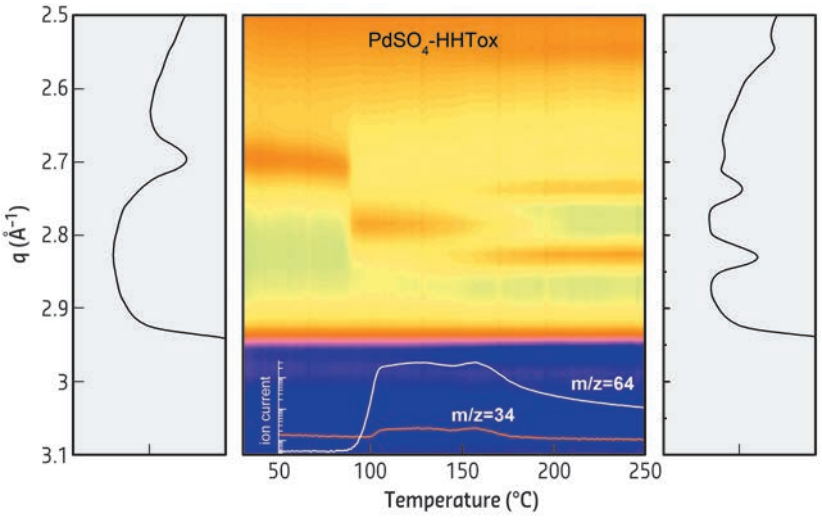

Fig. 46: Intensity contour maps of the HEXRD patterns obtained during temperature-programmed reduction in hydrogen/helium from room temperature up to 250°C.

No structural changes were noticed in the phase formed during reduction in hydrogen at 250°C during the time of exposition to reaction mixture and switching to hydrogen at both 100 and 150°C temperatures. The MS analysis shows the high selectivity of the catalyst for the partial hydrogenation of butadiene (m/z = 39) into butenes (m/z = 41). The stability of the Pd_4S phase under reaction conditions was also proved by a long-term catalytic run performed in a fixed bed reactor at 100°C. Activity and selectivity were maintained throughout the run.

These XRD-based results suggest that reduction under hydrogen of the carbon supported palladium sulfate precursor should provide a facile method to synthesise a well-defined single palladium sulfide structure which has significant activity, appropriate selectivity, and high stability under reaction conditions.

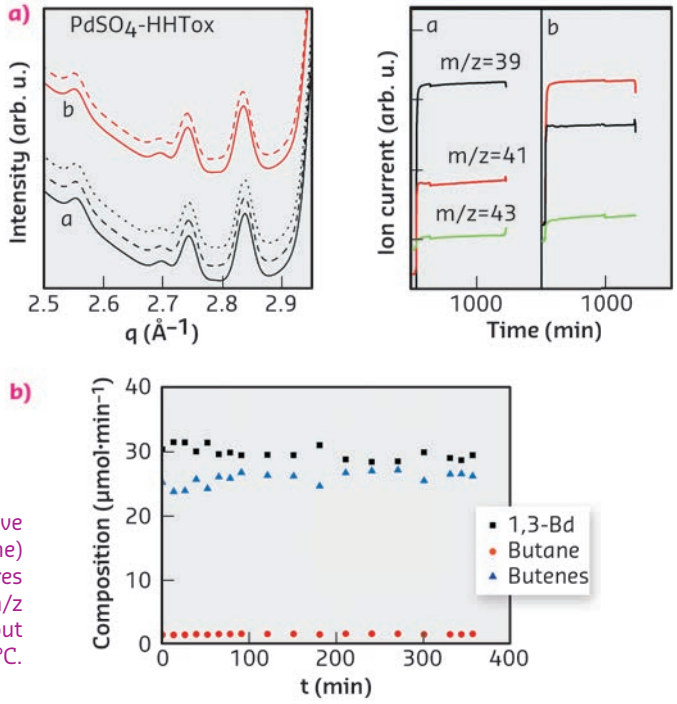

Fig. 47: (a) HEXRD patterns obtained under consecutive H_2 (full line), H_2 + Bd (dashed line), H_2 (dotted line) atmospheres at several constant temperatures (a: 100°C; b: 150°C) and MS results for selected m/z values under H_2 + Bd. (b) Stability test carried out at 100°C.

PRINCIPAL PUBLICATION AND AUTHORS

Detecting the genesis of a high-performance carbon-supported Pd sulfide nanophase and its evolution in the hydrogenation of butadiene, B. Bachiller-Baeza (a), A. Iglesias-Juez (a), E. Castillejos-López (b), A. Guerrero-Ruiz (b), M. Di Michiel (c), M. Fernández-García (a) and I. Rodríguez-Ramos (a), *ACS Catal.* **5**, 5235–5241 (2015); doi: 10.1021/acscatal.5b00896.
(a) Instituto de Catálisis y Petroleoquímica, CSIC, Madrid (Spain)
(b) Departamento de Química Inorgánica y Química Técnica, UNED, Madrid (Spain)
(c) ESRF

REFERENCES

[1] A. Cooper *et al.*, *Catal. Sci. Technol.* **4**, 1446–1455 (2014).
[2] B. Bachiller-Baeza *et al.*, *Catal. Today* **249**, 63–71 (2015).

Electronic structure, magnetism and dynamics

The Electronic Structure, Magnetism and Dynamics (EMD) Group was formed in 2015 and includes the beamlines ID12 (Circular Polarisation), ID20 (Inelastic X-ray scattering I), ID26 (X-ray Absorption and Emission Spectroscopy), ID28 (Inelastic X-ray scattering II) and ID32 (Soft X-ray Spectroscopy). Research performed at these beamlines covers all fields of natural sciences and has a common theme that all beamlines apply spectroscopy to study excited states of matter. Excellent facilities for X-ray absorption spectroscopy are also available at CRG beamlines and this chapter therefore includes some highlights of work performed at BM08 (LISA), BM20 (ROBL), BM26 (DUBBLE) and BM28 (XMaS). We realised that a common forum to present scientific results and discuss instrumentation would be of great benefit and the ESRF now organises public seminars that cover either experimental techniques such as spectroscopy and high pressure or research fields such as magnetism and catalysis. All users are invited to attend the meetings when visiting the ESRF and are encouraged to present their work.

The first phase of the ESRF Upgrade Programme was completed in 2015 and the past months have been particularly exciting for the team of ID32 and the UPBL7 project. The XMCD branch started taking users at the end of 2014. Many groups have used the branch with several very interesting projects being carried out and now the first publications are starting to appear. The sample preparation facility allows UHV preparation of samples. There is a chamber for metal evaporation with LEED and Auger (CMA) diagnostic tools and a separate chamber for molecule evaporation with a MCP-LEED. All the chambers are interconnected also allowing samples to be characterised by an STM. The superconducting high-field magnet 9 Tesla / 4 Tesla (along/perpendicular to the beam) with a low temperature sample probe is ideal for XMCD and XMLD experiments under UHV conditions (see the article from Willers *et al.*).

The RIXS branch of ID32 started its commissioning in May 2015 with the medium resolution setup. The day one resolution aims were rapidly achieved at the copper L edge: 50-55 meV combined energy bandwidth. The high resolution branch started commissioning in November and achieved a combined bandwidth of 30-35 meV at the copper L edge, already close to the ultimate aim of the project. In addition, the flexibility given by the 5 axis sample goniometer and the continuous rotation of the scattering arm (50-150 degrees scattering angle) is opening up new experimental possibilities which will hopefully be exploited in the coming year. First tests of the RIXS polarimeter have shown that the concept works well although the instrument still needs to be fully commissioned in the coming months (see Braicovich *et al.* and Minola *et al.*).

ID20 (UPBL6) entered its second year of full user operation in 2015. The beamline currently holds the world record in energy resolution at the Ir L_3 edge, an achievement that attracts many groups interested in the physics of iridates. The high flux combined with a small focal spot size and high energy resolution has enabled new research in particular in high pressure IXS experiments. The large solid angle of the X-ray Raman scattering (XRS) instrument on ID20 has accelerated data acquisition such that time-resolved studies with sub-minute resolution are now possible using this photon-hungry technique. Inkinen *et al.* monitored the chemical reaction of cinnamic acid with both time (30 seconds) and spatial (50 µm) resolution. They measured C K-edge spectra using XRS and show the effect of dimerisation. The experimental data are nicely supported by calculations of the spectra. Diffuse magnetic scattering with energy resolution was used by Chun *et al.* to better disentangle the elastic and inelastic scattering response of Na_2IrO_3. This provides insights into the bond-directional nature of magnetic correlations in this material and supports a magnetic model with dominant Kitaev-type interaction.

An important milestone was reached at ID26 in collaboration with the Crystal Analyser Laboratory (CAL) and the EcoX partnership when a new type of spherical analyser was tested. This new analyser provides a 4-times larger solid angle without degrading the energy resolution. The increased detection efficiency allows samples to be measured with absorber concentrations of a few ppm and accelerates the data acquisition which is particularly important for *in situ* studies.

The two highlights from ID26 presented in this chapter address the charge transfer after optical excitation in Au/TiO_2 nanoparticles (Amidani *et al.*) and the mechanism for removal of NO_x by selective catalytic reduction in vehicle exhaust gases (Günter *et al.*).

The experimental station at ID12 that is dedicated to X-ray magnetic circular dichroism at low temperatures (down to 2 K) and high magnetic field (up to 17 Tesla) has become a unique experimental platform for basic research on magnetism and the workhorse for XMCD measurements. Two examples in this chapter illustrate its outstanding performance. A long-standing question concerning the modelling of the complex structure of 5f electrons that give rise to the magnetic properties of actinides was addressed by Magnani *et al.* The second example by Badía-Romano *et al*. demonstrates how element-selective magnetisation curves probed with XMCD can be used to unravel the mechanism of magnetic interactions in "butterfly" $\{Fe_3LnO_2\}$ molecules.

Beamline ID28 upgraded the multi-element low noise detector of the IXS spectrometer. CdTe is now employed that can be used at ambient temperature instead of Peltier cooled silicon. This migration brings the advantages of a more compact design and a more sustainable detector technology, as CdTe is widely used. In the first highlight from ID28, Antonangeli *et al.* show how combined measurements of density and sound velocity on both body-centered cubic (bcc) and fcc iron as a function of temperature and pressure lead to a revised model of the Moon's metallic core. A study of the elastic properties of an out-of-equilibrium glass as a function of its age is presented in a second highlight by Pogna *et al*. The authors conclude that conventional wisdom claiming that glass ceases to flow at a finite temperature could be wrong.

P. GLATZEL

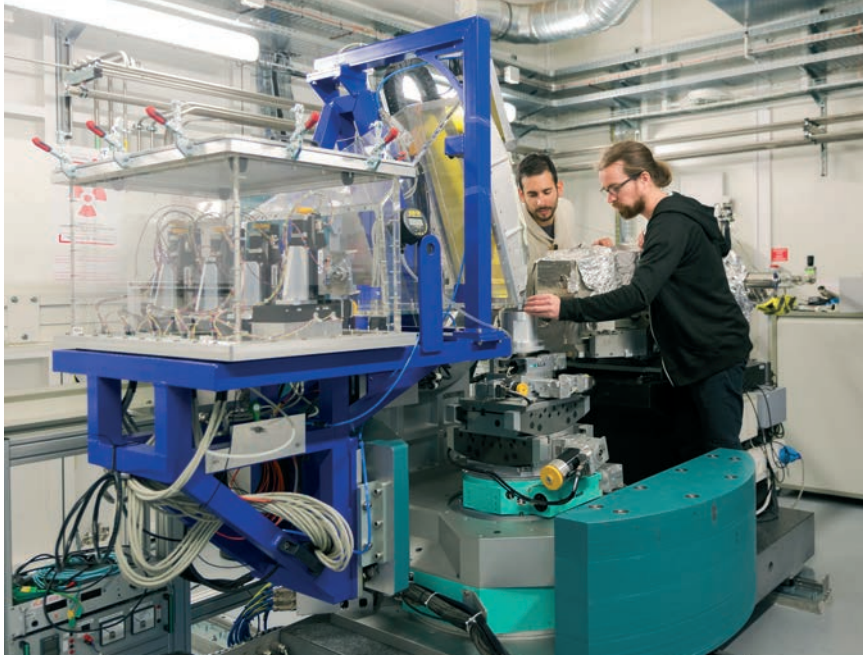

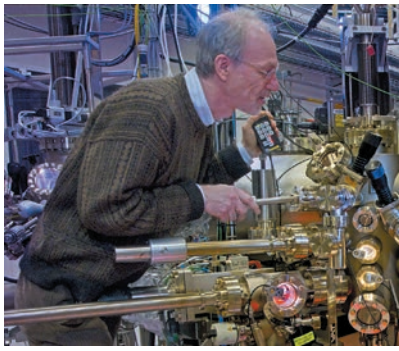

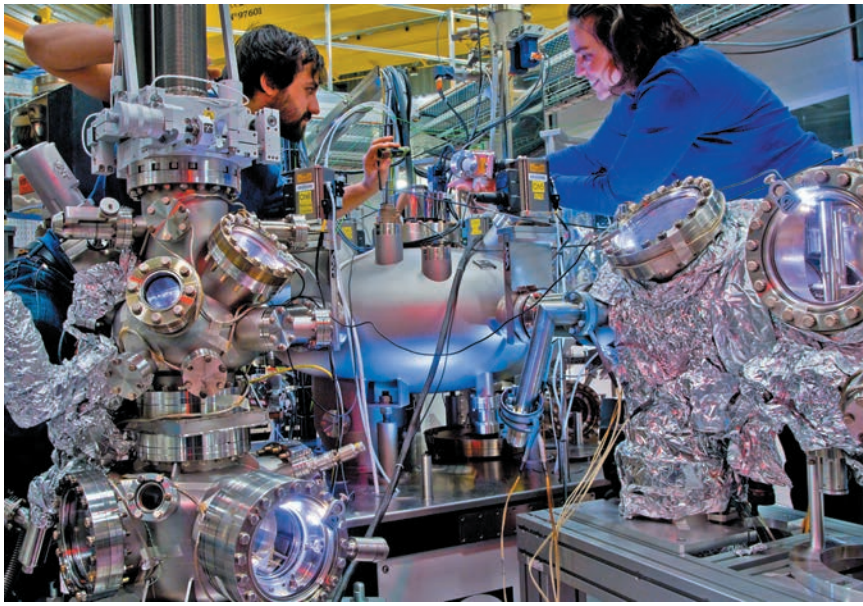

FULLY-POLARISED SOFT X-RAY RIXS AT THE ESRF

Simultaneous measurements of energy and polarisation of the scattered X-rays has been made using soft X-ray RIXS (resonant inelastic X-ray scattering) for the first time. For high temperature superconductors of the yttrium barium copper oxide (YBCO) family the results were instrumental in demonstrating the collective nature of the magnetic excitations.

Copper-based high-critical-temperature superconductors (HTcS) have a layered structure, for which the fundamental building units are CuO_2 planes that have a square lattice with spin 1/2 Cu^{2+} ions bound to oxygen. The superconductivity arises upon doping either with holes or electrons. The antiferromagnetic coupling of Cu, typical of the undoped parent compound, is not destroyed in the short range upon doping. Therefore, to assess whether the low energy magnetic excitations are collective or band-like is of great interest for the long standing debate on high Tc superconductivity. In ref. [1] the collective nature of magnetic excitations in the YBCO family was demonstrated with RIXS. Indeed RIXS can be thought of as resonant Raman scattering and the observation of a constant energy-loss at increasing incident energy rules out the band-like picture that would lead to constant emitted-energy. The experiment is complicated by the superposition of the magnetic peaks with non-magnetic excitations. Due to angular momentum conservation, spin excitations are characterised by the change of the linear polarisation of the scattered light, as shown in Figure 48 and explained in [1]. In effect, in two superconducting $YBa_2Cu_3O_{6+\delta}$ samples, the full analysis of the polarisation of the scattered X-rays demonstrates that the spectra with π incident polarisation, at large positive wave-vector, are largely dominated by a crossed polarisation process, which is the fingerprint of spin excitations (Figure 48, *a* and *b*). The measurements vs. incident energy were made at the Swiss Light Source (SLS), without observing the outgoing polarisation, while the spectra with full control of the polarisation discussed here were taken at the ESRF.

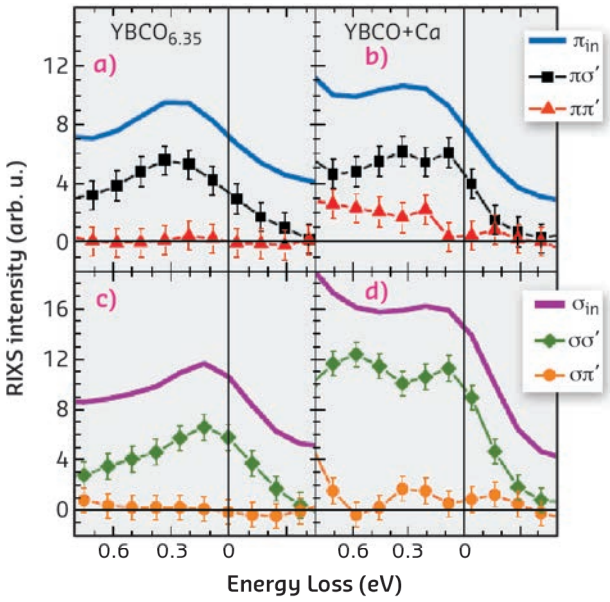

Fig. 48: Polarisation-resolved RIXS spectra from underdoped (left; p = 0.062) and overdoped (right, p = 0.21) YBCO. Scattering angle 130° and near normal incidence. The spectra were measured by tuning the photon energy to the peak of the Cu L_3 absorption.

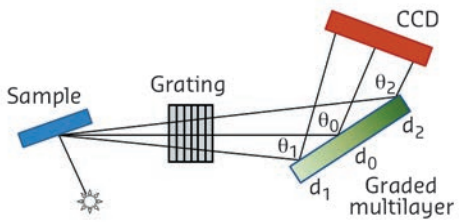

Fig. 49: Schematic of the apparatus used in the measurements given in Figure 48.

RIXS has recently become a powerful approach, cross fertilising with neutrons, and having the great advantage of being possible on very small amounts of material down to a layer of a single unit cell of a cuprate. Normally, the polarisation of the scattered photons is not measured in the soft X-ray range and this is one of the most severe limitations at present. This is largely due to polarisation analysis being a real technical challenge. Starting in 2011, at beamline **ID08**, a preliminary prototype of a polarimeter (used in [1]) was designed, realised, field tested and progressively improved, using the AXES spectrometer available at that time for RIXS. The work was carried out jointly by a team from the Politecnico di Milano (Italy) and by ESRF staff [2]. The polarimeter works as shown schematically in Figure 49. Inside the spectrometer, a plane multilayer mirror deflects the beam by a large angle (~40 deg), so that the σ and π components of linear polarisation are reflected with significantly different efficiency. An appropriate linear combination of the spectra measured with and without the multilayer provides the polarisation-resolved RIXS spectra. This valuable information comes at the price of a loss in intensity of more than a factor 10 in the prototype. The major technical difficulty is given by the horizontal divergence of the beam coming from the sample, which requires a graded multilayer to accept a sizeable horizontal aperture. The system has an energy bandpass of about 1.5 eV and it goes rapidly out of tune when changing energy.

In the meantime, the new beamline **ID32** has been equipped with an 11 metre RIXS spectrometer. Its first mirror collimates the radiation horizontally, so that the new polarimeter has a vertical gradient matching the grating dispersion as suggested in [2] and ensuring a flat bandpass of

at least 10 eV. Preliminary tests at the Cu L_3 edge gave good results with 11000 resolving power. Note that, without the polarimeter, the instrument can provide a resolving power of up to 30000.

PRINCIPAL PUBLICATION AND AUTHORS

[1] *Collective nature of spin excitations in superconducting cuprates probed by resonant inelastic X-ray scattering*, M. Minola (a), G. Dellea (b), H. Gretarsson (a), Y.Y. Peng (b), Y. Lu (a), J. Porras (a), T. Loew (a), F. Yakhou (c), N.B. Brookes (c), Y.B. Huang (d), J. Pelliciari (d), T. Schmitt (d), G. Ghiringhelli (b), B. Keimer (a), L. Braicovich (b) and M. LeTacon (a), *Physical Review Letters* **114**, 217003 (2015); doi: 10.1103/PhysRevLett.114.217003.
(a) Max-Planck-Institut fur Festkorperforschung, Stuttgart (Germany)
(b) CNISM, CNR-SPIN and Dipartimento di Fisica, Politecnico di Milano (Italy)
(c) ESRF
(d) Swiss Light Source, Paul Scherrer Institut, Villigen (Switzerland)

[2] *The simultaneous measurement of energy and linear polarization of the scattered radiation in resonant inelastic soft X-ray scattering*, L. Braicovich (a), M. Minola (b), G. Dellea (a), M. LeTacon (b), M. MorettiSala (c), C. Morawe (c), J.C. Peffen (c), R. Supruangnet (c), F. Yakhou (c), G. Ghiringhelli (a) and N.B. Brookes (c), *Review of Scientific Instruments* **85**, 115104 (2014); doi: 10.1063/1.4900959.
(a) CNISM, CNR-SPIN and Dipartimento di Fisica, Politecnico di Milano (Italy)
(b) Max-Planck-Institut fur Festkorperforschung, Stuttgart (Germany)
(c) ESRF

CORRELATION OF GROUND STATE PROPERTIES AND ORBITAL ANISOTROPY IN HEAVY FERMION MATERIALS

The interplay of structural, orbital, charge, and spin degrees of freedom is at the heart of many physical phenomena, including superconductivity. Unraveling the underlying forces requires an understanding of each of these degrees of freedom as well as the interplay between them. Cerium-based heavy fermion compounds are an ideal playground for investigating these interdependencies, and a correlation between the orbital anisotropy and the ground states in a representative family of materials has been shown.

The detailed mechanism of high-temperature superconductivity is not yet understood, neither in the copper oxide nor in the Fe-pnictide high-temperature superconductors. It is believed though, that the interplay of magnetism and superconductivity is of central importance. Here, the so called *heavy fermion* compounds enter the stage. They are conducting materials where the charge carriers move as if their mass were 1000 times heavier than the mass of the free electron and for this reason they are called heavy fermions. This mass enhancement originates from strong interactions between electrons. The heavy fermion phenomenon can be found in many solids containing cerium (Ce) or ytterbium (Yb). Many heavy fermion compounds also exhibit unconventional superconductivity, therefore, we should gain new insights into the mechanism of high-temperature superconductivity if we could understand heavy fermion phase diagrams.

The members of the heavy fermion family Ce*M*In5 with *M* = Co, Rh or Ir exhibit superconducting and magnetic ground states when substituting one *M* element for another (see Figure 50) [1]. These materials are therefore recognised as important model systems in which a search for parameters that *correlate* with the formation of a magnetic or superconducting ground state could be successful.

Here we investigated the 4*f* crystal-electric field ground-state wave functions of the strongly correlated materials $CeRh_{1-x}Ir_xIn_5$ across the phase diagram (see Figure 50). The ground state wave functions were measured with great accuracy using linear polarisation-dependent soft X-ray absorption spectroscopy (XAS) at the cerium *M*-edges (see top of Figure 51). To assure that only the ground state was probed, the measurements were performed at low temperature. The data were analysed with a full multiplet routine including a crystal-field model

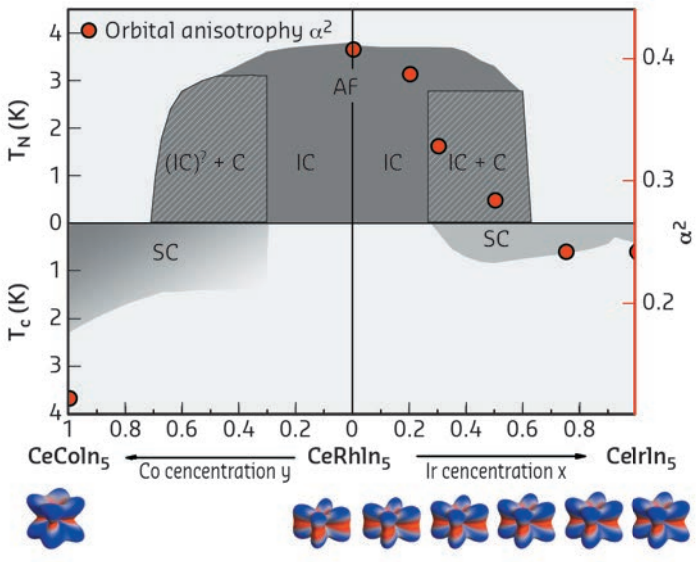

Fig. 50: Substitution phase diagram of Ce*M*In$_5$ compounds; SC stands for superconducting and AF for antiferromagnetic. The dots are the orbital anisotropy α^2 as a function of x for $CeRh_{1-x}Ir_xIn_5$ and for $CeCoIn_5$ with the scale on the right hand side. The respective angular distributions of the 4*f* CEF ground-state orbitals in $CeRh_{1-x}Ir_xIn_5$ and $CeCoIn_5$ is shown below the phase diagram.

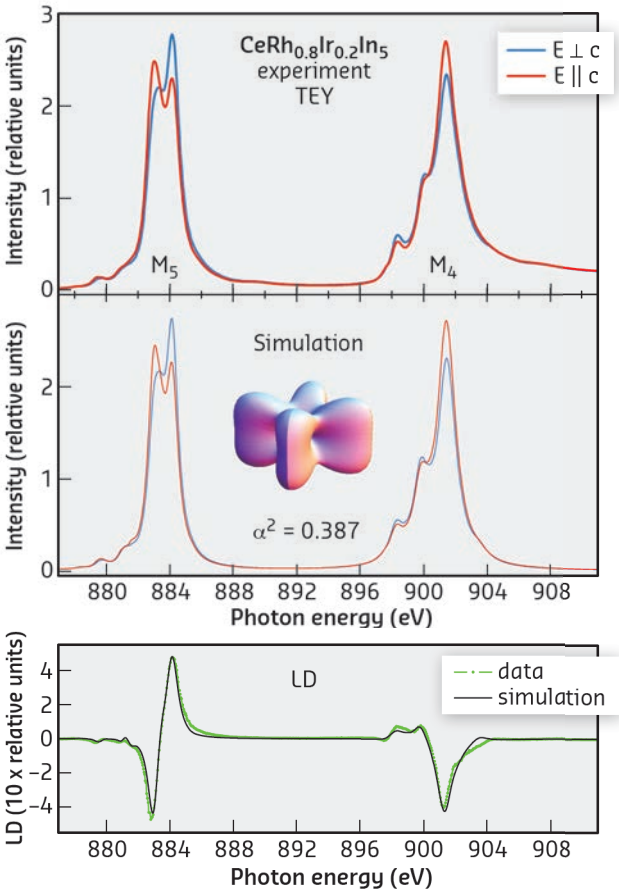

Fig. 51: Top: measured *M*-edge of $CeRh_{0.8}Ir_{0.2}In_5$ for linear polarised light. Middle: simulation with the full multiplet routine including the crystal-field model. Bottom: experimental and simulated linear dichroism.

(see middle and bottom of Figure 51), and a ground state wave function of the type

$$\alpha \left|\pm\frac{5}{2}\right> + \sqrt{1-\alpha^2}\left|\pm\frac{3}{2}\right>$$

was assigned to each Ir concentration. Here α, which stands for the amount of J_z = 5/2 and 3/2 in the ground state, determines the shape of the orbitals. The wave functions of the full compounds were determined in an earlier experiment [2]. We found that the parameter α scales very sensitively with the respective ground state (see red dots in Figure 50) such that *flatter* orbitals correlate with magnetic order, while *more extended* orbitals occur in the superconducting compositions (see Figure 50). The more extended orbitals can intermix (hybridise) more easily with other electrons and therefore contribute more to the electric conductivity. These observations are independent of lattice effects. Such a correlation had been theoretically suspected, but it was only now proven experimentally thanks to these polarised X-ray absorption measurements at beamline **ID08**.

Our results yield a microscopic picture of these materials as they become superconducting; this will hopefully stimulate further theoretical descriptions.

PRINCIPAL PUBLICATION AND AUTHORS

Correlation between ground state and orbital anisotropy in heavy fermion materials, T. Willers (a), F. Strigari (a), Z. Hu (b), V. Sessi (c), N.B. Brookes (c), E.D. Bauer (d), J.L. Sarrao (d), J.D. Thompson (d), A. Tanaka (e), S. Wirth (b), L.H. Tjeng (b) and A. Severing (a), *PNAS* **112, 2384,** (2015); doi: 10.1073/pnas.1415657112.

(a) Institute of Physics II, University of Cologne (Germany)
(b) Max Planck Institute for Chemical Physics of Solids, Dresden (Germany)
(c) ESRF
(d) Los Alamos National Laboratory (USA)
(e) Hiroshima University (Japan)

REFERENCES

[1] J.D. Thompson and Z. Fisk, *J. Phys. Soc. Jpn.* **81**, 011002 (2012), and references therein.
[2] T. Willers *et al.*, *Phys. Rev. B* **81**, 195114 (2010).

EXHAUST GAS CATALYSTS IN ACTION: OPERANDO HERFD-XAS AND XES FOR ELUCIDATING THE MECHANISM OF NOx-REMOVAL BY AMMONIA-SCR

Stringent emission legislation for vehicles requires high performance catalysts to reduce pollutant gases. A knowledge-based design and improvement of these catalysts and their implementation in the vehicle can be achieved by understanding the reactions occurring on the catalyst. The interaction of gases with the catalyst was studied under working conditions with complementary X-ray absorption and emission techniques to identify the reaction mechanism.

Optimisation of combustion engines combined with modern catalytic converters has contributed to a significant reduction of pollutant emissions [1,2]. Recently, new catalysts for diesel cars have been introduced to decrease NOx-emissions. Cu-based zeolites are the active component for the selective catalytic reduction (SCR) of NOx using NH_3, which is obtained by decomposition of urea (AdBlue®). There is a debate in the literature on the structure and position of active Cu-sites within the zeolite. A profound understanding of the catalyst operation will support rational catalyst design and the development of control algorithms for exhaust gas aftertreatment

systems. Characterisation of the material before and after the reaction can provide initial ideas on the catalyst's behaviour. However, for comprehensive characterisation, it is essential to study the catalyst under working conditions since many intermediate steps are only observable while the reaction is occurring because the structure of catalysts is dynamic.

As indicated in **Figure 52**, X-rays offer the possibility to monitor the catalyst under operating conditions. In addition, they can be used to selectively probe one element, allowing visualisation of the interaction of gas molecules with these sites while ignoring adsorption on the catalyst support material. Using high-energy-resolution fluorescence-detected (HERFD) X-ray absorption spectroscopy (XAS), we could overcome the limitations of standard XAS, leading to detailed measurement of the Cu K edge that contains information on the oxidation state and coordination of the metal sites. Additional valence-to-core X-ray emission spectroscopy (v2c-XES) made identification of adsorbed species at these metal sites possible (*e.g.* NOx, NH_3, H_2O), while distinguishing between atoms with close atomic numbers such as O and N.

Here we demonstrate the application of these techniques in order to characterise the catalytic sites of Cu-SSZ-13 under reaction conditions. A quartz capillary microreactor was used to mimic a plug-flow reactor as closely as possible. The sample was heated to a realistic reaction temperature and the gas composition analysed at the reactor outlet. To understand the SCR-reaction, model gas conditions were tested in addition to the SCR mixture, allowing the influence of each gas component and interactions between the gases to be studied separately.

We were able to follow small spectroscopic changes in the presence of different gases via HERFD-XAS and v2c-XES at beamline **ID26** (**Figure 53**). Cu oxidation state and geometry could be quantified by using the pre-edge feature (*e.g.* Cu^{2+}, $1s^2 \rightarrow 3d^9$). A more intense feature in the rising edge region is related to Cu^+ and becomes even more pronounced for linear coordination

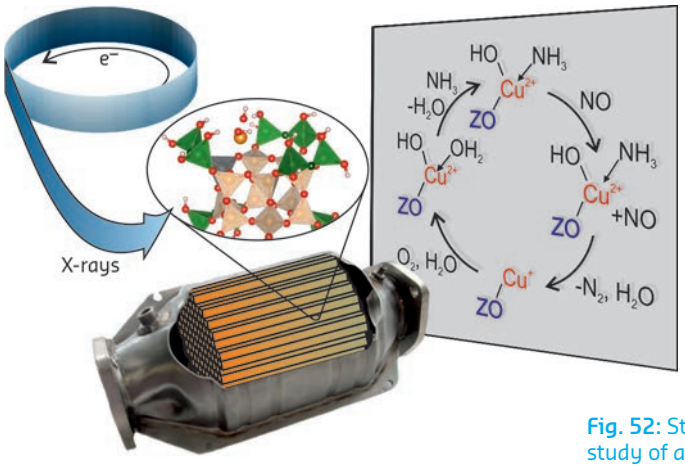

Fig. 52: Strategy of the study of automotive catalysts using X-rays and the suggested mechanism.

of Cu. As **Figure 53a** shows, this feature is clearly visible in the presence of NH_3, indicating reduction and change in coordination at the Cu-site. A decrease of the pre-edge feature under SCR-reaction conditions shows that the mechanism involves a redox step, with slow reoxidation of Cu-sites. XES gives complementary information on the electronic structure which is characteristic for coordinating ligands/adsorbates at the Cu-sites. This was substantiated by DFT calculations.

The small satellite feature Kß" is a valence to core transition from a molecular orbital, based on the interaction of metal orbitals with ligand 2s orbitals. As the energy of the ligand 2s orbital mainly depends on the element present, the position of the Kß" feature acts as a fingerprint for the coordinating atom and can distinguish between the ligand bonding mode of nitrogen or oxygen. The adsorption of NH_3 shifted this feature to higher energies, indicating direct coordination via N at the Cu-site (**Figure 53b**). In the presence of water and under reaction conditions, this feature is broadened to lower energies due to competitive adsorption of NH_3 and H_2O at the active sites. Weak adsorption of NO could only be observed under NO in He without any additional gases, suggesting weak interaction with the Cu-sites, or reaction from the gas phase with NH_3.

In contrast to these results, we observed adsorption of NO via a triple-coordinated oxygen atom for the iron-based SCR-catalyst Fe-ZSM-5 [3].

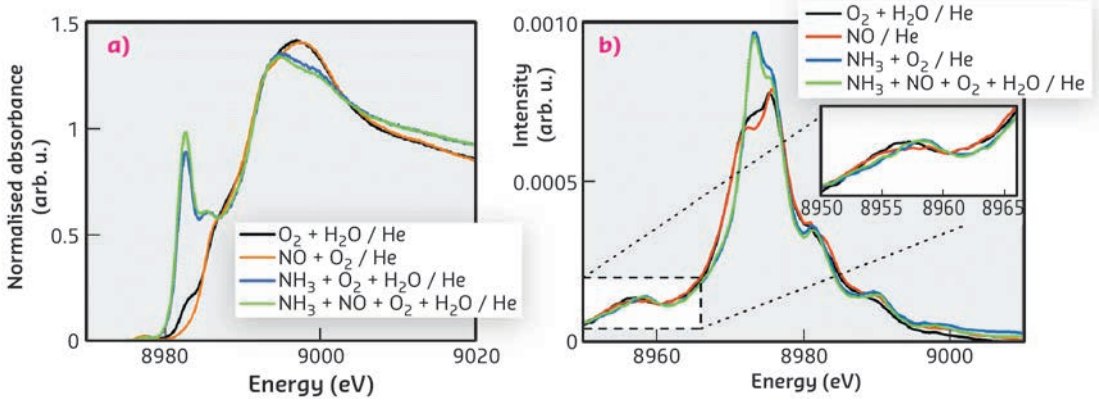

Fig. 53: (*a*) HERFD-XANES and (*b*) valence-to-core XES of Cu-SSZ-13 under selected gas compositions at 200°C.

PRINCIPAL PUBLICATION AND AUTHORS

Structural snapshots of the SCR reaction mechanism on Cu-SSZ-13, T. Günter (a), H.W.P. Carvalho (a), D.E. Doronkin (a), T. Sheppard (a), P. Glatzel (b), A.J. Atkins (a), J. Rudolph (c), C.R. Jacob (c), M. Casapu (a) and J.-D. Grunwaldt (a), *Chem. Commun.* **51**, 9227-9230 (2015). doi: 10.1039/c5cc01758k

(a) Karlsruhe Institute of Technology (Germany)
(b) ESRF
(c) TU Braunschweig (Germany)

REFERENCES

[1] E.S.J. Lox in *Handbook of Heterogeneous Catalysis*, Vol 5, p 2274, Wiley-VCH (2008).
[2] O. Deutschmann, J.-D. Grunwaldt, *Chem. Ing. Tech.* **85**, 595-617 (2013).
[3] A. Boubnov *et al.*, *J. Am. Chem. Soc.* **136**, 13006-13015 (2014).

RIXS REVEALS WHERE TiO_2 NANOPARTICLES STORE HOT ELECTRONS AFTER PLASMON-INDUCED ELECTRON TRANSFER FROM Au

The chase for efficient photocatalysts is pivotal for clean energy production and understanding charge generation and storage after light absorption is fundamental for materials optimisation. Adding plasmonic nanoparticles to oxides for catalysis is particularly promising. The modification of the TiO_2 electronic structure following charge transfer from Au nanoparticles was studied with resonant inelastic X-ray scattering (RIXS) to address the question of where TiO_2 stores the additional charge.

Titanium dioxide is one of the reference materials for photocatalysis. Its characteristics should make it an ideal photocatalyst for water splitting, but it absorbs sunlight poorly because of its wide energy gap [1]. Adding an efficient light absorber able to transfer energy to TiO_2 is a means to enhance its photo-catalytic activity, for example in dye-sensitised solar cells. Plasmonic nanoparticles are outstanding light absorbers due to the localised surface plasmon resonance (LSPR). Devices coupling TiO_2 and plasmonic materials show promising results, indicating that charge transfer to TiO_2 is indeed triggered by LSPR excitation [2]. However, efficient charge transfer is essential but not sufficient for optimal photocatalysts as the catalytic process is slow and requires long-lived charges on active sites. We investigated modifications of the TiO_2 electronic structure induced by plasmon-induced long-lived charges and addressed the question of where TiO_2 stores the transferred charge.

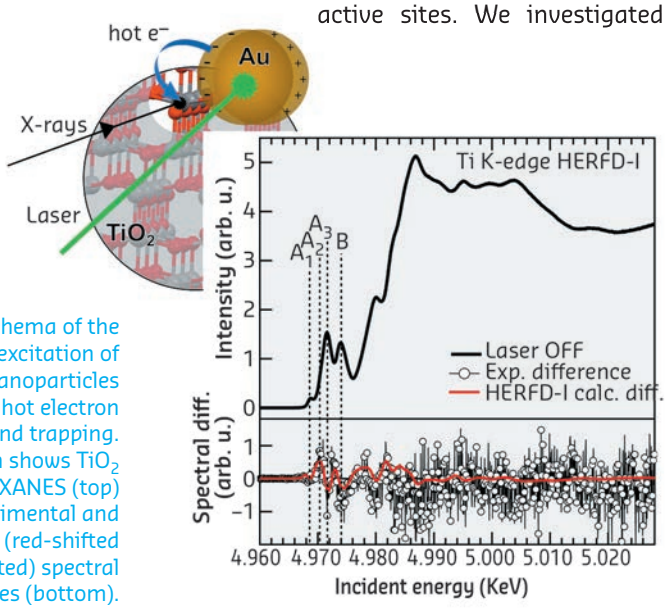

Fig. 54: Schema of the process: laser excitation of LSPR of Au nanoparticles induces hot electron injection and trapping. The graph shows TiO_2 HERFD-XANES (top) and experimental and calculated (red-shifted minus unshifted) spectral differences (bottom).

High-energy-resolution fluorescence-detected (HERFD) XANES at the Ti K-edge is obtained by collecting only a small energy bandwidth (~1 eV) at the maximum of the $K\beta_{1,3}$ line. We excited the LSPR of Au with a continuous laser in a TiO_2/Au powder and simultaneously probed Ti electronic structure by HERFD-XANES at the Ti K-edge at beamline **ID26**. By subtracting laser on and laser off measurements, we obtained a non-zero spectral difference (**Figure 54**), which is dominated by contributions from excited states with long lifetimes (>µs) as both X-ray probing and laser irradiation were continuous [3]. The detected signal is thus a signature of long-lived charges that affect the electronic structure of a small percentage of Ti atoms. Measurements on bare N-doped TiO_2 confirm that Au supplies charges. To obtain more information on how the injected charge is trapped, we recorded full Kβ profiles at incident energies across the pre-edge. The resulting distribution of spectral intensity along the incident and the transferred energy axis is called a RIXS plane with diagonal cuts corresponding to a HERFD-XANES scan (**Figure 55**). Four characteristic pre-edge peaks, A_1, A_2, A_3 and B, are found on different HERFD diagonals: A_3 and B on HERFD-I, and A_1 and A_2 on HERFD-II. This separation reflects different contributions of Ti atomic orbitals to the spectral features, with contributions from more delocalised orbitals (Ti *p*) lying on HERFD-I

and those from more localised orbitals (Ti *d*) on HERFD-II.

We also collected the spectral difference induced by LSPR excitation on HERFD-II and found small but marked differences in the pre-edge (inset Figure 55), as for HERFD-I. The HERFD-I spectral difference can be modelled by a –0.8 eV spectral shift, while the difference observed on HERFD-II arises from a modulation of the A_1 and A_2 intensities. This twofold behaviour provides important insight making it possible to understand that, after charge injection, some photo-induced charges remain trapped in Ti *p*-orbitals and the signal coming from these sites appears red-shifted compared to the rest of Ti atoms. The modulation of A_1 and A_2 intensities is inconsistent with a charge trapped in Ti d-orbitals, *i.e.* with reduction of Ti^{4+} into Ti^{3+}, but can be assigned to small structural rearrangements needed to accommodate the charge in Ti *p*-orbitals. Pre-edges are indeed very sensitive to *p-d* hybridisation.

In conclusion, following LSPR excitation, charges are injected from Au into TiO_2 and the longest lived ones are trapped in Ti *p*-orbitals. Traps are probably distorted TiO_6 octahedra near the Au/TiO_2 interface. The possibility to induce trapped charges with long lifetimes at the surface via LSPR excitation endorses the use of plasmonic nanoparticles to improve TiO_2 catalytic activity.

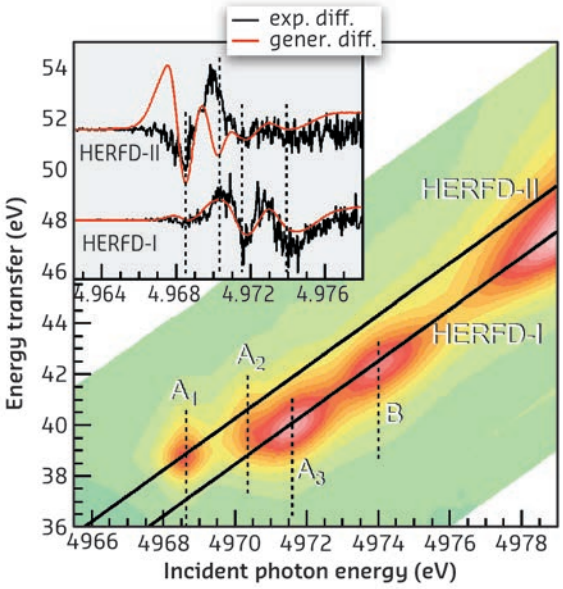

Fig. 55: 1s3p RIXS plane of Ti pre-edge of N-doped TiO_2. The characteristic four peaks A_{1-3} and B lie along two different cuts, HERFD-I (A_1 and A_2) and HERFD-II (A_3 and B). The inset shows the experimental difference (black) between laser on and laser off scans compared to the difference between the spectrum recorded without laser and the same spectrum red-shifted by 0.8 eV (red). A red-shift models the spectral difference observed on HERFD-I, while the effect on HERFD-II is not a shift but a modulation of A_1 and A_2 intensities.

PRINCIPAL PUBLICATION AND AUTHORS

Probing long-lived plasmonic-generated charges in TiO_2/Au by high-resolution X-ray absorption spectroscopy, L. Amidani (a,b), A. Naldoni (c), M. Malvestuto (d), M. Marelli (c), P. Glatzel (b), V. Dal Santo (c) and F. Boscherini (a), *Angewandte Chemie Int. Ed.* **54**, 5413-5416 (2015); doi: 10.1002/anie.201412030.

(a) Department of Physics and Astronomy, University of Bologna, Bologna (Italy)
(b) ESRF
(c) CNR-Istituto di Scienze e Tecnologie Molecolari, Milano (Italy)
(d) Elettra-Sincrotrone Trieste, Trieste (Italy)

REFERENCES

[1] A. Fujishima, K. Honda, *Nature* **238**, 37 (1972).
[2] S. Mubeen *et al.*, *Nat. Nanotechnol.* **8**, 247 (2013).
[3] M.H. Rittmann-Frank *et al.*, *Angew. Chem. Int. Ed.* **53**, 5858 (2014).

THE CORE OF THE MOON REVEALED BY SYNCHROTRON EXPERIMENTS

Sound velocity and density measurements carried out on iron at pressure and temperature conditions expected at the centre of the Moon have been used to reinterpret seismic records obtained at the time of the Apollo space programme and to propose a structural, compositional and velocity model of the Moon's metallic core.

Iron (Fe) is the main component of the core of telluric planets (those with an overall layered structure similar to that of Earth). Fe adopts a hexagonal close packed structure (hcp or ε phase) under pressure (P) and temperature (T) conditions of the Earth's inner core, whereas a face-centred cubic structure (fcc or γ phase) is expected under the more moderate P-T characteristic of the cores of smaller planetary bodies, such as the Moon, Mercury and Mars. Accordingly, the knowledge of the physical properties of the different iron phases at pertinent thermodynamic conditions is essential to model planetary cores. Above all, density and sound velocities are of primary importance for the proper interpretation of the seismological data and ultimately to produce accurate planetary models.

The Moon is the only other planetary body beside the Earth for which multiple direct seismic observations are available. The Apollo Lunar Surface Experiments Package has provided very precious information on the Moon's interior. However, seismic investigations of the

deepest lunar interior (> 900 km depth) remain challenging. In particular, the structure of the core is controversial, with only a single seismic study that directly detects the existence of a solid inner and a fluid outer core [1]. However, a complete and consistent set of measurements of compressional and shear wave sound velocities (respectively, V_P and V_S) and density (ρ) at high pressure and high temperature for γ-Fe was absent. Therefore, our understanding was based on untested assumptions on the physical properties of iron and iron alloys at relevant P-T conditions.

In this study, we have carried out density and sound velocity measurements on both body-centred cubic (bcc) and fcc iron between 0 GPa and 19 GPa and 300 K and 1150 K, using inelastic X-ray scattering (IXS) combined with X-ray diffraction (XRD) measurements at beamline **ID28**. IXS allows a clear identification of longitudinal aggregate excitations in polycrystalline samples, the direct derivation of V_P, and the estimation of V_S. This technique has been proven very suitable for measurements on metallic samples compressed in diamond anvil cell under simultaneous high P–T conditions [2]. Furthermore, combined XRD measurements yield an unambiguous phase determination and the direct derivation of the sample density.

The results obtained are displayed in **Figure 56**. Both bcc and fcc phases show a linear V_P–ρ relationship over the investigated P-T range. The sound velocity of the fcc phase is about 400 m/s lower than that of the bcc phase at the same density. Most importantly, the V_P value proposed for the Moon's inner core [1] after a reanalysis of Apollo lunar seismograms is significantly below those of γ-Fe. Such a large difference is hardly explainable even when considering anharmonic effects at higher temperatures, frequency-dependent viscoelastic relaxations, or effects of alloying with nickel or other plausible light elements.

Nonetheless, seismic data analysis and refinements of the lunar moment of inertia require the Moon to have a solid inner core and a liquid outer core. We then use our experimental results to construct a direct lunar core model, reinterpreting the seismic observations on the basis of our measurements. The resulting velocity and density model is shown in **Figure 57**. We put forward a solid inner core, made of pure-Fe, having a radius of ~245–250 km, surrounded by a sulfur-bearing (6-11 wt%) liquid outer core ~85–80 km thick. We further validated our model by comparison with Moon observables such as mass and moment of inertia, finding values that fall within 0.1% of known values.

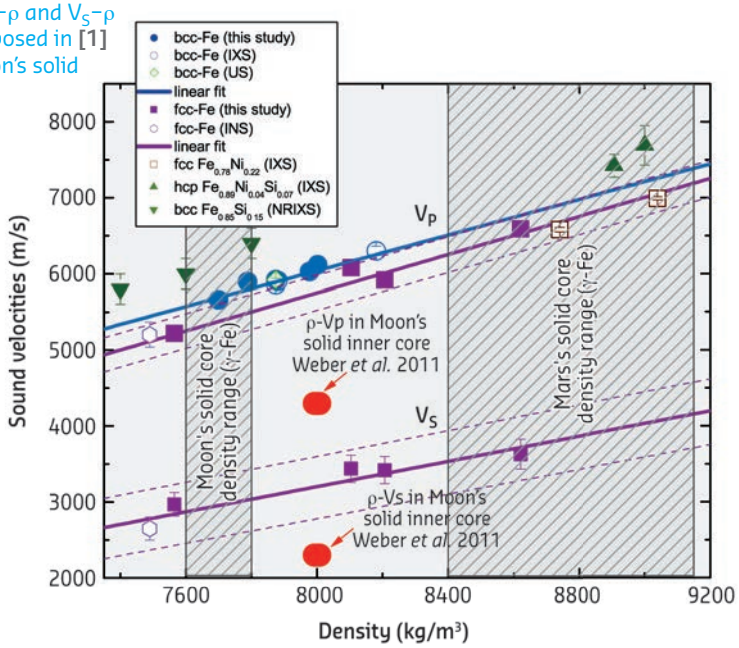

Fig. 56: Density evolution of the aggregate compressional and shear sound velocities of pure-Fe and selected Fe-alloys. The arrows point to V_P–ρ and V_S–ρ values proposed in [1] for the Moon's solid core.

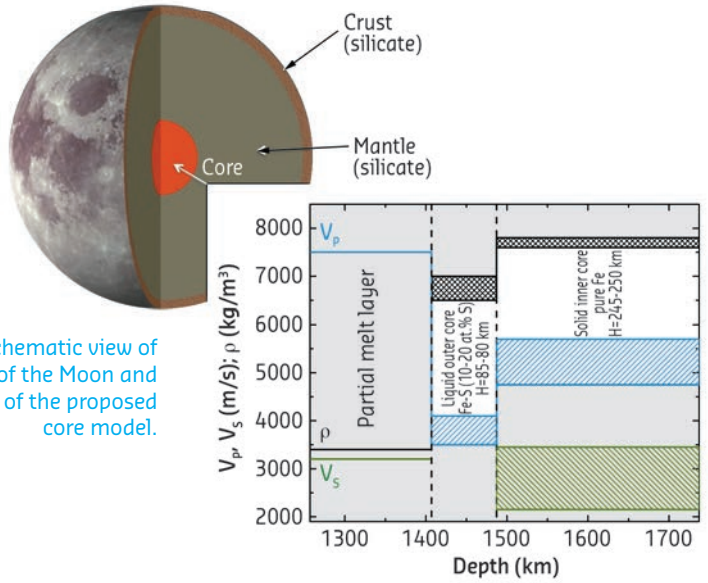

Fig. 57: Schematic view of the interior of the Moon and a close-up of the proposed core model.

PRINCIPAL PUBLICATION AND AUTHORS

Toward a mineral physics reference model for the Moon's core, D. Antonangeli (a), G. Morard (a), N.C. Schmerr (b), T. Komabayashi (c), M. Krisch (d), G. Fiquet (a) and Y. Fei (e), *Proc. Natl. Acad. Sci. USA* **112**, 3916 (2015).

(a) Institut de Minéralogie, de Physique des Matériaux, et de Cosmochimie (IMPMC), UMR CNRS 7590, Sorbonne Universités – UPMC, Muséum National d'Histoire Naturelle, IRD Unité 206, Paris (France)
(b) Department of Geology, University of Maryland, College Park MD (USA)
(c) Department of Earth and Planetary Sciences, Tokyo Institute of Technology (Japan)
(d) ESRF
(e) Geophysical Laboratory, Carnegie Institution of Washington, Washington DC (USA)

REFERENCES

[1] R.C. Weber *et al.*, *Science* **331**, 309 (2011).
[2] D. Antonangeli *et al.*, *Earth Planet. Sci. Lett.* **331**, 210 (2012).

HOW SLOW DOES GLASS FLOW?

A fundamental question for glass transition theories is whether an equilibrium glass ceases to flow at some finite temperature. However, direct measurement would require unfeasibly long observation times. An alternative means was provided by relating the ultraviscous flow to the elastic properties of an out-of-equilibrium glass as function of its age.

Glass-forming liquids can be cooled below the melting temperature to a metastable state, avoiding crystallisation. During this process, the molecular diffusion progressively slows down until the system falls out of equilibrium at the glass transition temperature, Tg.

Accordingly, viscosity increases dramatically and, based on its temperature dependence upon approaching Tg, glass-formers are classified into strong or fragile. Strong glass-formers follow an Arrhenius behaviour, *i.e.* the logarithm of viscosity linearly increases with the inverse of temperature, while fragile glass-formers display a super-Arrhenius behaviour: the faster they slow down, the more fragile they are.

A pivotal aspect for modern glass transition theories is whether this classification is still physically meaningful below Tg, *i.e.* whether or not viscosity diverges at a finite temperature. Answering this question is hampered by the fundamental unfeasibility of experimental investigations of relaxation processes in the ultraviscous glass state, which would require an impractically-long observation time.

We circumvent these limitations, by extending the correlation [1] between the slow diffusive motion (described by the viscosity) and the vibrational properties of the glass (sound velocity) as function of the age of the glass. The older the glass is, the lower the temperature at which viscosity can be determined.

Being in an out-of-equilibrium state, glasses spontaneously evolve (ageing) towards lower (more stable) potential energy minima (inherent structures) on a timescale dictated by the relaxation time.

Glass stability (or, equivalently, age) can be quantified by determining the fictive temperature Tf from the endothermic jump of specific heat upon fast heating the glass. The lower the Tf, the higher the stability of the glass is.

We used physical vapour deposition (PVD) to rapidly obtain glasses of indomethacin (Tg = 315 K) with Tf ranging from Tg down to 0.88 Tg, corresponding to "ages" reached by standard cooling and waiting for millennia (like if a winemaker could produce a mature wine without having to wait).

Growing samples thicker than a few tens of micrometres by PVD, however, is extremely challenging. By taking advantage of the tight focusing capabilities of beamline **ID28**, together with the availability of a 9 crystal analysers bench to simultaneously record the inelastic spectra at different fixed values of momentum transfer, we managed to repeat the measurement on PVD films as thin as 50 µm.

By combining the IXS [2] data with Brillouin light scattering in frequency (BLS) [3] and time domain (BPA), we determined the energy dispersion of the longitudinal vibrational modes in the most stable sample (Figure 58). In the low-frequency region, the linear energy dispersion indicates the existence of propagating vibrational excitations corresponding to a single acoustic-like phonon branch. Remarkably, their propagating nature lingers up to the THz frequency regime, where, because of disorder, the plane-wave description inherited from crystals is no longer valid.

We measured the sound velocity for all the available glasses in order to determine the behaviour of the apparent fragility (Figure 59a), *i.e.* the generalisation of viscosity temperature

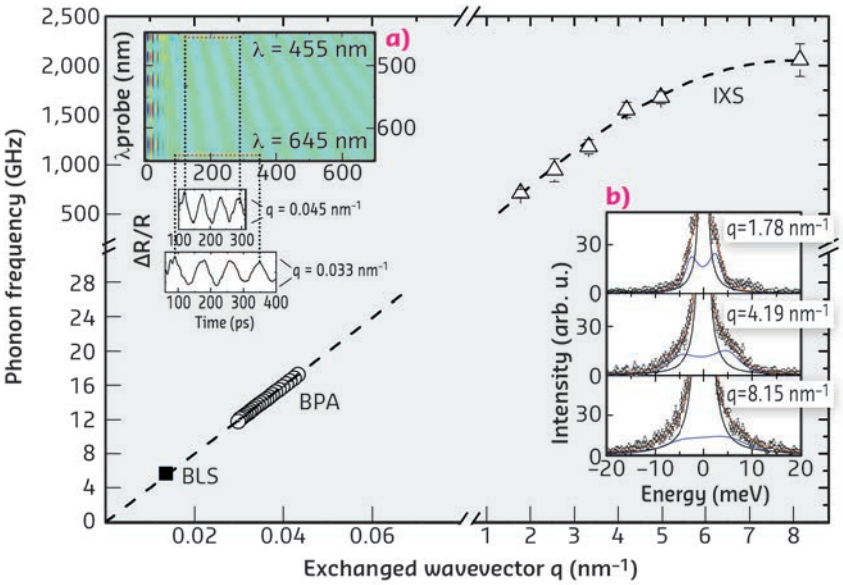

Fig. 58: Longitudinal acoustic phonon dispersion in ultrastable PVD glass, investigated by BPA (○ and panel a), IXS (Δ and panel b) and Brillouin measurement (□).

steepness index to glasses at Tf << Tg. From the apparent fragility we could finally quantify viscosity along the equilibrium line (Figure 59b). The super-Arrhenius behaviour documented for indomethacin above Tg is reported as a dashed line representing a Vogel-Fulcher-Tamman function. For Tf < Tg a remarkable deviation is observed: the apparent fragility initially increases (though less than expected by the VFT), while decreases below Tf = 295 K indicating a transition from fragile-to-strong system. With this approach, we found an Arrhenius behaviour far below Tg up to exapoise values.

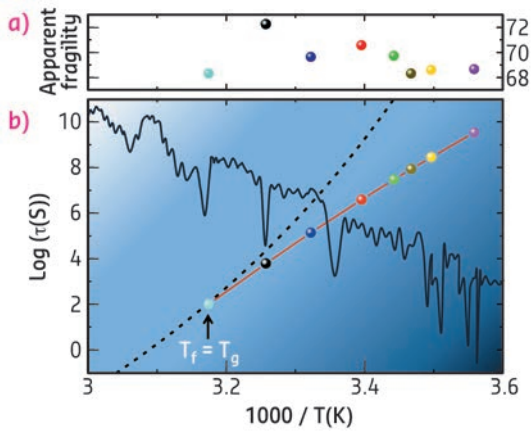

Fig. 59: (a) Apparent fragility determined from the sound velocity jump in glasses with different Tf. (b) Arrhenius plot for T < Tg, obtained by integrating data from (a). Sketched in the background (black solid line) is the potential energy minima explored for a glass of fictive temperature T.

In conclusion, our results suggest that the conventional wisdom picture of a glass ceasing to flow at a finite temperature could be wrong. A reconsideration of old paradigms based on the dynamical divergence may be needed for a definitive understanding of the glass transition to be reached.

PRINCIPAL PUBLICATION AND AUTHORS

Probing equilibrium glass flow up to exapoise viscosities, E.A.A. Pogna (a), C. Rodriguez-Tinoco (b), G. Cerullo (c), C. Ferrante (a), J. Rodriguez-Viejo (b) and T. Scopigno (a), *Proc. Natl. Acad. Sci.* **112,** 2331–2336 (2015); doi: 10.1073/pnas.1423435112.
(a) Dipartimento di Fisica, Universitá di Roma "La Sapienza" (Italy)
(b) Physics Department, Universitat Autònoma de Barcelona (Spain)
(c) Dipartimento di Fisica, Politecnico di Milano (Italy)

REFERENCES

[1] T. Scopigno *et al.*, *Science* **302**, 849-852 (2003).
[2] E.A.A. Pogna *et al.*, *Sci. Rep.* **3**, 2518 (2013).
[3] S. De Panfilis *et al.*, *Phys. Chem. Chem. Phys.* **16**, 14206–14211 (2014).

EXPLORING ACTINIDE MAGNETISM WITH XMCD

Experiments performed on $AmFe_2$ have demonstrated that the magnetic dipole term of actinide materials can be determined by X-ray magnetic circular dichroism (XMCD) together with the spin and orbital magnetic moments. Accessing this information with a single experiment will help researchers solve the long-standing problem of modelling the complex electronic structure of the actinides.

Actinides are the heaviest elements in the periodic table that can be studied on a macroscopic scale. The complexity of their electronic structure often produces exotic physical properties such as the unconventional superconductivity of $PuCoGa_5$ and the "hidden order" phases found in NpO_2 and URu_2Si_2.

The magnetic moment carried by an atom is given by the sum of two components, one associated with the spin of the atom, the other with its angular momentum, $\mu = \mu_S + \mu_L$. The determination of these quantities in actinide compounds has been of interest since several decades ago, but it is still a formidable experimental and theoretical challenge. XMCD is a well-established tool to determine these quantities by using two "sum rules" that correlate the measured dichroic signal at two distinct spectral edges with μ_S and μ_L. Contrary to neutron techniques, XMCD does not require single-crystal samples, is element- and shell-specific, and microgram samples are sufficient. This is important for actinides, as single crystals are seldom available, and large quantities are difficult to manipulate. Unfortunately, the situation is complicated by the spin-dependent asphericity of the electronic cloud. While μ_L can be directly measured by XMCD, the accessible "effective" spin value is not equal to μ_S, but is the sum of μ_S and a quantity proportional to the expectation value of the magnetic dipole operator $\langle T_z \rangle$. The latter is an elusive quantity that is experimentally accessible only in a limited number of cases, and not with any single experiment.

Our experiment was performed at beamline **ID12** by recording across the $M_{4,5}$ absorption edges of Am (Figure 60). It took advantage of the fact that trivalent americium ions have an f^6 configuration with L = 3 = –S and J = L + S = 0. Thus, Am^{3+} ions have no intrinsic magnetic moment, but their electrons can be strongly spin-polarised. A purely induced magnetic moment can be created in Am^{3+} by applying a magnetic field; this induced magnetic moment μ has the peculiar property

that μ_S is always opposite and twice as large as μ_L. To maximise the effect, we took advantage of the strong exchange coupling in $AmFe_2$; the ferromagnetically ordered iron sublattice generates a much larger field at the Am^{3+} ions than can be applied externally. Measuring μ_L by the first XMCD sum rule led by the reasoning above to a value of μ_S, and, by comparing its value to the effective spin moment obtained by the second sum rule, the contribution of $\langle T_z \rangle$ was quantified. Furthermore, the obtained value of $\langle T_z \rangle$ is in agreement with calculations performed by a single-ion model, which is consistent with earlier results on lighter actinides (independent of their crystal structure or the details of their electronic configuration). Therefore, by applying this correction it is possible to obtain a reliable value of μ_S for any actinide-based compound from a single XMCD experiment.

By comparing the value of $3\langle T_z \rangle / \langle S_z \rangle$ for $n_f = 6$ to that of other 5f compounds (Figure 61) with $n_f \leq 5$, we infer that this quantity is well described within a single-ion, intermediate coupling theory for all light actinides, in a way that is independent of their electronic (de)localisation. This finding resolves a longstanding issue of what to use for $\langle T_z \rangle$ in interpreting XMCD experiments at the actinide $M_{4;5}$ (or $N_{4;5}$) edges.

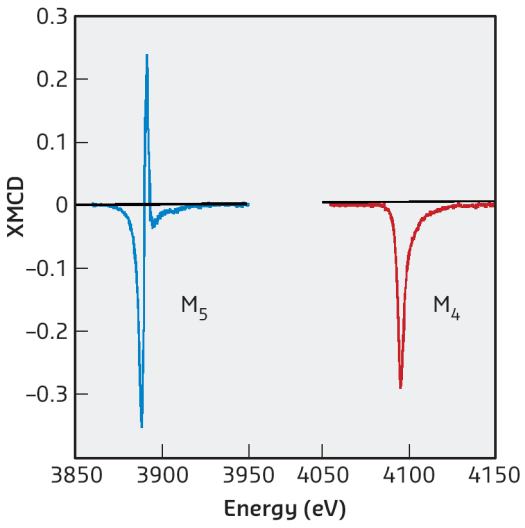

Fig. 60: XMCD spectroscopic shapes for the Am M_5 and M_4 edges in $AmFe_2$. The sum of the areas under the two curves is proportional to the orbital component of the magnetic moment. A weighted difference of the two areas provides the sum of the spin component with the expectation value of an operator related to the spin-dependent asphericity of the electronic cloud.

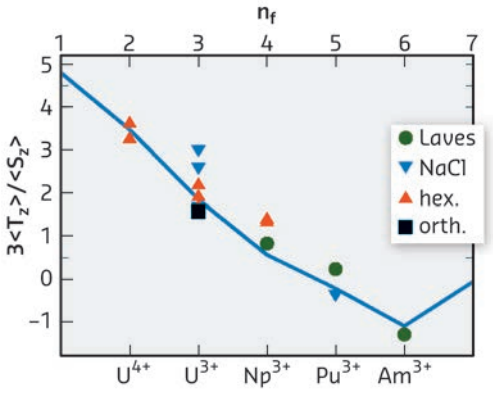

Fig. 61: Ratio between the expectation values of the magnetic dipole operator $3\langle T_z \rangle$ and the spin operator $\langle S_z \rangle$ as a function of the 5f shell occupation number n_f. Experimental data for different compounds are represented by symbols identifying their crystal structure. Calculated values are shown by the solid line.

PRINCIPAL PUBLICATION AND AUTHORS

Magnetic polarization of the americium J = 0 ground state in $AmFe_2$, N. Magnani (a), R. Caciuffo (a), F. Wilhelm (b), E. Colineau (a), R. Eloirdi (a), J.-C. Griveau (a), J. Rusz (c), P. M. Oppeneer (c), A. Rogalev (b) and G.H. Lander (a), *Physical Review Letters* **114**, 097203 (2015); doi: 10.1103/PhysRevLett.114.097203.

(a) European Commission, Joint Research Centre (JRC), Institute for Transuranium Elements (ITU), Karlsruhe (Germany)
(b) ESRF
(c) Department of Physics and Astronomy, Uppsala University (Sweden)

DETERMINATION OF LANTHANIDE-IRON CLUSTER INTERACTION IN BUTTERFLY MOLECULES THROUGH COMBINED XMCD AND STANDARD MAGNETOMETRY

Lanthanide organic compounds containing 3*d* transition elements are promising candidates for the development of single-molecule magnets with a high energy barrier. The goal of this work was to combine the magnetic moment and the relatively strong exchange interactions of 3*d* transition metals with the anisotropy naturally provided by lanthanide ions.

Butterfly molecules $\{Fe_3LnO_2\}$ consist of a cluster of three Fe^{+3} ions forming a triangle ("Fe3") and a single lanthanide ion Ln^{+3}, all connected by oxygen atoms and surrounded by an organic envelope. The Fe3-Ln cluster shows a butterfly shape (Figure 62). Magnetically, the Fe3 subcluster behaves as a robust entity with total spin 5/2 antiferromagnetically coupled to the Ln magnetic moment [1]. The precise determination of the interaction between the Fe3 cluster and Ln requires their magnetic moments to be measured. Standard methods such as vibrating sample magnetometry (VSM) produce the total moment of the molecule. This allows m_{Fe3} to be obtained from, *e.g.*, the $\{Fe_3YO_2\}$ compound, where Y plays the role of a nonmagnetic pseudo rare earth, but in the case of magnetic rare earths, the Fe3 and Ln magnetic moments cannot be discriminated one from the other. In contrast, for an applied magnetic field, the combination of XMCD and

VMS makes this separation possible. The results and analysis for the Kramers ions Gd^{+3} and Dy^{+3} were reported previously [1], while those of the non-Kramers ions Tb^{+3} and Ho^{+3} are highlighted here.

A set of XMCD spectra recorded at the $L_{2,3}$ edges as a function of the applied magnetic field up to $\mu_0 H$ = 17 T was collected at beamline **ID12** at 2.7 K (Tb) and 2.2 K (Ho). Constant temperature $M(H)$ curves plotted in intensity (arbitrary) units were constructed from the spectra (**Figure 63a**). On the same samples and at the same temperatures, $M(H)$ curves in absolute units were obtained by VMS, as well as for the $\{Fe_3YO_2\}$ complex to estimate the contribution of the Fe3 cluster. At saturation, collinearity of the Ln and Fe3 magnetic moments is assured. This allows the determination of the Ln magnetic moment at high fields, which can be used to scale the XMCD magnetisation curve to absolute units. In this way, the $M_{Ln}(H)$ curve specific to the lanthanide can be extracted (**Figure 63b**).

A theoretical model for the Fe3-Ln magnetic cluster is proposed with a hamiltonian including crystal field and Zeeman terms, as well as an exchange interaction term between the Fe3 cluster and the lanthanide ion. The Ln moment is modelled through a fictitious ½ spin. While this is straightforward for the groundstate doublet of the Kramers ions case [1], it is only possible for the non-Kramers ions like Tb and Ho under particular conditions. These are well fulfilled at very low temperature, as in the XMCD and VSM measurements, for the two lowest energy singlet states of Tb^{+3} and roughly fulfilled for Ho^{+3}, according to *ab initio* calculations. A fit of the calculated $M_{Ln}(H)$ curves to the scaled XMCD experimental curve yields to interaction constants along the spin direction $J_{Tb\text{-}Fe3}/k_B$ = –1.5 K and $J_{Ho\text{-}Fe3}/k_B$ = –2.8 K. The evolution of the cluster groundstate with increasing applied field shows a reorientation of the Fe3 cluster magnetic moment from antiparallel to parallel to that of the lanthanide.

The determination of the exchange interaction between transition metal and lanthanide ions in single molecule magnets can be tackled by a combination of XMCD and standard magnetometries to extract magnetic moments, along with a theoretical framework which includes all the relevant terms in the magnetic cluster. The method has been proven in the series of $\{Fe_3LnO_2\}$ complexes with Ln = Gd, Dy, Tb and Ho, at very low temperatures, using a fictitious ½ spin to simulate the lowest energy states in both Kramers and non-Kramers ions.

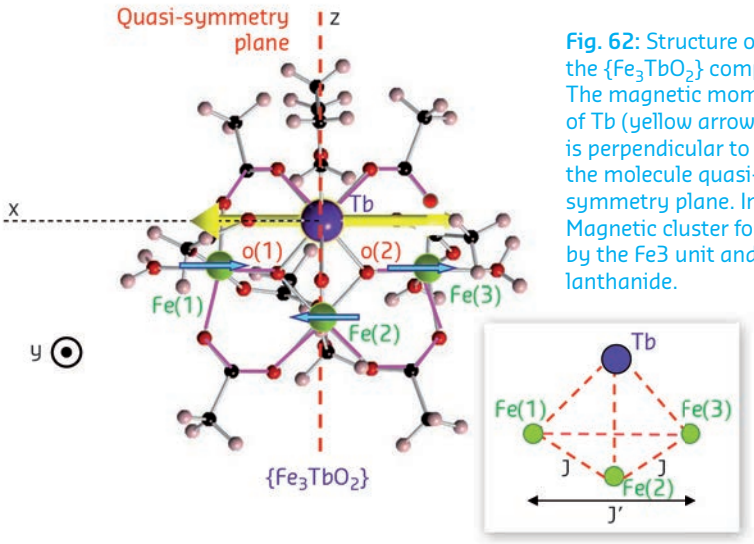

Fig. 62: Structure of the $\{Fe_3TbO_2\}$ complex. The magnetic moment of Tb (yellow arrow) is perpendicular to the molecule quasi-symmetry plane. Inset: Magnetic cluster formed by the Fe3 unit and the lanthanide.

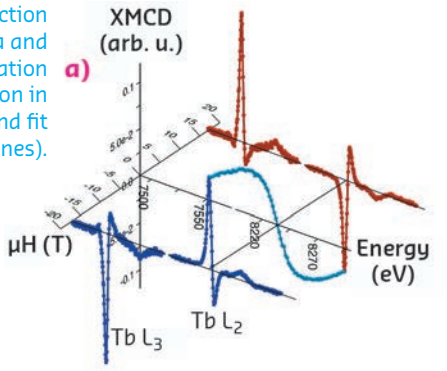

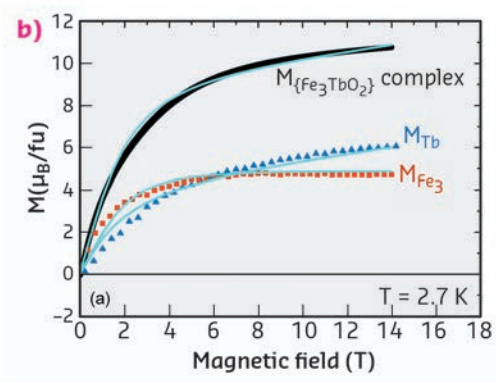

Fig. 63: The process to determine interaction constants in $\{Fe_3TbO_2\}$: (a) XMCD spectra and derived $M(H)$ curve in a.u.; (b) Total magnetisation from VSM (black), lanthanide contribution in absolute units from XMCD (blue triangles) and fit within an interaction model (continuous lines).

PRINCIPAL PUBLICATION AND AUTHORS

Intracluster interactions in butterfly $\{Fe_3LnO_2\}$ molecules with the non-Kramers ions Tb(III) and Ho(III), L. Badía-Romano (a,b), J. Rubín (a,c), F. Bartolomé (a,b), J. Bartolomé (a,b), J. Luzón (a,d), D. Produis (e),C. Turta (e), V. Mereacre (e), F. Wilhelm (f) and A. Rogalev (f). *Phys. Rev. B* **92**, 064411 (2015);

doi: 10.1103/PhysRevB.92.064411.

(a) Instituto de Ciencia de Materiales de Aragón, CSIC-Univ. Zaragoza (Spain)
(b) Dept. Física de la Materia Condensada, Univ. Zaragoza (Spain)
(c) Dept. Ciencia de Materiales e Ingeniería Metalúrgica, Univ. Zaragoza (Spain)
(d) Centro Universitario de la Defensa, Academia General Militar, Zaragoza (Spain)
(e) Institute of Chemistry, Academy od Sciences of Moldova, Chisinau (Republic of Moldova)
(f) ESRF

REFERENCES

[1] L. Badía-Romano *et al., Phys. Rev. B* **87**, 184403 (2013).

A NOVEL ROUTE TO QUANTUM SPIN LIQUIDS

Bond-directional interactions provide a novel alternative to conventional Heisenberg interactions for designing and implementing quantum magnets. In particular, they serve as building blocks for the celebrated Kitaev model, which has a quantum spin liquid as its exact ground state. Here, a direct observation of this novel type of magnetic interaction has been made for the first time in a real material by using diffuse magnetic X-ray scattering.

Quantum spin liquid is an elusive state of matter in which spins fluctuate in a liquid form without ever solidifying even at a temperature of absolute zero [1]. Observed only in the past decade [2], quantum spin liquids are currently the focus of intense research, with historical links to high temperature superconductivity and potential applications to quantum computation. The Kitaev model, based on the simplest form of bond-directional interactions, occupies a special position as a rare example of exactly solvable models with well-defined signatures of a quantum spin liquid [3,4]. This work takes a big experimental leap towards the realisation of a quantum spin liquid by unambiguous identification of such interactions leading to strong magnetic frustration in the 5d transition metal oxide Na_2IrO_3.

Na_2IrO_3 has a monoclinic stacking of two-dimensional honeycomb lattices that breaks the ideal three-fold rotational symmetry of the honeycomb lattice on which the Kitaev model is constructed. Structurally, it further deviates from the ideal model as the stacking compresses the IrO_6 octahedra, which in turn distorts the Ir-O-Ir bonds – the main magnetic exchange pathway. Magnetically, Na_2IrO_3 orders at a finite temperature into the so-called zigzag pattern, rather than being the spin liquid predicted by the model. As the same spin pattern is found in other conventional magnets, the role, or even the presence of the bond-directional interactions has remained unknown.

Using the spectrometer designed for resonant inelastic X-ray scattering at ESRF beamline **ID20** and beamlines at the Advanced Photon Source, we set out to look for the defining properties of the bond-directional interactions. Specifically, the magnetic interactions should differ on different bonds, particularly in the spin component that each bond couples. Our strategy was to measure the instantaneous correlation of spins, which amounts to taking a "snapshot" of spins in the Fourier-transformed (momentum) space. In this measurement a particular spin component was filtered out by orienting the sample with respect to the X-ray polarisation in such a way that, by rotating the azimuth angle, the spin channel being probed is continuously tuned.

Figure 64 shows a systematic evolution of the momentum-space spin-correlation map as one tunes the spin channel by rotating the azimuth angle. The location of the diffuse peaks provides information about the direction along which the spin correlations propagate, and their intensity is maximal when the azimuth angle is turned to the "right" spin component. This map provides evidence of the entanglement between the spin and the real space, a direct consequence of the bond-directional interactions.

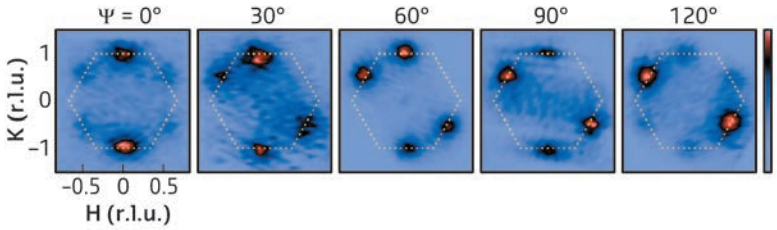

Fig. 64: Diffuse magnetic X-ray scattering intensities above the ordering temperature, T_N. Intensity plots in the HK-plane measured at T = 17 K (>T_N = 12 K) for selected azimuth angles (Ψ) summing π-σ' and π-π' channels. The diffuse peaks are located at Q = ±(0,1), ±(0.5,0.5), and ±(0.5,-0.5) corresponding to three short-range ordered zigzag states. Ψ dependence of the intensities arises due to the distinct magnetic anisotropies of each state.

A theoretical calculation using the exact diagonalisation of a 24-site cluster indicates that the observed pattern is attributed to the bond-directional interactions overwhelming the conventional Heisenberg interactions, and thus the system should be on the verge of making a transition to the spin-liquid state. However, the transition can be hindered by other types of magnetic interactions not fully identified in this study. The full understanding of this material awaits further improvement of the spectrometers in terms of energy resolution, which would allow the full dynamics of the interacting spins to be resolved. In the meantime, these findings highlight the benefits of using the resonant inelastic X-ray scattering spectrometer at ID20 to probe the instantaneous spin correlations through diffuse magnetic X-ray scattering.

PRINCIPAL PUBLICATION AND AUTHORS

Direct evidence for dominant bond-directional interactions in a honeycomb lattice iridate Na_2IrO_3, S.H. Chun (a), J.-W. Kim (b), J. Kim (b), H. Zheng (a), C.C. Stoumpos (a), C.D. Malliakas (a), J.F. Mitchell (a), K. Mehlawat (c), Y. Singh (c), Y. Choi (b), T. Gog (b), A. Al-Zein (d), M. Moretti Sala (d), M. Krisch (d), J. Chaloupka (e), G. Jackeli (f,g), G. Khaliullin (f) and B.J. Kim (f), *Nature Physics* **11**, 462 (2015); doi:10.1038/nphys3322.

(a) Materials Science Division, Argonne National Laboratory (USA)
(b) Advanced Photon Source, Argonne National Laboratory (USA)
(c) Indian Institute of Science Education and Research (IISER), Mohali (India)
(d) ESRF
(e) Central European Institute of Technology, Masaryk University (Czech Republic)
(f) Max Planck Institute for Solid State Research (Germany)
(g) Institute for Functional Matter and Quantum Technologies, University of Stuttgart (Germany)

REFERENCES

[1] L. Balents, *Nature* **464**, 199 (2010).
[2] T.-H. Han *et al.*, *Nature* **492**, 7429 (2012).
[3] A. Kitaev, *Ann. Phys.* (Amsterdam) **321**, 2 (2006).
[4] G. Jackeli and G. Khaliullin, *Phys. Rev. Lett.* **102**, 017205 (2009).

CHEMICAL REACTION OF CINNAMIC ACID FOLLOWED BY TIME-RESOLVED X-RAY RAMAN SPECTROSCOPY

Bonding between atoms to form molecules originates from the electronic structure of the system, which changes in chemical reactions. In this spectroscopic study, the changes in electronic structure were monitored in real time on a timescale of minutes for a crystal undergoing a dimerisation reaction. The study yields information on the reaction progression and demonstrates the ability of a novel imaging technique to map the chemical composition inside the macroscopic solid-state sample.

In crystalline materials, ultraviolet light can be used to induce topochemical reactions, in which pathways and products are governed by the crystal structure of the material. This offers an opportunity to synthesis processes with an amazing specificity and removes the need for solvents allowing more environment-friendly processes [1]. However, the dependence of the reaction pathways on photon energy is poorly understood, especially in the energy range of X-rays, where core-excited molecular species are created. Thus, novel X-ray techniques for probing these reactions are desirable as they can yield new results by allowing access to novel reactions in a variety of thermodynamic conditions.

A canonical example of a topochemical reaction is the dimerisation of crystalline cinnamic acid. In this reaction, depicted in Figure 65a, two cinnamic acid molecules are bound together to form a dimer, a truxillic acid molecule. Previously it has been shown that the kinetics of this transformation, when induced by UV illumination, can be described by a Johnson-Mehl-Avrami-Kolmogorov (JMAK) model. The JMAK model describes reactions proceeding via formation of nuclei and their subsequent growth. In the current case the growth of the nuclei can be understood by noting that the dimerisation can occur preferentially close to the existing dimers.

In our time-resolved *in situ* study, performed at beamline **ID20**, we observed this reaction to be induced by X-rays for the first time. The carbon *K*-edge spectra (Figure 65b) measured using non-resonant X-ray Raman spectroscopy (XRS) show on a short timescale the effect of dimerisation, which we explain in detail with the help of spectral simulations. The dimerisation competes with another reaction that occurs at a slower rate and seems to produce carbon monoxide. Spectral decomposition using nonnegative matrix factorisation allowed us to obtain the component spectra and time-dependent weights for cinnamic acid, truxillic acid, and final products (Figure 66a and b). To quantify the reaction kinetics, we fit a JMAK-reaction model to the component weights, the results of which suggest that the X-ray induced dimerisation proceeds more homogeneously than the UV-induced reaction.

We also utilised the ability of **ID20** for direct tomography with spectral contrast [2]. In this imaging technique chemical bonding inside the sample is mapped using the XRS spectrum. The incident X-ray beam illuminates a section of a sample, from which the scattered X-rays are recorded to form a hyperspectral image that contains an individual spectrum for each voxel. We utilised this method for following the chemical composition within the crystal. Figure 66c shows the images of a section of the crystal as a function of time, with colours representing the weights of each component spectrum (Figure 66a) fitted to the hyperspectral images. The reaction rate is seen to be higher in the front of the crystal, where the dose rate is higher, than at the back. Our work paves the way to other novel time-resolved *in situ* studies of X-ray-induced chemical reactions using XRS for spectral imaging.

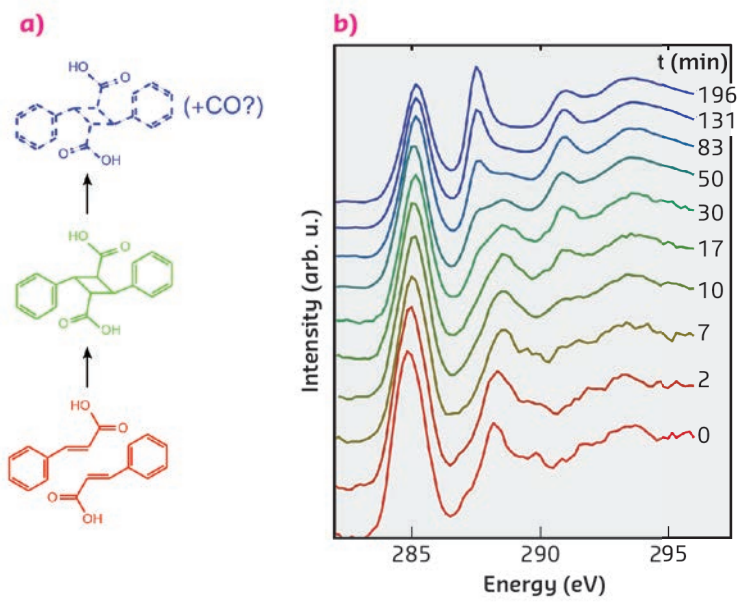

Fig. 65: (a) The reaction scheme of the dimerisation of α-trans-cinnamic acid to α-truxillic acid and a subsequent disintegration reaction. (b) The time-resolved carbon K-edge spectra show the effects of dimerisation on a short time-scale (0-17 minutes) and disintegration on a longer time-scale. The spectra are offset for clarity.

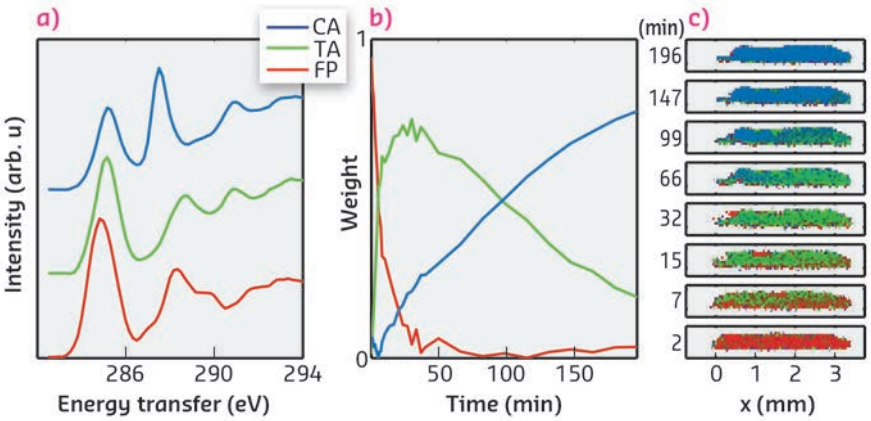

Fig. 66: (a) The component spectra of α-trans-cinnamic acid, α-truxillic acid, and final products (CA, TA, and FP, respectively). (b) The weight of each component as a function of irradiation time. (c) The progression of the chemical composition inside the sample crystal mapped by hyperspectral imaging. Red, green, and blue channel in each pixel corresponds to the weight of CA, TA, and FP components, respectively.

PRINCIPAL PUBLICATION AND AUTHORS

X-ray induced dimerization of cinnamic acid: time-resolved inelastic X-ray scattering study, J. Inkinen (a), J. Niskanen (a), T. Talka (a), C.J. Sahle (b), H. Müller (b), L. Khriachtchev (c), J. Hashemi (a), A. Akbari (a), M. Hakala (a) and S. Huotari (a), *Scientific Reports* **5**, 15851 (2015); doi: 10.1038/srep15851.
(a) Department of Physics, University of Helsinki (Finland)
(b) ESRF
(c) Department of Chemistry, University of Helsinki (Finland)

REFERENCES

[1] K. Biradha and R. Santra, *Chem. Soc. Rev.* **42**, 950–967 (2013).
[2] S. Huotari *et al.*, *Nat. Mater.* **10**, 489–493 (2011).

FORMATION OF NEPTUNIUM DIOXIDE NANOCRYSTALS UNDER THE AQUEOUS CONDITIONS RELEVANT TO DEEP GEOLOGICAL DISPOSAL

The present study investigates the potential formation of colloidal species of tetravalent neptunium (Np(IV)) under the aqueous conditions relevant to the geological disposal of radioactive wastes. Np(IV) possesses an intrinsic nature to form nanosized crystalline NpO_2 particles, which could potentially facilitate the transport of Np nuclides from nuclear waste repositories.

The management of radioactive wastes is still a significant challenge facing the nuclear power industry. One plausible option for the management of high-level radioactive wastes is deep geological disposal, in which the wastes are buried deep underground. Due to its long-lived radiotoxicity, a major isotope of neptunium, ^{237}Np ($T_{1/2}$ = 2.14 × 10^6 y), is considered to be one of the problematic radionuclides in high-level radioactive wastes in terms of the long-term safety assessment of the waste repositories. For this reason, the chemical behaviour of Np has been investigated extensively under geochemically relevant conditions [1]. One possible pathway that would potentially release

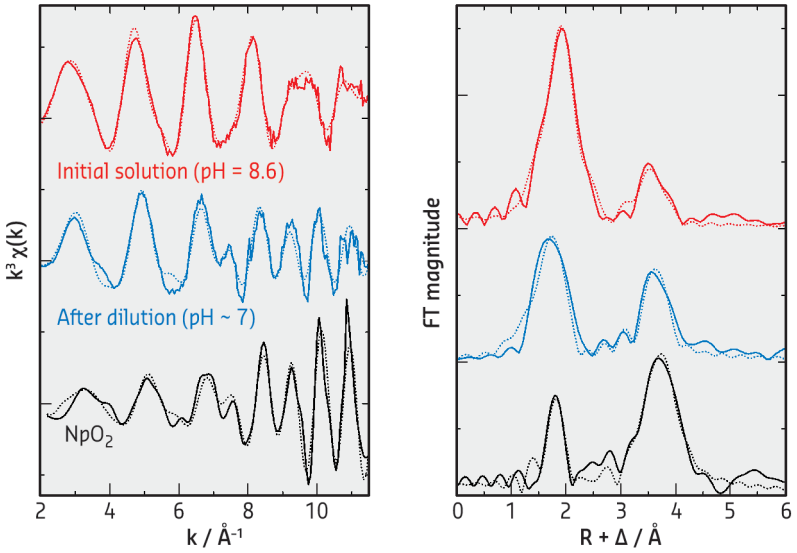

Fig. 67: (left) k^3-weighted Np L_{III}-edge EXAFS spectra for Np(IV) in 1 M $NaHCO_3$ at pH = 8.6 (red), after the dilution of the initial Np(IV) solution with deionised water (blue) and reference NpO_2 powder (black), and (right) their corresponding Fourier transforms (FTs). Solid lines, experimental data; dotted lines, theoretical fit. The magnitude of the data for NpO_2 is reduced by one forth relative to the *y* axes for clear comparison of the spectra.

radionuclides from the waste repositories into the surrounding environment is the formation of mobile colloids. As a matter of fact, such mobile colloids have been reported for plutonium (Pu), the formation of which eventually facilitates the migration of Pu for several kilometres in groundwater [2].

To characterise the Np(IV) species formed in different aqueous conditions, we performed X-ray absorption spectroscopy (XAS) at **BM20 (**ROBL CRG). Shown in Figure 67 are the Np L_{III}-edge extended X-ray absorption fine structure (EXAFS) spectra for the Np(IV) species in aqueous carbonate solutions at different pH (left, k^3-weighted) and their corresponding Fourier transforms (FTs, right). The initial Np(IV) sample at pH = 8.6 (red data in Figure 67) showed a longer frequency EXAFS oscillation which produced two significant peaks in the FT. This data can be interpreted as a soluble pentacarbonate Np(IV) complex, $[Np^{IV}(CO_3)_5]^{6-}$. When the initial Np(IV) sample was diluted with deionised water, which also involved a slight decrease in pH from 8.6 to ~7, the resultant solution exhibited a complicated EXAFS pattern with a shorter frequency in the higher *k*-range (blue data in Figure 67). The observed EXAFS oscillation feature is comparable with that for NpO_2 (black data in Figure 67), indicating that the Np(IV) species in the diluted solution is composed of NpO_2-like structure. Additional UV-visible and light scattering measurements on this diluted Np(IV) solution revealed the formation of colloids. Hence, the Np(IV) species formed in the diluted solution is actually the colloidal particles with a NpO_2-like framework.

To further characterise the colloidal Np(IV) species, high-resolution transmission electron microscopy (HR-TEM) was performed on the precipitate obtained from the diluted Np(IV) solution. Figure 68 shows typical TEM micrographs acquired from the precipitate, clearly demonstrating the agglomeration of particles with 2-5 nm in diameter (a) as well as some clear lattice images (b) which are consistent with the fluorite-type NpO_2 structure ($Fm\bar{3}m$) (c). These results, together with the EXAFS results, suggest that the dilution of the initial Np(IV) solution induces the dissociation of soluble Np(IV) species ($[Np^{IV}(CO_3)_5]^{6-}$), which eventually results in the formation of nano-sized NpO_2 crystalline particles. This pathway of nanocrystalline NpO_2 formation could be a possible scenario for the potential transport of Np nuclides from waste repositories (near field with alkaline conditions) to the surrounding environment (far field with neutral conditions) involving diffusion processes (dilution). These findings could be of particular importance in terms of the long-term prediction of radionuclide transport in geological environments, as nanosized NpO_2 particles are expected to be stable for a long period of time and would potentially facilitate long-distance transport of Np nuclides from the repositories.

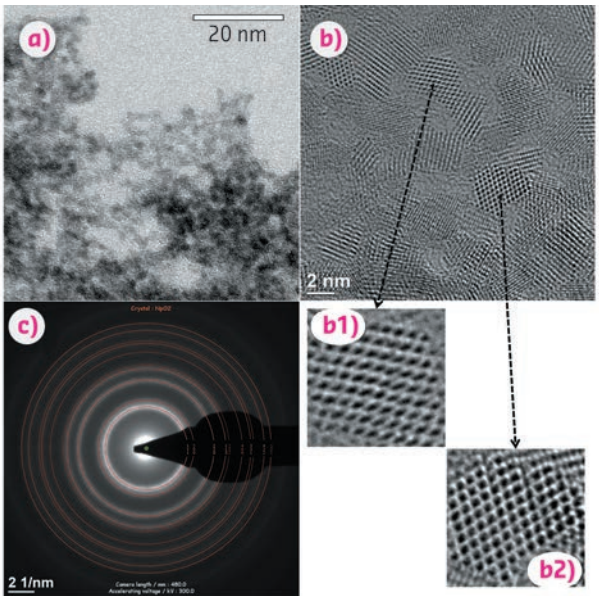

Fig. 68: (a) Bright field TEM micrograph of the dried precipitate obtained from the diluted Np(IV) solution, (b) their HR-TEM images and (c) selected area electron diffraction (SAED) patterns. Red rings in (c) are the simulated diffraction patterns based on fluorite-type NpO_2 structure.

PRINCIPAL PUBLICATION AND AUTHORS

R. Husar (a), R. Hübner (b), C. Hennig (a,c), P. M. Martin (d), M. Chollet (d), S. Weiss (a), T. Stumpf (a), H. Zänker (a) and A. Ikeda-Ohno (a), *Chem. Comm.* **51**, 1301-1304 (2015); doi: 10.1039/c4cc08103j.

(a) Helmholtz-Zentrum Dresden-Rossendorf (HZDR), Institute of Resource Ecology, Dresden (Germany)
(b) Helmholtz-Zentrum Dresden-Rossendorf (HZDR), Institute of Ion Beam Physics and Materials Research, Dresden (Germany)
(c) The Rossendorf Beamline, ESRF
(d) Commissariat à l'énergie atomique et aux énergies alternatives (CEA), Cadarache (France)

REFERENCES

[1] *Chemical Thermodynamics of Neptunium and Plutonium*, R.J. Lemire *et al.*, (Eds.), Elsevier Science, Amsterdam, The Netherland (2001, updated in 2003).
[2] A.B. Kersting, *et al.*, *Nature* **397**, 56-59 (1999).

A MULTI-TECHNIQUE APPROACH TO INVESTIGATE SILICA-SUPPORTED ZIEGLER–NATTA CATALYSTS

Heterogeneous Ziegler–Natta catalysts are the most widely used catalysts for polyolefin production. A significant improvement in the definition of the structure of the active sites at a molecular level, and in the understanding of the mutual interactions among all the catalyst's components has been achieved by using X-ray absorption and emission spectroscopy coupled with XRD, DR UV-Vis and IR laboratory techniques.

Heterogeneous Ziegler–Natta catalysts for the production of polyolefins are among the most widely used and versatile catalysts in the chemical industry and probably those having the largest impact not only in science but also in everyday life. The extraordinarily large number of polymer architectures available today and the remarkably rapid progress in polyolefin technology are closely associated with the catalyst's development. Since their discovery in 1960s, heterogeneous Ziegler–Natta catalysts have progressed enormously, making it possible to produce advanced polyolefin materials with tailored properties. Today, Ziegler–Natta catalysis allows a precision synthesis of polyolefins based on the exact assembly of the olefin monomers on the active catalytic sites. However, Ziegler–Natta catalysts remain substantially a black box despite many efforts to understand them. The structural and electronic properties of the titanium active sites and their relation to the catalytic body as a whole are hampering the rational design of better catalysts.

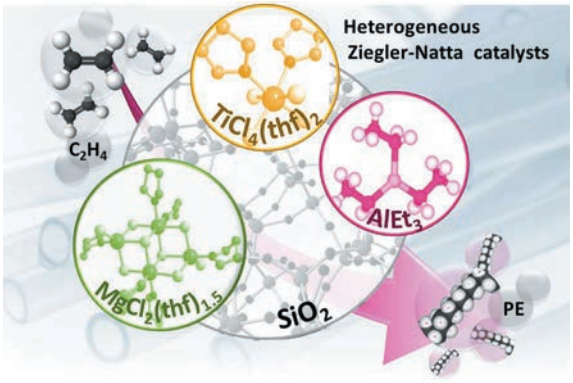

Fig. 69: Schematic representation of all the components of a silica-supported Ziegler-Natta catalyst based on titanium and magnesium chloride tetrahydrofuranates activated by an aluminum–alkyl compound. The catalyst polymerises ethylene, producing polyethylene.

Recently, we have been involved in a systematic investigation of industrially-relevant heterogeneous Ziegler–Natta catalysts for polyethylene production that are based on titanium and magnesium chloride tetrahydrofuranates (**Figure 69**) [1-3]. The structural, vibrational, and electronic properties were investigated in detail by means of a multi-technique approach at each step of catalyst preparation, including pre-catalyst activation [4]. In particular, we combined *in situ* XAS and XES experiments (at beamlines **BM26A** and **ID26**, respectively) with XRD, DR UV-Vis and IR (both Mid-IR and Far-IR) measurements (**Figure 70**).

It was found that in the pre-catalyst, the $TiCl_x$ phase is grafted mainly to the silica surface

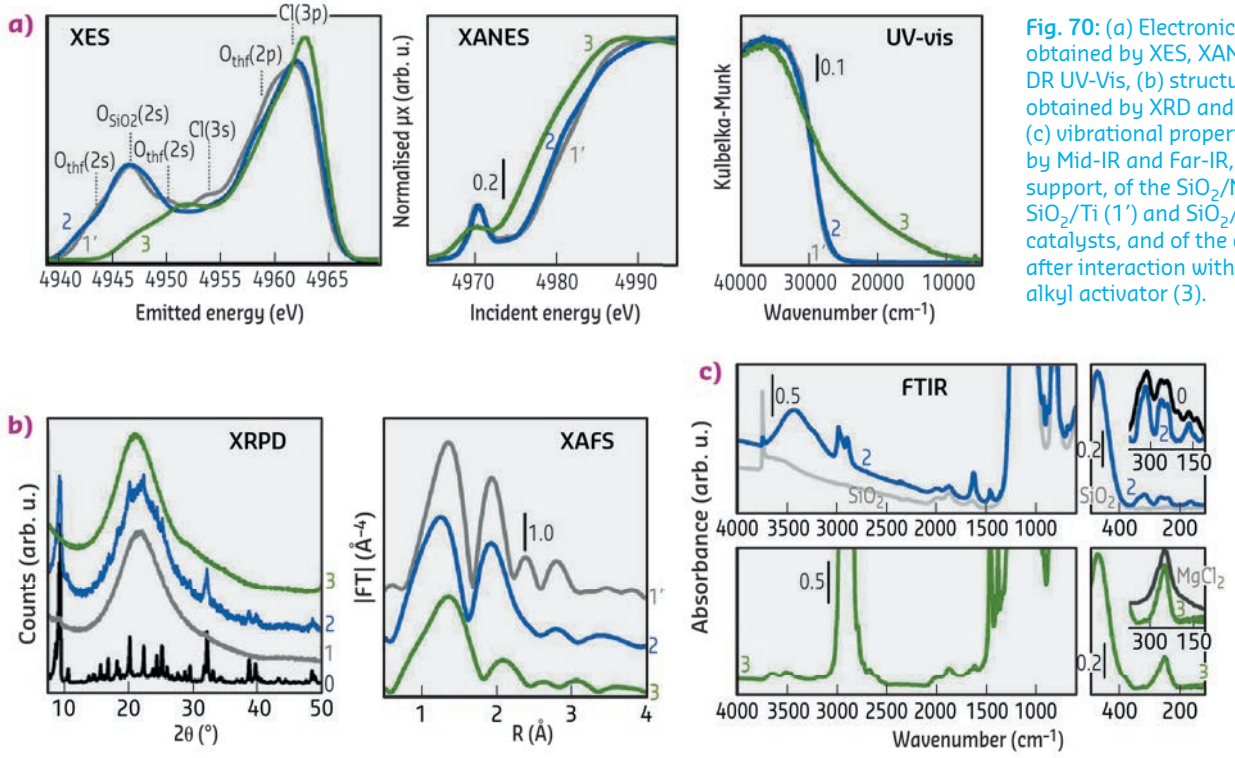

Fig. 70: (a) Electronic properties obtained by XES, XANES and DR UV-Vis, (b) structural properties obtained by XRD and EXAFS and (c) vibrational properties obtained by Mid-IR and Far-IR, of the silica support, of the SiO_2/Mg (1), SiO_2/Ti (1') and SiO_2/TiMg (2) pre-catalysts, and of the catalyst obtained after interaction with the aluminium-alkyl activator (3).

and almost independent of the supported $MgCl_x$ phase. However, the subsequent activation by means of an aluminum–alkyl compound causes important changes to both the supported $MgCl_x$ phase and the $TiCl_x$ phase. The resulting catalyst is entirely reconstructed. In particular, the activator removes most of the tetrahydrofuran originally present in the pre-catalyst, reduces the titanium sites and detaches most of them from the silica surface, simultaneously promoting the formation of a $MgCl_2$ phase highly dispersed on the silica surface. The formed $TiCl_x$ species are connected to the silica-supported $MgCl_2$ phase through bridging chlorine ligands and are characterised by the presence of terminal chlorine ligands at shorter distances. Hence, the resulting active phase resembles the most famous and highly investigated Ziegler–Natta catalysts (not silica-supported), although probably much more dispersed. Moreover, the catalyst performances were monitored by means of *in situ* FT-IR spectroscopy, simulating industrially significant pre-polymerisation conditions.

These results demonstrate that it is now possible to achieve a complete description at a molecular level of all the constituents of Ziegler–Natta catalysts at each step of the catalyst preparation. Such a systematic investigation of all the catalyst's components by means of a multitechnique approach might be the first fundamental step toward understanding their mutual interactions and functions down to a level of detail rarely reached by other methods, making the design of these catalysts a realistic goal for the future.

PRINCIPAL PUBLICATION AND AUTHORS

Activation and *in situ* ethylene polymerization on silica-supported Ziegler–Natta catalysts, E. Groppo (a), K. Seenivasan (a), E. Gallo (a,b), A. Sommazzi (c), C. Lamberti (a,d) and S. Bordiga (a), *ACS Catal.* **5**, 5586–5595 (2015); doi: 10.1021/acscatal.5b01108.

(a) Department of Chemistry, NIS Centre and INSTM Reference Center, University of Turin, Turin, (Italy)
(b) ESRF
(c) Versalis – Novara Research Center, Istituto Eni Donegani, Novara, (Italy)
(d) Southern Federal University, Rostov-on-Don (Russia)

REFERENCES

[1] K. Seenivasan *et al.*, *Chem. Eur. J.* **17**, 8648–8656 (2011).
[2] E. Groppo *et al.*, *ChemCatChem* **7**, 1432–1437 (2015).
[3] K. Seenivasan *et al.*, *Dalton Trans.* **42**, 12706–12713 (2013).
[4] E. Groppo *et al.*, *Catal. Sci. Technol.* **3**, 858–878 (2013).

OPERANDO X-RAY ABSORPTION SPECTROSCOPY SHOWS STRUCTURAL DYNAMICS OF Cu-CONTAINING CATALYSTS FOR BIO-BASED BUTADIENE FORMATION

The production of commodity chemicals from renewable resources such as biomass, will aid the necessary transition to a more sustainable society. Butadiene, a key building block for rubbers and polymers, such as ABS, can, for instance, be produced from bioethanol. Detailed insight was obtained by operando X-ray absorption spectroscopy into the complex structure of the catalyst materials used for this process, allowing for improved catalyst design.

Future biorefinery operations should produce high-value bio-based chemicals in addition to biofuels in order to be economically competitive. The bio-based chemicals can be either new compounds or can be 'drop-in' replacements, *i.e.* molecularly-identical to the chemical building blocks that we obtain today from petrochemical refining. The latter class holds the advantage of serving existing markets and can make use of existing infrastructure for further processing. One particularly interesting route to a drop-in commodity chemical is the conversion of bio-based ethanol to butadiene [1]. Butadiene, mainly produced as byproduct of naphtha steam cracking, is one of the major chemical commodities with a forecasted production of 12 Mt in 2015 and is used mainly as a monomer for rubbers, polymers and latexes. The one-step conversion of ethanol to butadiene is known as the Lebedev process and has been operated commercially during the first half of the twentieth century in the Soviet Union and elsewhere, eventually losing out to petrochemical production processes. The current availability of large volumes of bioethanol and its possible exploitation as a renewable feedstock has rekindled the academic and industrial interest in this process. SiO_2-MgO based catalysts have long been considered as the prototypical catalysts for the Lebedev process and have been

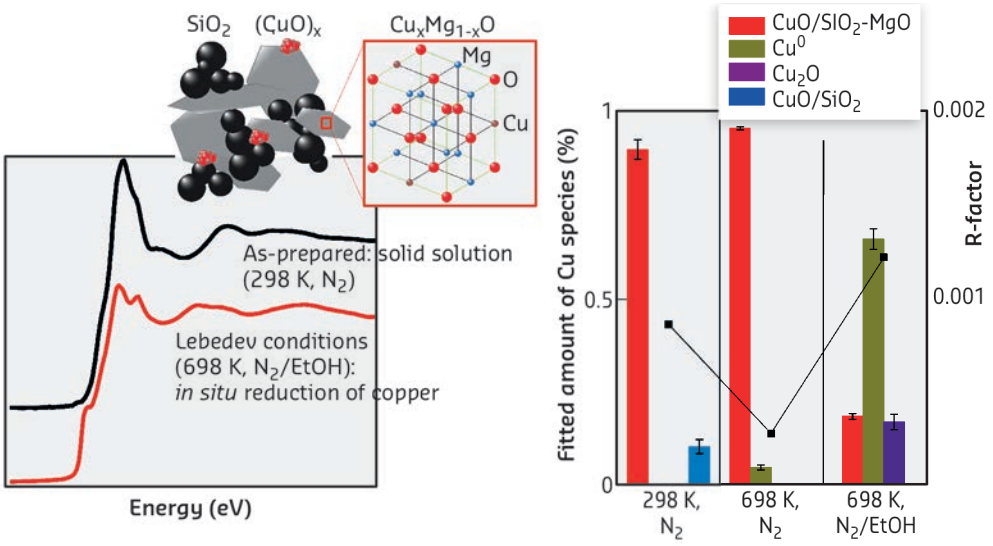

Fig. 71: Left: Operando XAS studies show changes in copper speciation under reaction conditions; right: fitting of the XANES region allowed estimation of the different copper species present under reaction conditions.

applied industrially. The performance of such catalysts can be greatly enhanced if a third component, a transition metal or metal oxide (*e.g.*, metallic Ag or Cr, Ni, Zn, or Cu oxides), is added [2]. Fundamental understanding of the structure-function relationships that govern the performance of these (promoted) materials, together with how they are influenced by the method of catalyst preparation, is required for the efficiency improvements necessary for making this route a viable alternative. However, the knowledge available on the structural and morphological properties of such promoted SiO_2-MgO based catalysts, as well as on how the structure evolves under reaction conditions, is still rather limited.

We have studied CuO-promoted SiO_2-MgO catalysts in great detail with a combination of characterisation techniques in order to get more insight into the nature, dispersion and role of CuO in the Lebedev process (**Figure 71**). Operando studies of these Lebedev catalysts also provided insight into the evolution in copper speciation under reaction conditions. *Ex situ* and operando XANES and EXAFS measurements recorded at beamline **BM26A (DUBBLE CRG)**, provided pivotal information of the speciation, oxidation state and geometry of the Cu promoter in the fresh catalysts and allowed for copper structural changes to be elucidated under typical Lebedev conditions, *i.e.* in the presence of ethanol at 698 K. As expected, the preparation method of the CuO/SiO_2-MgO catalyst strongly influenced its catalytic performance. In combination with other characterisation techniques, *ex situ* XAS and EXAFS allowed the copper oxidation state and geometry to be firmly established, with all copper found to be Cu^{2+} in a distorted octahedral geometry in a $Cu_xMg_{1-x}O$ solid solution. XAS measurements of the CuO/SiO_2-MgO catalyst under operando conditions, evidenced by butadiene formation detected by mass spectrometry, provided detailed insight into the remarkable changes in copper speciation under the reducing conditions of the process. The system was shown to evolve to a mixture of copper species, which could be distinguished by fitting the XANES, with 60% of the copper being reduced to Cu^0 and the remainder present as Cu^+ or Cu^{2+}. This steady state was obtained regardless of the pretreatment history of the catalyst, emphasising the dynamics of the system. Some of the resulting copper species are thought to be involved in boosting the dehydrogenation activity of the catalyst, while others modify the acid-base characteristics of the material, the balance of which is essential to selective butadiene formation. The detailed insights into catalyst structure and its dynamics can now serve as input for the development of the next generation of Lebedev catalysts.

PRINCIPAL PUBLICATION AND AUTHORS

Ex situ and operando studies on the role of copper in Cu-promoted SiO_2–MgO catalysts for the Lebedev ethanol-to-butadiene process, C. Angelici (a), F. Meirer (a), A.M.J. van der Eerden (a), H.L. Schaink (a), A. Goryachev (b), J.P. Hofmann (b), E.J.M. Hensen (b), B.M. Weckhuysen (a) and P.C.A. Bruijnincx (a), *ACS Catal.* **5**, 6005-6015 (2015); doi 10.1021/acscatal.5b00755.
(a) Inorganic Chemistry and Catalysis, Utrecht University (The Netherlands)
(b) Laboratory of Inorganic Materials Chemistry, Eindhoven University of Technology (The Netherlands)

REFERENCES

[1] C. Angelici *et al.*, *ChemSusChem* **6**, 1595-1614 (2013).
[2] C. Angelici *et al.*, *ChemSusChem* **7**, 2505-2515 (2014).

COMBINING HARD AND SOFT XAS TO CHARACTERISE THE DEACTIVATION PATHWAY OF AN IMMOBILISED TRANSFER HYDROGENATION CATALYST

A multi-element X-ray absorption spectroscopy study was performed on an immobilised iridium transfer hydrogenation catalyst. *Ex situ* measurements probing the Ir L-edge and the Cl-K edge showed the loss of an Ir-Cl bond during activation of the catalyst, followed by further loss of a second Ir-Cl bond throughout the depreciation of catalytic activity. Build-up of potassium cation, from the KO^{t}Bu used as co-catalyst, was detected in the deactivated samples. An operando experiment was carried out using a spectroscopic flow cell to monitor the loss of chloride and accretion of potassium throughout deactivation. Its findings corroborated the *ex situ* measurements and kinetic data to support a second order deactivation mechanism.

Immobilisation of molecular catalysts is a common strategy in modern synthetic science to facilitate catalyst recovery and reuse. This allows reduction of the cost of application of these often complex and sophisticated catalysts while improving the sustainability of such manufacturing processes, particularly when precious metals are used. Most immobilisation technology, however, is developed empirically due to a lack of suitable and effective characterisation techniques once the catalyst is immobilised. It is quite common to find the behaviour of the catalyst changed upon immobilisation through either interaction with the solid support or isolation from other catalyst molecules.

We have previously reported a novel approach to immobilisation of organometallic catalysts containing the Cp* ligand [1]. By linking the catalyst, $[Cp^*IrCl_2]_2$, with the support through the strongly binding Cp* ligand, metal leaching is suppressed to a negligible level. Slow deactivation over 30 recycling uses was however still observed due to chemical changes at the metal centre. Thus, an XAS study was developed to characterise the catalyst deactivation process.

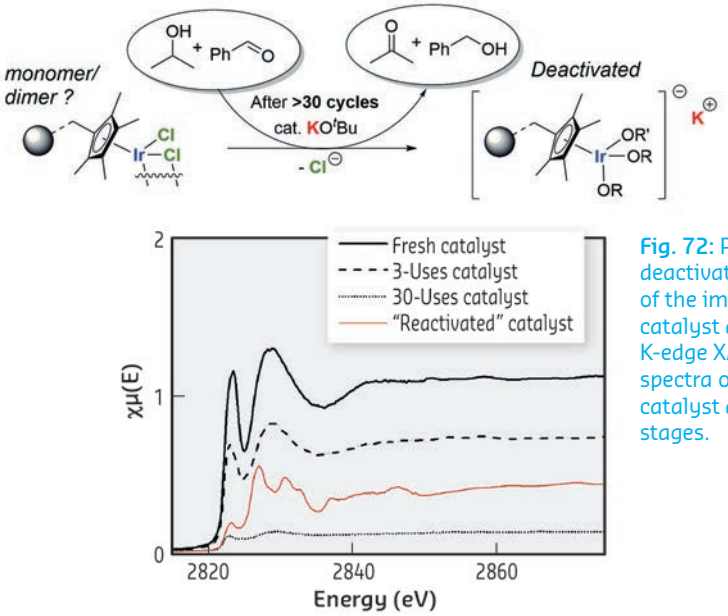

Fig. 72: Proposed deactivation form of the immobilised catalyst and Cl K-edge XANES spectra of the catalyst at various stages.

A novel multi-element approach was adopted to fully characterise the catalyst at various stages of the deactivation process. Instead of solely observing the Ir centre through Ir L-edge (11.2 keV), both the Ir L-edge EXAFS and Cl K-edge XANES were probed, using beamline **BM28 (XMaS CRG)**. *Ex situ* spectra of the fresh catalyst, and catalysts after 3 (still highly active) and 30 cycles of use (inactive) clearly showed a rapid loss of about 50% of the Cl and Ir-Cl signals, without loss of catalytic activity, followed by a slow loss of the remaining chloride ligand and subsequent deactivation. These results link the deactivation process with a second ligand exchange of the immobilised catalyst.

Treatment of the deactivated catalyst with dilute aqueous hydrochloric acid temporarily restored catalytic activity, which was rapidly lost after 3 cycles of use. Cl XANES spectrum of this 'reactivated' catalyst indicated a change in speciation of the Cl content to KCl. This new and unexpected observation pointed to a presence in the deactivated catalyst of the potassium cation, introduced in the form of co-catalyst KO^{t}Bu under catalytic conditions. A hypothesis on the activation and deactivation of this immobilised catalyst, taking into account all experimental observations, was developed (Figure 72).

To correlate the structural changes above with changes in catalytic activity, an *operando* experiment was performed using a spectroscopic flow-cell. Spectra of the catalyst at Cl K-edge and K K-edge were monitored over 24 hours as the reaction mixture was flowed through the catalyst. The decrease in catalytic activity was found to match the concurrent decrease of Cl content and increase of K content, confirming the hypothesis above (Figure 73).

The results, particularly the unexpected detection of the potassium cation in the deactivated catalyst, highlight multi-element XAS as a powerful combination of spectroscopic techniques for immobilised molecular catalysts. The specific deactivation pathway determined in this study will now be pivotal in developing strategies to reactivate the catalyst or to suppress catalyst deactivation.

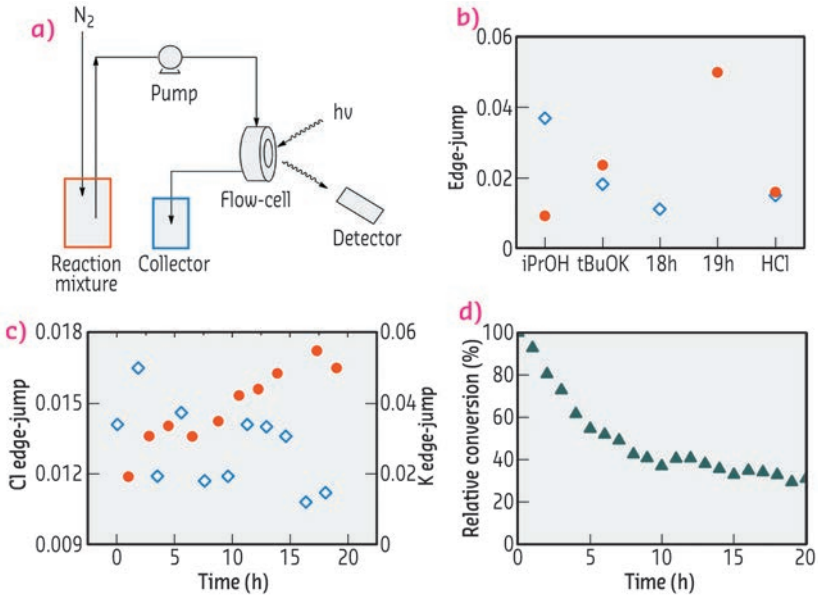

Fig. 73: (a) *Operando* experimental setup; (b) Cl (blue) and K (red) edge jumps at various stages of the experiment; (c) Cl (blue) and K (red) edge jumps during catalytic reaction; (d) concurrent catalytic activity vs time.

PRINCIPAL PUBLICATION AND AUTHORS

Activation and deactivation of a robust immobilized Cp*Ir-transfer hydrogenation catalyst: a multi-element *in situ* X-ray absorption spectroscopy study, G.J. Sherborne (a), M.R. Chapman (a), A.J. Blacker (a), R.A. Bourne (a), T. Chamberlain (b), B.D. Crossley (c), S.J. Lucas (a), P.G. McGowan (a), M.A. Newton (d), T.E.O. Screen (c), P. Thompson (d), C.E. Willans (a) and B.N. Nguyen (a), *JACS* **137**, 4151-4157 (2015); doi: 10.1021/ja512868a.

(a) Institute of Process Research and Development, School of Chemistry, University of Leeds (UK)
(b) School of Chemistry, University of Nottingham (UK)
(c) Yorkshire Process Technology Ltd., Leeds Innovation Centre, Leeds (UK)
(d) Department of Physics, University of Liverpool (UK); Xmas CRG, ESRF, Grenoble (France)

REFERENCES

[1] S.J. Lucas *et al.*, *Chem. Commun.* **49**, 5562-5564 (2013).

THE RESISTIVE SWITCHING MECHANISM OF CONDUCTIVE-BRIDGING RANDOM-ACCESS MEMORY CLARIFIED BY XAS

Ag:GeS_x-based conductive-bridging random-access memory (CBRAM) were characterised using synchrotron techniques before and after electrical switching. These experiments gave fundamental insight related both to the diffusion phenomenon of Ag^+ in Ag-GeS_x glass and to the structure of the solid electrolyte used in CBRAM devices.

Resistive random-access memories have received extensive interest in recent years since they constitute promising candidates for future data storage and information technologies with applications such as non-volatile memories and neuromorphic computing. Among the different approaches, CBRAM based on an Ag:GeS_x glass sandwiched between an Ag electrochemically active anode and an inert cathode are considered as one of the most promising technologies [1]. Under the influence of an electric field, it is supposed that Ag ions are produced at the anode and migrate in the electrolyte to form a conducting path. This process is reversible by applying an opposite bias. However to date, the lack of understanding of the switching mechanisms at a nanoscale level has prevented the successful transfer of such a technology to industry. In this context, we report the characterisation of Ag/GeS_x/W CBRAM devices using synchrotron techniques.

Our approach was based on the design of CBRAM devices (**Figure 74a**) specifically-adapted in order to be finely characterised depending on their resistive states by means of depth-selective X-ray absorption spectroscopy (XAS) at beamline **BM08 (**LISA-CRG**)**. The CBRAM devices were tested electrically prior to the experiment in order to simulate a memory in its different states (electrically switched or not). **Figure 74b** illustrates the typical I(V) curves obtained and the reversible switching from the high to the low resistive state (SET and RESET, respectively).

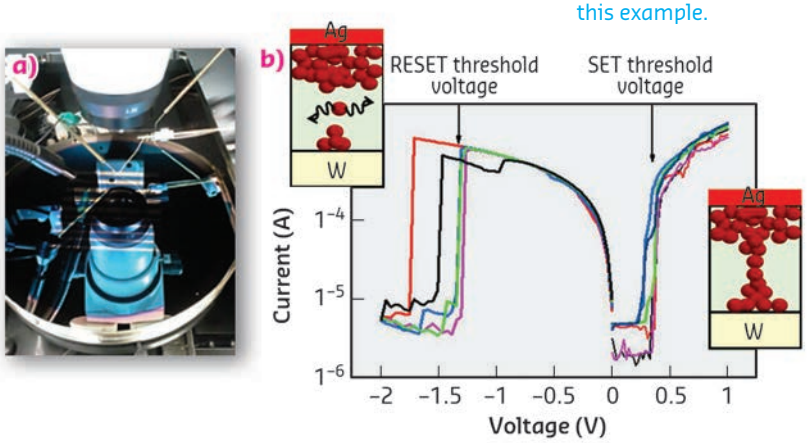

Fig. 74: (a) The CBRAM devices during an electrical test. The devices consist of a GeS_x electrolyte layer (50 nm) deposited on a tungsten bottom electrode (25 nm) and covered by an Ag active top electrode (20 nm). After switching, the Ag top electrode was completely removed by ion beam etching prior to the XAS experiments. (b) Typical I(V) curves of a CBRAM device during cycles of SET and RESET between the low and high resistive states. 4 cycles are reported in this example.

Figure 75a shows the XAS spectra depending on the switching state of the device and on the depth within the sample from which the signal originated. CBRAM devices that never underwent any switching show a lower silver metal fraction whereas the switched ones present a higher value. Moreover, XAS surface data show a higher metal fraction below the anode in comparison to the entire layer. Our experiments highlight that the switching process involves the formation of metallic Ag and the formation of this phase is initiated at the Ag electrode. This supports a model of the formation of nanofilaments consisting of Ag metallic cones with their base on the active electrode as metal reduction happens more rapidly than ion migration. Moreover, the study of the local environment around Ag atoms in such devices reveals that Ag is in two very distinct environments with short Ag-S bonds due to Ag dissolved in the GeS_x matrix and longer Ag-Ag bonds related to an Ag metallic phase.

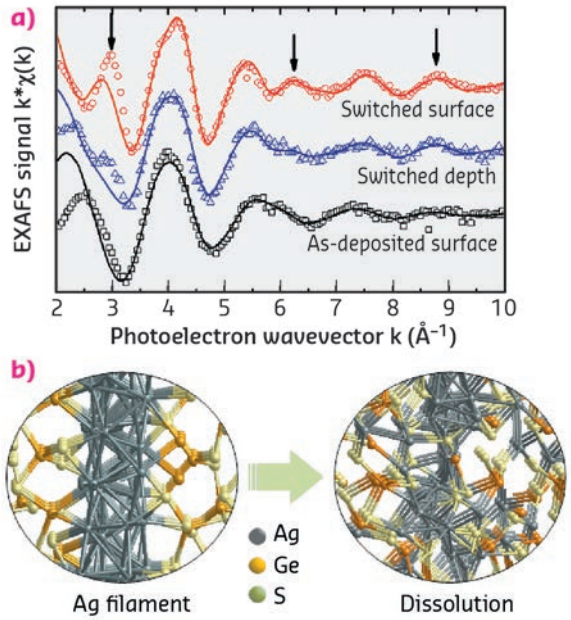

Fig. 75: (a) EXAFS spectra of 3 prototypical samples (switched CBRAM using surface and depth collection mode and a non-switched CBRAM on the surface) with the best fit curves (continuous lines). The vertical arrows mark the features that grow with increasing Ag–metal content. (b) Schematic drawing of a silver nano-filament in GeS_x and the silver filament dissolution scheme.

These experimental results are well supported by *ab initio* molecular dynamics simulations showing that Ag favourably bonds to S atoms. From these results, we were able to deduce the origin of the main limitation of this type of devices [2]: the instability of the ON state can be attributed to the sulfidation of Ag and hence rupture of the Ag–Ag metallic conduction path in the GeS_x layer.

This work illustrates the importance of designing specific samples for characterisation with synchrotron radiation in order to understand the mechanisms involved in the operation of nano-electronic devices. Finally, the principle of the nondestructive method described here can be extended to other types of resistive memory concepts (including memristors based on transition metal oxides), and will give fundamental clues about the resistive switching mechanisms.

PRINCIPAL PUBLICATION AND AUTHORS

The role of the local chemical environment of Ag on the resistive switching mechanism of conductive bridging random access memories, E. Souchier (a), F. D'Acapito (b), P. Noé (a), P. Blaise (a), M. Bernard (a) and V. Jousseaume (a), *Phys. Chem. Chem. Phys.* **17**, 23931 (2015); doi: 10.1039/C5CP03601A.
(a) Univ. Grenoble Alpes and CEA, LETI, MINATEC Campus, Grenoble (France)
(b) CNR-IOM-OGG c/o ESRF, Grenoble (France)

REFERENCES

[1] I. Valov *et al.*, *Nanotechnology*, **22** 254003 (2011).
[2] E. Vianello *et al.*, *Proceedings of the IEEE International Electron Devices Meeting (IEDM) San Francisco*, 741 (2012).

COMPLEX MODULATED MAGNETISM IN PrPtAl

The discovery and characterisation of complex modulated magnetism in PrPtAl at the interface between ferromagnetism and paramagnetism suggests a new route for creating complex magnetic order.

The transition between ferromagnetism and paramagnetism is one of the simplest examples of a continuous phase transition. Interesting behaviour is expected when the transition temperature becomes small because incoherent fluctuations above the transition temperature then exist to low temperatures. Ultimately, for lower transition temperatures, either the transition must become first order or new forms of order must appear to satisfy the third law of thermodynamics. A new theory known as "order-by-disorder" [1] clarifies how the fluctuations associated with different competing ground states may stabilise new forms of order under these circumstances. Our findings on PrPtAl provide the first concrete vindication of one of the predictions of this approach: the formation of modulated magnetic structures.

Resonant X-ray diffraction provides a powerful method for studying magnetism affording both magnetic site selectivity and high resolution. Polarisation analysis and azimuthal scans can determine the direction of the magnetic moments and dichroism can be used to study domains of different helicity. In the current case, a diffraction study at beamline **BM28** (XMaS CRG) has allowed us to characterise complex magnetic states discovered in PrPtAl at the boundary between ferromagnetism and paramagnetism. Much of the observed behaviour is consistent with the predictions of the order-by-disorder theory, including a change from ferromagnetism to a modulated state whose modulation vector increases with temperature (see Figure 76). Surprisingly, the phase diagram is also more complex. Rather than this modulated state changing directly into the paramagnetic state as the temperature is further increased, it changes to a doubly modulated state before paramagnetism is finally attained. This second modulated state is very unusual, having two simultaneous collinear incommensurate ordering vectors. We focus below on the first modulated state, which has only one incommensurate vector (together with a strong third harmonic) (see Figure 76).

A temperature dependent modulation vector above a jump from ferromagnetism is also found for the rare earth elements Tb and Dy. Differences in other physical quantities, however, indicate a new mechanism is at play in PrPtAl. Hexagonal Tb and Dy inherently 'want' to form helical magnetic structures (owing to their band structure and the RKKY interaction). However, the anisotropy energy, which grows extremely strongly with the magnitude of the ordered moment, pushes them into a ferromagnetic state at low temperature. The conjecture for PrPtAl is the opposite: PrPtAl 'wants' to be a ferromagnet but the extra-fluctuations available for a modulated structure stabilise modulations close to 'T_C'. In order to tell these two cases apart experimentally, one possibility is to consider how the modulated state changes the electronic density of states and magnetic fluctuations. In the first case (Tb and Dy) the gapping of the Fermi-surface decreases the fluctuations where they are the strongest. This contrasts with the order-by-disorder mechanism in which the dominant fluctuations are centred on

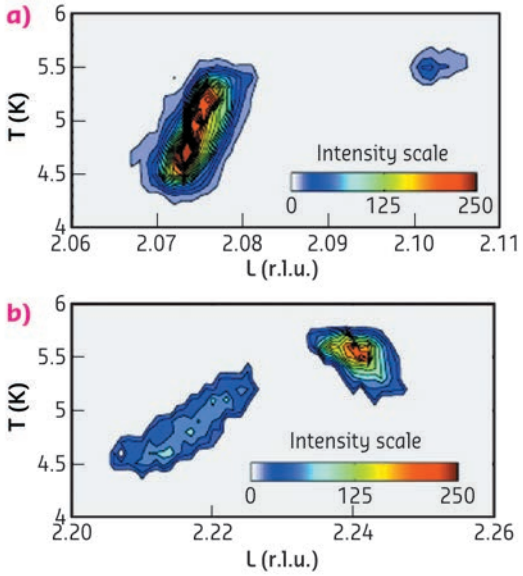

Fig. 76: Intensity maps around satellites at (00L) close to the (002) Bragg peak as a function of temperature for PrPtAl measured at the Pr L_{II} edge. At lower temperatures, a single modulation wavevector q ≈ 0.07 (rlu) (a) and a third harmonic (b) are seen. The change of wavevector of this peak with temperature and the strong third harmonic are well explained by the "order-by-disorder" theory. Just before 6 K, two new vectors appear at q≈0.1 (rlu) (a) and 0.24 (rlu) (b).

q = 0, rather than at the spin density wave (SDW) ordering vector and the formation of the SDW actually increases their strength. This should have consequences for the heat capacity and electrical conductivity: the order-by-disorder theory predicts that they will be enhanced in the modulated state if order-by-disorder is at play, but reduced otherwise. This is indeed what we observed experimentally.

PrPtAl is special because it is an induced moment magnet. Isolated Pr ions in the crystal structure do not have intrinsic moments; the moment is induced by mixing different individually non-magnetic excited levels together. The total moment on each site (the sum of the ordered moment and low energy fluctuations) is therefore not fixed. This aspect resembles an itinerant magnet for which the order-by-disorder model was developed. The added ingredient is a source of spin-anisotropy associated with the induced moments. This favours the formation of modulated states via the order-by-disorder mechanism.

To summarise, we have demonstrated a new way to achieve complex magnetic structures not requiring Fermi-surface nesting, anti-symmetric (Dzyaloshinskii-Moria) exchange interactions or magnetic frustration. Given the recent interest in complex magnetic structures such as skyrmions for spintronic applications [2], this could form the basis for new enabling technology in the longer term.

PRINCIPAL PUBLICATION AND AUTHORS

Modulated magnetism in PrPtAl,
G. Abdul-Jabbar (a) , D.A. Sokolov (a) ,
C.D. O'Neill (a), C. Stock (a), D. Wermeille (b,c),
F. Demmel (d), F. Krüger (d,e), A.G. Green (e),
F. Lévy-Bertrand (f), B. Grenier (g) and
A.D. Huxley (a), *Nature Physics* **11**, 321 (2015);
doi:10.1038/nphys3238.
(a) School of Physics and CSEC, University of Edinburgh (UK)
(b) XMaS (BM28), ESRF
(c) Department of Physics, University of Liverpool (UK)
(d) ISIS, STFC, Rutherford, Appleton Laboratory, Chilton (UK)
(e) London Centre for Nanotechnology, University College London (UK)
(f) CNRS, Institut Néel, Grenoble (France)
(g) Université Grenoble Alpes and CEA, INAC-SPSMS, Grenoble (France)

REFERENCES

[1] G.J. Conduit, A.G. Green and B.D. Simons, *Phys. Rev. Lett.* **103**, 207201 (2009).
[2] *e.g.* Y. Zhou and M. Ezawa, *Nat. Commun.* **5**, 4652 (2014).

Complex systems and biomedical sciences

The new group "Complex Systems and Biomedical Sciences" (CBS) was formed in July 2015 in order to foster synergy and collaboration in soft matter, surface and biomedical science in preparation of the EBS project. The group has five beamlines: ID02 (WAXS/SAXS/USAXS), ID03 (surface diffraction), ID09 (structural dynamics), ID10 (coherent diffraction imaging, correlation spectroscopy, soft surfaces and interfaces structure) and ID17 (medical beamline). The joint ILL/ESRF laboratories in the Partnership for Soft Condensed Matter (PSCM) are also included in the group. The main news from the beamlines are described below.

The upgrade of the time-resolved ultra-small-angle scattering beamline, ID02, the UPBL9a project, was completed at the end of 2014 and the beamline performance has reached most of the design specifications during its first year. The combined USAXS/SAXS/WAXS setup using the 34 m detector tube and multiple detectors can probe structural scales over 0.15 – 6000 nm with time resolution down to a millisecond with appropriate samples. ID02 can also exploit the coherence of the beam at extremely low angles to probe dynamics by X-ray photon correlation spectroscopy (XPCS). The high spatial resolution together with access to ultra low angles has initiated a new approach for the structural dynamic studies of cardiac muscle activation, especially by resolving the interference fine structure during muscle contraction. The availability of a wide q range is also very useful for industrial clients and the demand for proprietary beam time has increased significantly during the year.

ID03 was reviewed in November 2015 and the committee congratulated the beamline for excellent user support and in-house research. In addition to classical surface crystallography under ultra high vacuum, the trend in recent years has been to study catalysis and electrochemistry under real conditions in suitably designed reaction chambers. The efficiency of the data collection on ID03 was significantly improved by the use of a large CCD detector with software for quick reciprocal-space mapping and data analysis. This new software, named Binoculars, was developed in a very fruitful collaboration with Leiden University. A fast atomic force microscope (AFM) for measuring the morphology and mechanical properties of the sample *in situ* during X-ray data collection was also tested successfully in 2015. Finally the coherence of the beam was exploited in a few experiments which eventually might allow the catalytic activity of nanoparticles to be imaged with the future EBS lattice.

After 18 years at the ESRF Roberto Felici has moved to SPIN-CNR in Rome. Roberto took the position of scientist in charge of beamline ID03 in 2005. During the last 10 years he has led the technical developments of ID03, pushing the research activity of the beamline to the cutting edge of surface science. We wish Roberto success in his new position.

The beamline for structural dynamics, ID09, became dedicated to time resolved (TR) studies in November 2015 when the high-pressure branch of ID09A moved to ID15. With the increase in beamtime, more advanced and time consuming experiments can now be conducted. For example, a new transient optical/optical absorption spectrometer allows the users to test the laser excitation parameters, *i.e.* the optimal wavelength and pulse energy prior to the X-ray experiment. In addition, a new X-ray emission Johann spectrometer (XES) is now available for measuring atom specific changes in valence and spin of transition metals during chemical reactions. The local information from XES is complementary to WAXS which probes the change in the average electron density during a chemical reaction.

Beamline ID10 has setups for soft matter surfaces studies, CDI and XPCS. Thanks to a four-fold increase in the coherent flux and the high efficiency of the Maxipix detector, the reconstruction of frozen-hydrated cells, in three dimensions and with sub 100 nm resolution, is now feasible which is very important for biomedical research. For the study of liquid interfaces, the trend is to study self-assembled two-dimensional superlattices from nanocrystals, nanoparticles and macromolecules with the aim of tailoring electro-optical properties via controlled growth and structure. For more details the reader is referred to H. Mendez *et al.*, *Nature Communications* 6, 8560 (2015). A new diffractometer for studies on liquid surfaces and interfaces with a double crystal deflector will be ready for user operation from the beginning of 2016. The deflector will speed up the data collection, decrease the liquid surface agitation and increase the q range for reflectivity measurements on liquids.

Microbeam radiation therapy (MRT) and phase contrast biomedical imaging continue to be

the most requested techniques at ID17. Several MRT user programmes aim to study the normal tissue sparing and tumouricidal properties of high doses of X-rays delivered by microbeams and to compare these properties with conventional homogeneous irradiation. Other MRT programmes progress in the study of the efficiency of microbeams to alleviate seizures in epilepsy models. The ID17 imaging capabilities were also expanded in 2015 with the installation of a high-speed PCO.Edge5.5 camera. This detector will be used in combination with several optics available to provide a range of resolutions and fields of view. In 2015, a new 1X-2X magnification optics developed in house has extended ID17's capabilities towards high resolution (pixel size down to 3.5 micrometres). This was developed in response to user requests in particular in neuroimaging. These studies are made possible by the presence on site of the Biomedical Facility, a technical biology platform supporting biomedical and life sciences research projects related to experiments carried out at ESRF beamlines, especially the Biomedical Beamline. The suite of laboratories provides *ad hoc* infrasctructures and expertise for the preparation of preclinical research programmes.

The PSCM made great progress in 2015 with the refurbishment and upgrade of a rheology platform, a multimodal optical microscope and a Brewster-angle microscope coupled to a Langmuir trough. With the support of the PSCM Steering Committee, ILL-owned equipment is progressively made available to the ESRF. This includes an interface tensiometer, a zeta potential analyser and a dynamic light scattering apparatus. The AFM platform from the former Scientific Infrastructure Group will be transferred to the PSCM in 2016. Additional capacities in terms of sample environment developments will be directed in particular towards the exploitation of microfluidic technologies to enhance synchrotron and neutron studies of soft and biological matter. The scientific programme includes the synthesis and self-assembly of nanomaterials in bulk and at interfaces, and innovative studies of soft biomaterials.

Finally, the preparation for the 4th International Soft Matter Conference (ISMC2016) is progressing well and further details can be found at URL: www.ismc2016.org.

M. WULFF

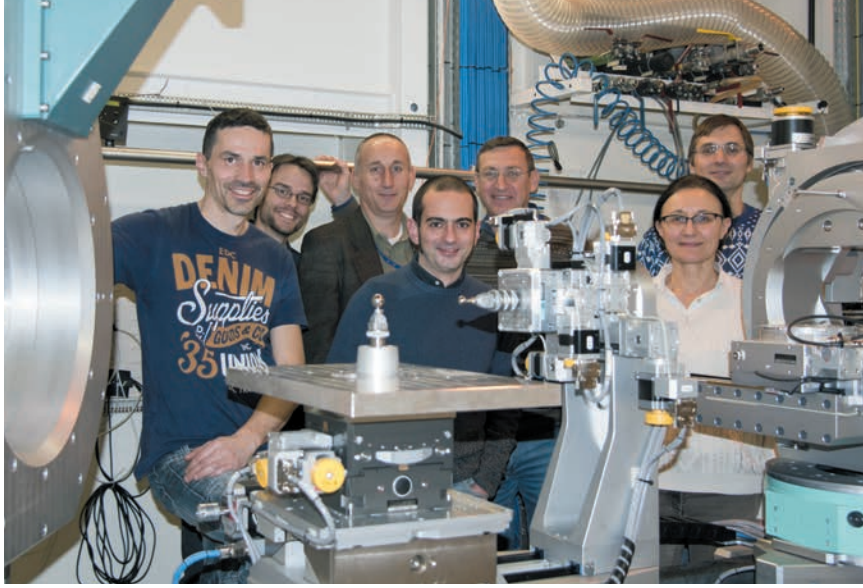

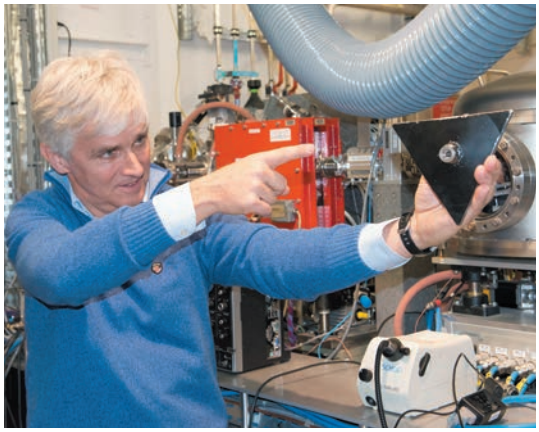

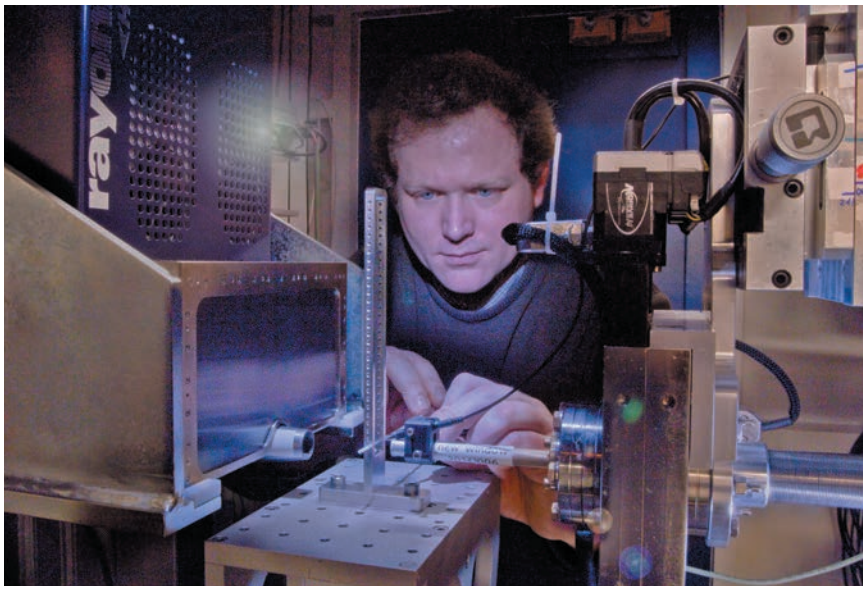

INTERFACE ALLOY FORMATION DURING THE PREPARATION OF MAGNETIC HETEROSTRUCTURES CAPPED WITH GRAPHENE

Graphene capped Co/Ir heterostructures have promising technological perspectives for the development of ultra-dense magnetic storage devices and of spintronic materials. Their preparation has been characterised with atomic resolution using surface X-ray diffraction techniques. Depending on the preparation procedure, a few atoms thick layer of a surface alloy can form and affect the final magnetic response of the system. This needs to be taken into account when tailoring the magnetic properties of such materials.

Graphene, the first easily accessible two-dimensional crystalline material, carries many promises for next generation technologies. Recently it has been shown that it is possible to induce a stable magnetic moment in the otherwise diamagnetic graphene by creating magnetic nanopatterns [1] or to manipulate the magnetisation of the ferromagnetic materials [2]. One relevant process to prepare magnetic graphene based heterostructures is intercalation, which consists of inserting species in between graphene and its support. This process is usually promoted by annealing a starting structure, *e.g.* a metallic layer deposited on top of the graphene sheet, at relatively high temperatures, typically a few hundred degrees centigrade.

Regarding the intercalation process itself, much effort has been focused on unveiling the intercalation pathways through a plain graphene sheet, but little attention has been given to the stability of the intercalated atomic layers. In particular, the interface between the ferromagnet intercalant and the metallic substrate has not yet been probed because the commonly used scanning probe microscopies and electron based spectroscopic techniques cannot directly and unambiguously characterise it. To overcome this problem, we have employed surface sensitive techniques based on synchrotron X-ray radiation. These techniques are able to penetrate deeply into matter and provide structural/morphological information of buried interfaces. The structure of Co films obtained by deposition on a clean Ir(111) surface and on graphene-covered Ir(111), and subsequent annealing at 770 K, shows that the intercalation process facilitates the intermixing between Co and Ir and the formation of an interface alloy.

The qualitative evolution of the Co morphology was obtained by an observation of the X-ray reflectivity (XRR) profiles, presented in **Figure 77**. XRR measured before and after Co deposition on clean Ir(111) (**Figure 77a, b**) reveals that the Co/Ir interface has a very low roughness, similar to the one of the clean Ir(111) surface, while the vacuum/Co interface is rough. Annealing at 770 K for 5 min yields a Co thin film with a sharp Co/Ir interface and with a low surface roughness (**Figure 77c**).

The morphology of the thin Co film is different in the presence of graphene. Co deposition at room temperature yields a very inhomogeneous film (**Figure 77d, e**) and the graphene/Ir(111) substrate seems to be practically unmodified by the presence of the Co layer. Annealing at 570 K followed by 770 K results in a roughening of the Co/Ir interface (**Figure 77f**). STM images show that the surface of the system is much flatter than before and that graphene is again visible, confirming Co intercalation between the graphene layer and the Ir substrate.

The XRR results are summarised schematically in **Figure 78**, where electron density profiles projected in the direction perpendicular to the surface are plotted together with the best fit

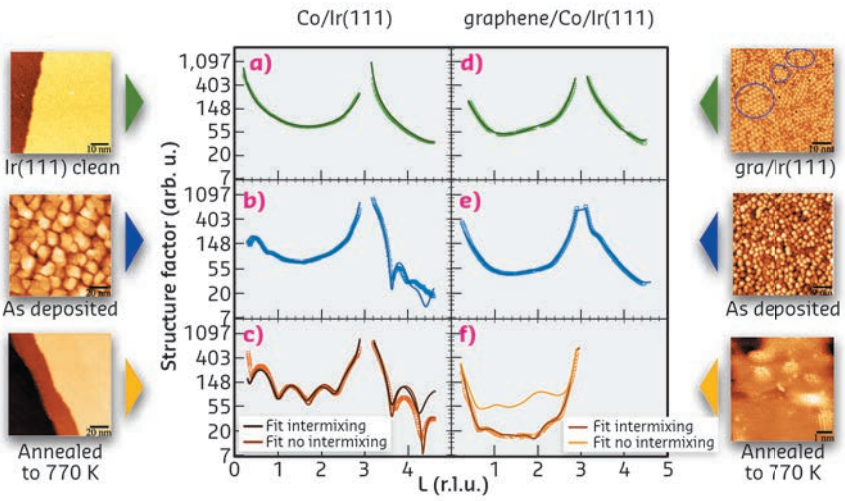

Fig. 77: X-ray reflectivity measured at RT (symbols) and fitted (solid lines) for: (a) bare Ir(111), (b) Co deposited on Ir(111) at RT, (c) the same sample annealed at 770 K, (d) graphene on Ir(111), (e) Co deposited at RT on graphene/Ir(111), (f) the same sample first annealed at 570 K and then further annealed at 770 K. Corresponding STM images are shown on the side.

models. The fits discriminate well between the sharp (non-intermixed) and rough (intermixed) interfaces.

In conclusion, we showed that an intermixing involving about 2 monolayers of the intercalant occurs during Co intercalation at 770 K. These results are valid only for the indicated temperatures and for defective graphene as different annealing temperatures will lead to a different intermixing. Our work suggests that annealing conditions must be chosen with care when targeting specific properties in graphene-based intercalated systems.

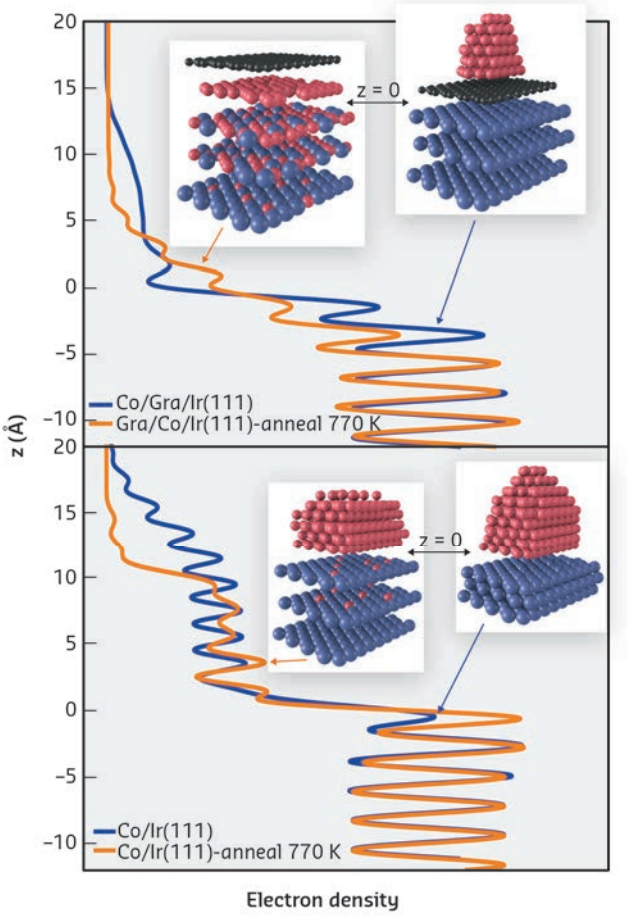

Fig. 78: Electronic density profiles projected in the z direction perpendicular to the surface as deduced from fits of the XRR data, for Co deposited on Ir(111) at RT (bottom plot, blue line), the same sample annealed at 770 K (bottom plot, orange line), Co deposited on graphene/Ir(111) at RT (top plot, blue line), Co intercalated between graphene and Ir(111) at 770 K (top plot, orange line).

PRINCIPAL PUBLICATION AND AUTHORS

Principal publication and authors
Surface alloying upon Co intercalation between graphene and Ir(111), J. Drnec (a), S. Vlaic (b,c,d), I. Carlomagno (a,c,e), C.J. Gonzalez (b,c), H. Isern (a), F. Carlà (a), R. Fiala (f), N. Rougemaille (b,c), J. Coraux (b,c) and R. Felici (a), *Carbon* **94**, 554-559 (2015); doi:10.1016/j.carbon.2015.07.039.
(a) ESRF
(b) CNRS, Inst NEEL, Grenoble (France)
(c) Univ. Grenoble Alpes, Inst NEEL, Grenoble (France)
(d) LPEM-UMR8213/CNRS-ESPCI ParisTech-UPMC, Paris (France)
(e) Università degli Studi Roma Tre (Italy)
(f) Charles University, Prague (Czech Republic)

REFERENCES

[1] R. Decker *et al.*, *Phys. Rev. B* **87**, 041403 (2013).
[2] N. Rougemaille *et al.*, *Appl. Phys. Lett.* **101**, 142403 (2012).

3D IMAGING OF WHOLE CELLS USING CRYOCOOLED COHERENT X-RAY DIFFRACTION

X-ray imaging of whole cells using coherent diffraction could bridge the gap between optical and electron microscopy, but is limited by radiation damage. Cryocooling could be used to mitigate this limitation. Cryocooling is demonstrated here in conjunction with coherent diffractive imaging (cryo-CDI) to reveal the 3D structure of a parasitic cell with an overall spatial resolution better than 100 nm.

A long way from Robert Hooke's first description of cells in cork, we are now experiencing a revolution in bioimaging. Optical microscopes are peering closer into cells than ever before, and electron microscopy approaches atomic resolution for single protein molecules. A type of X-ray microscopy known as coherent X-ray diffraction imaging (CDI) [1], which can recover a quantitative map of the 3D structure of a cell, promises to bridge these two imaging modalities.

3D CDI is similar to computed tomography (CT). It involves a synthesis of multiple projections of the same object from different angles. However, whereas CT relies on transmission images of an object, CDI interprets diffraction patterns from an object illuminated by a coherent X-ray beam (Figure 79). Because of this difference, CDI lacks phases, half of the data required to produce an interpretable image of the object. CDI uses computers as an X-ray lens to recover those phases and the structure of the object.

CDI was first demonstrated experimentally in 1999 [2]. Since then, CDI has been used to image a range of samples including whole cells. Biological specimens pose a particular challenge for CDI since they scatter X-rays weakly and cannot tolerate the higher X-ray doses required to compensate for such weak scattering.

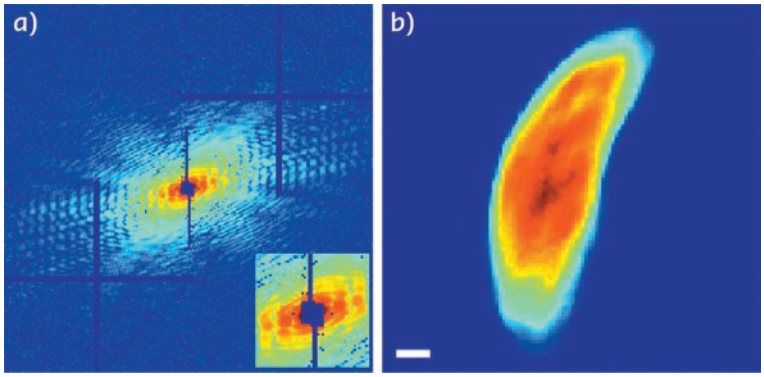

Fig. 79: A representative diffraction pattern taken at the 0° tilt angle (left panel) in which the horizontal and vertical bars are caused by the tiling of the 2 x 2 modules of the MAXIPIX detector. The inset shows an enlarged central part of the diffraction pattern (low spatial frequency region) where the missing data at the centre is due to a beam stop. A 2D projection (right panel) of the reconstructed 3D cell at the 0° tilt angle. Scale bar: 500 nm.

Cryogenic preservation techniques can safeguard a cell against irradiation, keeping it in a deeply frozen state during long-term exposure to X-rays. In a proof-of-principle experiment, we combined cryogenic techniques and 3D CDI at beamline **ID10** to reveal the architecture of a parasite known as *Neospora caninum*. *N. caninum* primarily infects dogs, but is closely related to *Plasmodium* and *Toxoplasma*, the causative agents of malaria and toxoplasmosis in humans. The distinctive shape of *N. caninum* and the organisation of its inner structures are important for infection of its hosts and are highlighted in the recovered structure (**Figure 80**).

This first experimental demonstration of cryo-CDI of frozen-hydrated cells using hard (8 keV) X-rays forecasts the routine and quantitative 3D imaging of whole cells with spatial resolutions in the tens of nanometres.

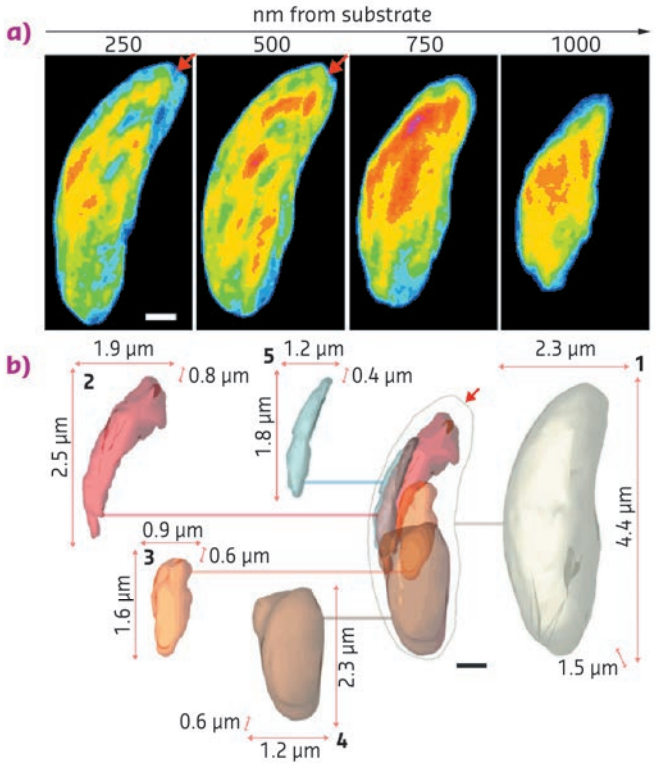

Fig. 80: A series of thin slices through the cell (top panel) at a distance ranging from 250 to 1000 nm away from the silicon nitride substrate, in which the red arrows indicate a conoid-like region. Images are false coloured according to normalised arbitrary density, lowest in blue, highest in red.
A deconstructed isosurface model (bottom panel) shows features of the *N. caninum* cell as 2D projections of 3D renderings. At the centre, the boundary of the cell is shown, as well as other important organelles in their appropriate locations within the cell. A line extends from each of these regions to their cutouts, which are numbered and bound by the three lengths of the box that circumscribes them: 1. Cell boundary, 2. Rhoptries, 3. Apicoplast, 4. Nucleus, 5. Mitochondrion.
Scale bars: 500 nm.

PRINCIPAL PUBLICATION AND AUTHORS

Three-dimensional coherent X-ray diffractive imaging of whole frozen-hydrated cells, J.A. Rodriguez (a), R. Xu (b), C.-C. Chen (c), Z. Huang (d), H. Jiang (e), A.L. Chen (f), K.S. Raines (g), A. Pryor Jr (b), D. Nam (h), L. Wiegart (i), C. Song (h), A. Madsen (j), Y. Chushkin (k), F. Zontone (k), P.J. Bradley (f) and J. Miao (b), *IUCrJ* **2**, 575–583 (2015); doi:10.1107/S205225251501235X.
(a) UCLA-DOE Institute for Genomics and Proteomics, University of California, Los Angeles (USA)
(b) Department of Physics and Astronomy and California NanoSystems Institute, University of California (USA)
(c) National Sun Yat-sen University, Kaohsiung (Taiwan)
(d) Carl ZEISS X-ray Microscopy Inc., Pleasanton (USA)
(e) Shandong University, Jinan (People's Republic of China)
(f) Department of Microbiology, Immunology, and Molecular Genetics, University of California, Los Angeles (USA)
(g) Department of Applied Physics, Stanford University (USA)
(h) Department of Physics, Pohang University of Science and Technology (South Korea)
(i) NSLS-II Photon Sciences Division, Brookhaven National Laboratory, Upton (USA)
(j) European X-ray Free Electron Laser, Hamburg (Germany)
(k) ESRF

REFERENCES

[1] J. Miao *et al.*, *Science* **348**, 530–535 (2015).
[2] J. Miao *et al.*, *Nature* **400**, 342–344 (1999).

INTERMITTENT AGEING DYNAMICS IN A METALLIC GLASS

Understanding how metallic glasses age on the atomic level is necessary in order to design more resilient and robust amorphous alloys. In this study, it was found that microscopic ageing occurs via a heterogeneous mechanism of intermittent atomic rearrangement and is not the steady, continuous process that has been observed in macroscopic studies.

Due to their amorphous glasslike structure, metallic glasses can exhibit remarkable and technologically-attractive properties such as a high strength and resistance to fracture. However, ageing can result in severe embrittlement and bring about profound changes to their fracture and fatigue properties. Therefore, the ability to understand and characterise the micromechanisms of ageing in metallic glasses will play a crucial role in ensuring their success in a broad range of applications. Using X-ray photon correlation spectroscopy (XPCS) at beamline **ID10**, we found evidence that ageing in a palladium-based metallic glass occurs in an intermittent and highly heterogeneous fashion on the atomic level.

Ageing in metallic glasses is usually investigated through the long-time equilibration of macroscopic quantities like volume and viscosity [1]. These studies show that structural relaxation occurs in a steady fashion and is described by an empirical stretched exponential function $\phi(t) \propto \exp[-(t/\tau)^{\beta}]$, where τ is the relaxation time and β is an exponent < 1, indicating that the relaxation proceeds more slowly than expected from a simple exponential decay. However, novel XPCS studies on metallic glasses have revealed the existence of an atomic dynamics described by compressed exponential relaxation functions ($\beta > 1$), which are characteristic of ballistic-type motions that arise from the presence of internal stresses stored into glassy (or jammed) states during structural arrest [2].

Our recent XPCS investigations shed even more light onto this unique phenomenon by showing that ageing on the atomic level does not occur in the steady and temporally homogeneous manner as revealed by macroscopic measurements. Figure 81 gives an exemplary illustration of this. The overall broadening trend of the XPCS intensity profile shows that the dynamics is slowing down significantly during annealing, as is expected from physical ageing. A remarkable feature, however, is the occurrence of rapid decorrelation events – characterised by a sudden narrowing of the intensity profile – which appear intermittently as the measurement progresses. We interpret these as signatures of the relief of atomic-level stresses, which act as important mediators in the ageing of metallic glasses.

We believe the origin of this unique behaviour to be rooted in the evolution of internal stresses, which are stored at the atomic level during vitrification and whose gradual release mediates

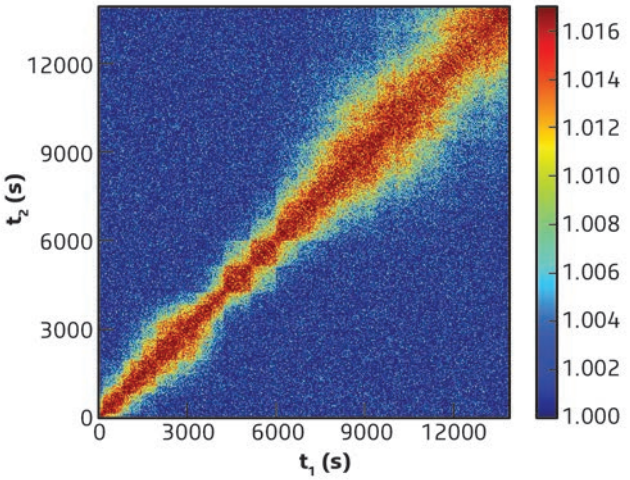

Fig. 81: Two-time correlation function of a palladium-based metallic glass measured during ageing at 538 K.

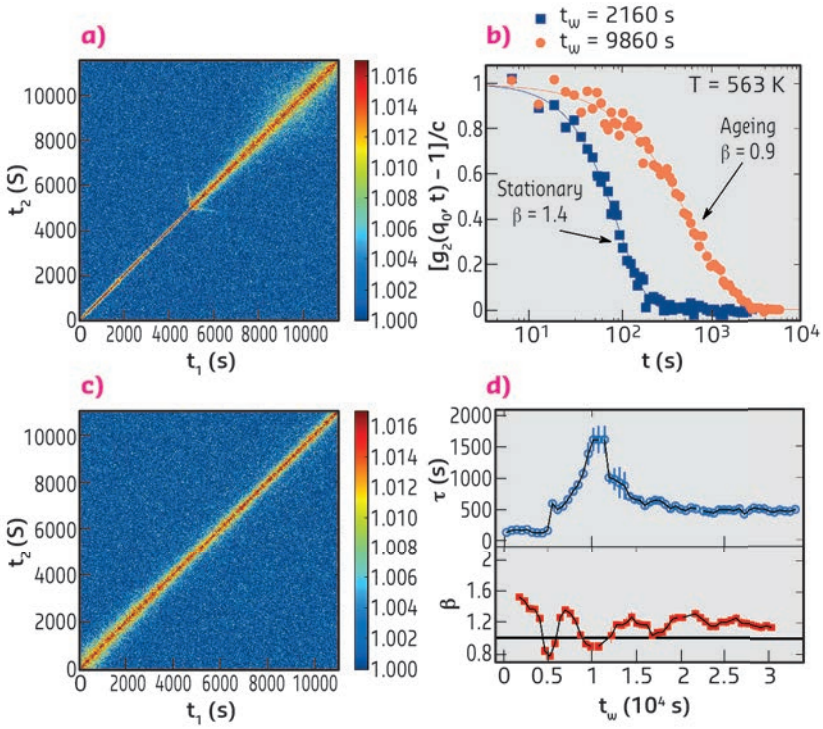

Fig. 82: (a) Two-time correlation function after heating the aged sample directly to 563 K. (b) Normalised one-time correlation functions calculated in the stationary and ageing regimes. (c) Two-time correlation function corresponding to the continuation of the measurement at 563 K. (d) Evolution of τ and β over the entire length of the measurement at 563 K.

physical ageing in metallic glasses. Structurally, this can be thought to correspond to localised micro-collapses of groups of particles, which trigger subsequent collapses in neighbouring regions through the formation of stress dipoles. In **Figure 82** we quickly heated the partially aged metallic glass to a higher temperature, thereby observing the effect of the previous ageing on the microscopic dynamics. We notice here a long regime of fast, stationary dynamics, which is interrupted by a sudden, then gradual broadening of the intensity profile (**Figure 82a**). The change in β between these two regimes from 1.4 to 0.9 (**Figure 82b**) signals the transition from compressed to stretched exponential relaxation, suggesting a cross-over from ballistic to diffusive, liquid-like atomic motion as the glasses ages. However, complete relaxation back into the equilibrium liquid is – at least in the microscopic sense – astonishingly difficult. This is evidenced by the gradual return of β to values greater than 1, indicating that the system is still stuck in the non-equilibrium state (**Figures 82 c-d**).

The intermittent dynamics reported here for the first time in a structural glass is indicative of a complex energy landscape, characterised by numerous minima, in which the system dwells for long periods of time in stable configurations. This is further confirmation that macroscopic and microscopic ageing in metallic glasses clearly obey different laws. Moreover, the observation of a similar intermittent dynamics over a range of physical processes such as crystallisation, deformation and shear flow suggests a universal underpinning.

PRINCIPAL PUBLICATION AND AUTHORS

X-ray photon correlation spectroscopy reveals intermittent aging dynamics in a metallic glass, Z. Evenson (a,b), B. Ruta (c), S. Hechler (d), M. Stolpe (d), E. Pineda (e), I. Gallino (d) and R. Busch (d), *Phys. Rev. Lett.* **115**, 175701 (2015); doi: 10.1103/PhysRevLett.115.175701.

(a) Heinz Maier-Leibnitz Zentrum (MLZ) and Physik Department, Technische Universität München (Germany)
(b) Institute of Materials Physics in Space, German Aerospace Center (DLR), Cologne (Germany)
(c) ESRF
(d) Department of Materials Science and Engineering, Saarland University, Saarbrücken (Germany)
(e) Department of Physics, Universitat Politècnica de Catalunya-BarcelonaTech, Castelldefels (Spain)

REFERENCES

[1] Z. Evenson and R. Busch, *Acta Mater.* **59**, 4404 (2011).
[2] B. Ruta *et al.*, *Phys. Rev. Lett.* **109**, 165701 (2012).

WATCHING QUANTUM DOTS GROW IN REAL TIME

Time-resolved SAXS/WAXS at beamline ID02 was used to unravel the steps of nanoparticle nucleation and growth from molecular precursors in an *in situ* experiment.

Discovered in the early eighties, quantum dots are nanoparticles composed of a crystalline core surrounded by a layer of ligands (**Figure 83a**) [1-4]. Their core is made of a semi-conducting material whose band-gap varies with the size of the particle due to a confinement effect. In the case of CdSe, these particles are fluorescent in the visible range and emit a bright, intense light when illuminated by UV radiation (**Figure 83b**). The wavelength at which the quantum dots emit only depends on their size: from 1 nm for a blue emitting particle to 5 nm for red (**Figure 83b**). These outstanding optical properties can be exploited in diverse applications such as light-emitting devices, biological imaging or displays. Interestingly, TVs containing quantum dots exhibit superior colour quality to existing technologies and will soon hit the market.

Making these nanoparticles requires mixing and heating inorganic precursors with surfactants in an organic solvent. Though a lot of these recipes are now available in the literature, optimising existing synthesis or discovering new nanoparticles with desired shape or composition is a lengthy process demanding tedious variation of the experimental parameters. Our mechanistic understanding of nanocrystal formation is still in its infancy and only recently efforts have been put towards this. Similar to other fields of synthetic chemistry, deeper mechanistic insight will accelerate the discovery of new products and enable larger-scale syntheses. From a fundamental standpoint, various models have been proposed for the nucleation and growth of nanocrystals but experimental evidence lags behind.

Acquiring experimental data during the formation of the particles is a difficult experimental challenge since it requires the structure of the solution to be probed on small time (below the second) and length scales (nanometre). Here, we used time-resolved small and wide angle X-ray scattering at beamline **ID02** to probe the formation of quantum dots in real time. We chose

a synthesis of quantum dots where the precursors are mixed at ambient temperatures and heated to 240°C [5]. We mounted a precursor filled capillary on a heating stage and heated it while acquiring SAXS and WAXS patterns (**Figure 83c** and **d**) during the course of the reaction. Before the onset of nanoparticle formation, we found that the inorganic precursors self-organised into a lamellar phase which melts at 100°C. We detected the appearance of the first nanoparticles at 173°C. The SAXS signal was fitted to a model of polydisperse spheres using a Monte-Carlo algorithm [6]. From these fits, we extracted the mean radius and polydispersity as well as the nanocrystal concentration (**Figure 84a** and **b**). This analysis reveals that the formation mechanism can be decomposed into two stages: a nucleation phase during which new particles appear that is followed by a growth phase during which the nanocrystal concentration is almost constant while the mean radius increases. We compared our experimental data to classical theoretical models (diffusion or reaction limited growth) and proved that growth was in fact limited by the supply of soluble selenium (**Figure 84c**).

To address the crystalline structure of the nanocrystals during their formation, WAXS patterns were also acquired. The (220) peak of the zinc blende structure was fitted to a gaussian line shape. Surprisingly, the position of the peak shifted towards smaller q values with time indicating an expansion of the crystal lattice as the nanoparticle grow. The physical basis of the phenomenon is not clear yet and its comprehension requires further studies.

These results demonstrated the feasibility of studying quantum dot formation *in situ* at high temperatures. Future work will address the effect of the variation of the different experimental parameters and anisotropic growth of nanoparticles such as 2D nanoplatelets.

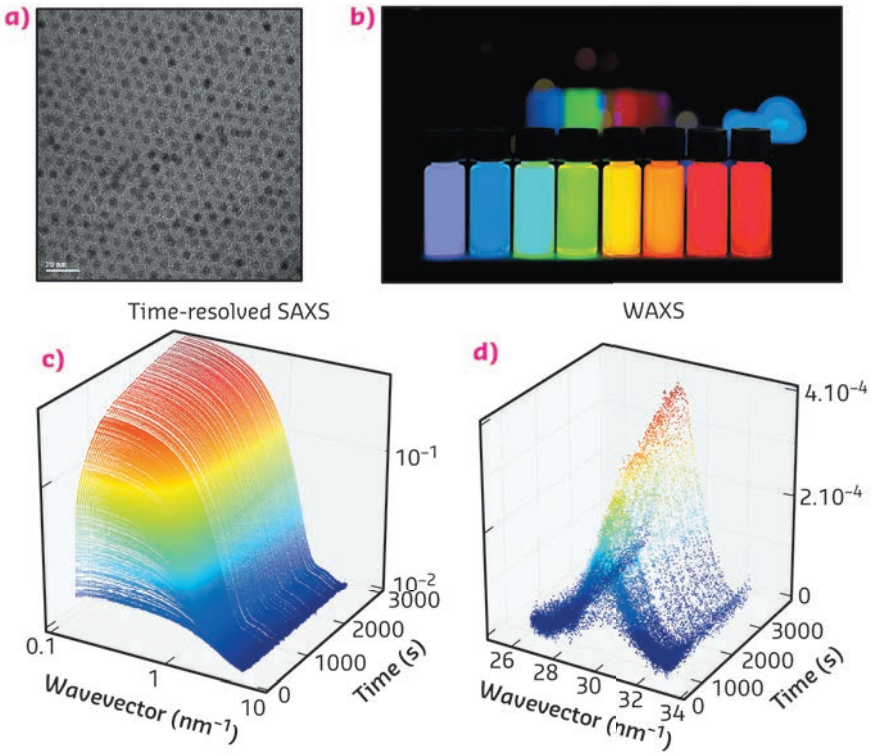

Fig. 83: (a) Electron microscopy image of CdSe quantum dots. (b) Vials containing a dispersions of quantum dots under UV illumination. From left to right, the size of the quantum dots increases from 1 to 5 nm. (c) and (d) Sequence of time-resolved SAXS and WAXS diagrams obtained *in situ* during the formation of quantum dots.

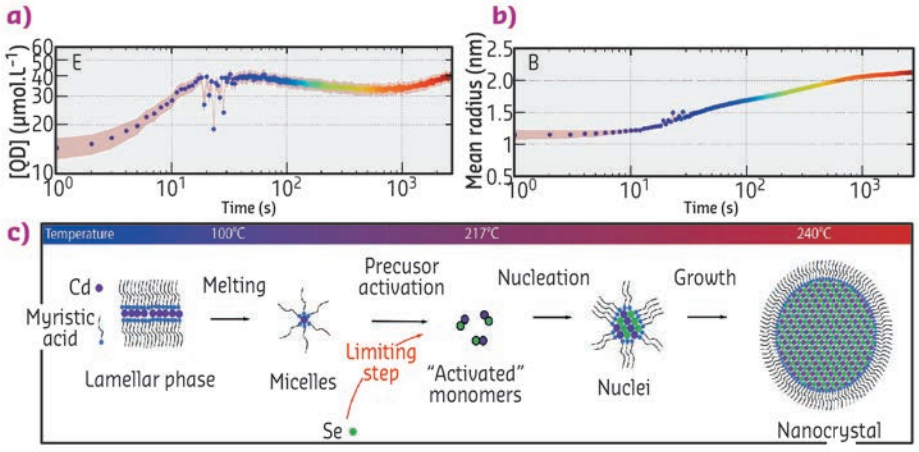

Fig. 84: (a) and (b) Concentration of nanoparticles and mean radius obtained from the Monte-Carlo fitting of the SAXS patterns. (c) Scheme describing the formation mechanism of the quantum dots.

PRINCIPAL PUBLICATION AND AUTHORS

Real-time *in situ* probing of high-temperature quantum dots solution synthesis, B. Abécassis (a), C. Bouet (b), C. Garnero (a), D. Constantin (a), N. Lequeux (b), S. Ithurria (b), B. Dubertret (b), B.R. Pauw (c) and D. Pontoni (d), *Nano Lett.* **15**, 2620–2626 (2015); doi: 10.1021/acs.nanolett.5b00199.

(a) Laboratoire de Physique des Solides, Univ. Paris-Sud, CNRS, UMR 8502, Orsay (France)
(b) LPEM, ESPCI-ParisTech, PSL Research University, CNRS UMR 8213, Sorbonne Universités, UPMC Paris 06, Paris (France)
(c) National Institute for Materials Science (NIMS), Tsukuba (Japan)
(d) ESRF

REFERENCES

[1] L.E. Brus, *J. Chem. Phys.* **80**, 4403 (1984).
[2] A.I. Ekimov *et al.*, *Solid State Commun.* **56**, 921 (1985).
[3] A.P. Alivisatos, *Science* **271**, 933 (1996).
[4] Y. Yin, A.P. Alivisatos, *Nature* **437**, 664 (2005).
[5] Y. Yang *et al.*, *Angew. Chem. Int. Ed.* **44**, 6712 (2005).
[6] B.R. Pauw *et al.*, *J. Appl. Crystallogr.* **46**, 365 (2013).

TWO-STEP NUCLEATION IN PROTEIN CRYSTALLISATION REVEALED BY REAL-TIME SAXS

How critical nuclei gain the density and structure from a supersaturated state is still a mystery. By following the kinetics of protein crystallisation using real-time SAXS, it is demonstrated here that nucleation can follow a step-by-step mechanism, *i.e.* proteins first form disordered aggregates, and then the structure develops inside.

According to the classical nucleation theory, nucleation starts as solute molecules reversibly aggregate in supersaturated solutions and form nuclei with the exact density and structure of the crystals in the final stage. While classical nucleation theory provides a successful description in many systems, studies on the crystallisation of proteins and colloids as well as on biomineralisation have shown features beyond the classical view. A two-step nucleation mechanism has been proposed by ten Wolde and Frenkel [1], where the two order parameters (density and structure) develop sequentially instead of simultaneously, i.e. a metastable intermediate phase (MIP) forms first from the supersaturated solution, and nucleation occurs afterwards inside the MIP (**Figure 85a**). Despite the existing theoretical concepts, clear experimental evidence and suitable methods to study the early stage of nucleation are rather rare - in particular, when aiming for an ensemble average of the rare-event nucleation process of a real system.

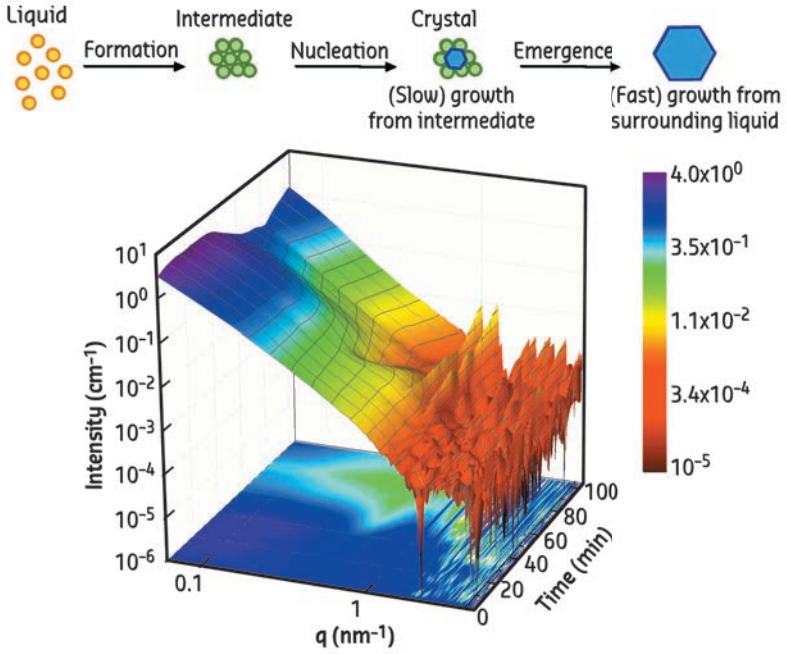

Fig. 85: (a) Schematic of the two-step nucleation mechanism. (b) 3D surface illustration of typical real-time SAXS data.

In our work, we studied the crystallisation of β-lactoglobulin (BLG) in solutions in the presence of the divalent salt cadmium chloride ($CdCl_2$). This system has a pseudo-reentrant condensation phase behaviour [2,3]. Interestingly, near the second transition zone, protein aggregates form before crystallisation and are consumed later by crystal growth. Such a system provides ideal conditions for identification of the pathway of crystal nucleation.

Benefiting from its high resolution in time and space, real-time small-angle X-ray scattering (SAXS) was employed to follow the early stage of crystallisation. SAXS measurements were performed at beamline **ID02**. A typical real-time SAXS profile from a sample with 20 mg/ml BLG and 15 mM $CdCl_2$ is shown in **Figure 85b**. The first curve (t = 0) already indicates the formation of protein aggregates. With increasing time, a broad peak at intermediate q-values appears. This peak increases in intensity until Bragg peaks start to appear, with the two most pronounced peaks located at 1.01 and 1.27 nm^{-1} overlapping with the broad maximum. The Bragg peaks increase in intensity with time, whereas the broad peak shrinks, and eventually disappears. To quantify the relationship between the aggregates and crystals, we evaluated the area under the broad peak and under the two main

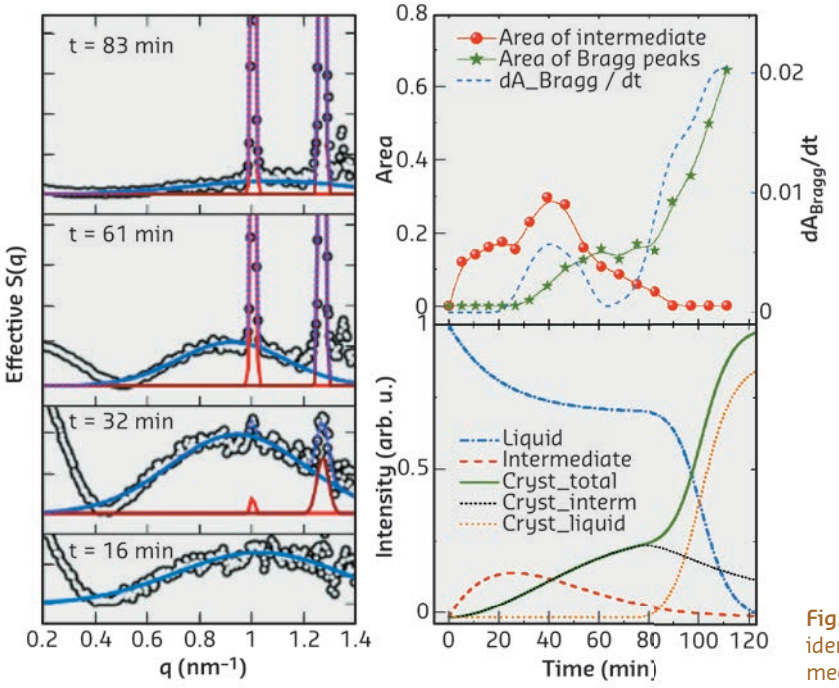

Fig. 86: Analysis of real-time SAXS data and identification of the two-step nucleation mechanism.

Bragg peaks. The overall crystallisation kinetics can be described by plotting these parameters as a function of time (Figure 86). The amount of MIP and crystalline phases are labeled in red and green, respectively. The blue curve is the first derivative of the green curve, representing the crystallisation rate. First, the maximum in the green curve coincides with a local maximum in the crystallisation rate, indicating that the crystallisation rate is proportional to the amount of MIP. Second, when the MIP is nearly consumed (~ 80 min), the fraction of the crystalline phase reaches a plateau value. After that, it increases again, even more rapidly.

From the crystallisation kinetics obtained from time-resolved SAXS, we can identify the kinetic signature of a two-step nucleation process in the early stage of protein crystallisation. The first regime of the kinetics is dominated by a two-step nucleation and growth within the MIP, *i.e.* protein aggregates are formed as a MIP, followed by the nucleation of crystals within the MIP. During this period, the number of crystals increases with time, but the growth rate is slow due to the low mobility in the surrounding aggregates. The second regime of the kinetics is dominated by the growth in the dilute phase: the consumption of the MIP leads to the exposure of the crystals to the free molecules in the dilute phase, which accelerates the crystal growth. This real-time study not only provides evidence for a two-step nucleation process for protein crystallisation, but also elucidates the role and the structural signature of the metastable intermediate phase in this process.

PRINCIPAL PUBLICATION AND AUTHORS

Real-time observation of nonclassical protein crystallization kinetics, A. Sauter (a), F. Roosen-Runge (b), F. Zhang (a), G. Lotze (c), R.M.J. Jacobs (d) and F. Schreiber (a). *J. Am. Chem. Soc.* **137**, 1485-1491 (2015); doi: 10.1021/ja510533x.
(a) Institut für Angewandte Physik, Universität Tübingen (Germany)
(b) ILL, Grenoble (France)
(c) ESRF
(d) Department of Chemistry, CRL, University of Oxford (UK)

REFERENCES

[1] P.R. ten Wolde and D. Frenkel, *Science* **277**, 1975-1978 (1997).
[2] F. Zhang *et al.*, *Phys. Rev. Lett.* **101**, 148101 (2008).
[3] A. Sauter *et al.*, *Faraday Discuss.* **179**, 41-58 (2015).

SMALL ANGLE X-RAY DIFFRACTION REVEALS MUSCLE'S GEARBOX

Skeletal muscles are the motors of the human body, they allow us to walk, run and breathe. Sometimes they need to lift heavy weights and at other times to make very fast movements against a lighter load. A man-made motor would typically use a gearbox to match its output to the load. Here, experiments show how muscles do the same.

Contraction of skeletal muscles is driven by the relative sliding motion of two sets of filaments, thick filaments, mainly composed of the motor protein myosin, and thin filaments, containing the track protein actin (Figure 87a). Each myosin molecule has a long tail and two heads (only one is shown in the figure for simplicity), which are sometimes called motor domains because they can change shape when bound to actin (Figure 87c), driving the motion of the thin filaments. This shape change is coupled to the splitting of an ATP molecule, providing the energy for contraction. Contraction of an individual muscle cell is switched on by an electrical signal in its motor nerve, which triggers the release of calcium ions in the muscle cell; these calcium ions bind to thin filament regulatory proteins (hexagons in Figure 87a, c), causing a structural change in the thin filaments that allows the myosin motors to bind to them.

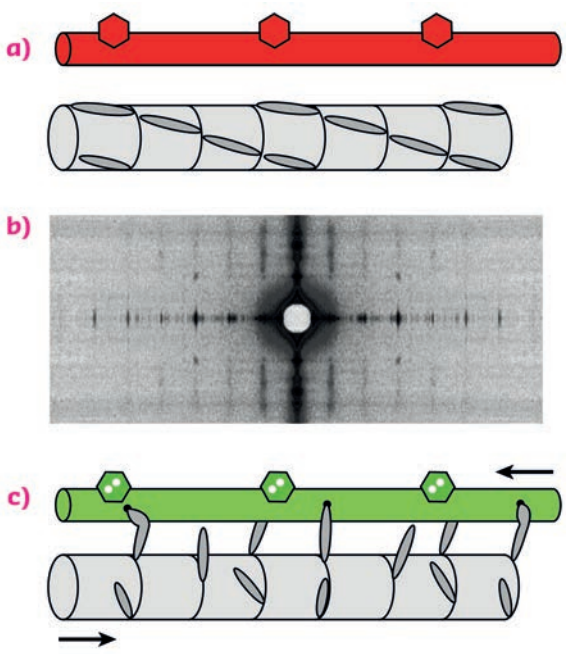

Fig. 87: Arrangement of the thick and thin filaments in skeletal muscle and conventional model of thin-filament regulation. (a) resting muscle; (c) active contraction, triggered by calcium ions binding to thin filament regulatory proteins (hexagons). Red (green) denotes the OFF (ON) state of the thin filament. (b) X-ray diffraction pattern from a resting muscle fibre.

In this textbook view of the regulation of muscle contraction, muscle is regulated by the track – the thin filament – rather than through the myosin motors themselves. This left a puzzle since the myosin motors in resting muscle lie in a helical array on the surface of the thick filament (**Figure 87a**), and it was not known how they sense the structure of the thin filament. Moreover, although it was clear that calcium ions are the trigger for contraction, it was not known how the response of the myosin motors is coupled to the load, *i.e.* how the gearbox works.

Experiments at beamline **ID02** have now provided answers to these longstanding questions. X-ray diffraction patterns were recorded from single muscle cells (**Figure 87b**) while they were stimulated electrically under conditions whereby the length and load on the muscle cell could be controlled precisely. The very high brilliance and collimation of the X-ray beam combined with the high sensitivity and resolution of the 2D X-ray detectors overcame the major technical challenge of these experiments: to record X-ray signals from a single muscle cell on the millisecond timescale with very high spatial resolution.

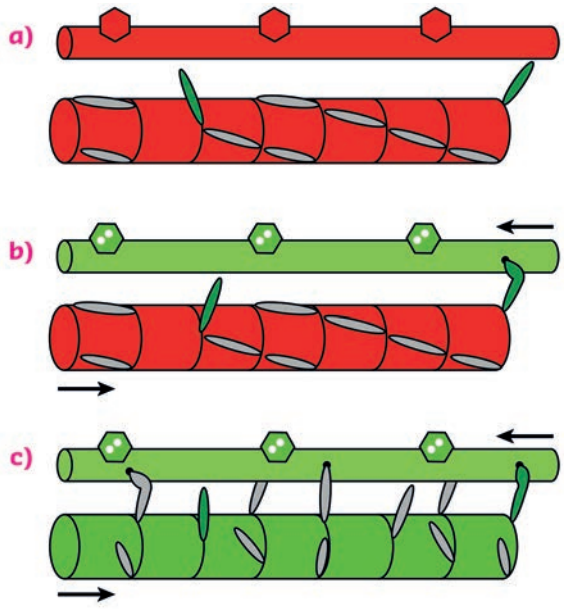

Fig. 88: The dual filament model of muscle regulation. (a) resting muscle; (b) and (c), calcium-activation at low and high load respectively. At high load (c), force generated by constitutively ON motors (green) switches the thick filament to a slightly longer axial periodicity, releasing the remaining motors.

The results showed that, when the load on the muscle cell is kept low in the first few milliseconds after calcium activation, nearly all the myosin motors stay parked in the helical array on the surface of the thick filaments (**Figure 88a, b**). Only a few percent of the myosin motors are required to drive muscle shortening at high velocity after calcium ions have activated the actin filament. These constitutively active "switched ON" motors escape the helical packing (**Figure 88a**). However when the load is high, these motors generate a stress in the backbone of the thick filament which triggers a change in the packing of the myosin tails to one with a slightly longer periodicity along the filament axis (**Figure 88c**). This filament extension releases the remaining myosin motors from their helical parked state, making them available for actin binding and force generation against the high load. This intrinsic mechanical switch in the thick filament is the gearbox of muscle, enabling it to mobilise only a few myosin molecules when the external load is low at very low metabolic cost, and then switching on many more motors when they are needed to work against a high load.

These results lead to a novel dual-filament concept of the regulation of contraction in skeletal muscle. In addition to the well-established structural change in the thin filaments controlled by calcium, a mechano-sensitive structural switch in the thick filament links muscle performance to its external load. This new paradigm of muscle regulation should help to guide therapeutic strategies to counter muscle weakness. Since the thick and thin filaments in heart muscle are very similar to those in skeletal muscle, dual-filament regulation may also control the heartbeat.

PRINCIPAL PUBLICATION AND AUTHORS

Force generation by skeletal muscle is controlled by mechano-sensing in myosin filaments, M. Linari (a), E. Brunello (b), M. Reconditi (a), L. Fusi (b), M. Caremani (a), T. Narayanan (c), G. Piazzesi (a), V. Lombardi (a), M. Irving (b), *Nature* **528**, 276-279 (2015); doi:10.1038/nature15727.

(a) Università di Firenze, Firenze (Italy)
(b) King's College London, London (UK)
(c) ESRF

NONLINEAR MIXING OF LATTICE VIBRATIONS

The first example of nonlinear phonon wave mixing at the nanoscale was demonstrated by generating the second harmonic of an excited phonon. This experiment opens up a new field which we call "nonlinear phononics" in analogy to nonlinear optics where a kaleidoscope of interesting optical effects is the fundament of today's laser physics.

Phonons are quasiparticles of lattice vibrations with certain energy and momentum. In physics textbooks, they are introduced for a periodic structure of atoms connected by harmonic springs. The eigenmodes of the vibrations in harmonic crystals are those lattice motions

that are uncoupled. Any quantum of energy in such phonon modes would remain in this mode forever and makes the entire crystal oscillate at the corresponding eigenfrequency. To explain the phenomena of a finite heat transport of dielectric materials and the thermal expansion of crystals, the springs have to be anharmonic. This leads to the coupling of modes and therefore the respective phonons can be interconverted if the respective quasiparticle properties of energy and momentum are conserved.

For future materials and devices it would be of high interest to understand and manipulate the coupling of phonons with frequencies in the GHz to THz range in complex materials. This is important for nanoscale heat transport, thermoelectric materials and phonon computing.

In this work we present a scheme to excite high-amplitude, nanometric and narrowband phonon wave packets with a certain energy and momentum. The use of time-resolved X-ray diffraction at beamline **ID09B** enabled us to measure the occupation of the phonon modes composing these wave packets transiently. As the phonon coupling changes the occupation of the modes, the coupling between specific phonon modes can be measured.

As a first example of "nonlinear phononics", we present the second harmonic generation of phonons with a wavelength in the nanometre range. This is analogous to nonlinear optics where photons interact with each other in a nonlinear crystal. We excited a narrowband phonon wave packet by shining a train of four ultrashort laser pulses with a temporal displacement τ on an epitaxially-grown nanometric $SrRuO_3$ metal film on top of a $SrTiO_3$ substrate, as shown in **Figure 89a**. The metal film's temperature rose rapidly due to the absorption of the laser pulses. The quasi-instantaneous occupation of phonons leads to an expansive force on the crystal via the anharmonicities. This expansion triggers a hyper-sound wave entering the substrate [1]. Using four pulses, the metal film should oscillate with the frequency $1/\tau$ and generate a phonon wave packet with this frequency propagating through the substrate.

We used X-ray diffraction to observe the transient spectral content of the excited phonon wave packet. X-rays scatter from crystal lattice planes described by their corresponding reciprocal lattice vector G and phonons given by their wave vector Q, as depicted in **Figure 89b** [2]. Here, an incident X-ray pulse was diffracted by the lattice planes of the $SrTiO_3$ substrate resulting

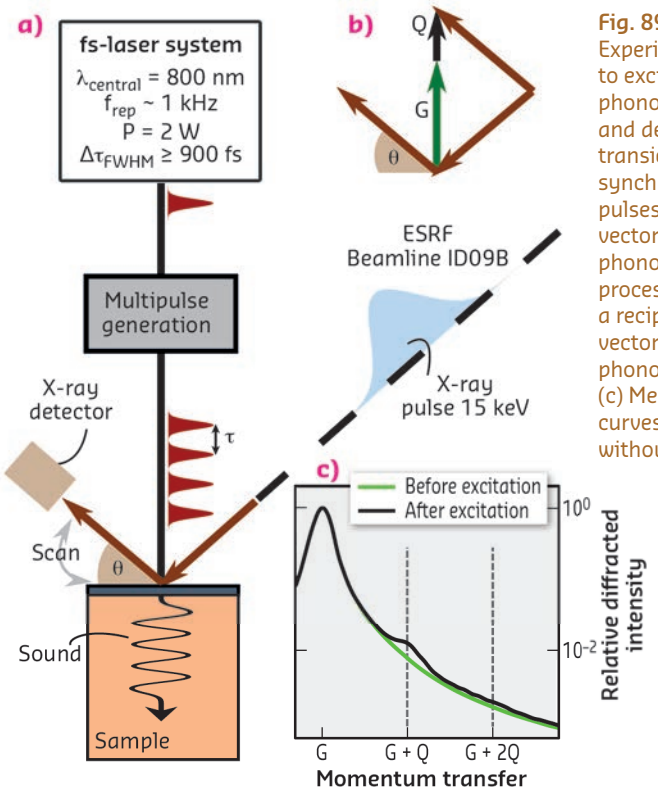

Fig. 89: (a) Experimental setup to excite narrowband phonon wave packets and detect them transiently with synchrotron X-ray pulses. (b) Wave vector diagram of a phonon scattering process, where G is a reciprocal lattice vector and Q the phonon wave vector. (c) Measured rocking curves with and without excitation.

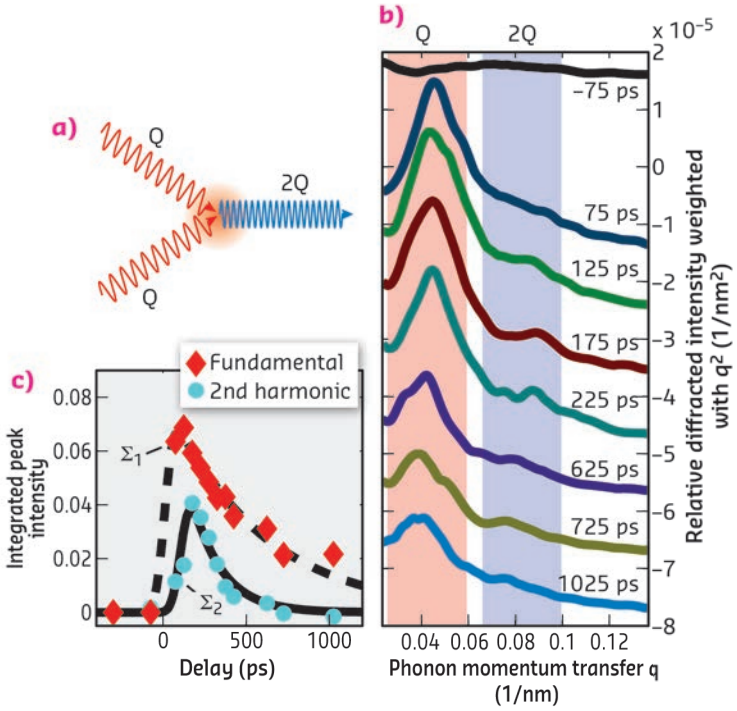

Fig. 90: Second harmonic generation of monochromatic phonon wave packets. (a) The scattering process of two phonons with wavevector Q generate a phonon with the doubled wavevector 2Q. (b) Scattering intensity weighted with q^2 of the excited fundamental (red) and its second harmonic (blue). (c) The transient change in the integrated scattering intensity of the fundamental and its second harmonic.

in the peak at G in **Figure 89c** before and after excitation with the laser pulses. After excitation, additional diffraction at G+Q was detected, which is evidence that a narrowband phonon wave packet with wave vector Q was excited.

To demonstrate second harmonic generation of monochromatic phonon wave packets, as depicted in Figure 90a, we repeated the time-resolved X-ray diffraction experiment with a slightly thicker metal film that absorbs more optical energy and used only two laser pulses while keeping the total incident laser energy constant. This doubles the local atomic displacement and quadruples the acoustic energy density of the wave packet. This increased the up-conversion efficiency of phonons at the expense of monochromaticity according to the higher wave packet localisation in space. Figure 90b shows the diffracted intensity weighted with q^2 for better visibility of peaks at high q. The red shaded region is the diffraction related to the excited wave vector Q and the blue region highlights diffraction assigned to the second harmonic with the wave vector 2Q. It can be seen that the second harmonic 2Q starts rising 125 ps after excitation of Q. This delay is evidence that the second harmonic is not directly excited by the laser pulses, rather it is generated by anharmonic coupling within the phonon wave packet. Figure 90c shows the transient change of the integrated intensity of the peaks corresponding to the wave vectors Q (Σ_1) and 2Q (Σ_2). In addition to the delay between both maxima, one can easily see that the second harmonic damps out more rapidly than the phonons with wave vector Q, which is in accordance with known phonon damping theory.

PRINCIPAL PUBLICATION AND AUTHORS

Second harmonic generation of nanoscale phonon wave packets, A. Bojahr (a), M. Gohlke (a), W. Leitenberger (a), J. Pudell (a), M. Reinhardt (b), A. von Reppert (a), M. Roessle (a), M. Sander (a), P. Gaal (b) and M. Bargheer (a,b) *PRL* **115**, 195502 (2015); doi: 10.1103/PhysRevLett.115.195502.

(a) Institut für Physik und Astronomie, Universität Potsdam (Germany)
(b) Helmholtz Zentrum Berlin (Germany)

REFERENCES

[1] D. Schick *et al.*, *Struct. Dyn.* **1**, 064501 (2014).
[2] A. Bojahr *et al.*, *Opt. Express* **21**, 21188 (2013).

IMAGING THE MICROVASCULAR NETWORK AND THE NEURONAL SYSTEM IN A MOUSE SPINAL CORD

The repair capacity of an injured spinal cord relies on the interplay between the vascular network and the neuronal system. Our knowledge of how these two intricate systems overlap at the submicrometric level has been limited by the imaging tools available. Simultaneous imaging of both the vascular and neuronal architecture of the mouse spinal cord in 3D at scales spanning from millimetres to hundreds of nanometres using X-ray phase-contrast tomography has provided new insight into the neuro-vascular coupling. These results are expected to have a major impact on the investigation of neurodegenerative diseases.

Trauma and disease in spinal cord blood vessels and neurons lead to a wide range of neurodegenerative conditions. However, current imaging tools do not generate sufficient resolution and contrast to investigate these conditions or to understand the relationship between the vascular and neuronal systems [1]. Using a phase contrast imaging technique at beamline **ID17**, we have been able to visualise the complete architecture of both the vascular network and the neuronal system of the mouse spinal cord, imaging single elements of the networks such as microcapillaries and micrometric nerve fibres, axon-bundles and neuron soma. This imaging was carried out without sectioning or other destructive sample preparation procedures.

The combination of high spatial resolution (0.6 micrometre pixel size) with a large field of view for the tomographic images (1.2 mm in thickness) allows access to information on the large-scale architecture of the vascular network down to the level of the microcapillary organisation (Figure 91). This image also displays the long range connectivity of the neuronal system together with details down to the scale of a single neuron soma. We achieved a striking contrast between the white and the grey matter. Single neuron cells and nerve fibres are easily distinguishable at the white/grey matter interface in the anterior horn of the spinal cord. This spinal cord region is highly enriched with somatic motoneurons with a characteristic stellate morphology (Figure 91).

The single nerve fibre (Figure 91a, b, c) is imaged at the interface with the grey matter, while a longitudinal projection of the sample (about half a millimetre in length) at the same

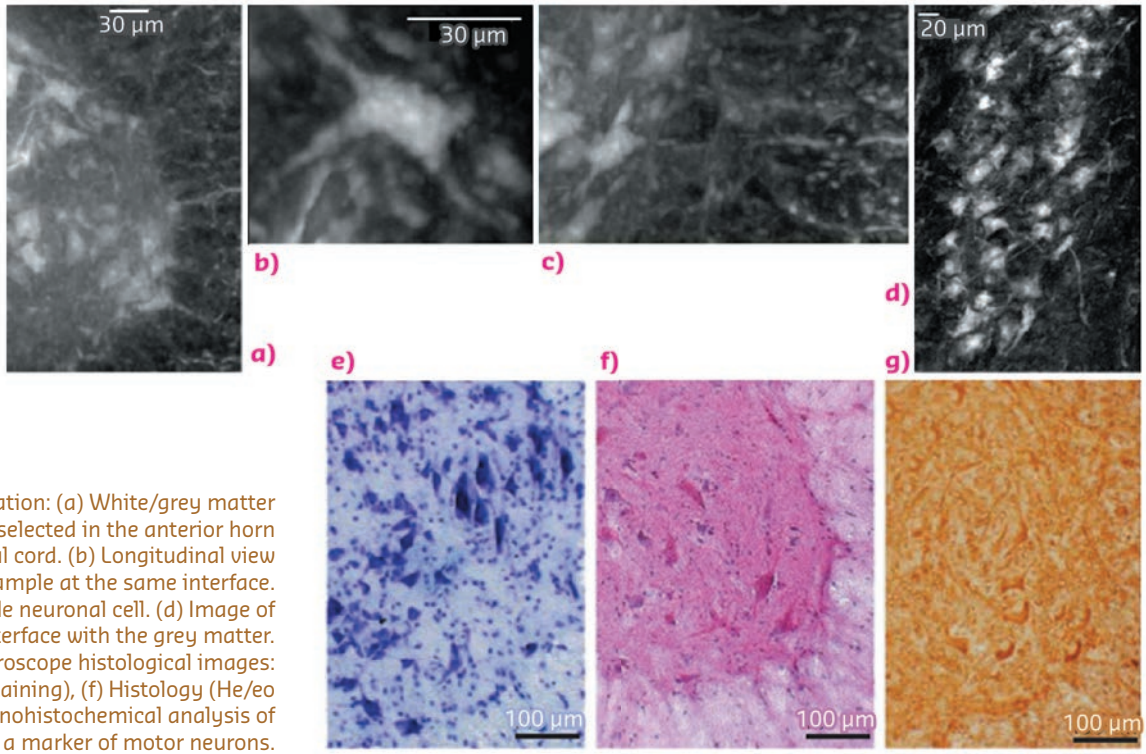

Fig. 91: Neural population: (a) White/grey matter interface of a thick slab selected in the anterior horn of the lumbar-sacral spinal cord. (b) Longitudinal view (length: 0.5 mm) of the sample at the same interface. (c) Magnification of a single neuronal cell. (d) Image of one nerve fibre at the interface with the grey matter. For comparison, microscope histological images: (e) Histology (Nissl staining), (f) Histology (He/eo staining) and (g) Immunohistochemical analysis of SMI-32, a marker of motor neurons.

interface shows the connections between the cells, compatible with the dendrite branches (**Figure 91d**). Histological sections are shown for comparison in **Figure 91e, f, g**.

A twin sample was prepared with Microfil®, a contrast agent able to enhance the contrast of the microvasculature. The architecture of the vascular network was processed and is shown in **Figure 92**. The spatial distribution of the vascular network confirms that there is a small peripheral and large central vascular supply that is characteristic of the lumbar-sacral region.

Thus, our approach shows the potential of synchrotron X-ray phase contrast microtomography for pre-clinical investigations of the vascular system and degenerative pathologies of the central nervous system.

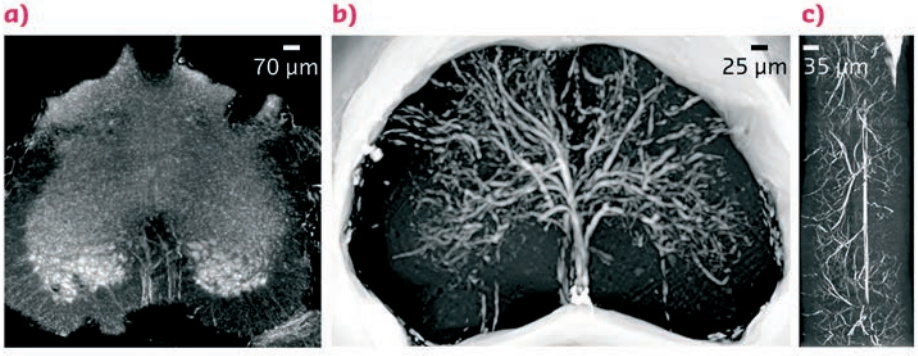

Fig. 92: (a) X-ray phase contrast microtomography of the lumbar-sacral region of the spinal cord (size: 1.2 mm), (b) Reconstructed volume of the lumbar-sacral region after administration of the Microfil contrast agent. The image was obtained with a pixel size of 3.5 µm. (c) Longitudinal view of (b), 1 mm long.

PRINCIPAL PUBLICATION AND AUTHORS

M. Fratini (a,b), I. Bukreeva (c), G. Campi (d), F. Brun (e,f), G. Tromba (f), P. Modregger (g), D. Bucci (h), G. Battaglia (h), R. Spanò (i), M. Mastrogiacomo (i), H. Requardt (j), F. Giove (a,k), A. Bravin (j) and A. Cedola (c), Simultaneous submicrometric 3D imaging of the micro-vascular network and the neuronal system in a mouse spinal cord, *Scientific Reports* **5**, 8514 (2015); doi:10.1038/srep08514.
(a) "Enrico Fermi" Centre MARBILab c/o Fondazione Santa Lucia, Rome (Italy)
(b) Department of Science, Roma Tre University (Italy)
(c) Institute for Physical and Chemical Process-CNR c/o Physics Department at Sapienza University, Rome (Italy)
(d) Institute of Crystallography-CNR, Monterotondo, Rome (Italy)
(e) Department of Engineering and Architecture, University of Trieste (Italy)
(f) Elettra – Sincrotrone Trieste (Italy)
(g) Swiss Light Source, Paul Scherrer Institut, Villigen, and Centre d'Imagerie BioMedicale, Ecole Polytechnique Federale de Lausanne (Switzerland)
(h) I.R.C.C.S. Neuromed, Pozzilli (Italy)
(i) Department of Experimental Medicine, University of Genova and AUO San Martino - IST Istituto Nazionale per la Ricerca sul Cancro, Genova (Italy)
(j) ESRF
(k) Department of Physics, Sapienza University, Rome (Italy)

REFERENCES

[1] M. Fratini *et al.*, *Journal of Tissue Engineering and Regenerative Medicine* **8**, 192 (2014).

DIFFERENCES IN GENE EXPRESSION AFTER MICROBEAM RADIATION THERAPY

The efficiency of microbeam radiation therapy (MRT) to improve the survival of tumour bearing rats is already well documented. A description of early molecular events after MRT could complete our understanding of the biology of this particular irradiation. By the use of microarray gene technology, we have previously documented the whole transcriptomic response of normal and tumour brain tissues to MRT and more recently identified genes or molecular pathways potentially involved in MRT efficiency or tumour resistance to this treatment.

Microbeam radiation therapy is a novel kind of radiation therapy which uses arrays of quasi-parallel low-energy photons. Beamline **ID17** provides photons with an energy range of 40 - 350 keV, a very high photon flux and a low divergence that fulfills the requirements of collinearity and dose rate for MRT necessary to produce plane parallel spatially-fractionated microbeams. Preclinical research in small animal models has shown tumour control by MRT, while offering an excellent level of normal tissue sparing.

The preferential controlling effects observed for tumour vessels may not entirely explain the efficiency of MRT and other biological mechanisms may be involved in tumour control. On a well characterised model (9L gliosarcoma) [1], the early whole transcriptomic responses of normal and tumoural tissues 6h after unidirectional MRT (400 Gy, 50 µm-wide microbeams, 200 µm spacing) (**Figure 93**) and the associated biofunctions and pathways have already been described [2]. This provided a data base with the expression of 28,000 transcripts which has allowed the identification of transcripts involved in both tumour and normal brain responses to MRT [1].

The specific response of tumour tissues to MRT consisted of the significant transcriptomic modulation of 316 transcripts (431 probsets) which are mainly related to the regulation of cell cycle and the immune/inflammatory response. Of these, 30 were not detected in normal brain tissues, neither before nor after MRT and could be divided into 3 groups of relevant targets. These targets were monitored over several days and weeks after irradiation and their modulation was studied. In summary (i) Polo-like kinase 1 (Plk1), known to be necessary for efficient cell division and proposed as potential therapeutic targets in human tumours, showed decreased expression a fews hours and a fews days after MRT (**Figure 94a**). A cluster of 20 genes (including Ccnb1, Cdc20 and Pttg1) presented the same kinetic of expression and may partially explain the control of tumour growth by MRT through the deregulation of cell division - they could be amplified to continue the tumour growth inhibition; (ii) in tumours, the expression of the 7 transcripts of *Clec group,* related to immune cells, was inhibited 6 h after MRT but increased significantly 2, 8 and 15 days after MRT (**Figure 94b**). Clecsf6 is known to be expressed at the surface of monocytes, macrophages and dendritic. The kinetic of transcriptomic expression of this group coincides temporally with the presence of leukocytes in tumour tissues, a fact that may indicate a progressive recruitment of immune cells in the tumour after MRT. (iii) Areg (encoding for amphiregulin) is

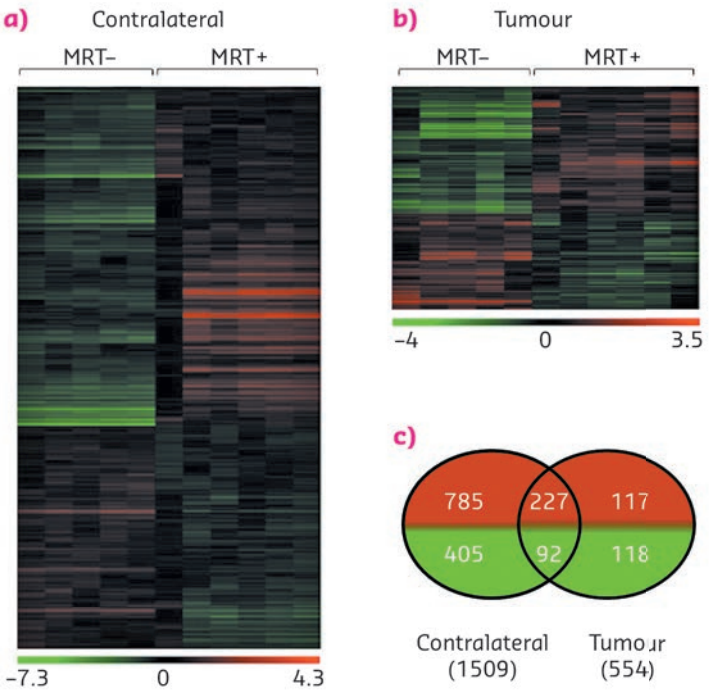

Fig. 93: Influence of MRT on gene expression. a) and b) Heat map showing either significant loss or gain of mRNA expression after MRT in tumour and normal brain tissues. Colours indicate expression levels above (red) or below (green) the median for each gene. Vertical columns indicate individual arrays and horizontal rows indicate genes. c) Venn diagrams showing the numbers of significantly increased (red) or decreased (green) genes after MRT in tumour and contralateral brain tissues [2].

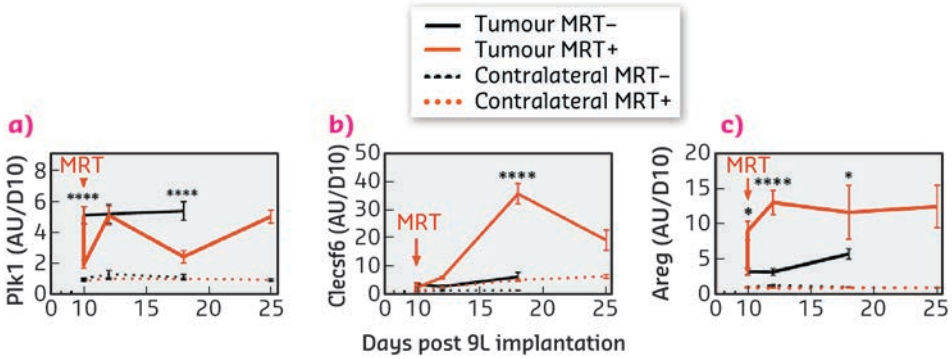

Fig. 94: Kinetic expression of genes from three target groups associated with brain tumour tissue response to MRY. Transcriptomic expression of Plk1 (a), Clecsf (b) and Areg (c) measured 6 hours, 2, 4, 8 and 15 days after MRT. Untreated are presented in black, MRT-treated in red; normal and tumour tissue in dashed and solid lines respectively.

overexpressed in tumours after MRT (**Figure 94c**) and its involvement described in the literature for chimio/radioresistance suggests that its inhibition might help in tumour control after MRT.

PRINCIPAL PUBLICATION AND AUTHORS

Identification of AREG and PLK1 pathway modulation as a potential key of the response of intracranial 9L tumour to microbeam radiation therapy, A. Bouchet (a,b), N. Sakakini (c,d), M. El Atifi (a,e), C. Le Clec'h (b), E. Bräuer-Krisch (b), L. Rogalev (b), J. Laissue (f), P. Rihet (c,d), G. Le Duc (b) and L. Pelletier (a,e), *Int J Cancer* **136**, 2705-2716 (2015); doi: 10.1002/ijc.29318.

(a) INSERM U836, Team Nanomedicine and brain, La Tronche (France)
(b) ESRF
(c) UMR1090 TAGC, INSERM, Marseille (France)
(d) Aix-Marseille Université, Marseille (France)
(e) Grenoble University Hospital, Grenoble (France)
(f) University of Bern, Bern (Switzerland)

REFERENCES

[1] A. Bouchet *et al. Tumour Biol* **35**, 6221–6233 (2014).
[2] A. Bouchet *et al.* PLoS One **8**, e81874 (2013).

ANCIENT SCROLLS CHARRED BY THE ERUPTION OF MOUNT VESUVIUS UNVEIL SOME OF THEIR SECRETS

Writing that has lain undiscovered for centuries inside a scroll blackened as a consequence of the eruption of Mount Vesuvius in 79 AD has been uncovered for the first time. The text written inside a so called 'papyrus roll' of the only surviving library from Antiquity, has been partly deciphered in a computed tomography experiment.

The explosion of Vesuvius in 79 AD, destroyed several Roman towns in Campania, especially Pompeii and Herculaneum. After the first discovery of papyrus rolls in 1752, an entire library was discovered in 1754 inside a small room of a huge villa containing hundreds of handwritten carbonised papyrus scrolls carefully stored in shelves covering its walls. These philosophical and literary texts have remained a mystery to scholars.

Many attempts have been made to look at the texts inside the scrolls in order to acquire more knowledge about ancient (presumably Greek) literature and philosophy. The main problem has, however, been that the scrolls are easily damaged by attempts to unroll them. Moreover, the carbonised papyri and the black ink have a similar composition: papyri were written using a black carbon-based ink obtained from smoke residues, the density of which is almost the

same as that of the charred papyrus. This has been one of the reasons for the failure during previous non-destructive attempts to unveil the texts using conventional X-ray techniques [1].

Two scrolls were examined (one unrolled and the other still unopened), which had been presented as a 'gift' to the Premier Consul Napoléon Bonaparte in 1802 and currently belonging to the collection of the *Institut de France*. The first sample is a fragment of the unrolled scroll, PHerc.Paris. 1, while the second (PHerc.Paris. 4) is an entirely rolled-up scroll. Our results show that X-ray phase contrast tomography, performed at beamline ID17, is the first non-destructive technique that enables

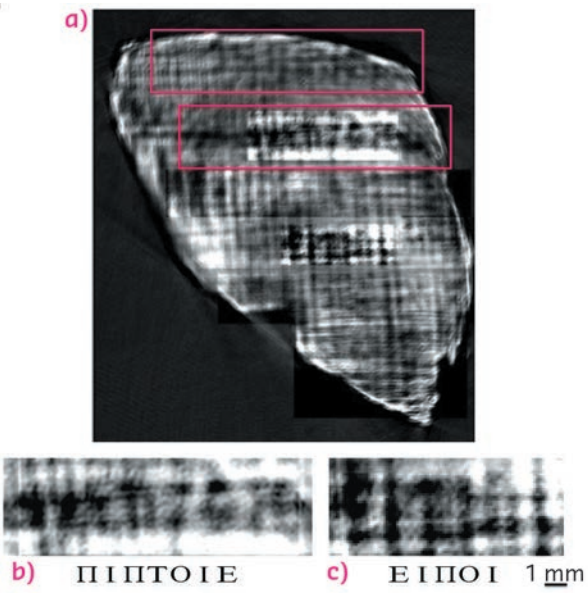

Fig. 95: (a) Hidden layer of fragment 101 from PHerc. Paris.1 and two sequences of Greek capital letters from within it: (b) ΠΙΠΤΟΙΕ; (c) ΕΙΠΟΙ.

many Greek letters and some words inside the windings of rolled-up Herculaneum papyri to be recovered without impairing their physical integrity. This is extremely important because the fragility of carbonised papyri hampers mechanical unfolding, even with the most careful manipulation.

An initial experiment was performed on a very small part of fragment 101 from PHerc. Paris. 1. In **Figure 95a**, a hidden papyrus layer is shown where a sequence of letters are clearly distinguishable. In **Figure 95b**, the sequence of Greek capital letters ΠΙΠΤΟΙΕ (pi-iota-pi-tau-omicron-iota-epsilon), could be recovered. This word means 'would fall'. In **Figure 95b**, it is possible to read another sequence of letters, almost certainly ΕΙΠΟΙ (epsilon-iota-pi-omicron-iota), meaning 'would say'.

The main object of the investigation was a nearly complete scroll that is typical of rolled-up Herculaneum papyri (**Figure 96a**). The tremendous pressure of the pyroclastic material compressed the scroll and deformed its internal spiral structure, the windings of which are folded in a nearly chaotic entangled fashion. As a consequence, the letters are more or less badly distorted, since they lie on highly non-planar surfaces that are cut by selected planar sections for rendering purposes. All this makes data analysis a formidable challenge, since it is necessary to ascertain the phase contrast associated with the text on a surface, the shape and topology of which exhibit an extremely high degree of complexity. Despite these difficulties, we were able to discern evidence of contrast in the reconstruction (see **Figure 96b**). An almost entire alphabet recovered from this sample is presented in **Figure 96c**. It comes from

Fig. 96: (a) Photograph of the Herculaneum papyrus scroll PHerc.Paris.4. (b) Extraction of a sequence of letters from within the scroll. (c) Recovered alphabet from different locations in the scroll.

different images of the scroll acquired during the experimental scans. In the figure, the 24 letters of the Greek alphabets are arranged in three superimposed lines. Lines 1 and 2 consist of letters taken from several internal regions of the sample. Line 3 contains infrared images of the same letters from an unrolled papyrus (PHerc. 1471), which was used as a reference for the writing style of the period.

The discovery that phase contrast computed tomography can recover writing inside carbonised papyrus rolls has an impact that reaches far beyond the study of one particular Herculaneum papyrus. Many philosophical works from the library of the 'Villa dei Papiri' could potentially be deciphered without damaging the papyrus in any way. Moreover, the phase contrast technique offers exciting new and unexpected prospects for application to other unreadable ancient texts.

PRINCIPAL PUBLICATION AND AUTHORS

V. Mocella (a), E. Brun (b,c), C. Ferrero (b) and D. Delattre (d), *Nature Comm* **6**, 5895 (2015); doi: 10.1038/ncomms6895.
(a) CNR-IMM-Istituto per la Microelettronica e Microsistemi-Unità di Napoli, Napoli (Italy)
(b) ESRF
(c) Ludwig-Maximilian-Universität, Garching bei München (Germany)
(d) CNRS-IRHT-Institut de Recherche et d'Histoire des Textes, Paris (France)

REFERENCES

[1] W.B. Seales and D. Delattre, *Cronache Ercolanesi* **43**, 191–208 (2013).

Matter at extremes

The Matter at Extremes Group (MEx) was created in July 2015 and composed of beamlines originating from the previous Dynamics and Extreme Conditions (DEC) and Electronic Structure and Magnetism (ESM) groups. Most of the beamlines are either devoted to studies of matter at extreme conditions of pressure and temperature (ID27 and the new ID15B are both fully dedicated to high pressure XRD), or run an important extreme conditions programme in parallel to other fields of research (ID18 - Nuclear Resonance, ID06 - Large Volume Press and Hard X-ray Microscope, ID24 - Energy Dispersive XAS and BM23 – EXAFS).

This chapter reflects the diversity of the science areas covered by the beamlines of the MEx group and also reports related research from the CRG beamlines BM30B and BM26A.

A major milestone of 2015 was the closure of the Phase I upgrade projects. UPBL11, completed in 2012, involved the upgrade of ID24 and the transfer and mild upgrade of BM29 to BM23. The performance of ID24 was boosted by an increase in acquisition speed of two orders of magnitude (readout time decreased from ~ 200 to 2 microseconds). The quality of EXAFS data acquired with a single (100 ps) X-ray bunch at the upgraded beamline witnessed a leap in quality, opening the way to new experiments to probe matter at the extremes of thermodynamic states (pressure, temperature, magnetic field) that can only be maintained for a very short time. New facilities for users include a micro-XAS station (BM23), an "*in situ*" laser heating facility for the diamond anvil cell (ID24), and a new IR spectrometer for synchronous XAS/DRIFTS structure-function studies of catalysts (ID24 and BM23). New reference papers for both beamlines appeared recently (BM23: O. Mathon *et al.*, *JSR* 2015, ID24: S. Pascarelli *et al.*, *JSR* 2016).

After 21 years of faithful and very productive operation, ID09A was closed in November 2015. The beamline will be upgraded and transferred to ID15B. As these highlights go into press, the hutch complex and its infrastructure are finished on schedule, and newly-designed optical components are being delivered. The new beamline will accept proposals for the upcoming round and user operation at ID15B should start after the summer shutdown. Unfortunately, only a small fraction of the exciting results published this year from work at ID09A made it into this chapter, and I would like to mention two that were left out. The first concerns a detailed and accurate single crystal XRD structural study of CrOCl in a diamond anvil cell (M. Bykhov, *Sci. Rep.* 2015). Contrary to the expectation that materials should approach high symmetry close-packed structures on increasing pressure, a number of elements possess extraordinary complex incommensurately modulated or self-hosting composite structures at high pressures. The significance of this work lies in showing for the first time this incommensurability as an intrinsic high-pressure effect. The second is devoted to a detailed study of the crystal structures of $Mg_2Fe_2C_4O_{13}$, with tetrahedrally coordinated carbon, and $Fe_{13}O_{19}$, synthesised at pressures and temperatures corresponding to the top of the Earth's D'' layer (135 GPa and 2650 K) (M. Merlini, *American Mineralogist* 2015). These structures suggest that the mineralogy of the lower mantle and D'' region may be more complex than previously estimated.

The Hard X-ray Microscope (HXRM) project at ID06, a collaboration between the Technical University of Denmark (DTU), Norwegian University of Science and Technology (NTNU) and Utrecht University, is entering its final installation phase and commissioning with beam is planned for the autumn of 2016. This microscope will enable 3D mapping of orientation and stresses down to 100 nm in spatial resolution. Proof of concept experiments (H. Simons *et al.*, *Nat. Commun* 2015; see chapter Enabling Technologies) have continued with first experiments on multiferroics and 3D dislocation networks. Si refractive lens are now routinely used as condenser for line beams in HXRM experiments, with a first paper already published (H. Simons *et al. Optics Communications* 2016). This year, much time was devoted to the characterisation of Be and Al refractive lenses using grating interferometry (F. Koch *et al. Proc. of SPIE* 2015).

The large volume press (LVP) at ID06 has continued operation at 30% of the standard allocation time throughout 2015. The most significant results this year were related to studies of deformation under high pressure high temperature conditions (HP-HT), typically in the field of earth sciences. The main goal is to quantify rheological materials and to understand the deformation mechanisms of relevant minerals in order to build flow-laws at HP-HT that can be used in global geodynamic modelling. A first paper describing the HP-HT deformation apparatus has been published

(J. Guignard, *Rev. Sci. Instr.* 2015), and provides examples of strain and stress measurements, stress partitioning, simple shear and texture analysis. Due to an increasing user demand for the LVP and to the reorganisation of the activities at ID06, starting from spring 2016, the beamtime for the LVP user programme has been increased to 40-50% which will allow increased user access and boost the visibility of this instrument. The deformation projects will be extended in 2016 towards high strain (>30%) and transition zone pressures.

The Nuclear Resonance Beamline, ID18, had a very busy year 2015. A review of its medium term scientific plans took place in November, linked to a discussion on further developments of the beamline within ESRF-EBS. In parallel to the preparation of this important event, several exciting articles were published. Although not included here, a surface science study by nuclear inelastic scattering (NIS) stands out. It deals with the investigation of phonons in ultrathin oxide films, and discusses the 2D to 3D transition in FeO on Pt(111) (N. Spiridis, *Phys. Rev. Lett.* 2015). This work addressed a long standing general quest in vibrational spectroscopy, and could be achieved due to special preparation of the sample and the nuclear resonance techniques.

Finally, the year 2015 has seen the usual dearth of high impact papers from the high pressure beamline ID27. Among the benchmarks, I would like to mention the first paper exploiting the new Soller slit system for collection of high quality XRD patterns at HP-HT on liquids (G. Weck, *PRB* 2015). Here, accurate measurements of the liquid hydrogen structure factor to 5 GPa show evidence of a crossover between two density evolutions. Another article worth mentioning deals with high pressure studies of nitrogen-hydrogen compounds (H. Wang, *Sci. Rep.* 2015) that appear particularly appealing as high energy density materials (HEDM), *i.e.* materials that release a large amount of energy at their, possibly explosive, decomposition to the most stable species. Results from these investigations open a way for the practical synthesis of these extremely high energetic materials as the formation of nitrogen-hydrogen compounds is favourable already at pressures above 2 GPa according to calculations.

S. PASCARELLI

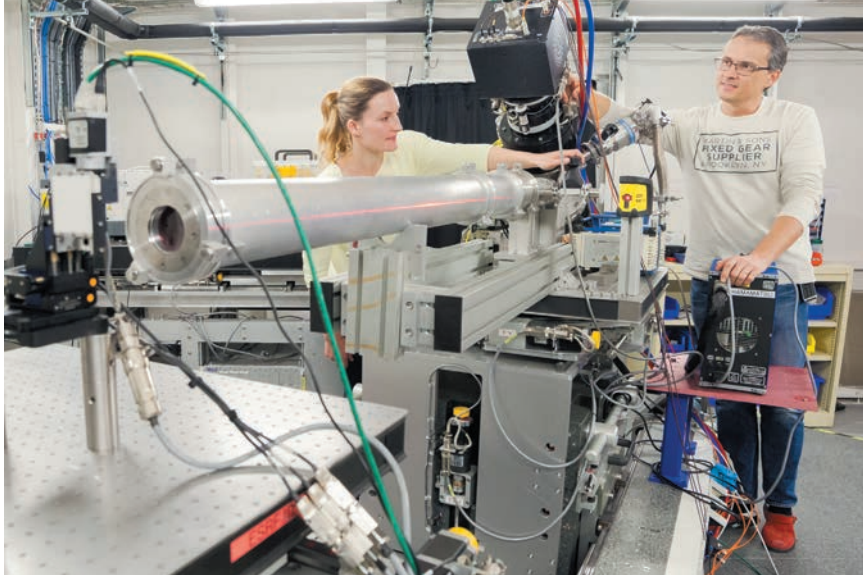

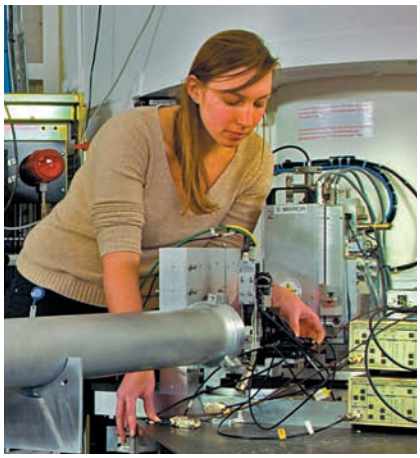

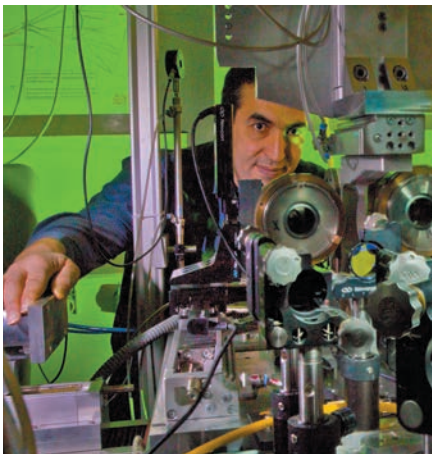

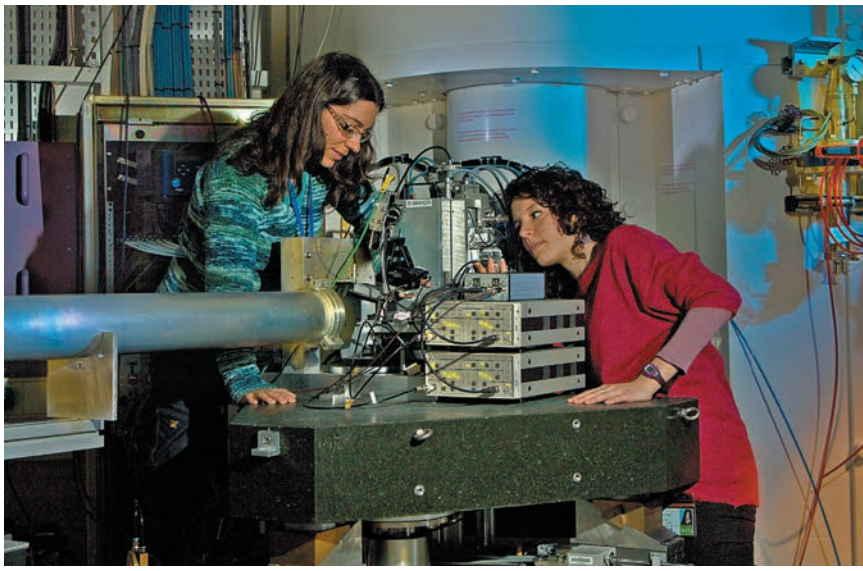

RESOLVING THE ENIGMA OF GOLD DEPOSIT FORMATION USING X-RAY ABSORPTION SPECTROSCOPY

To better understand how gold economic resources form on Earth, *in situ* X-ray absorption spectroscopy (XAS) and solubility measurements were combined with molecular dynamics and thermodynamic simulations to show that the trisulfur radical ion S_3^- strongly binds gold in aqueous solution and enables very efficient extraction, transport, and precipitation of the metal by hydrothermal fluids, explaining many enigmatic features of gold deposits.

Gold economic resources on Earth result from an exceptional concentration phenomenon yielding metal contents in ore of thousand to million times higher than those in common rocks. This process is thought to be controlled by aqueous fluids enriched in salt, sulfur and CO_2, which flow through the Earth's crust, extract the metal from rocks or magmas and transport and precipitate it in the right place at the right moment. Yet, the factors responsible for this transfer remain enigmatic in the face of the extraordinary chemical inertness of gold and the weak capacities of the major fluid components, chloride (Cl^-), hydrogen sulfide (H_2S/HS^-) and sulfate (SO_4^{2-}), to solubilise this noble metal. In particular, all gold and sulfur speciation models ignore sulfur radical ions (S_3^-) recently shown to be stable in aqueous fluid phase at elevated temperature (from 200 to 700°C) and pressure (to 30 kbar) [1,2].

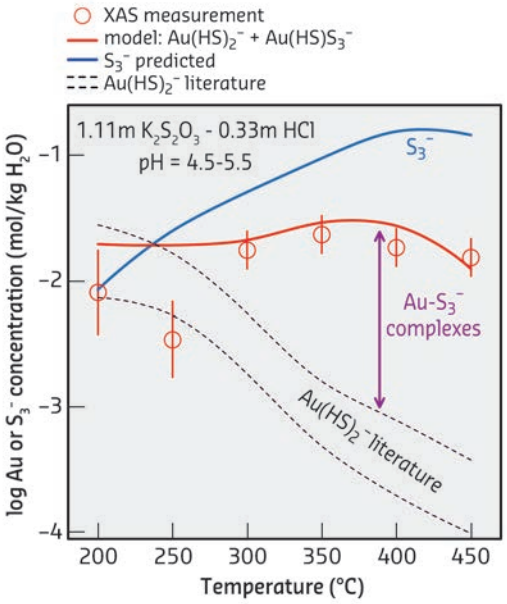

Fig. 97: Direct evidence for gold-trisulfur ion complexes from *in situ* solubility measurements of gold in a sulfur-bearing aqueous solution as a function of temperature at 600 bar.

To quantify the effect of the radical ions on Au behaviour in hydrothermal fluids, we combined *in situ* X-ray absorption spectroscopy and solubility measurements with first-principles molecular dynamics (FPMD) and thermodynamic modelling of Au structure and speciation in aqueous solutions saturated with gold metal and containing hydrogen sulfide, sulfate and S_3^-. These experimental solutions are representative of fluids that formed major types of gold deposits in the crust (temperatures to 500°C, pressures to 200 MPa equivalent to ~ 7 km depth, sulfur contents to 3 wt%, and NaCl-KCl salt contents to 20 wt%).

XAS experiments were carried out at beamline **BM30B** (FAME) using a unique spectroscopic cell that enables simultaneous measurement of both total metal concentration in the fluid and its local atomic structure [3]. We found that the

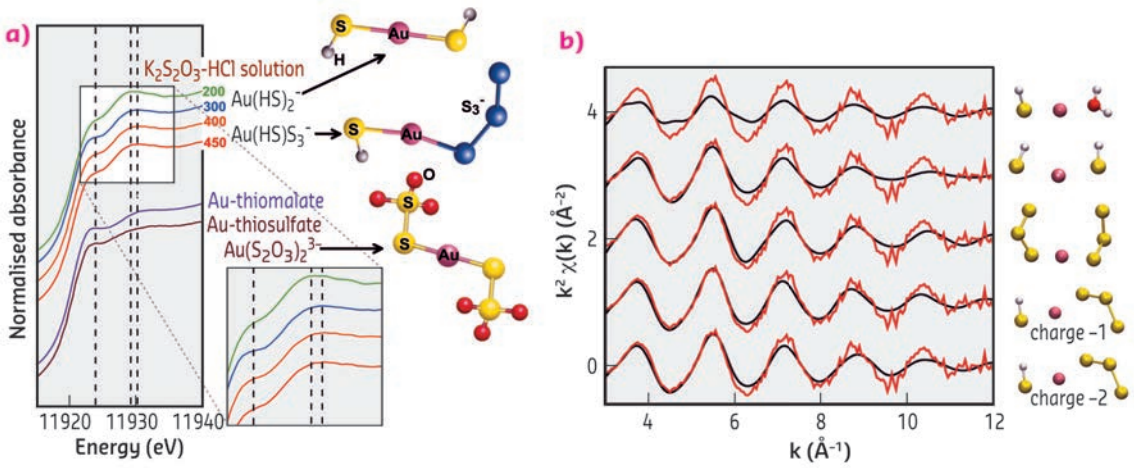

Fig. 98: (a) XANES spectra at Au L_3-edge of S-bearing experimental solutions and reference compounds indicating the formation of Au-S_3^- bonds in S_3^--rich solutions. (b) Experimental EXAFS spectrum at 400°C and 600 bar of the solution from **Figure 97** (red curve) compared with FPMD simulated spectra (black curves) of different Au-H-O-S clusters (Au = pink, S = yellow, H = grey, O = red), showing the best match between experiment and theory for clusters [HS-Au-S_3].

presence of S_3^- in the fluid yields Au solubility enhancement by a factor of 10 to 100 compared to the traditional Au chloride and sulfide complexes such as $Au(HS)_2^-$ and $AuCl_2^-$ (Figure 97). XAS spectra, aided by FPMD simulations, indicate that S_3^- binds Au by forming complexes of the type $Au(HS)S_3^-$ (Figure 98). These data, complemented by Au solubility measurements using a flexible-cell hydrothermal reactor, were analysed with a thermodynamic model that allowed the stability of the new Au-trisulfur ion species to be constrained across a wide range of geological conditions, from deep subduction-zone magmas to thermal springs at the surface.

Applying this model to natural fluids shows that sulfur radical ions, even though less abundant than sulfide or chloride, are capable of extracting large amounts of gold from magmas or rocks at depth and transporting the metal in high concentrations through the Earth's crust. When these hot fluids rise to the surface, cool down or encounter a rock of different composition (*e.g.*, carbonate or organic-rich), the sulfur radicals break down and deposit the metal in veins and cavities. As such, the discovery of soluble and mobile $Au\text{-}S_3^-$ complexes helps explain the enigma of gold deposit formation and offers new possibilities for resource prospecting. Furthermore, such complexes may find applications in ore processing and hydrothermal synthesis of Au-based nanomaterials. This study shows that old gold known from Antiquity has yet to reveal all its secrets.

PRINCIPAL PUBLICATION AND AUTHORS

Sulfur radical species form gold deposits on Earth, G.S. Pokrovski (a), M.A. Kokh (a), D. Guillaume (a), A.Y. Borisova (a), P. Gisquet (a), J.-L. Hazemann (b), E. Lahera (c), W. Del Net (c), O. Proux (c), D. Testemale (b), V. Haigis (d, e), R. Jonchière (d,e), A.P. Seitsonen (d), G. Ferlat (e), R. Vuilleumier (d), A.M. Saitta (e), M.-C. Boiron (f) and J. Dubessy (f), *Proc. Nat. Acad. Sci. USA (PNAS)* **112**(42), 13484-13489 (2015); doi: 10.1073/pnas.1506378112.

(a) Groupe Métallogénie Expérimentale, Géosciences Environnement Toulouse (GET), Observatoire Midi-Pyrénées, Université de Toulouse, CNRS, IRD, Toulouse (France)
(b) CNRS, Université Grenoble Alpes, Institut NEEL, Grenoble (France)
(c) Observatoire des Sciences de l'Univers de Grenoble, CNRS, Université Grenoble Alpes, Saint Martin d'Hères (France)
(d) École Normale Supérieure, PSL Research University, Département de Chimie, Sorbonne Universités, UPMC, Université Paris 06, CNRS, UMR 8640 Pasteur, Paris (France)
(e) Sorbonne Universités, UPMC, Université Paris 06 and CNRS, UMR 7590, Institut de Minéralogie, de Physique des Matériaux et de Cosmochimie (IMPMC), Paris (France)
(f) Université de Lorraine, CNRS, CREGU, GeoRessources, Vandoeuvre lès Nancy (France)

REFERENCES

[1] G.S. Pokrovski and L.S. Dubrovinsky, *Science* **331**, 1052-1054 (2011).
[2] G.S. Pokrovski and J. Dubessy, *Earth Planet. Sci. Lett.* **411**, 298-309 (2015).
[3] D. Testemale *et al.*, *Rev. Sci. Instrum.* **76**, 043905-043909 (2005).

XAS: A NOVEL APPROACH TO DETERMINE IRON MELTING AT MEGABAR PRESSURES

The core of the Earth is composed mainly of iron. The determination of the iron melting temperature at conditions in which the solid core of the Earth becomes liquid is one of the main concerns in geophysics as this value represents a fixed point in the thermal profile of our planet. The latter rules the heat flow from the core allowing us to understand the dynamo of the Earth and therefore has implications for the terrestrial magnetic field which, in turn, has influences for every living being on Earth. There is a long-standing controversy over the melting curve of Fe at the inner core boundary and here changes in X-ray absorption spectra are used as a criterion to detect melting under pressure.

The melting curve of iron at high pressure has been studied both experimentally and theoretically [1-4]. Nonetheless, a large plethora of results have been found with discrepancies up to 2000 K in the melting curve at the inner core boundary (ICB). Such discrepancies are too large to build unambiguous thermal evolution and dynamic models. X-ray absorption spectra have been used as a diagnostic tool to determine the solid-liquid phase boundary of iron compressed to over 100 GPa in a laser heated diamond anvil cell (LHDAC). X-ray absorption spectroscopy (XAS) is a chemically selective technique and the data contain solely the signal relative to the absorbing element without any interference from the sample environment. At the same time, it provides structural information within a few angstroms around the photoabsorbing atom maintaining the same sensitivity and accuracy regardless of the physical state of the investigated sample. These are assets with respect to diffraction techniques in which the onset of melting appears as a weak diffuse halo superimposed on strong Bragg reflections from partially molten sample

and sample environment. In addition, by using XAS in the energy dispersive geometry available at beamline **ID24**, it is possible to quickly acquire the whole spectrum while using a small focal spot. These are significant advantages for studies of molten systems at high pressure with *in situ* LHDAC, in which samples are small and unstable under laser heating.

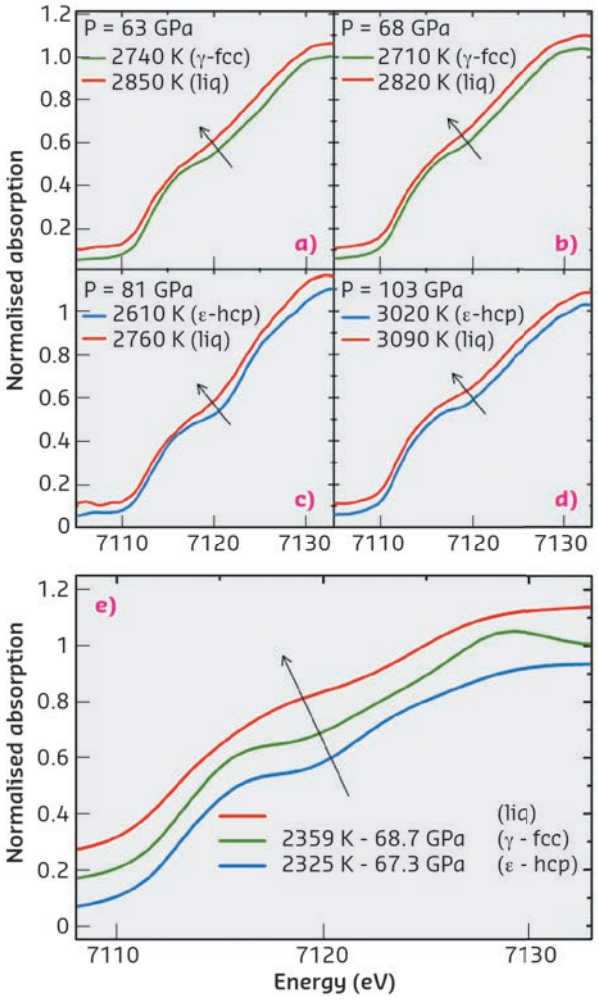

Fig. 99: (a-d) Experimental XANES spectra at 63, 68, 81, and 103 GPa respectively recorded at the solid-liquid phase transition. The arrows indicate the change in the onset of the absorption that can be used as diagnostic tool to detect melting. (e) Calculated XANES spectra of iron in the ε-hcp phase (blue line), γ-fcc phase (green line), and liquid phase (red line).

The melting criterion adopted here was based on changes occurring in the near-edge region of the absorption spectrum (XANES) that is known to be less affected by thermal damping and by the noise associated with extreme experimental conditions. **Figure 99 (a-d)** reports the XANES spectra at different pressures at the solid-to-liquid phase transition. At all recorded pressures and regardless of the structure of the solid phase, the modifications of the onset of the absorption can be used as a signature for the solid-liquid phase transition. In fact, the shoulder at the onset of the absorption is discontinuously smoothed out upon heating as shown by the arrows. The broadening with increasing temperature of the near edge part of the spectrum is ascribed to the thermal motion of the atoms. However at melting, the broadening increases discontinuously following the breakdown of crystalline order characteristic of the liquid phase. **Figure 99e** shows full multiple-scattering calculations to simulate the XANES region of the spectra at thermodynamic conditions comparable to the experimental ones. Consistent with the experimental data, the XANES calculation shows the same modifications of the feature between 7115 eV and 7120 eV in the liquid phase with respect to the solid phases characteristic of the disruption of the crystalline order.

The melting temperatures obtained in this work result in a flat melting curve around 100 GPa. Our results are in agreement with previous data to 200 GPa [1]. The latter suggests a melting temperature of iron below 5000 K when extrapolated to ICB conditions.

The combination of XAS and elevated pressure and temperature conditions offers great potential to probe Earth's deep interior. In addition, the experiment reported here holds promises for studies related to the structure and phase diagram of compressed melts, the investigation of polyamorphism in the liquid phase or the extent of icosahedral ordering whose investigation has been limited until now to ambient conditions.

PRINCIPAL PUBLICATION AND AUTHORS

Melting of iron determined by X-ray absorption spectroscopy to 100 GPa, G. Aquilanti (a), A. Trapananti (b), A. Karandikar (c,d), I. Kantor (e), C. Marini (e), O. Mathon (e), S. Pascarelli (e) and R. Boehler (c), *PNAS* (2015); doi: 10.1073/pnas.1502363112.

(a) Elettra–Sincrotrone Trieste S.C.p.A., Trieste (Italy)
(b) CNR–IOM, OGG Grenoble c/o ESRF, Grenoble (France)
(c) Geophysical Laboratory, Carnegie Institution of Washington, Washington DC (USA)
(d) Geowissenschaften, Goethe-Universität, Frankfurt a.M. (Germany)
(e) ESRF

REFERENCES

[1] R. Boehler, *Nature* **363**, 534–536 (1993).
[2] S. Anzellini *et al.*, *Science* **340**, 464–466 (2013).
[3] D. Alfè *et al.*, *Nature* **401**, 462 (1999).
[4] A. Laio *et al.*, *Science* **287** 1027 (2000).

HIGH POISSON'S RATIO OF EARTH'S INNER CORE EXPLAINED BY CARBON ALLOYING

The behaviour of Fe_7C_3 was investigated up to pressure conditions of the Earth's core using X-ray diffraction, Mössbauer spectroscopy and nuclear inelastic scattering. These experiments revealed that the anomalous elastic properties of the Earth's inner core found by seismology may be explained by the presence of carbon as an alloying light element.

Most of our knowledge of the Earth's deep interior comes from comparison of laboratory measurements of physical properties of materials with data from bulk geophysical methods. In particular, seismology has been the traditional method for providing constraints on the physics of the Earth's interior. Seismology provides three independent physical parameters: density and compressional and shear sound wave velocities. Combining these constraints with geochemical and cosmochemical considerations, available data suggests that iron (or iron–nickel alloy) is the main component of the Earth's core. However, a large inconsistency still exists between the density of pure iron at pressure and temperature conditions of the Earth's core and seismological estimates, which can only be explained by the presence of light elements such as oxygen, silicon, sulfur, hydrogen or carbon. In addition, the low shear wave velocity and high Poisson's ratio of the Earth's core remains enigmatic. None of the available mineral physics data of light element bearing Fe alloys can explain the rubber like Poisson's ratio (0.45) present in the Earth's core.

In this study, we investigated the magnetic and elastic properties of Fe_7C_3 up to core conditions. Carbon is a plausible light element in the Earth's core and estimates based on current available data suggest that 1.1wt% of carbon may be present in the Earth's inner core. The equation of state (EOS) of single crystal Fe_7C_3 was measured up to 156 GPa using the unique capabilities of X-ray diffraction beamline **ID09** (**Figure 100**), which provides a small and intense beam and is equipped with a fast large area X-ray detector. The methodology and strategy for data collection was developed in collaboration between ESRF and Bayreuth scientists, allowing the range for single crystal diffraction experiments (structure solution and refinement) to be extended to pressures of the Earth's core. The novel synchrotron Mössbauer source (SMS) developed at **ID18** was used to investigate the electronic properties of Fe_7C_3 up to 132 GPa and nuclear inelastic scattering (NIS) was measured at **ID18** in order to obtain elastic properties up to 158 GPa, which was made possible by the recently improved capabilities including decreased X-ray beam size and better energy resolution. We found that Fe_7C_3 undergoes two magnetic

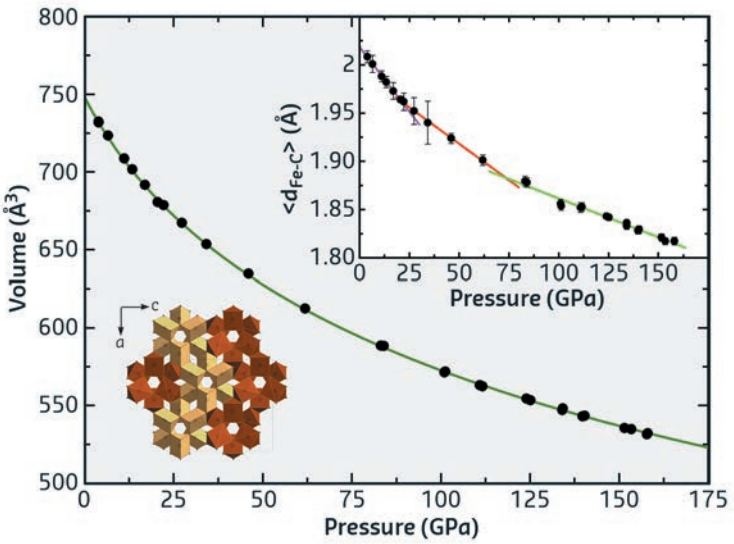

Fig. 100: Volume–pressure data for Fe_7C_3 with the fitted third-order Birch–Murnaghan equation of state (K_{300} = 168(4) GPa, K' = 6.1(1)). The upper inset shows the variation of mean carbon to iron distances, $<d_{Fe-C}>$ in Fe_7C_3 with pressure, whereby the data show three linear regions with transitions around 16 GPa and 70 GPa, marking the ferromagnetic to paramagnetic and paramagnetic to non-magnetic transitions, respectively (further details are given in the text). The lower left inset shows a polyhedral model of the crystal structure of Fe_7C_3 projected in the b-direction.

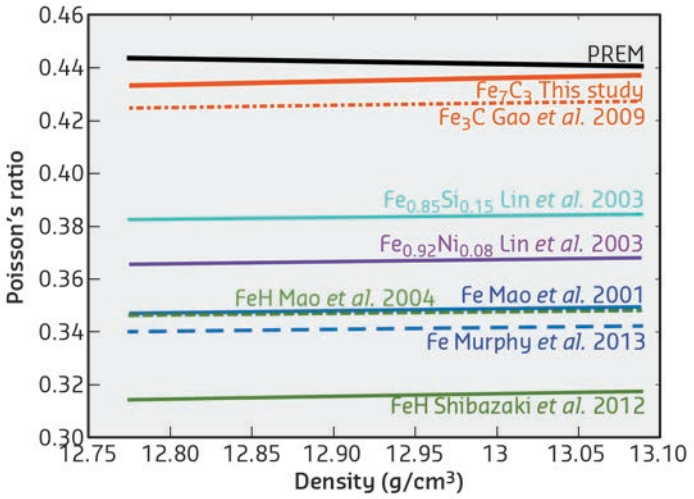

Fig. 101: Extrapolation of Poisson's ratio to the densities estimated in the Earth's inner core using Birch's law [1-7]. The only element which significantly increases the Poisson's ratio of iron is carbon. Moreover, the estimated Poisson's ratio of Fe_7C_3 nearly approaches the Poisson's ratio of the preliminary Earth reference model (PREM [7]) at densities near the centre of the inner core.

transitions, a ferromagnetic to paramagnetic transition at about 16 GPa and a paramagnetic to nonmagnetic transition at about 70 GPa. The EOS seems not to be affected by these transitions, only the mean Fe-C distances show an accompanying change in slope with pressure (Figure 100). By combining the EOS and NIS results, we obtained density, shear sound wave velocity and compressional sound wave velocity of Fe_7C_3 up to core conditions. Estimated extrapolated shear wave and compressional wave velocities show that Fe_7C_3 exhibits a lower shear wave velocity than pure iron and a Poisson's ratio similar to that of the Earth's inner core (Figure 101). We suggest that carbon alloying significantly modifies the properties of iron at extreme conditions to approach the elastic behaviour of rubber. Thus, the presence of carbon may explain the anomalous elastic properties of the Earth's core.

PRINCIPAL PUBLICATION AND AUTHORS

High Poisson's ratio of Earth's inner core explained by carbon alloying, C. Prescher (a,b), L. Dubrovinsky (a), E. Bykova (a,c), I. Kupenko (a,d), K. Glazyrin (a,e), A. Kantor (a,d), C. McCammon (a), M. Mookherjee (a,f), Y. Nakajima (a,g), N. Miyajima (a), R. Sinmyo (a), V. Cerantola (a), N. Dubrovinskaia (c), V. Prakapenka (b), R. Rüffer (d), A. Chumakov (d,h) and M. Hanfland (d), *Nature Geoscience* **8**, 220-223 (2015); doi: 10.1038/NGEO2370.
(a) Bayerisches Geoinstitut, Universität Bayreuth (Germany)
(b) Center for Advanced Radiation Sources, University of Chicago (USA)
(c) Laboratory of Crystallography, Material Physics and Technology at Extreme Conditions, University of Bayreuth (Germany)
(d) ESRF
(e) Petra III, P02, Deutsches Elektronen Synchrotron, Hamburg (Germany)
(f) Earth and Atmospheric Sciences, Cornell University (USA)
(g) Materials Dynamics Laboratory, RIKEN Spring-8 Center, Hyogo (Japan)
(h) National Research Center "Kurchatov Institut", Moscow (Russia)

REFERENCES

[1] L. Gao *et al.*, *Geophys. Res. Lett.* **35**, 1 (2008).
[2] J.-F. Lin *et al.*, *Geophys. Res. Lett.* **30**, 2112 (2003).
[3] H.K. Mao *et al.*, *Science* **292**, 914 (2001).
[4] W.L. Mao *et al.*, *Phys. Res. Lett.* **31**, L15618 (2004).
[5] C.A. Murphy *et al.*, *J. Geophys. Res. B* **118**, 1999 (2013).
[6] Y. Shibazaki *et al.*, *Earth Planet. Sci. Lett.* **313-314**, 79 (2012).
[7] A.D. Dziewonski and D.L. Anderson, *Phys. Earth Planet. Inter.* **25**, 297 (1981).

POLYAMORPHISM OF A Ce-BASED METALLIC GLASS UNDER HIGH PRESSURE

Hierarchical densification processes under pressure were observed at 293 K and 390 K in a Ce-based metallic glass, arising from the hierarchy of interatomic interactions. A relatively abrupt and discontinuous transformation around 5.5 GPa was observed at 390 K, suggesting a possible weak first-order nature. Furthermore, both positive and abnormal-negative thermal expansion behaviours on medium-range order were observed in different pressure windows, due to the low-energy vibrational motions and relaxation of the weakly linked solute-centred clusters.

The microstructure transformations in glasses and/or liquids induced by high pressure or temperature, such as the liquid-liquid, liquid-glass and glass-glass transformations are the central issues in amorphous material research. The lack of long range ordered structure like in crystalline solids makes these issues still very elusive today. Polyamorphism has been observed for a long time in some glasses involving directional and open coordination environments (such as ice, silica, silicon and chalcogenide glasses). However, it was unknown whether the polyamorphous states could exist in metallic glasses, which have a very densely packed structure without directional coordination, until the work of Sheng *et al.*, in 2007 [1]. Nevertheless, the nature of the polyamorphism in metallic glasses, such as the 4*f* electron delocalisation mechanism and the change of short-to-medium range ordered structures under pressure is poorly understood. Furthermore, the polyamorphic transformation process in all the previously reported metallic glass systems is gradual and occurs in a broad pressure range. Therefore, it was unclear whether the polyamorphic transition nature was of first order in the amorphous metallic system.

We studied the densification processes of metallic glass $Ce_{65}Co_{25}Al_{10}$ (fabricated by melt-spinning technique) under high pressure both at room temperature (293 K) and 390 K, which is near the glass transition temperature (Tg ~ 396 K), using *in situ* high-pressure X-ray diffraction at beamline **ID27**. We observed a hierarchical densification processes (from low density amorphous state, through medium density amorphous state, to high density amorphous

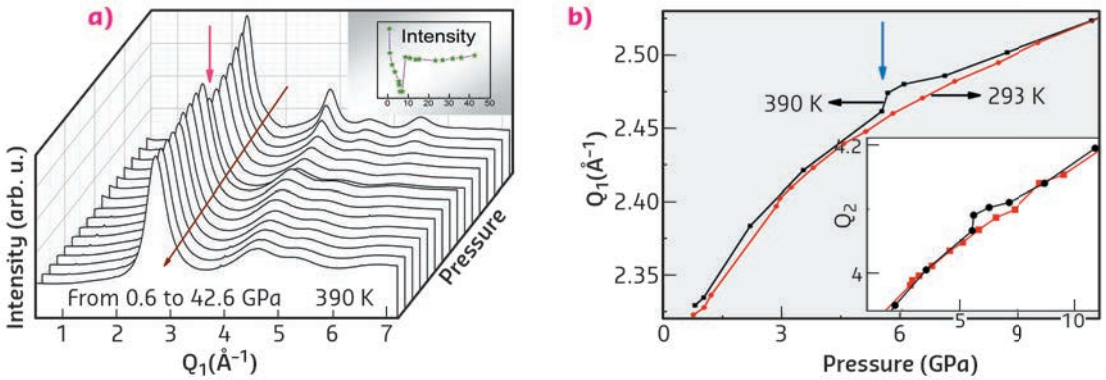

Fig. 102: (a) *In situ* XRD patterns of the metallic glass under high pressure from 0.6 to 42.6 GPa at 390 K. The inset shows the pressure dependence of the diffraction intensity. (b) Pressure dependence of Q_1 and Q_2 (the inset) below 10 GPa measured at 293 and 390 K.

state) at both temperatures (**Figure 102** and **Figure 103**), arising from the inherent structural inhomogeneity and hierarchy of interatomic interactions. That is, different degree of contribution from changes of free volume zone, medium range order and short range order. The low density amorphous state-to-low density amorphous state transformation, which primarily is related to the shortening of the weak Ce-Ce bonds among the solute-centred clusters and does not undergo significant change in short-range order, is similar to the first-order isostructural α-γ transition of pure Ce. In contrast, the medium density amorphous state-to-high density amorphous state transformation, associated with the change of short-range order, is somehow similar to the normal polymorphic transition in crystals involving a distinct change of the unit cell. During the densification process, the special 4*f* electron delocalisation of the Ce atoms assists largely in the bond shortening. Moreover, a relatively discontinuous change of volume is observed around 5.5 GPa when the experiment was performed at 390 K, while only a smooth and continuous change is observed at room temperature (293 K). The discontinuous change in volume implies a possible first-order-like nature of the polyamorphic transformation, which was hidden thus far in previous experiments due to kinetic sluggishness at lower temperatures. In addition, the $Ce_{65}Co_{25}Al_{10}$ metallic glass shows abnormal-negative thermal expansion under a pressure range of 0.6–9.0 GPa, which could arise from a combination of the relaxation (minor role) and tilting or rocking motions of the tightly bonded polyhedral clusters linking to the weakest atom zones. The pressure-induced variation of the hierarchical bonding, will exert significant impact on the mechanical, dynamics and glass transition of various metallic glass systems due to their strong dependence on both the short range order, medium range order and linkage-atom (free volume) zones.

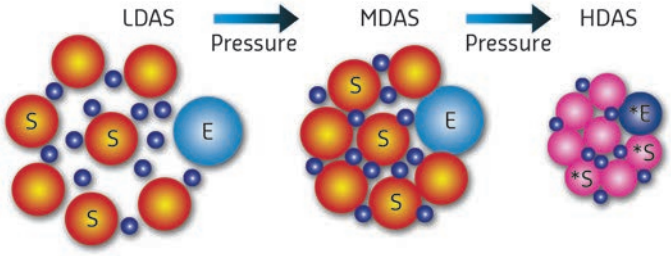

Fig. 103: Illustration of hierarchical densification of Ce-based metallic glass. The smallest cyan balls represent the Ce atoms, the medium sized colour (orange and blue) balls represent the solute-centred cluster (S) and the largest colour (orange and blue) balls represent the supercluster (E).

PRINCIPAL PUBLICATION AND AUTHORS

Hierarchical densification and negative thermal expansion in Ce-based metallic glass under high pressure, Q. Luo (a), G. Garbarino (b), B. Sun (c), D. Fan (d,e), Y. Zhang (f), Z. Wang (c), Y. Sun (a), J. Jiao (a), X. Li (g), P. Li (g), N. Mattern (c), J. Eckert (c,h) and J. Shen (a), *Nature Communications* **6**, 5703-5711 (2015): doi: 10.1038/ncomms6703.

(a) School of Materials Science and Engineering, Tongji University, Shanghai (China)
(b) ESRF
(c) IFW Dresden, Institute for Complex Materials, Dresden (Germany)
(d) Key Laboratory of High-temperature and High-pressure Study of the Earth's Interior, Institute of Geochemistry, Chinese Academy of Sciences, Guiyang, (China)
(e) Center for High Pressure Science and Technology Advanced Research (HPSTAR), Changchun (China)
(f) Ames Laboratory-USDOE, Iowa State University, Ames (USA)
(g) Institute of High Energy Physics, Chinese Academy of Sciences, Beijing (China)
(h) TU Dresden, Institute of Materials Science, Dresden (Germany)

REFERENCES

[1] H.W. Sheng, *et al.*, *Nature* **6**, 192–197 (2007).

UNCONVENTIONAL HIGH-T_C SUPERCONDUCTIVITY IN FULLERIDES

Molecular superconductors such as the fullerides are characterised by periodic arrangements of molecules. Here, for the A_3C_{60} fullerides, T_c was found to have a dome-like variation with the density of fulleride molecules, controlled by pressure, and that the peak of this dome occurs precisely at the point where the molecular and extended lattice features of the electronic structure are optimally balanced.

Fulleride superconductors are the simplest members of the unconventional superconductivity family, *i.e.* the pairing interaction is something other than simply the conventional BCS electron-phonon interaction. This was demonstrated by showing that, in both polymorphs (A15– and face-centred-cubic–structured) of the most expanded binary fulleride Cs_3C_{60}, superconductivity emerges upon applied pressure out of an antiferromagnetic Mott-Jahn-Teller insulating state and displays an unconventional behaviour – a superconductivity dome – explicable by the prominent role of strong electron correlations [1-5]. However, although the similarities with the electronic phase diagrams of exotic superconductors such as the cuprates, the iron pnictides, and the heavy fermions are striking, there existed to date no information on the nature of the parent normal metallic state out of which both the insulating and superconducting states of fullerides emerge. The relation of this parent state to both the superconducting pairing mechanism and the proximate antiferromagnetic insulator is at the heart of any attempt to understand unconventional superconductivity and has been pursued for decades in the cuprates. The high symmetry and structural simplicity of the fullerides are advantageous in pursuing a direct connection from (molecular) building unit to extended structure properties.

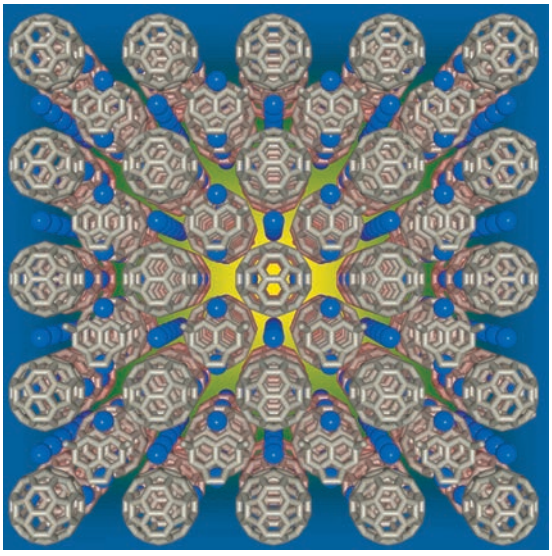

Fig. 104: Three-dimensional depiction of the crystal structure of the molecular A_3C_{60} fulleride superconductors. The fullerene molecules pack in an isotropic cubic-close-packed array in three dimensions. Alkali metal ions (blue spheres) occupy vacant interstitial holes of octahedral and tetrahedral symmetry.

We deployed a panoply of experimental techniques to probe the evolution of the electronic and crystal structure changes associated with the Mott insulator-metal transition in fcc-structured fullerides (**Figure 104**). The entire bandwidth-controlled electronic phase diagram can be traversed by changing an electronic parameter – the extent of overlap between the outer wavefunctions of the fulleride anions – as monitored by the application of (physical or chemical) pressure. Synchrotron X-ray powder diffraction measurements at both ambient (beamline **ID31**) and elevated pressures (beamline **ID27**) down to temperatures below the observed T_c show that the high-symmetry isotropic fcc structure remains robust at all relevant values of temperature and pressure and allow us to extract the dependence of the electronic properties on C_{60} packing density V, which in turn accurately tracks experimentally the change in bandwidth. Combining the structural results with those from spectroscopic and thermodynamic probes demonstrated for the first time the influence of the molecular origin of the electrons at the Fermi level on the collective transport and superconducting pairing properties. We found an anomalous correlated metallic phase – the Jahn-Teller metal – which dominates the phase diagram at temperatures well above T_c and is the normal state at the top of the superconductivity dome when T_c is maximum

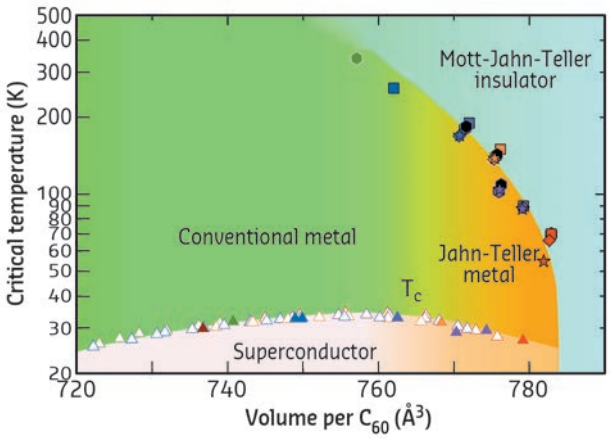

Fig. 105: Global electronic phase diagram of fcc-structured A_3C_{60} fullerides showing the evolution of the superconducting transition temperature, T_c (superconductivity dome) and the Mott-Jahn-Teller insulator to Jahn-Teller metal crossover temperature, T' as a function of volume per C_{60}. Within the metallic (superconducting) regime, gradient shading from orange to green schematically illustrates the Jahn-Teller metal to conventional metal (unconventional to weak-coupling BCS conventional superconductor) crossover.

and where the superconducting pairing crosses over from conventional weak-coupling to unconventional strong coupling (Figure 105). The Jahn-Teller metal is a dynamic, microscopically heterogeneous coexistence of itinerant metallic electrons with localised electrons, which produce Jahn-Teller on-molecule distortions driven by the degeneracy of the frontier orbitals of the C_{60} building unit. This central electronic state is the parent of an unconventional strongly-coupled superconducting state and fades away into a conventional Fermi liquid metal and weak-coupling BCS superconductor when the molecular electronic signatures disappear with lattice contraction.

The optimal T_c in the fullerides – and highest for any molecular material – is found precisely at the boundary between unconventional and conventional normal and superconducting state behaviour, where the balance between molecular (Jahn-Teller distortion) and extended lattice (itinerant metallic electrons) features of the electronic structure is optimised.

PRINCIPAL PUBLICATION AND AUTHORS

Optimized unconventional superconductivity in a molecular Jahn-Teller metal, R.H. Zadik (a), Y. Takabayashi (a), G. Klupp (a,b), R.H. Colman (a), A.Y. Ganin (c), A. Potočnik (d), P. Jeglič (d), D. Arčon (d), P. Matus (b), K. Kamarás (b), Y. Kasahara (e), Y. Iwasa (e), A.N. Fitch (f), Y. Ohishi (g), G. Garbarino (f), K. Kato (h), M.J. Rosseinsky (c) and K. Prassides (a,i,j), *Science Advances* **1**, e150059 (2015).
(a) Department of Chemistry, Durham University (UK)
(b) Institute for Solid State Physics and Optics, Wigner Research Centre for Physics, Hungarian Academy of Sciences, Budapest (Hungary)
(c) Department of Chemistry, University of Liverpool (UK)
(d) Institute Jožef Stefan, Ljubljana (Slovenia)
(e) Quantum-Phase Electronics Center and Department of Applied Physics, University of Tokyo (Japan)
(f) ESRF
(g) Japan Synchrotron Radiation Research Institute, SPring-8, Hyogo (Japan)
(h) RIKEN SPring-8 Center, Hyogo (Japan)
(i) WPI-Advanced Institute for Materials Research (WPI-AIMR), Tohoku University, Sendai (Japan)
(j) Japan Science and Technology Agency (JST), ERATO Isobe Degenerate π-Integration Project, Tohoku University, Sendai (Japan)

REFERENCES

[1] A.Y. Ganin *et al., Nature Mater.* **7**, 367 (2008).
[2] Y. Takabayashi *et al., Science* **323**, 1585 (2009).
[3] A.Y. Ganin *et al., Nature* **466**, 221 (2010).
[4] G. Klupp *et al., Nature Commun.* **3**, 912 (2012).
[5] A. Potočnik *et al., Sci. Rep.* **4**, 4265 (2014).

NANOSIZE EFFECT ON MAGNETISM

The nanosize effect of spherical templates to the evolution of magnetism in various thicknesses of iron film was investigated. The spatial distribution of magnetic moments was modelled and different magnetic evolution mechanisms were found depending on the sphere size. This led to the conclusion that the geometrical properties of the template play a fundamental role in the magnetic ordering which is crucial for industrial application.

Gordon E. Moore [1] predicted in 1965 that the number of transistors in an integrated circuit will double approximately every two years, which has proven to be valid for the past five decades. An analogous tendency was observed by Mark Kryder for magnetic disk storage density [2]. Based on the enormous increase of bit density in hard drives between 1990 and 2005, he assumed that the capacity of a 2.5" disk will reach 40 TBit/in^2 by 2020. Unfortunately, 5 years before this date, the most enhanced magnetic hard disk had a factor of 30 less storage capacity. Several developments are now on the way, not only to reach, but maybe to pass 40 Tbit/in^2.

In a conventional hard disk, the information is stored in collectively magnetised grains. There are two dilemmas about storage capacity increase. The magnetic grains are already so small, that further reduction would lead to the superparamagnetic effect, where the spontaneous magnetisation fluctuation would result in data loss. On the other hand, the magnetostatic and exchange interaction among the adjacent grains sets a limit on how "strong" the magnetisation should be in a grain without being perturbed by the vicinity.

A possible solution could rely on the information unit being bounded to a nanostructure, hence the strong exchange coupling within the particle, the shape anisotropy and the isolation of the particles would increase the energy barrier for thermal switching. This solution is called bit patterned media and was predicted to be eligible to store as much as 20 - 300 Tbit/in^2 [3]. Although, this technique appears to be appropriate for future magnetic recording devices, it is well known that material properties may differ from bulk when entering the nanoscale regime and this is particularly true for magnetic materials. For this reason, scientists

from all over the world are working to reveal the nanosize effects on magnetism. The Nuclear Resonance Beamline **ID18** is also participating in this challenge. In the latest work, an ultrathin iron film was deposited on a flat silicon substrate as well as on 20 nm and 400 nm diameter silica spheres, and the effect of curvature and interparticle distances on the evolution of magnetism was studied. The thickness of the iron film was varied in the range where iron has a nonmagnetic/magnetic transition by gradual deposition, using molecular beam epitaxy under high vacuum conditions. To model the magnetic moment configurations in the iron cap, micromagnetic simulations based on the data obtained from *in situ* nuclear forward scattering (NFS), X-ray reflectivity, grazing-incidence small-angle X-ray scattering and *ex situ* atomic probe microscopy techniques were carried out.

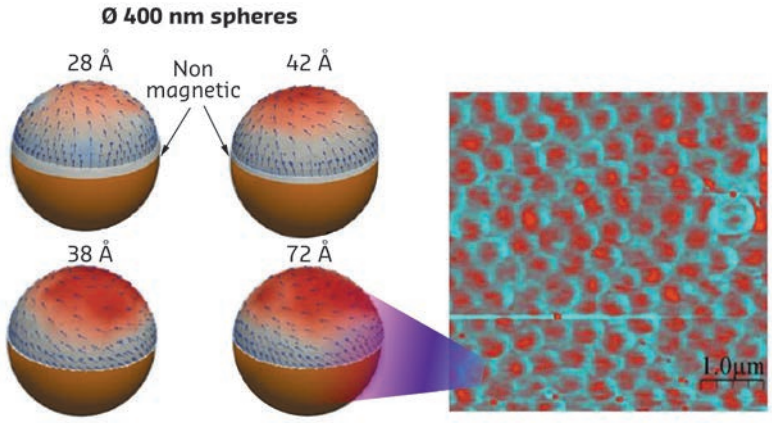

Fig. 106: Magnetic moment configuration calculated by micromagnetic simulation for 28 Å, 38 Å, 42 Å and 72 Å- thick iron deposited on 400 nm diameter spheres (left) and the magnetic force microscopy image of the thickest iron layer (right).

In the case of the 400 nm diameter spheres, the formed magnetic structure was determined by the topology of the spheres and the system could be considered as a sum of individual magnetic particles. At an iron thickness of 28 Å, the upper part of the sphere became magnetic, showing a spiral like (vortex) magnetic ordering on top and out of plane magnetisation at the side. The micromagnetic simulation of this magnetic moment configuration is shown in **Figure 106**. With increasing iron thickness, the out of plane component was gradually eliminated and replaced by a magnetic vortex (**Figure 106**).

In contrast, for iron deposited on 25 nm diameter particles, iron became magnetic at a thickness of 26 Å in the contact region of the spheres and a uniformly distributed, well isolated magnetic structure was created (**Figure 107**). With further deposition, the whole layer became magnetic and a topology independent magnetic structure incorporating several particles with in plane magnetisation could be observed (**Figure 107**).

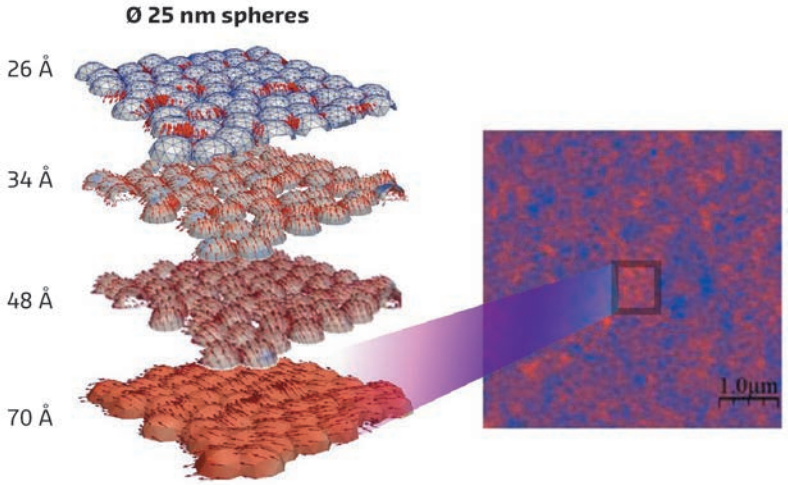

Fig. 107: Magnetic moment configuration calculated by micromagnetic simulation for 26 Å, 34 Å, 48 Å and 70 Å-thick iron deposited on 25 nm diameter spheres (left) and the magnetic force microscopy image of the thickest iron layer (right).

PRINCIPAL PUBLICATION AND AUTHORS

Evolution of magnetism on a curved nano-surface, D.G. Merkel (a,d), D. Bessas,(a), Z. Zolnai (b), R. Rüffer (a), A.I. Chumakov (a), H. Paddubrouskaya (c), C. Van Haesendonck (c), N. Nagy (b), A.L. Tóth (b) and A. Deák (b), *Nanoscale* **7**, 12878-12887 (2015); doi: 10.1039/C5NR02928G.
(a) ESRF
(b) CER, Institute of Technical Physics and Materials Science, Budapest (Hungary)
(c) KU Leuven, Solid-State Physics and Magnetism Section, Leuven (Belgium)
(d) Wigner RCP, Institute for Particle and Nuclear Physics, , Budapest (Hungary)

REFERENCES

[1] G.E. Moore, *Electronics Magazine* **38**, 114 (1965).
[2] C. Walter, *Scientific American*, August (2005).
[3] R.A. Griffiths *et al.*, *J. Phys. D: Appl. Phys.* **46**, 503001 (2013).

NUCLEAR RESONANCE SCATTERING CLARIFIES THE STRUCTURE OF A PHARMACOLOGICALLY RELEVANT IRON SULFUR PROTEIN AND ITS INTERACTION WITH INHIBITORS

The LytB/IspH protein catalyses the last step of the biochemical MEP-pathway used by most pathogenic bacteria for the biosynthesis of essential terpenoids. Due to its absence in humans, the MEP pathway is a target for the development of new antimicrobial agents. Nuclear resonance vibrational spectroscopy (NRVS) combined with quantum chemical-molecular mechanical (QM/MM) calculations have provided more insight into the active site structures of LytB in its substrate-free and inhibitor bound forms.

The LytB protein, also called IspH, catalyses the last step of the methylerythritol phosphate (MEP) pathway that carries out the biosynthesis of essential terpenoids in most pathogenic bacteria. The MEP pathway is essential for the survival of microorganisms, but it does not exist in mammals and humans. Humans too have to synthesise terpenoids such as cholesterol and hormones, but for this purpose a totally different biochemical pathway exists. Therefore, the MEP pathway is a promising target for the development of new antimicrobial agents. Inhibitors of the LytB protein may qualify for new potent antibiotics which are effective also for pathogens resistant to present drug therapies.

The LytB protein has a 4Fe-4S cluster which is essential for the catalytic activity of this enzyme, the conversion of (*E*)-4-hydroxy-3-methylbut-2-en-1-yl diphosphate (HMBPP, 1) into a mixture of isopentenyl diphosphate (IPP) and dimethylallyl diphosphate (DMAPP). The structure of the LytB protein has been solved but the reported structure for substrate free LytB shows a 3Fe-4S cluster.

In collaboration with the nuclear resonance scattering groups at beamlines **ID18**, ESRF, and P01, PETRA III, the structure of 4Fe-4S cluster in the substrate free LytB could be clarified. This was possible by sensing specifically the iron ligand vibrations by means of nuclear resonance vibrational spectroscopy (NRVS). NRVS, also called nuclear inelastic scattering (NIS) of synchrotron radiation, can be regarded as an extension of the conventional energy-resolved Mössbauer spectroscopy to energies in the order of molecular vibrations. The energy of the incoming synchrotron radiation is varied by high resolution monochromators within an interval of up to ±100 meV (± ~800 cm^{-1}) or more around the resonance energy E_γ =14.4 keV of the ^{57}Fe-Mössbauer nucleus with an experimental resolution < 1 meV (8 cm^{-1}).

Our experimental results, in combination with quantum chemical-molecular mechanical calculations on the whole protein, have shown that the substrate-free LytB protein contains an unusual $[4Fe\text{-}4S]^{2+}$ cluster, the apical iron atom of which is linked to three water molecules (**Figure 108**). The presence of three labile water ligands on the apical iron may explain the instability of the $[4Fe\text{-}4S]^{2+}$ cluster in crystallisation experiments causing the very high oxygen sensitivity of the isolated enzyme. To our knowledge, the coordination of the unique site of a 4Fe-4S cluster by three water molecules, as seen for LytB, is unprecedented. Whether the water ligands can also serve as proton donors for the enzymatic reaction of LytB is currently under investigation.

The interaction of LytB with inhibitors has also been investigated. **Figure 109** shows the partial

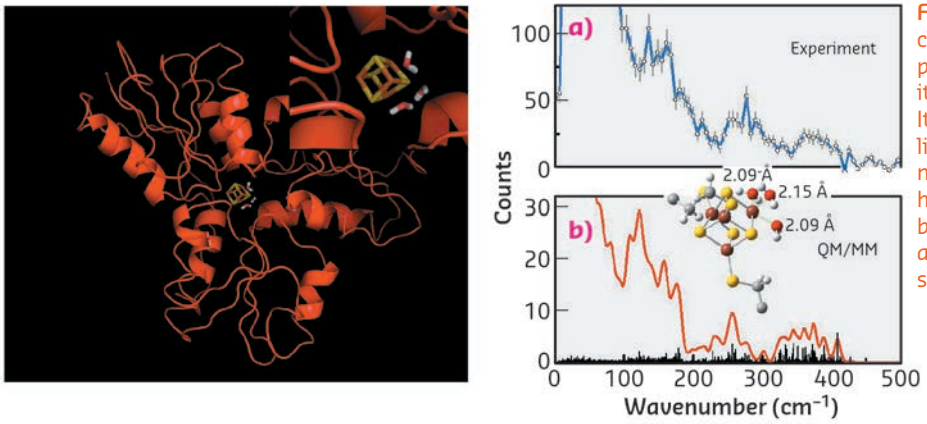

Fig. 108: Left: The [4Fe-4S] cluster of the LytB/IspH protein is essential for its enzymatic function. Its apical iron atom is linked to three water molecules. Right: This has been determined by NRVS experiments and corresponding simulations.

density of vibrational states (pDOS) of LytB bound to its natural substrate 1 as well as to the inhibitors (*E*)-4-amino-3-methylbut-2-en-1-yl diphosphate, 2, and (E)-4-mercapto-3-methylbut-2-en-1-yl diphosphate, 3. There is reasonable agreement between calculated and experimental data and the deviations have been attributed to the presence of slightly different protein conformations in protein crystals and in solution. As already indicated by Mossbauer spectroscopy and more recently by X-ray structure studies, the inhibitor 2 coordinates with its amino group and the inhibitor 3 coordinates with its thiol group to the special site of the 4Fe-4S cluster of LytB [1,2]. However, for the interaction of the amino inhibitor 2 there are two different X-ray structures found in the pdb database. The present work shows that the vibrational properties of the enzyme complexed with inhibitor 2 are better reproduced by one of the two structures (3ZGL.pdb) indicating that this structure is present in solution.

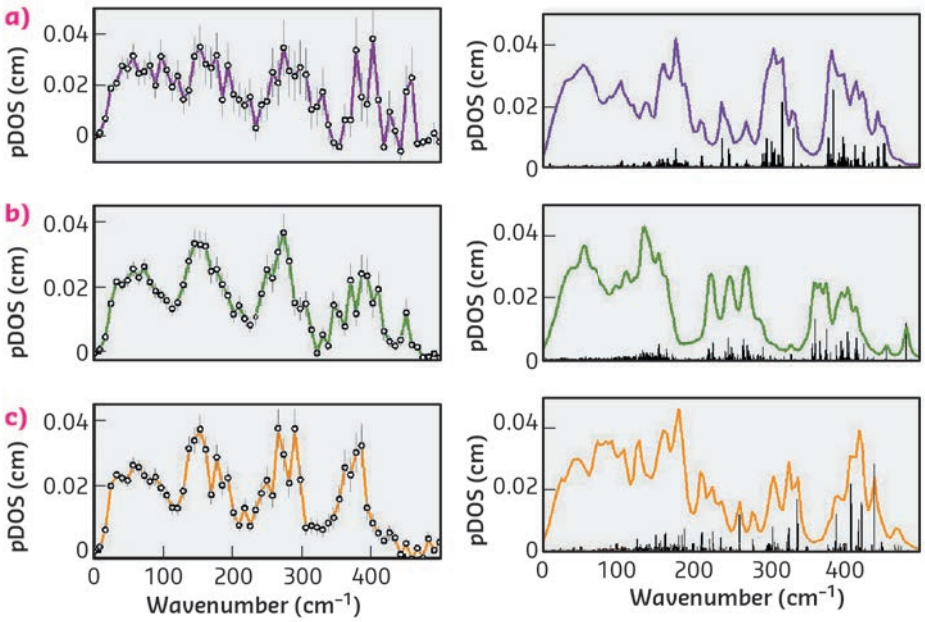

Fig. 109: Left: Partial density of states (pDOS) of the substrate-bound form of LytB (*a*), LytB in complex with inhibitor 2 (b), and LytB in complex with inhibitor 3 (c). Right: pDOS simulations assuming model structures of the active site/inhibitor complexes: (a) substrate-bound LytB; (b) amino inhibitor bound LytB (3ZGL.pdb), (c) thiol-inhibitor bound LytB (4H4E.pdb).

PRINCIPAL PUBLICATION AND AUTHORS

Isoprenoid biosynthesis in pathogenic bacteria: nuclear resonance vibrational spectroscopy provides more insight into the unusual [4Fe-4S] cluster of the LytB/IspHprotein, I. Faus (a), A. Reinhard (a), S. Rackwitz (a), J.A. Wolny (a), K. Schlage (b), H.-C. Wille (b), A. Chumakov (c), S. Krasutsky (d), P. Chaignon (e), C.D. Poulter(d), M. Seemann (e) and V. Schünemann (a), *Angew. Chem. Int. Ed.*, **54**, 12584-12587 (2015); doi: 10.1002/anie.201502494.
(a) University of Kaiserslautern (Germany)
(b) Petra III, DESY, Hamburg (Germany)
(c) ESRF
(d) University of Utah, Salt Lake City (USA)
(e) Université de Strasbourg/CNRS, UMR 7177 (France)

REFERENCES

[1] A. Ahrens-Botzong *et al., Angew. Chem., Int. Ed.* **50**, 11976–11979 (2011).
[2] I. Span *et al., Angew. Chem. Int. Ed.* **52**, 2118 –2121 (2013).

BIMETALLIC NANOALLOYS AS HIGHLY EFFECTIVE HYDROGENATION CATALYSTS

The sugar-derived compounds levulinic acid and γ–valerolactone are expected to play a major role in future schemes for the more sustainable production of both fuels and chemicals. Bimetallic catalysts, if properly prepared, were shown to hold much potential for the conversion of levulinic acid to γ-valerolactone, a key conversion step in biorefinery operations.

Many different types of biomass feeds and many conversion routes, involving numerous different building blocks and end products, are currently being explored for the production of bio-based chemicals. Nonetheless, a limited number of building blocks, so-called platform molecules, are emerging with the potential to play a central role in future biorefinery schemes. Levulinic acid, which is easily obtained from the carbohydrate fraction of (preferably lignocellulosic) biomass, is one such platform molecule and can be catalytically converted to a multitude of value-added products, including polymer monomers, solvents, plasticisers and fuel components. In turn, the production of many of these end products involves the compound γ-valerolactone, which is obtained by hydrogenation of levulinic acid and is in itself a valuable platform molecule. The hydrogenation of levulinic acid to γ-valerolactone is typically

and most conveniently done with heterogeneous, supported metal-based catalysts, in particular Ru-based ones, and molecular hydrogen.

The use of supported bimetallic heterogeneous catalysts can be advantageous, as combinations of two metal in the appropriate proportion and with the nanostructure can lead to superior catalytic performance, in terms of activity, selectivity and/or stability of the catalyst material. Even though such nanoalloyed bimetallic catalysts might have many advantages, so far, their exploitation has been limited for biomass reactions, such as the conversion of levulinic acid to γ-valerolactone. The performance of supported bimetallic nanoparticles is governed by their composition and structural characteristics, which are in turn ultimately determined by the preparation method. It was previously shown that an 'excess-anion', modified impregnation method allowed for the synthesis of supported Au-Pd nanoparticles. The nanoparticles are characterised by a narrow size distribution and a quite homogeneous random nanoalloy structure [1]. We have now demonstrated that the controlled preparation of supported Au-Pd as well as Ru-Pd nanoalloy nanoparticles via this modified impregnation method provides access to catalyst materials that show markedly improved performance in the selective hydrogenation of levulinic acid to γ-valerolactone. Indeed, nanoalloying was found to positively affect the activity and selectivity as well as the stability of the bimetallic catalysts. For example, Au-Pd/TiO_2 showed good activity and excellent selectivity in the hydrogenation reaction, whereas its monometallic counterparts only showed negligible activity under identical conditions. The modified impregnation method was subsequently successfully extended to give a supported Ru-Pd nanoalloy catalyst, which proved to be more selective and more stable upon reuse than its monometallic Ru/TiO_2 counterpart. Extensive characterisation of the bimetallic catalysts was done by a combination of aberration-corrected scanning transmission electron microscopy (STEM), X-ray photoelectron spectroscopy (XPS), Fourier-transform infrared spectroscopy after CO adsorption (FT-IR/CO) and X-ray spectroscopy (XAS). Taken together, the STEM and extended X-ray sbsorption fine structure (EXAFS) measurements, performed at beamlines **BM26A** and **BM23**, showed that the nanoparticles are indeed bimetallic and have a random nanoalloy structure (**Figure 110**). While the bimetallic nature of the Au-Pd catalyst was immediately evident from the Fourier Transform data at both edges, the similarity in X-ray scattering efficiency of Ru and Pd precluded distinguishing between these two metal components. For the latter sample, however, a first shell analysis (on the basis that the STEM results confirmed the bimetallic nature) did indicate intimately mixed bimetallic particles. The XPS and FT-IR/CO data provided further insight into the consequences of the nanoalloying, allowing two distinct effects to be discerned. For the Au-Pd based catalyst, the remarkable increase in activity was attributed to electronic modification of Pd upon alloying with Au. The improved stability and selectivity of the Ru-Pd catalyst were in turn attributed to the dilution and isolation of Ru by Pd in the random nanoalloy. These results highlight the potential of using bimetallic catalysts for the production of bio-based fuels and chemicals, provided that use is made of carefully designed synthesis strategies.

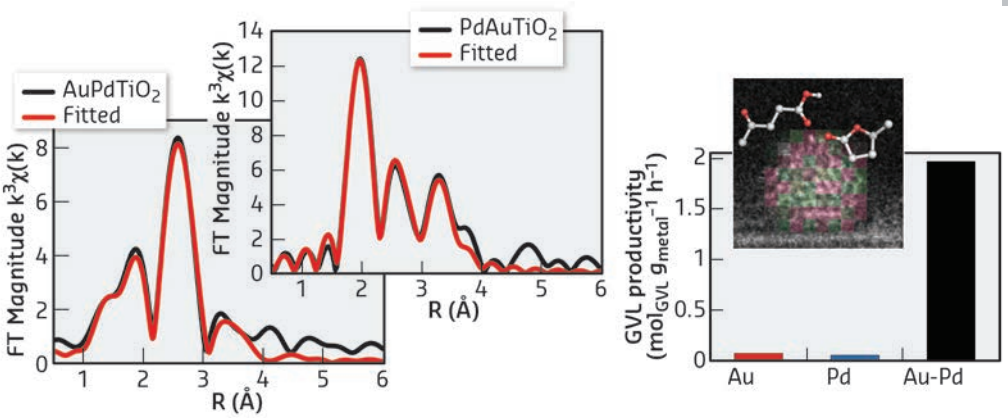

Fig. 110: Bimetallic catalysts show much improved performance in the selective hydrogenation of levulinic acid. EXAFS analysis confirmed the bimetallic nature of the nanoalloys, shown here for the Au-Pd/TiO_2 catalyst, which provides a remarkable improvement in productivity compared to its monometallic counterparts.

PRINCIPAL PUBLICATION AND AUTHORS

High performing and stable supported nano-alloys for the catalytic hydrogenation of levulinic acid to γ-valerolactone, W. Luo (a), M. Sankar (a), A.M. Beale (b,c), Q. He (d), C.J. Kiely (d), P.C.A. Bruijnincx (a) and B.M. Weckhuysen (a), *Nat. Commun.* **6**, 6540 (2015); doi:10.1038/ncomms7540.

(a) Inorganic Chemistry and Catalysis, Utrecht University (The Netherlands)
(b) UK Catalysis Hub, Research Complex at Harwell, Rutherford Appleton Laboratory, Oxford (UK)
(c) Department of Chemistry, University College London (UK)
(d) Department of Materials Science and Engineering, Lehigh University, Bethlehem (USA)

REFERENCES

[1] M. Sankar *et al.*, *ACS Nano* **6**, 6600-6613 (2012).

SYNCHROTRON X-RAY SPECTROSCOPY SHEDS LIGHT ON THE MAJOR Cu-SPECIES IN THE Cu-CHA deNO$_x$ CATALYST

The NH_3-SCR reaction catalysed by Cu-exchanged zeolites is a promising way to remove hazardous NO_x from diesel engine exhaust gases. Synchrotron-based spectroscopy unravelled the molecular-scale structure of Cu-sites in the dehydrated and working catalyst, a key step towards improved aftertreatment systems able to cut down harmful emissions from road traffic.

Road transport is a primary need in our everyday life and a major driving force of our economy. Unfortunately, the huge vehicle fleet moving people and freights all over Europe every day is also one of the major sources of air pollution in urban areas, with detrimental effects on human health and global ecology. The principal pollutants present in the exhausts from the increasingly popular diesel engines include mono-nitrogen oxides (NO_x), particulate matter (PM), hydrocarbons (HC) and carbon monoxide (CO). The development of aftertreatment systems able to abate these noxious emissions, meeting the increasingly demanding air-quality standards, is an ongoing challenge, which nowadays attracts an enormous research interest.

The state-of-the-art options combine separate catalytic reactors for the different exhaust gas cleaning operations (Figure 111a). Here, molecular-level knowledge of the complex active phases in each cleaning unit is becoming an urgency to further improve the system performance. The most efficient deNO$_x$ units employ selective catalytic reduction (SCR), with the addition of excess ammonia, *e.g.* from urea. Among the various catalysts developed for NH_3-SCR, the Cu-exchanged chabazite zeolite (Cu-CHA) has been selected as the best candidate for commercial applications due to its enhanced catalytic activity and hydrothermal stability (Figure 112b) [1,2].

The combination of XAS and XES experiments at beamlines **BM23** and **ID26**, respectively, allowed investigation of the Cu-species hosted in the CHA framework during the dehydration process as a function of temperature and gaseous environment, a crucial step towards unravelling the structure-properties relationships of this promising catalyst. A closed reactor cell connected to a gas rig allowed us to monitor the evolution of the copper coordination

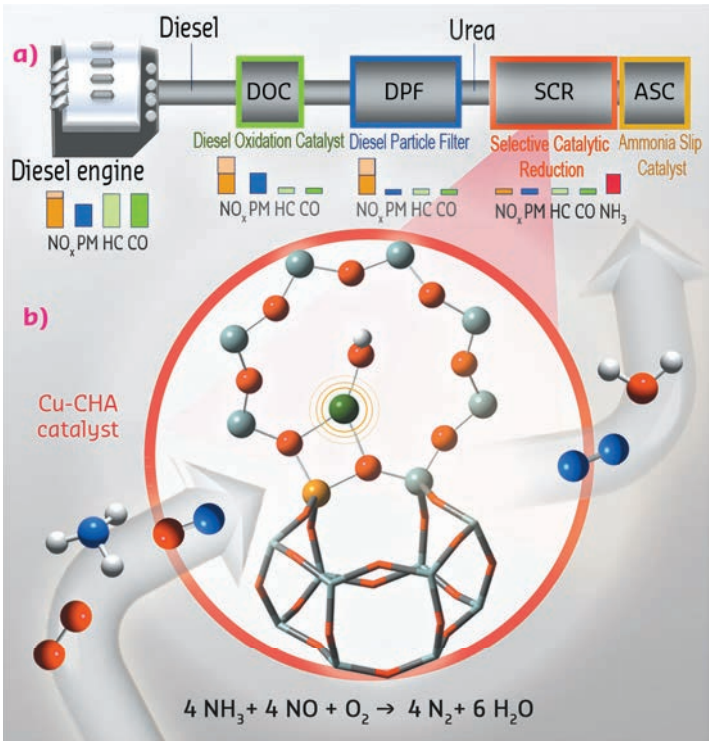

Fig. 111: (a) Schema of a state-of-the-art diesel aftertreatment system, showing the typical levels of major pollutants after each gas-cleaning unit. (b) Molecular-scale magnification of the deNO$_x$ unit, representing the NH_3-SCR reaction on a Cu-CHA catalyst.

environment and oxidation state at realistic exhaust gas compositions and temperatures (Figure 112a, b). The major species present in the catalyst after dehydration were identified by DFT-assisted EXAFS fits and XANES/XES simulations (Figure 112c, d), considering several possible Cu(II) and Cu(I) sites in the CHA framework.

Data analysis revealed that the dehydration process of Cu cations is essentially completed at 250°C, with the formation of dehydrated $[CuOH]^+$ species hosted in close proximity to 1 Al sites mostly in *8r* units of the CHA zeolite. These species persist at higher temperature only if a certain amount of O_2 is present in the gas feed, while in He-flux they undergo virtually total "self-reduction" as a consequence of an OH extra-ligand loss, resulting in bi-coordinated bare Cu^+ cations (Figure 112e).

These results pave the way to the development of a consistent scheme for the SCR reaction on isolated Cu sites in Cu-CHA, able to produce the correct stoichiometry while allowing adsorption and desorption of only stable molecules [3]. XAS and XES studies at the ESRF, carried out in *operando* and *in situ* conditions at the BM23 and ID26 beamlines [3, 4], were determinant to experimentally validate the proposed reaction mechanism.

All these findings resulted in a greatly improved understanding of the SCR chemistry on Cu-CHA, and demonstrated the power of synchrotron-based spectroscopy in tackling the 'catalyst characterisation challenge' to design improved aftertreatment systems for cleaner road vehicles.

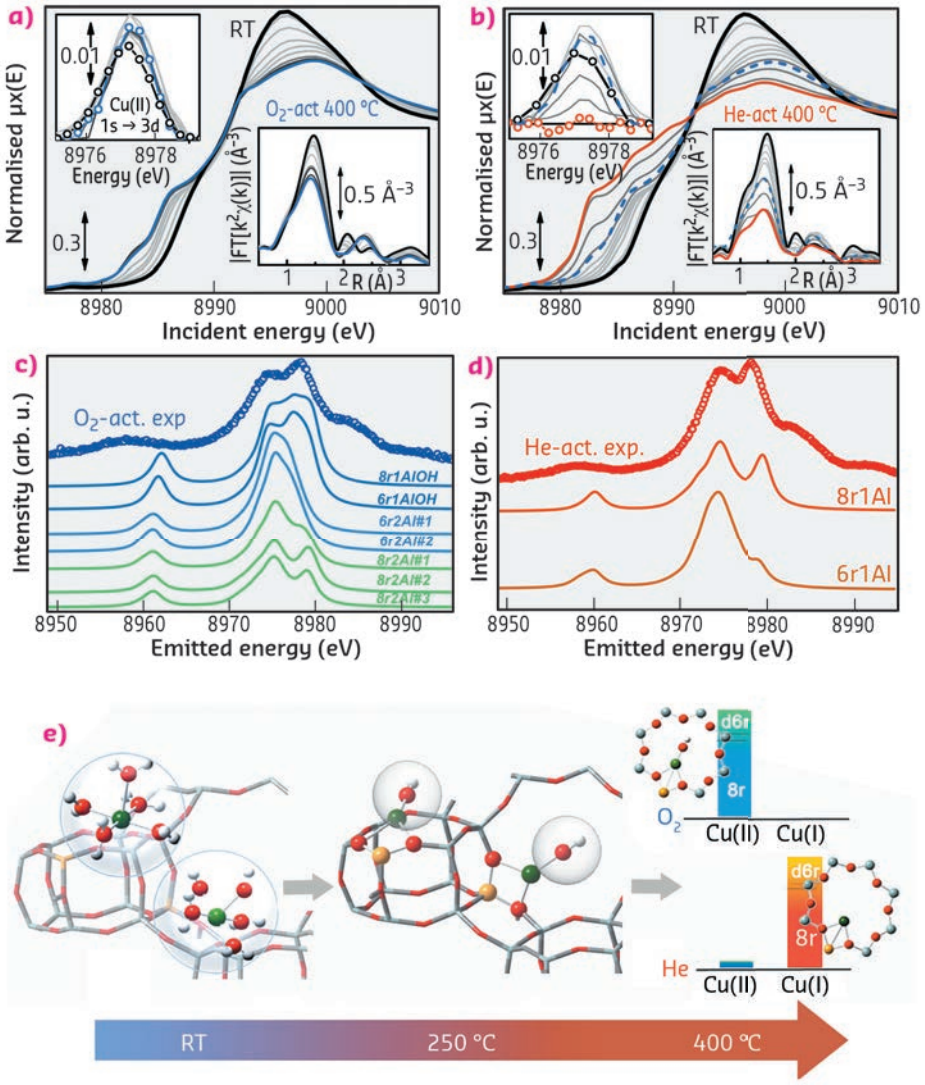

Fig. 112: (a,b) *In situ* XANES and EXAFS (insets) spectra collected at BM23 while heating the Cu-CHA catalyst from RT to 400°C in O_2/He (a) and He flux (b); (c,d) Experimental XES spectra (coloured circles) measured at ID26 after dehydration in O_2/He (c) and He flux (d) and corresponding theoretical curves from several DFT-optimised Cu(II) and Cu(I) sites in Cu-CHA; (e) Cu-speciation in the Cu-CHA catalyst as a function of the dehydration temperature and gaseous atmosphere, as derived from XAS and XES analysis.

PRINCIPAL PUBLICATION AND AUTHORS

Revisiting the nature of Cu sites in the activated Cu-SSZ-13 catalyst for SCR reaction, E. Borfecchia (a), K.A. Lomachenko (a,c), F. Giordanino (a), H. Falsig (b), P. Beato (b), A.V. Soldatov (c), S. Bordiga (a) and C. Lamberti (a,c), *Chem. Sci.* **6**, 548-563 (2015); doi: 10.1039/C4SC02907K.

(a) Department of Chemistry, NIS Centre and INSTM Reference Center, University of Turin (Italy)
(b) Haldor Topsøe A/S, Lyngby (Denmark)
(c) Southern Federal University, Rostov-on-Don (Russia)

REFERENCES

[1] U. Deka *et al.*, *ACS Catal.* **3**, 413-427 (2013).
[2] A.M. Beale *et al.*, *Chem. Soc. Rev.* **44**, 7371-7405 (2015).
[3] T.V.W. Janssens *et al.*, *ACS Catal.* **5**, 2832-2845 (2015).
[4] F. Giordanino *et al.*, *J. Phys. Chem. Lett.* **5**, 1552-1559 (2014).

IN SITU STUDIES OF PALLADIUM NANOPARTICLES DURING METHANE OXIDATION

Uncombusted methane is difficult to remove from the exhausts of natural gas vehicles using catalytic aftertreatment techniques because of methane's stability, it is the most stable hydrocarbon. A catalyst for the total oxidation of methane, composed of palladium nanoparticles, was studied with the aim of monitoring the composition of the catalytically active material while the reaction occurs.

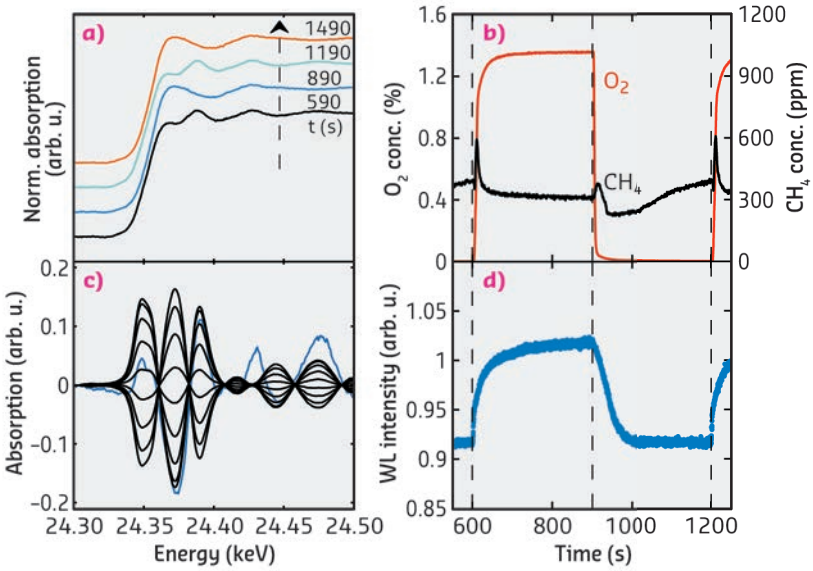

Fig. 113: Results from oxygen pulse experiments during methane oxidation over Pd/Al_2O_3 at 350°C. a) XANES spectra, (b) outlet concentration of oxygen (red) and methane (black), (c) demodulated spectra by phase sensitive detection (black) and difference spectrum Pd-PdO (blue), and (d) whiteline intensity at 24.37 keV.

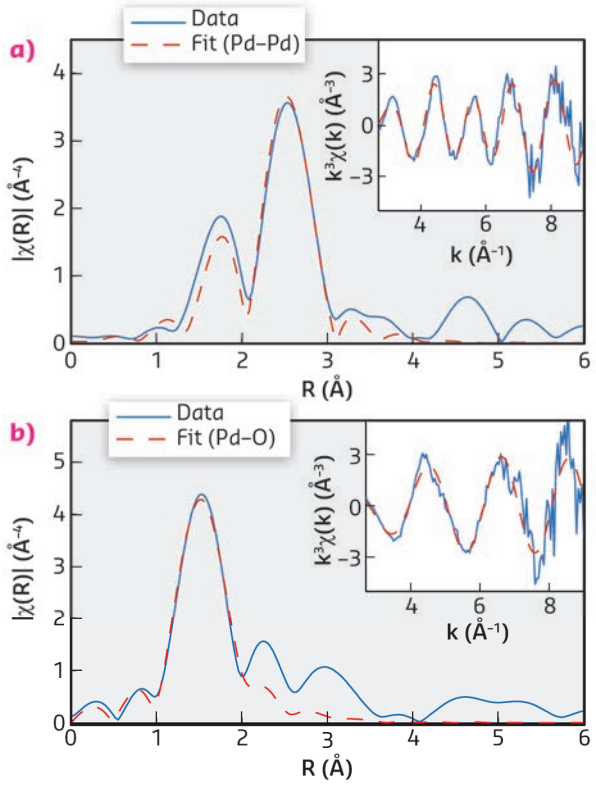

Fig. 114: (a) Fourier transformed EXAFS spectra and EXAFS fit recorded at: (a) the end of the rich period, and (b) at the end of the lean period.

Methane is the most stable hydrocarbon, its catalytic combustion requires relatively high temperatures to proceed at an acceptable rate. The noble metals palladium and platinum are the most active catalysts for methane oxidation and the metal which performs best generally depends on the operating conditions. For palladium, it has been reported that there are two phases of palladium with high activity for methane oxidation; a reduced phase and an oxidised phase [1]. Here we have investigated methane oxidation over Pd/Al_2O_3 and Pd/CeO_2 catalysts during periodic oxygen pulsing using time-resolved *in situ* X-ray absorption spectroscopy (XAS) to monitor the composition of the active phase.

X-ray absorption spectra monitoring the Pd K-edge with sub-second time resolution were recorded using the energy dispersive XAS technique at beamline **ID24**. 2% Pd/Al_2O_3 and 2% Pd/CeO_2 catalysts were subjected to alternating lean and rich feed gas compositions with 0.1% CH_4 + 1.5% O_2 and 0.1% CH_4, respectively. The outlet concentrations of reactants and reaction products were monitored with mass spectrometry.

Figure 113 shows results obtained from the Pd/Al_2O_3 catalyst at 350°C. The near-edge region of the X-ray absorption spectra (Figure 113a) changes reversibly over subsequent rich and lean periods. To analyse the changes in the near edge region, we utilised the phase sensitive detection (PSD) technique [2] which can be used when spectra change reversibly and periodically with time. Using a mathematical transformation, the spectra are transferred from the time domain to the domain of a phase angle and simultaneously static features like the absorption edge and the background are removed. Figure 113c shows the PSD demodulated spectra for phase angles 0-160°. These spectra are similar to the Pd-PdO difference spectrum which shows that oxidation and reduction are the main driving forces behind the changes in the spectra.

The methane outlet concentration over one pulse sequence is shown in Figure 113b. To follow the oxidation state of the catalyst as a function of time we plot the whiteline intensity

in Figure 113d. A first-shell EXAFS fit was performed to further analyse the state of the catalyst at the end of the rich and lean period (Figure 114). The EXAFS fits indicate that at the end of the rich period palladium is in a state similar to metallic Pd while at the end of the lean period palladium is in a state similar to bulk PdO.

At the start of the lean period there is an increase in methane outlet concentration when oxygen builds up on the surface of the reduced Pd catalyst. Palladium is rapidly oxidised, as indicated by the increasing whiteline intensity, also the methane outlet concentration decreases and then holds steady for the remainder of the lean period. At the start of the rich period the methane outlet concentration increases when the oxygen concentration in the gas phase decreases, however, after the reduction of palladium has started, as indicated by the decreasing whiteline intensity, the methane outlet concentration decreases and reaches the lowest value observed during the pulse sequence. In the later parts of the rich period the methane concentration increases when oxygen becomes a limiting reactant.

In conclusion we have used time-resolved *in situ* X-ray absorption spectroscopy to monitor the state of palladium in supported Pd catalysts during methane oxidation. The highest conversion of methane is observed during the reduction of oxidised palladium to metallic palladium, which indicates that reduced palladium or partially reduced palladium has high activity for methane oxidation.

PRINCIPAL PUBLICATION AND AUTHORS

Chemistry of supported palladium nanoparticles during methane oxidation, J. Nilsson (a,b), P.-A. Carlsson (a,b), S. Fouladvand (a,b), N.M. Martin (a,b), J. Gustafson (c), M.A. Newton (d), E. Lundgren (c) and H. Grönbeck (b,e) and M. Skoglundh (a,b), *ACS Catalysis*, **5**, 2481-2489 (2015);
doi: 10.1021/cs502036d.

(a) Department of Chemistry and Chemical Engineering, Chalmers University of Technology, Göteborg (Sweden)
(b) Competence Centre for Catalysis (KCK), Chalmers University of Technology, Göteborg (Sweden)
(c) Division of Synchrotron Radiation Research, Lund University (Sweden)
(d) ESRF
(e) Department of Applied Physics, Chalmers University of Technology, Göteborg (Sweden)

REFERENCES

[1] A. Hellman *et al.*, *J. Phys. Chem. Lett.* **3**, 678–682 (2012).
[2] D. Ferri *et al.*, *Top. Catal.* **54**, 1070–1078 (2011).

Structural biology

The completion of Phase I of the ESRF Upgrade project in December 2015 has marked a major milestone for the ESRF Structural Biology Group. The four beamlines MASSIF-1 [ID30A-1], MASSIF-3 [ID30A-3], BM29 and ID30B constructed as part of the UPBL10 project and designed to replace the almost mythical ID14 are now all in full operation, both increasing the functionality available to the ESRF Structural Biology User Community [1, 2] and ensuring that sufficient beamtime can be allocated for even the most challenging of projects. The new functionality available is impressive. BM29 is the state-of-the-art facility for BioSAXS while MASSIF-1 offers an increasingly popular hands-off, completely automatic diffraction data collection and, if necessary, structure solution service (see S. Kharde *et al.* [3] for an example of what is possible without any direct user intervention). The more recently commissioned MASSIF-3 – where we expect an Eiger 4M detector capable of operating at a maximal frame rate of 750 Hz to be available to users from spring 2016 – is a fixed-energy end-station providing a very high flux microbeam at the sample position while ID30B, the variable wavelength replacement for ID14-4, provides the possibility to vary the beamsize at the sample position, the possibility (summer 2016) of *in situ* (*i.e.* in crystallisation plate) data collection and is the test bed for a new Flex-HCD sample changing robot that will, over the next year or two, replace the SC3 sample changers installed on most end-stations.

A strength of the Structural Biology Group has been its ability to continue to provide world-leading service to our user community while commissioning new facilities. During the UPBL10 project, three of the group's beamlines, ID23-1, ID23-2 and ID29 have ensured that this has remained the case. Thus, while future editions of ESRF Highlights will surely contain articles based on data collected at the UPBL10 end-stations, this chapter necessarily focuses on some of the extremely interesting results obtained using diffraction data collected at these 'workhorse' beamlines. As is always the case, the highlights reported here cover a wide range of structural biology research, published in high-impact journals, including structural studies of membrane proteins (including the giant mitochondrial Complex 1), protein-protein and protein-DNA complexes and other systems that provide significant insights in understanding the molecular basis of diseases or their prevention. In this area, a particular highlight in 2015 is the elucidation, by Rey and colleagues, of the mechanism of action of a series of antibodies (bnAbs) which broadly neutralise the dengue virus. This study reveals that the bnAbs target an 'Achilles Heel' of the virus, conserved in all four serotypes and gives hope that a vaccine fully protecting against this disease might be available in the not too distant future.

The insights provided by the articles included here are not always the result of single-crystal X-ray diffraction data collection. Indeed, one of the highlights included here (by Giachin and colleagues) reports the results of an investigation, carried out using extended X-ray absorption fine structure (EXAFS) spectroscopy, of the influence of copper ion coordination in the conversion of the prion protein (PrP^C) into a misfolded isoform that causes prion-related diseases including so-called 'mad cow disease' in animals and the Creutzfeldt-Jakob disease in humans. This work amply illustrates the increasing use of complementary techniques in structural biology and we predict many more articles illustrating studies carried out using techniques available at beamlines outside the ESRF's Structural Biology Group portfolio in future editions of ESRF Highlights.

With Phase I of the ESRF Upgrade completed, 2015 also saw the official launch of Phase II of the project, ESRF-EBS, and our thoughts have now firmly turned to how best future generations of structural biologists can exploit the ultra-brilliant X-ray beams that will be produced. Data collection from single cryocooled crystals will clearly remain a staple technique. However, the reduction in the horizontal emittance of the electron beam in the storage ring and the corresponding reduction in X-ray beam size and divergence that the EBS project will bring, will allow the development of a new generation of ESRF MX beamlines with, in some cases, flux densities at the sample position ~5 orders of magnitude higher than is currently the case. Such beamlines, when operated in conjunction with high frame-rate (>1 kHz), continuous readout, detectors will be optimised for multi-crystal data collection techniques both at cryo [4] and room temperatures, synchrotron serial crystallography (SSX, see article by Nogly *et al.*, in this chapter). We also anticipate a revival in time-resolved crystallography studies employing pump-probe methods and predict that, in the future, crystal structure analysis will involved, for a single target, multiple structure determinations. This will enable the

conformational landscape of the molecule under study to be better mapped than is currently the case. This information, when combined with data from other techniques [5] including small-angle X-ray scattering, NMR spectroscopy, cryo-electron microscopy and theoretical calculations – all of which are available via the technical platforms of the Partnership for Structural Biology (http://www.psb-grenoble.eu/) – will enable and facilitate studies of the dynamics of biological macromolecules that are crucial to understanding the way in which they function.

We will, as usual, consult the ESRF Structural Biology User Community when planning the best way forward. To this end, following Phase-II-centred sessions at workshops organised at the 2014 (SSX) and 2015 (complementary techniques in Structural Biology), the ESRF User Meeting in 2016 features a micro symposium dedicated to possibilities in (time-resolved) room temperature crystallography.

G. LEONARD and
C. MUELLER-DIECKMANN

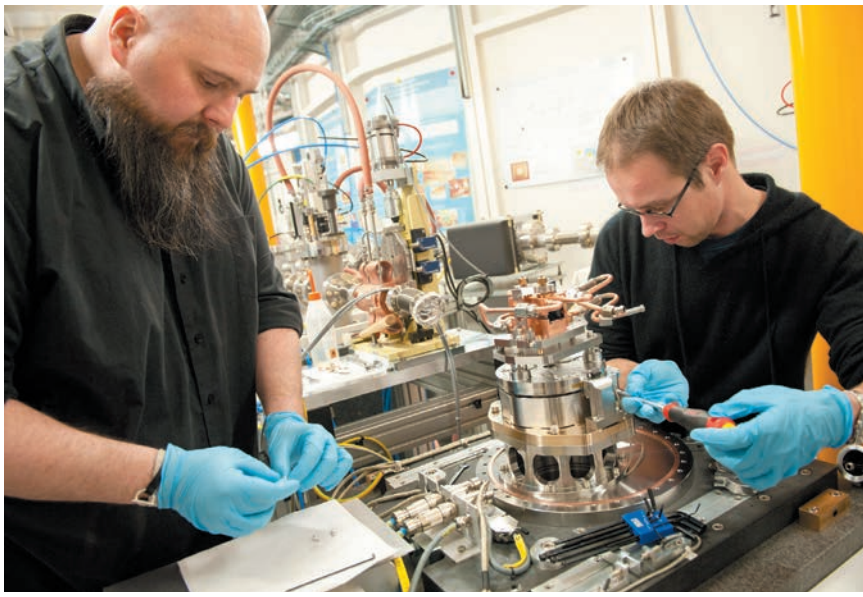

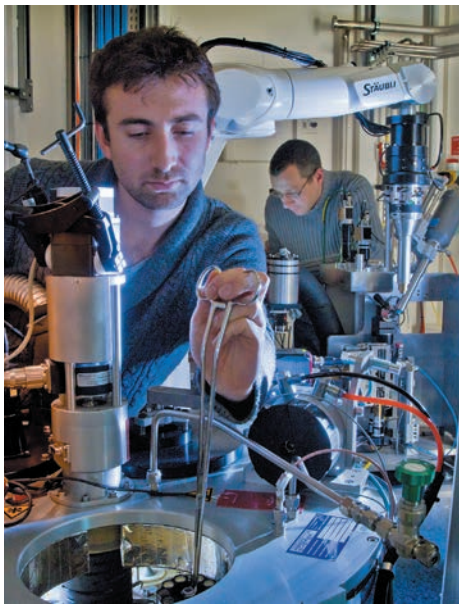

REFERENCES

[1] C. Mueller-Dieckmann *et al.*, *Eur. Phys. J. Plus* **130**, 70 (2015).
[2] A. Round *et al.*, *Acta Cryst.* **D71**, 67-75 (2015).
[3] S. Kharde *et al.*, *Nucleic Acids Res.* **43**, 7083–95 (2015).
[4] U. Zander *et al.*, *Acta Cryst.* **D71**, 2328-2343 (2015).
[5] S. Larsen, *IUCrJ*, **2**, 475-476 (2015).

STRUCTURE AND FLEXIBILITY OF ENDOSOMAL Vps34 COMPLEX II

The phosphatidylinsositol 3-kinase complexes have fundamental roles in endocytic sorting, cytokinesis and autophagy. The structure of the endosomal Vps34 complex II was solved. This is a heterotetrameric assembly composed of Vps34, Vps15, Vps30/Atg6 and Vps38. In addition, hydrogen-deuterium exchange mass spectrometry provided insights into the way the complex adapts to membranes.

Phosphoinositide 3-kinases (PI3Ks) are a diverse family of enzymes that produce lipid second messengers in signalling pathways, with an ancient role in nutrient sensing. The PtdIns3P produced by the class III PI3K, Vps34, is critical for cargo sorting and membrane trafficking in endocytosis, phagocytosis, autophagy and cell division. This enzyme is present in several complexes. Complex I functions in autophagy and has four subunits: lipid kinase Vps34, protein kinase Vps15 (p150), Vps30/Atg6 (Beclin 1) and Atg14 (ATG14L). Complex II has Vps38 (UVRAG) instead of Atg14 and is involved in endocytic trafficking, as well as autophagy and cytokinesis in mammalian cells. A third complex containing Vps34 and Vps15 but not Vps30, Vps38 or Atg14 has been described, however, it might also include other previously uncharacterised proteins. The Vps34 complexes have been implicated in cancer, neurodegenerative diseases and ageing, which has led to a great interest in the development of specific inhibitors and activators of the complexes as well as in gaining a deeper understanding of how Vps34 complexes are regulated. To undepin these efforts, we have determined a crystal structure of Vps34 complex II and studied its membrane interactions by hydrogen-deuterium exchange mass spectrometry (HDX-MS).

Crystallisation required the presence of a nanobody specifically recognising Vps34. A final resolution of 4.4 Å was achieved at beamline **ID29**. To enable structure solution, high quality phase information was obtained using a Ta_6Br_{12} derivative. High redundancy datasets were collected using the optimised data collection parameters from RADDOSE [1] together with the use of a mini-kappa goniometer to maximise the anomalous signal.

The structure revealed a Y-shaped complex, with the Vps34 C2 domain at its centre, engaging all the other subunits (Figure 115). In one arm, the lipid kinase Vps34 and the protein kinase Vps15 are intertwined, with their kinase domains directly interacting. Several catalytically important elements of Vps34, including the activation loop known to bind lipids, are found in close proximity to Vps15, which might indicate the way Vps15 modulates the kinase activity of Vps34. In the other arm, Vps30 and Vps38 form an extended bracket-like structure that fits on the Vps34/Vps15 catalytic heterodimer, suggesting a path for complex assembly.

To understand how the complex functions on membranes, we performed HDX-MS analysis in the presence and the absence of lipids. We identified a loop in the C-terminal domain of Vps30 (referred to as "aromatic finger") to be important for direct interaction with membranes (Figure 116). We have also observed several localised changes in HDX-MS rate away from the membrane interacting surface suggesting conformational changes in the complex upon membrane binding. These changes would be compatible with global opening/closing motions we observed in normal mode analysis.

Our kinase assays showed that complex I and II had very similar activities on small 100 nM vesicles which were significantly higher than the activity of Vps34/Vps15 heterodimer. An "aromatic finger" mutant reduced the activity of the complex II to that of Vps34/Vps15, highlighting the importance of both arms for membrane binding. On giant unilamellar vesicles (10 µm on average), only complex II was active, and its activity was abolished by the mutation of the "aromatic finger".

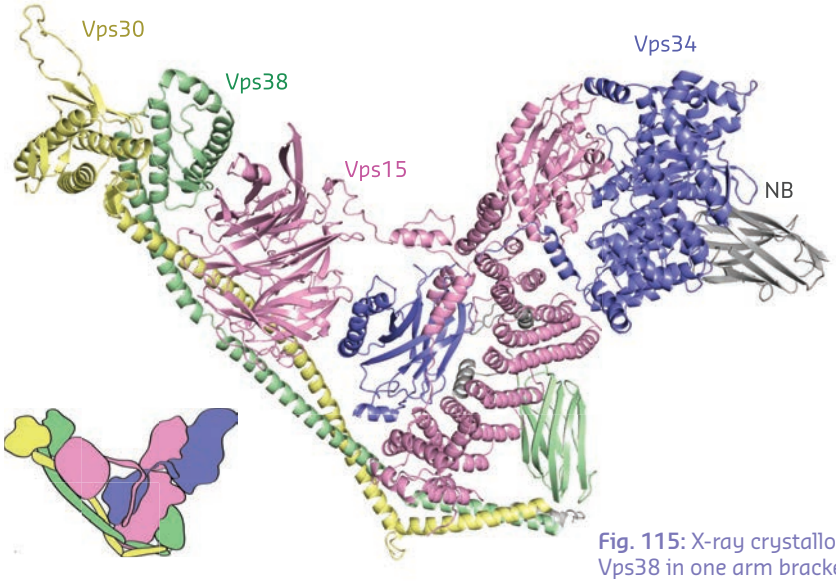

Fig. 115: X-ray crystallography shows that complex II has a Y-shape, with Vps30/Vps38 in one arm bracketing the Vps15/Vps34 heterodimer in the other arm.

Together, the structure of complex II, HDX-MS and kinase activity data allowed us to propose a model of how Vps34 complexes would adapt to membranes. The tips of the two arms would engage in membrane interaction, with the "aromatic finger" in one arm being required for the efficient catalysis by the other arm. In cells, complex I is involved in the initiation of autophagy where its activity would be restricted to small, highly curved tubular/vesicular structures, which could be related to the lack of activity on giant vesicles, exhibiting low curvature. On the other hand, complex II is involved in endocytic trafficking were it could encounter flat or curved membranes. To adapt to these differences in curvature, the two arms of the complex would open, providing the optimal interaction with the lipid substrate.

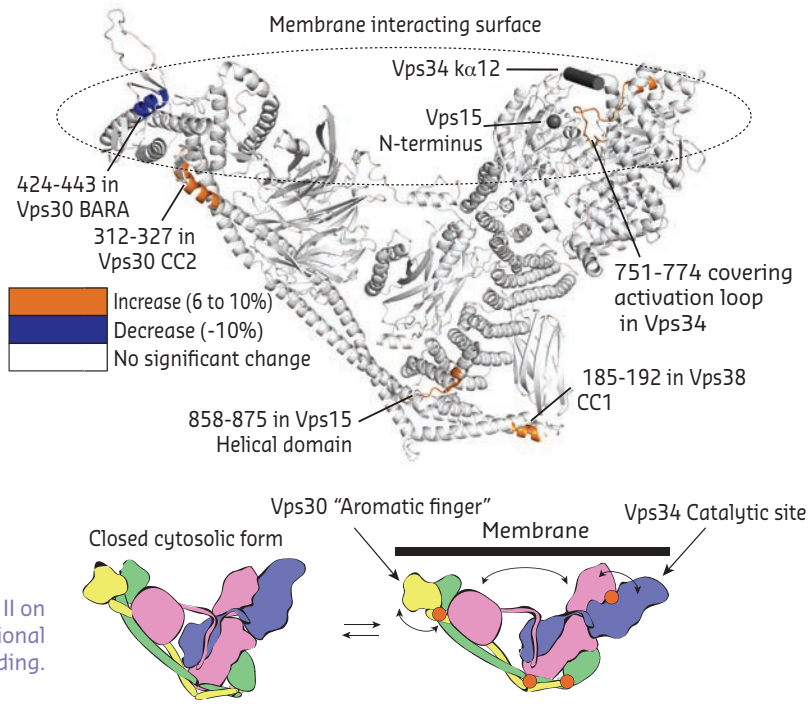

Fig. 116: Dynamics of Vps34 complex II on membranes. HDX-MS suggest conformational changes on membrane binding.

PRINCIPAL PUBLICATION AND AUTHORS

Structure and flexibility of the endosomal Vps34 complex reveals the basis of its function on membranes, K. Rostislavleva (a), N. Soler (a), Y. Ohashi (a), L. Zhang (a), E. Pardon (b), J.E. Burke (c), G.R. Masson (a), C. Johnson (a), J. Steyaert (b), N.T. Ktistakis (d) and R.L. Williams (a), *Science* **350**, 6257 (2015); doi: 10.1126/science.aac7365.

(a) MRC Laboratory of Molecular Biology, Cambridge (UK)
(b) Structural Biology Research Center, VIB, Brussels (Belgium)
Structural Biology Brussels, Vrije Universiteit Brussel (Belgium)
(c) Department of Biochemistry and Microbiology, University of Victoria (Canada)
(d) The Babraham Institute, Cambridge (UK)

REFERENCES

[1] K.S. Paithankar *et al.*, *Acta Crystallogr. D* **66**, 381–388 (2010).

MECHANISTIC CLUES FROM THE STRUCTURE OF MITOCHONDRIAL COMPLEX I

The crystal structure of mitochondrial complex I, a central player in cellular energy conversion, provided important insights into the mechanism and regulation of this giant membrane protein.

Complex I (proton pumping NADH:ubiquinone oxidoreductase) [1] is the first component of the respiratory chain in the mitochondrial inner membrane. Mitochondria gain energy by oxidising hydrogen extracted from nutrients, converting it into a proton gradient that is then used to synthesise adenosine tri-phosphate (ATP), the universal energy currency of the cell. Complex I couples the transfer of two electrons from NADH (reduced nicotinamide adenine dinucleotide) to ubiquinone with the pumping of four protons across the inner mitochondrial membrane. Defects in human complex I are the most frequent cause of inherited mitochondrial disorders and are implicated in numerous (neuro)degenerative diseases and ageing. The mitochondrial, but not the bacterial complex, is regulated by the so-called active/deactive (A/D) transition. Arresting the enzyme in the deactive conformation by modifying a specific cysteine residue [2] protects the heart from reperfusion injury by preventing complex I from producing reactive oxygen species.

Mitochondrial complex I is a very large membrane integral multiprotein assembly of more than 40 different subunits. 14 central subunits harbour the catalytic function and are conserved from bacteria to human. The functions of most of the remaining accessory subunits are still elusive.

We crystallised intact mitochondrial complex I (~1 MDa, 41 subunits) from the yeast *Yarrowia lipolytica*. Using initial phase information from TaBr derivatives, we had previously obtained a first electron density map at 6.3 Å resolution with data measured at several beamlines at the ESRF and the Swiss Light Source [3]. Since then,

markedly improved resolution was achieved through extensive optimisation of cryo-conditions, including rapid crystal cooling in liquid propane, and of data collection strategies that took advantage of the excellent beam quality at **ID29** and **ID23-1** coupled with Pilatus detectors. Using the microfocus beamline **ID23-2**, we could probe very large complex I crystals and conclude that they were largely homogeneous. This allowed the use of a larger beam size to illuminate a larger crystal volume yielding better datasets. Ultimately, datasets from the best crystal - diffracting X-rays anisotropically to 3.6 x 3.9 x 3.9 Å resolution - were collected at 5 K using helium cooling on beamline PXI at SLS. More phase information was obtained from additional derivatives, from the anomalous signal of the iron contained in the complex, and from selenomethionine labelled complex I.

Our current complex I structure comprises the 14 central subunits and the largest accessory subunit, with about half of the residues with side chains and the others as polyalanine chains, and additional polyalanine traces of accessory subunits. Overall, complex I is L-shaped consisting of a peripheral arm pointing into the mitochondrial matrix and a membrane arm integrated in the inner mitochondrial membrane (Figure 117). NADH oxidation occurs in the peripheral arm delivering electrons via a series of seven iron-sulfur clusters to the ubiquinone reduction pocket, which we could clearly identify using anomalous signals of a brominated substrate inhibitor analogue. From a narrow opening in the membrane domain, the pocket reaches about 30 Å into the peripheral arm and connects to a long 'central axis' of acidic and basic amino acid residues resembling an electric wire running through the middle of the entire membrane arm thereby connecting four putative proton pathways crossing the membrane. This remarkable arrangement spatially separates electron transfer and proton pumping covering a distance of more than 300 Å. Since the quinone-binding pocket connects these two functional branches, it seems likely that the redox chemistry of ubiquinone plays a pivotal role in transmitting energy into the membrane arm via the 'central axis' to drive proton translocation [1].

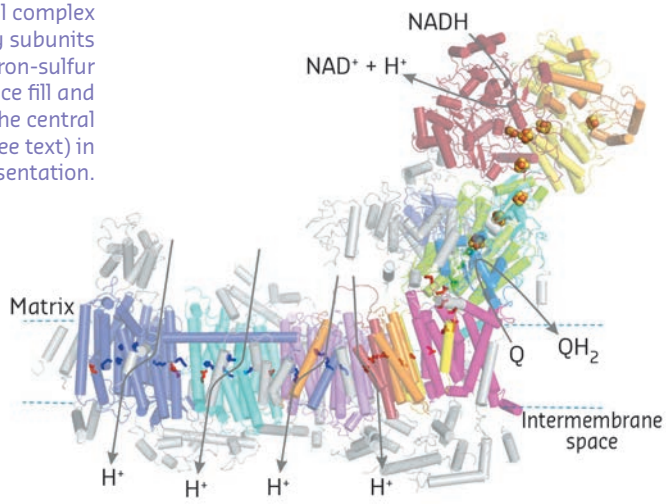

Fig. 117: Structural overview and functional topology of mitochondrial complex I. Accessory subunits in grey. Iron-sulfur clusters in space fill and selected of the central axis residues (see text) in stick representation.

Since we crystallised the deactive form, our structure provided important clues to the conformational changes associated with complex I regulation. Relocation of the ubiquinone-binding site seemed to render the enzyme deactive by moving the pocket away from the iron-sulfur clusters. Intriguingly, this implicates a defined rearrangement of surrounding structural elements including the loop carrying the cysteine controlling the A/D transition and a loop of the first membrane integral subunit comprising the start of the 'central axis'. Thereby our X-ray data provide a structural basis, for the active/deactive transition and for a previously proposed hypothetical energy conversion mechanism [4]. According to this mechanism, stabilisation of negatively charged ubiquinone intermediates provides the energy for specific conformational changes that are transmitted into the membrane arm to drive proton pumping of complex I.

PRINCIPAL PUBLICATION AND AUTHORS

Mechanistic insight from the crystal structure of mitochondrial complex I,
V. Zickermann (a,b), C. Wirth (c), H. Nasiri (d,e), K. Siegmund (a), H. Schwalbe (b,e), C. Hunte (c) and U. Brandt (b,f), *Science* **347**, 44-49 (2015); doi: 10.1126/science.1259859.
(a) Structural Bioenergetics Group, Institute of Biochemistry II, Medical School, Goethe-University, Frankfurt am Main (Germany)
(b) Cluster of Excellence Frankfurt "Macromolecular Complexes", Goethe-University, Frankfurt am Main (Germany)
(c) Institute of Biochemistry and Molecular Biology, BIOSS Centre for Biological Signalling Studies, University of Freiburg (Germany)
(d) Department of Chemistry, University of Cambridge (UK)
(e) Institute of Organic Chemistry and Chemical Biology, Goethe-University, Frankfurt am Main (Germany)
(f) Nijmegen Center for Mitochondrial Disorders, Radboudumc, Nijmegen (Netherlands)

REFERENCES

[1] U. Brandt, *Annu. Rev. Biochem.* **75**, 69-92 (2006).
[2] A. Galkin *et al.*, *J. Biol. Chem.* **283**, 20907-20913 (2008).
[3] C. Hunte *et al.*, *Science* **329**, 448-451 (2010).
[4] U. Brandt, *Biochim. Biophys. Acta* **1807**, 1364-1369 (2011).

CONVERGING PEPTIDE- AND DNA-NANOTECHNOLOGY: MOLECULAR SELF-ASSEMBLY OF PEPTIDE NUCLEIC ACIDS

A new family of nanostructures sharing properties of both peptide and DNA was discovered. Peptide nucleic acids containing a peptide-like backbone and nucleic acid side-chains has been found to efficiently form ordered assemblies of unique optical properties. X-ray crystallography demonstrated the combination of stacking interactions together with canonical Watson-Crick base-paring as observed in double-helix DNA.

Biology serves as a major inspiration for the assembly of ordered structures at the nanoscale. Two main directions for the development of bio-inspired nanomaterials are based either on the use of protein and peptide building blocks or, alternatively, on the use of DNA. Polypeptide structures have the advantage of structural integrity and robustness while nucleic acids have the advantage of specific molecular recognition between complementary bases.

Our group has been extensively involved in the study of molecular self-assembly by extremely short peptide fragments. We demonstrated in 2003 that simple dipeptides contain all the molecular information needed to form ordered nanostructures [1]. Furthermore, peptide assemblies have been shown to exhibit remarkable physical properties including high mechanical rigidity, luminescence, piezoelectricity, and semiconductivity [2]. The dipeptide assemblies act as supramolecular polymers including a clear phase transition governed by Ostwald's rule of stages [3] and thus may be compared to the polyamide covalent polymers mentioned above.

Parallel to the work on peptides, the field of DNA nanotechnology, pioneered by N.C. Seeman in the 1980s [4], is rapidly advancing and complex architectures at the nanoscale can be obtained.

We have sought to converge the two distinct fields of DNA and peptide self-assembly by using an artificially synthesised polymer that has attributes of both chemical families. This material, termed PNA (peptide nucleic acid) has the backbone of a peptide, but the residues of the DNA. This family of molecules that were developed in the 1990s are mainly used for gene regulation [5].

As we knew that dipeptides represent a minimalistic assembly unit, we synthesised 16 different di-PNAs with all possible combinations of the adenine (A), cytosine (C), guanine (G), and thymine (T) bases. We demonstrated the ability of very short di-PNA building blocks to self-assemble into ordered architectures. Intriguingly, only guanine containing building blocks were able to form ordered self-assembled structures. This is very interesting as guanine is readily used by nature to form physical colours and reflectors by molecular self-assembly.

The most interesting assemblies were of GC di-PNA that contain complementary cytosine and guanine that could undergo hydrogen bonded base-pairing (Figure 118). We found that *in vitro* the building blocks could self-associate to grow structures with an elongation rate 20 times faster than that of a microtubule. The optical properties

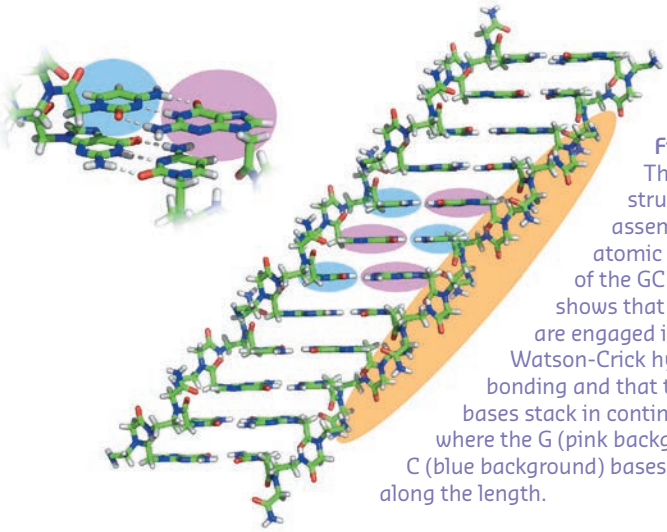

Fig. 118: The crystal structure of PNA assemblies. The atomic structure of the GC di-PNA shows that the bases are engaged in canonical Watson-Crick hydrogen bonding and that the aromatic bases stack in continuous chains where the G (pink background) and C (blue background) bases alternate along the length.

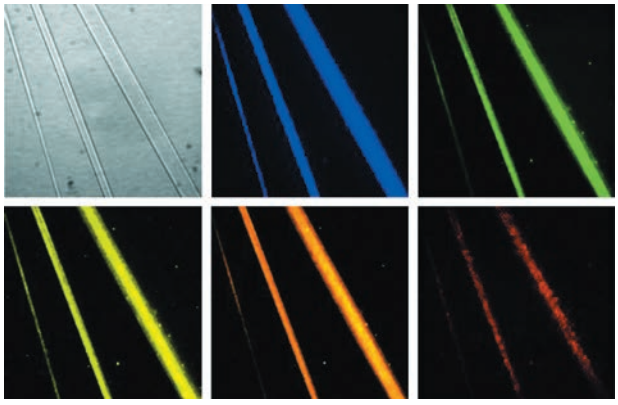

Fig. 119: The PNA assemblies exhibit a red edge excitation shift with a broad range of emission wavelengths at the visible region. One bright-field and five fluorescence images of the same microscopic field of GC di-PNA structures are shown. Each fluorescence image was taken with different excitation and emission filters: (excitation/emission) 387 nm/440 nm; 485 nm/525 nm; 537 nm/578 nm; 560 nm/607 nm; 650 nm/684 nm (from left to right).

of the newly characterised assemblies were also unique. We observed a clear fluorescent property of the assemblies with a very extensive red-edge excitation shift (REES) at the visible range of the electromagnetic spectrum (Figure 119). This phenomenon is often associated with dense structures such as glassy materials or graphene oxide and is exceptional for organic self-assembled structures.

We used the energy tuning capabilities of beamline **ID29** to collect X-ray data on thin, needle-like crystals of the GC di-PNA. By bringing the energy down to 15.59 eV, atomic resolution data could be measured. The resulting crystal structure shows that the GC bases form classical Watson-Crick hydrogen bonding and that the aromatic bases π stack in long, contiguous chains where the G and C bases alternate along the length of the stack.

The very unique architecture that results from both the peptide-like and DNA base pairing results also in unpredicted physical properties. The technological utilisation of this new family of self-assembled materials is now being explored.

PRINCIPAL PUBLICATION AND AUTHORS

Light-emitting self-assembled peptide nucleic acids exhibit both stacking interactions and Watson–Crick base pairing, O. Berger (a), L. Adler-Abramovich (a), M. Levy-Sakin (a), A. Grunwald (a), Y. Liebes-Peer (a), M. Bachar (a), L. Buzhansky (a), E. Mossou (b,c), V.T. Forsyth (b,c), T. Schwartz (a), Y. Ebenstein (a), F. Frolow (a), L.J.W. Shimon (d), F. Patolsky (a) and E. Gazit (a), *Nature Nanotechnology* **10**, 353–360 (2015); doi:10.1038/nnano.2015.27.
(a) Tel Aviv University (Israel)
(b) Partnership for Structural Biology, ILL, Grenoble (France)
(c) Faculty of Natural Sciences, Keele University (UK)
(d) Weizmann Institute of Science, Rehovot (Israel)

REFERENCES

[1] M. Reches and E. Gazit, *Science* **300**, 625–627 (2003).
[2] L. Adler-Abramovich and E. Gazit, *Chem. Soc. Rev.***43**, 6881–6893 (2014).
[3] A. Levin *et al.*, *Nature Commun.* **5**, 5219 (2014).
[4] N.C. Seeman, *J. Theor. Biol.* **99**, 237–247 (1982).
[5] P.E. Nielsen *et al.*, *Science* **254**, 1497–1500 (1991).

CELLULAR SODIUM AND POTASSIUM PUMPS LIGHT UP OPTOGENETICS

The structure of a light-activated ion pump has been solved. This discovery provides new tools in the emerging field of optogenetics, which has potential long-term applications such as vision and hearing regeneration.

Microbial rhodopsins are a large family of photosensitive membrane proteins that use light to transport ions into and out of the cell, generating phototaxis signals that cause the cell to move towards favourable illumination conditions. The most studied system, bacteriorhodopsin, was discovered in 1971 but thousands more have since been identified in microorganisms as diverse as bacteria, algae and viruses, exhibiting various light-gated channels and light-driven proton and anion pumps. Incorporating these proteins into neurons has allowed precise control of neural impulses and lies at the foundation of the growing field of optogenetics. So far, however, all the known light-driven pumps are unable to transport sodium and potassium – the ions whose motions across the cell membrane constitute natural neural impulses.

While investigating the marine bacterium *Krokinobacter eikastus*, K. Inoue and co-workers [1] unexpectedly discovered that *K. eikastus* cells are able to pump out sodium ions during early periods of growth. It turned out that the corresponding ion transporter, dubbed KR2, belongs to a new type of microbial rhodopsin in which some of the most important ionisable amino acids are replaced with polar ones, and vice versa. Even when expressed in another commonly employed bacterium, *E. coli*, KR2 could still transport sodium ions under illumination. Yet it appeared that potassium ions, despite being very similar to sodium ions, were not transported by KR2.

This and other curiosities displayed by KR2 attracted our interest because we had already carried out several structural studies of other microbial rhodopsins to investigate the molecular mechanisms behind their actions. However, membrane proteins are notoriously difficult to handle and producing them is usually expensive and time-consuming, and KR2 is no exception and the protein could be produced only in batches of several milligrams. Thus,

while thousands of crystallisation conditions should have been tested, we had to miniaturise and automate this process using the robotic and imaging systems available at the IBS. The diffraction signal from the first crystals obtained, which measured less than 20 µm across, was too weak to be measured using in-house X-ray sources. Recent advances at the ESRF's macromolecular crystallography beamlines – such as highly brilliant microfocus X-ray beams, automatic sample changers and convenient software protocols – greatly helped the search for the best crystals. After several months of trials at beamlines **ID23-1** and **ID29**, we were able to improve crystal size (Figure 120) and a resolution of the diffraction data collected from around 20 Å to better than 1.5 Å. Meanwhile we were also able to extract information about KR2's spectroscopic characteristics using optical absorption spectra collected at the cryobench laboratory (beamline **ID29S)**.

The crystal structure of the KR2 sodium pump (Figure 121) revealed a short protein helix that caps the outfacing opening of the pump like a lid. Another interesting feature of KR2 is the unusual structure of the inward facing ion uptake cavity, which is unexpectedly large and protrudes from the protein surface. Hypothesising that this feature could act as a filter that allows KR2 to be selective for sodium ions, we swapped specific amino acids at the relevant site using targeted mutations and found that KR2 indeed loses its sodium-pumping ability under such conditions. But we also found that one mutation transforms KR2 into a light-driven potassium pump – the first of its kind.

For potential optogenetic applications, this result is especially interesting because transporting potassium ions out of the cell is a natural neuron deactivation mechanism. Normally, activated neurons release these ions through passive potassium channels in the membrane, but a light-activated potassium pump would allow this process to be precisely controlled and provide a highly effective off-switch for neurons [2, 3].

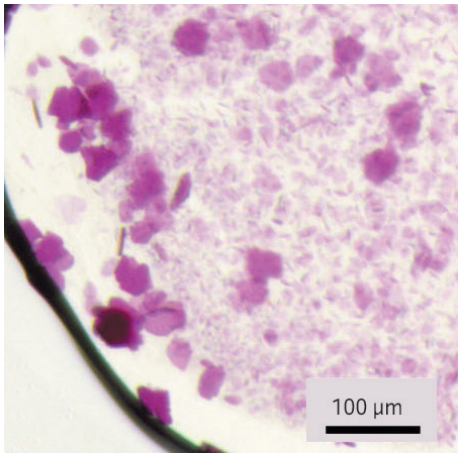

Fig. 120: The crystals of KR2 used for structure determination.

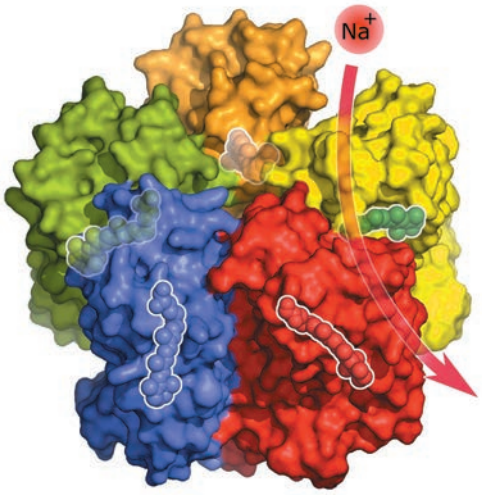

Fig. 121: Under physiological conditions, five KR2 molecules spontaneously form a star-shaped complex with each KR2 molecule being able to bind and transport a sodium ion across the membrane. Inside the proteins are highlighted the light-sensitive retinal cofactors that enable the pumping activity.

The next step is to find ways of integrating the pump into different types of cells. In combination with the light-activated Channelrhodopsin 2, which is a well-known molecular on-switch, the KR2 potassium pump would form a perfect pair of tools for the precise control of nerve cell activity.

PRINCIPAL PUBLICATION AND AUTHORS

Crystal structure of a light-driven sodium pump, I. Gushchin (a,b,c), V. Shevchenko (b,c,d), V. Polovinkin (a,b,c), K. Kovalev (b,c), A. Alekseev (b,c), E. Round (c), V. Borshchevskiy (b,c), T. Balandin (c), A. Popov (e), T. Gensch (c), C. Fahlke (c), C. Bamann (f), D. Willbold (c,g), G. Büldt (b,c), E. Bamberg (f) and V. Gordeliy (a,b,c), *Nature Structural and Molecular Biology* **22**, 390–395 (2015); doi:10.1038/nsmb.3002.

(a) Institut de Biologie Structurale, Grenoble (France)
(b) Laboratory for Advanced Studies of Membrane Proteins, Moscow Institute of Physics and Technology, Dolgoprudniy (Russia)
(c) Institute of Complex Systems (ICS), Research Center Jülich (Germany)
(d) Institute of Crystallography, University of Aachen (RWTH) (Germany)
(e) ESRF
(f) Max Planck Institute of Biophysics, Frankfurt am Main (Germany)
(g) Institut für Physikalische Biologie, Heinrich-Heine-Universität Düsseldorf (Germany)

REFERENCES

[1] K. Inoue *et al.*, *Nature Communications* **4**, 1678 (2013).
[2] H. Kato *et al.*, *Nature* **521**, 48–53 (2015); doi: 10.1038/nature14322.
[3] I. Gushchin *et al.*, *FEBS Journal* (2015); doi: 10.1111/febs.13585.

THE FIFTH COPPER BINDING SITE OF THE PRION PROTEIN ACTS AS A MOLECULAR SWITCH FOR PRION CONVERSION

The conversion of the prion protein (PrP^C) into a misfolded isoform in the brain causes prion diseases, a group of transmissible neurodegenerative disorders affecting humans and animals. The structural events underlying this conversion have escaped detailed characterisation due to the insoluble nature of prions. A novel copper-mediated mechanism has been identified that acts as a "switch" that turns PrP^C into its pathological alter ego.

In its physiological form, the prion protein (PrP^C) is beneficial and involved in several neuronal processes such as neuronal growth and differentiation and brain metal homeostasis. The latter function is attributed to the prion protein's ability to bind copper suggesting that PrP^C possesses metalloprotein function.

A conformational change of PrP^C into a "bad" form is responsible for a class of neurodegenerative diseases called prion diseases that include "mad cow disease" or Creutzfeldt-Jakob disease in humans. This form is termed "prion" or PrP^{Sc} and, once formed, acts as a template for the conversion of additional PrP^C to PrP^{Sc} facilitating a build-up of misfolded protein and subsequent neurodegeneration.

Although copper binding seems to be involved in many physiological PrP^C processes, the interplay between copper and prion conversion poses intriguing issues. There are five potential copper binding sites clustered along the unstructured N-terminal domain: four within the octapeptide repeats (OR) region (residues 60-91) and one close to the globular domain called non-OR or "fifth" copper binding site (residue 92-111) [1]. Interestingly, copper coordination to the non-OR region has garnered interest due to the possibility that this interaction may impact prion conversion.

Here, by means of extended X-ray absorption fine structure (EXAFS) spectroscopy, cell-biology approaches and molecular dynamic simulations, we have investigated the influence of copper coordination in the non-OR region on prion conversion.

Using X-ray absorption spectra collected at beamline **BM30B** FAME, we determined the copper coordination in the wild type (WT) human prion protein (HuPrP) and in pathological mutants at both pH 7.0 and pH 5.5. We found

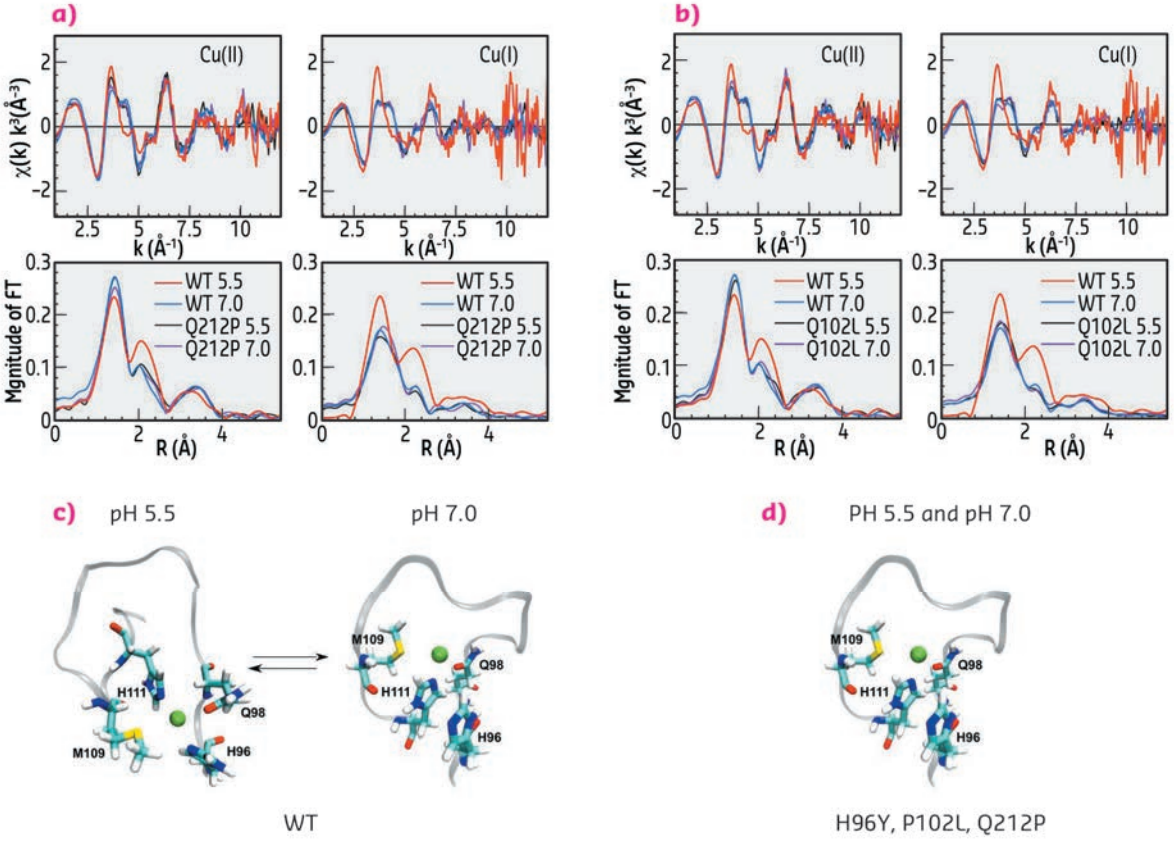

Fig. 122: Copper coordination in the WT and mutant human prion protein. k^3-weighted EXAFS spectra and Fourier transforms of Cu(II) and Cu(I) bound to WT HuPrP(90–231) and Q212P at pH 5.5 and 7.0 (a) and of Cu(II) and Cu(I) bound to WT HuPrP(90–231) and P102L at pH 5.5 and 7.0 (b). Schematic representations of copper binding sites in the WT HuPrP(90–231) (c) and in the mutants (d) at both pH 5.5 and 7.0.

that mutations (H96Y, P102L and Q212P) and pH changes cause a dramatic modification on both Cu(II) and Cu(I) coordination in the non-OR region. In the WT HuPrP Cu(II) and Cu(I) are anchored to His96 and His111 only at pH 5.5, while at pH 7 copper in both oxidative states is coordinated only by His111. Conversely, in the mutants copper is bound only to H111 independently of the pH (Figure 122).

The observed structural differences in the copper coordination among WT and pathological mutants at pH 5.5 may have relevant physiological implications since this alteration in the copper binding site might trigger PrP^C to PrP^{Sc} conversion. Hence, the non-OR region could be an important "hot spot" for prion conversion. To understand the implications of our EXAFS data, we performed cell-based assays. We used neuronal cell models expressing PrP^C in which the N-terminal His residues within the OR and non-OR regions were substituted by tyrosine (Tyr) and we evaluated the effect of single His to Tyr substitutions in the context of prion conversion. Only the H96Y mutation promoted significant prion conversion and generation (Figure 123a, b). His to Tyr96 substitution removes one crucial copper ligand, thus it may allow the effect caused by altered copper coordination to be linked with prion conversion.

These findings suggest a role for the non-OR region as a critical molecular switch for prion conversion. We therefore argue that copper bound to the non-OR region may stabilise this segment when coordinated by His96 and His111. Our study highlights the importance of the non-OR region for prion conversion and suggests a model in which PrP^C coordinating copper using only one His may be more prone to the conversion in acidic conditions (Figure 123c).

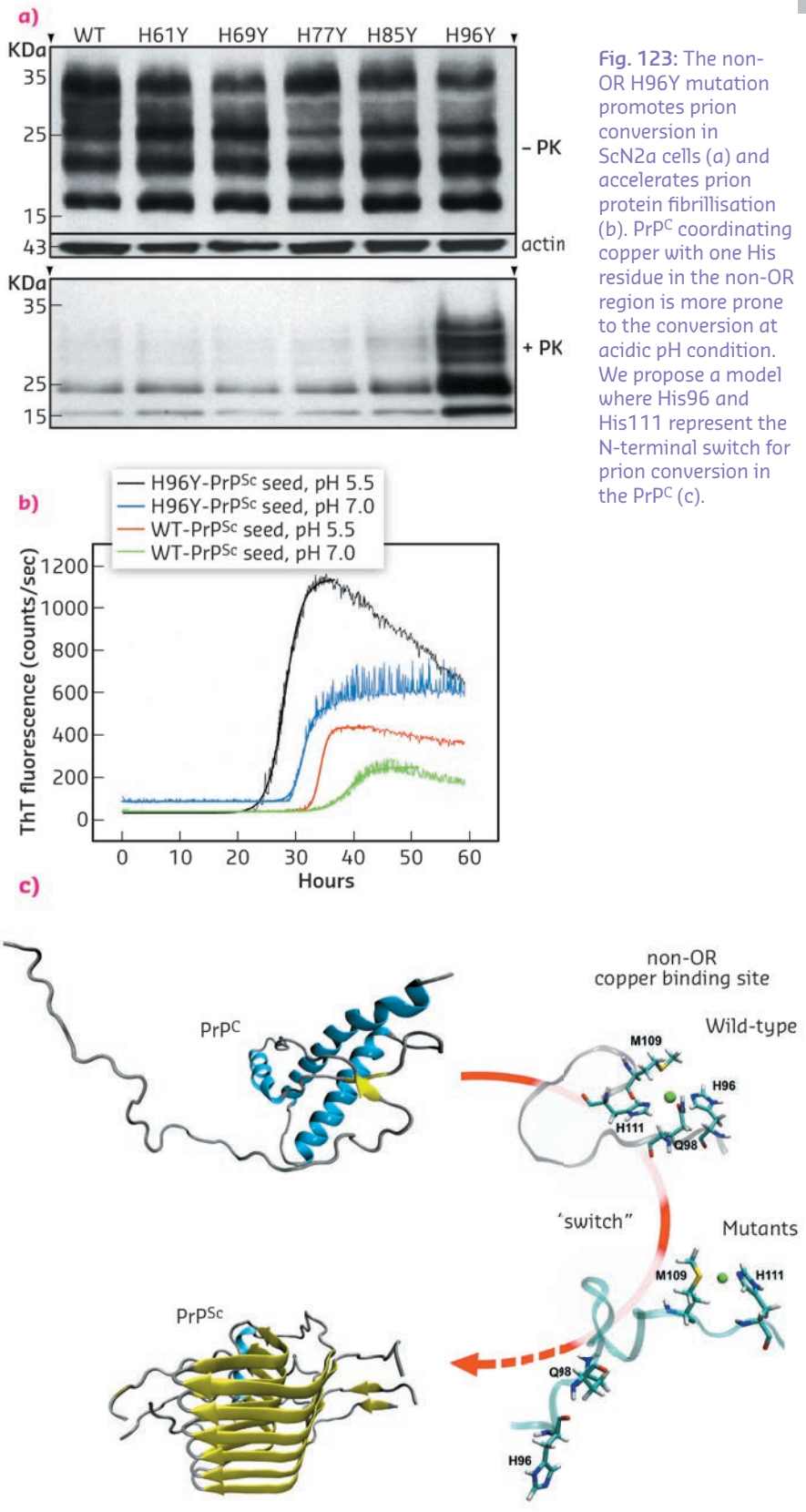

Fig. 123: The non-OR H96Y mutation promotes prion conversion in ScN2a cells (a) and accelerates prion protein fibrillisation (b). PrP^C coordinating copper with one His residue in the non-OR region is more prone to the conversion at acidic pH condition. We propose a model where His96 and His111 represent the N-terminal switch for prion conversion in the PrP^C (c).

PRINCIPAL PUBLICATION AND AUTHORS

The non-octarepeat copper binding site of the prion protein is a key regulator of prion conversion, G. Giachin (a), P.T. Mai (b), T.H. Tran (b), G. Salzano (b), F. Benetti (b), V. Migliorati (c), A. Arcovito (d), S.D. Longa (e), G. Mancini (f), P. D'Angelo (c) and G. Legname (b), *Sci Rep.* **5**, 15253 (2015); doi:10.1038/srep15253.

(a) ESRF
(b) Department of Neuroscience, Scuola Internazionale Superiore di Studi Avanzati (SISSA), Trieste (Italy)
(c) Department of Chemistry, Sapienza University of Rome (Italy)
(d) Istituto di Biochimica e Biochimica Clinica, Università Cattolica del Sacro Cuore, Rome (Italy)
(e) Department of Medicine, Public Health, Life and Environmental Science, University of L'Aquila, Coppito Aquila (Italy)
(f) Scuola Normale Superiore, Pisa (Italy)

REFERENCES

[1] P. D'Angelo *et al.*, *Biochemistry* **51**, 6068–6079 (2012).

HOW CHEMICALS CAN COMBINE TO FORM DEADLY COCKTAILS FROM HARMLESS COMPONENTS

Endocrine-disrupting chemicals act on nuclear hormone receptors such as the human pregnane X receptor (PXR). Two such chemicals were found to interact with each other in the PXR ligand-binding pocket forming a 'supramolecular ligand' that is a more potent PXR activator than either of the two chemicals alone.

Many chemicals released into the environment target nuclear receptors, proteins that control gene expression networks in response to small signalling molecules [1]. These external compounds are classed as endocrine-disrupting chemicals as they are thought to change gene expression patterns, leading to harmful physical effects. While these compounds are generally harmless individually at the doses at which we are exposed, the body is constantly in contact with mixtures of these compounds in the environment. It has long been known that combinations of these chemicals can have additive, antagonistic or synergistic effects, but there has been no understanding of the molecular basis for these effects.

We have used extensive screening methods and biophysical characterisation to identify two endocrine-disrupting chemicals that act synergistically on the human pregnane X receptor (PXR), located mainly in the nucleus of liver, colon and intestinal cells. The two compounds identified are the organochlorine pesticide *trans*-nonachlor (TNC), and the active ingredient of most contraceptive pills, the synthetic oestrogen derivative 17α-ethinylestradiol (EE2); two compounds with very different uses that are commonly found in our environment. Interestingly, we observed that the two compounds not only bind concomitantly to the ligand-binding pocket of the receptor, but they do so cooperatively, *i.e.* binding of one molecule promotes high affinity binding of the second. We found that the binary mixture interacts with PXR with a 50- to 100-fold greater affinity than each compound alone, and accordingly, induces a biological response at much lower doses than the individual components. By solving crystal structures of PXR bound to the two chemicals individually and in combination, we have been able to propose a molecular mechanism for the observed synergistic effect between the molecules (diffraction data were collected at beamline **ID23-2**). The crystal structures show that EE2 and TNC mutually stabilise each other *via* strong inter-ligand contacts within the ligand-binding pocket to form a so-called 'supramolecular ligand' (Figure 124). A large number of interactions with surrounding amino acids allow the supramolecular ligand to tightly hold the binding pocket in the active conformation, causing a sustained activation of the receptor.

These results constitute a proof of concept that opens the way to a wide field of study. There are about 150,000 compounds in our environment that could have unexpected effects on human

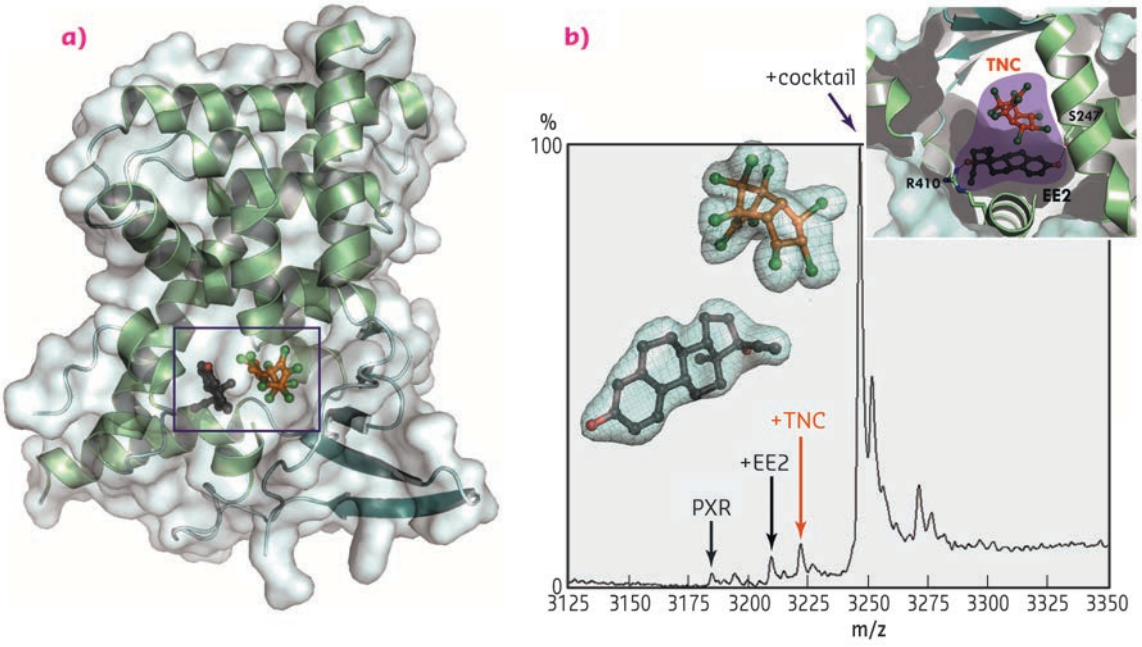

Fig. 124: *Trans*-nonachlor (TNC), a pesticide, and 17α-ethinylestradiol (EE2), the active ingredient of the contraceptive pill, combine within the human nuclear receptor PXR to form a supramolecular ligand with enhanced activity. (a) The structure of PXR bound to TNC (orange) and EE2 (dark grey). (b) Electrospray ionisation mass spectrometry under native conditions reveals that EE2 and TNC bind simultaneously to PXR with a much greater affinity than either compound alone. The electron density of the bound chemicals ($2F_o$-F_c contoured at 1σ) is shown as a mesh.

health through combined action, given their recognised or assumed safety as isolated substances. The results have the potential to change current policies in risk assessment for chemicals and could lead to the development of improved, safer chemicals in the future.

PRINCIPAL PUBLICATION AND AUTHORS

Synergistic activation of human pregnane X receptor by binary cocktails of pharmaceutical and environmental compounds, V. Delfosse (a,b,c), B. Dendele (c,d,e,f), T. Huet (a,b,c), M. Grimaldi (c,d,e,f), A. Boulahtouf (c,d,e,f), S. Gerbal-Chaloin (c,g), B. Beucher (a,h,i), D. Roecklin (j), C. Muller (j), R. Rahmani (k), V. Cavailles (c,d,e,f), M. Daujat-Chavanieu (c,g,l), V. Vivat (j), J-M. Pascussi (c,i,j), P. Balaguer (c,d,e,f) and W. Bourguet (a,b,c), *Nature Communications*, **6**, 8089 (2015); doi: 10.1038/ncomms9089.

(a) Inserm U1054, Montpellier (France)
(b) CNRS UMR5048, Centre de Biochimie Structurale, Montpellier (France)
(c) Université de Montpellier (France)
(d) IRCM, Institut de Recherche en Cancérologie de Montpellier (France)
(e) Inserm, U1194, Montpellier (France)
(f) ICM, Institut régional du Cancer de Montpellier (France)
(g) Inserm U1040, Montpellier (France)
(h) Inserm U661, Montpellier (France)
(i) CNRS UMR5203, Institut de Génomique Fonctionnelle, Montpellier (France)
(j) NovAliX, Illkirch (France)
(k) INRA UMR 1331,TOXALIM, Sophia-Antipolis (France)
(l) CHU de Montpellier, Institut de Recherche en Biothérapie (France)

REFERENCES

[1] V. Delfosse *et al.*, *Acta Pharmacol Sin* **36**, 88-101 (2015).

ELUCIDATING THE ARCHITECTURE OF TRANSCRIPTION FACTOR IIIC

The molecular machines that read the messages stored within DNA require the concerted action of transcription factors, molecules that ensure the right messages are read at the correct time. By obtaining a detailed picture of a transcription factor's atomic structure we can hope to understand how it functions.

In cells, transfer RNAs (tRNAs) play a vital role in the translation of the DNA message into proteins. Transcription of these relatively short RNA molecules is controlled by the proteins of the RNA polymerase III transcription machinery. The genes encoding tRNAs contain two highly conserved promoter sequences called 'A box' and 'B box', which bind to a protein called transcription factor IIIC (TFIIIC). This flexible, multi-subunit molecule is remarkable in that it can accommodate a great variety of different sized spacing's between the crucial A and B boxes. The precise nature of how TFIIIC can achieve this is unclear. The protein is hypothesised to be divided into two DNA-binding sub-complexes, known as τA and τB for their A box and B box binding ability, that are joined by a flexible linker.

We have pieced together many of the individual subunits of TFIIIC in previous studies [1-3], with all of the available crystal structures for this protein complex having been solved using beamlines at the ESRF. These valuable structures have provided high-resolution insights into the two DNA-binding sub-complexes of TFIIIC. Despite this, the question of how τA and τB are linked within the structure of TFIIIC has remained a mystery.

Using beamlines **ID23-1** and **ID23-2**, we were able to gain further understanding of the architecture of TFIIIC. Guided by low resolution chemical cross-linking data, we were able to crystallise fragments of the two largest subunits of TFIIIC, τ131 and τ138, which appeared to be critical in forming the linker between the two DNA-binding sub-complexes.

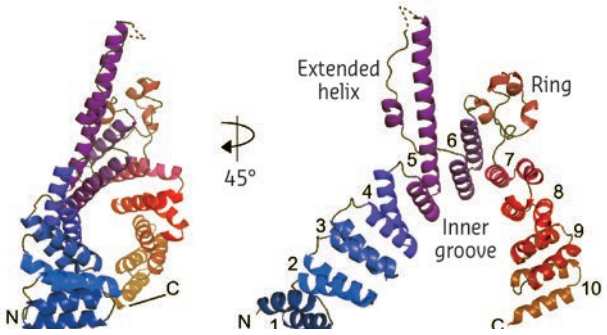

Fig. 125: The TPR array structure of τ131.

The 1.4 Å crystal structure of τ138 contained an extended winged helix domain, providing the first structural information for this, the largest subunit of TFIIIC. τ138 is predicted to contain several of these domains along its length, and this high-resolution structure will be valuable in modelling the rest of this subunit. However, subsequent biochemical analysis revealed that this particular fragment of TFIIIC was not essential for the linker between τ131 and τ138. We therefore focussed on the τ131 crystal structure, which we could show to be essential for the linker. This crystal structure was of particular interest, as this fragment of TFIIIC is also crucial in assembling other proteins

of the RNA polymerase III transcription machinery at tRNA genes.

In contrast to the τ138 structure, diffraction from the τ131 crystals was limited to 3.4 Å resolution. Nevertheless, we were able to solve and build the structure (Figure 125). The structure of τ131 reveals an unusual arrangement of several α-helical motifs called tetra-trico-peptide repeats (TPRs). TPRs are ubiquitous in protein complexes, forming extended surfaces over which many other proteins can assemble. However, the structure revealed some additional features, including an extended, flexible helix and a disordered coil that separates the TPR array into two arms (Figure 125). Further biochemical and *in vivo* analysis using mutants of this 'TPR array' have revealed that the τ131 subunit contains many overlapping binding sites for other proteins involved in RNA polymerase III transcription. These experiments, guided by the crystal structure, have led us to propose a model for how TFIIIC might assemble the other proteins required for tRNA transcription.

The τ131 structure has provided a rational framework with which to address many questions concerning the role of TFIIIC, from how the two DNA-binding sub-complexes are linked, to how TFIIIC interacts with DNA and how TFIIIC assembles the machines required at tRNA genes. The ESRF continues to help us address the structural questions related to this unusual molecule (Figure 126).

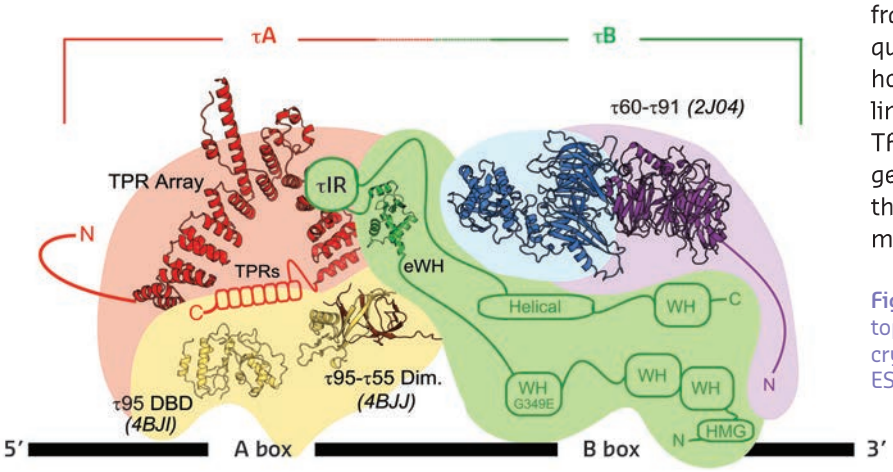

Fig. 126: The current model for the topology of TFIIIC. All of the available crystal structures have been solved at the ESRF.

PRINCIPAL PUBLICATION AND AUTHORS

Architecture of TFIIIC and its role in RNA polymerase III pre-initiation complex assembly, G. Male (a), A. Von Appen (a), S. Glatt (a), N.M.I. Taylor (a), M. Cristovao (a), H. Groetsch (a), M. Beck (a) and C.W. Müller (a), *Nature Communications* **6**, 7387 (2015); doi: 10.1038/ncomms8387.
(a) European Molecular Biology Laboratory (EMBL), Heidelberg (Germany)

REFERENCES

[1] N.M. Taylor *et al., Nucleic Acids Research* **41**, 9183-96 (2013).
[2] N.M. Taylor *et al., J. Biol. Chem.* **288**, 15110-15120 (2013).
[3] A. Mylona *et al., Molecular Cell* **24**, 221-32 (2006).

STRUCTURAL BASIS OF LESION RECOGNITION BY Rad14 (XPA)

Damage recognition mechanisms are a pivotal element in any DNA repair mechanism, since this step decides whether a DNA region should be repaired or not. To extend the knowledge of damage recognition strategies, the structures of Rad14 (XPA), an essential protein in nucleotide excision repair, have been analysed in the presence of different DNA damages.

Our DNA is constantly challenged by endogenous and exogenous sources. It is estimated that each cell in our body encounters approx. 10,000 lesions per day. Counteracting measures to maintain genomic integrity are thus essential. Among the different DNA repair systems, nucleotide excision DNA repair (NER) stands out due to its capability to recognise a vast variety of structurally diverse DNA damages. A defect in NER causes the disease xeroderma pigmentosum. One of the major hall-marks of this disease is the extreme sensitivity to sunlight associated with a highly increased risk of developing skin cancer. The entire repair process requires the presence of up to 30 different proteins, of which the XPA protein assumes a central role.

We solved crystal structures of the DNA binding domain of RAD14, the yeast homolog of XPA, in the presence of two different DNA damages: a cisplatin 1,2-GG intrastrand crosslink and a N-(deoxyguanosin-8-yl)-2-acetylaminofluorene

(AAF-dG) bulky adduct. The crystallographic data were in part collected at the beamlines **ID29** and **ID23-2**. The most striking feature of the two structures is the similar binding mode of Rad14 to the DNA (Figure 127) with two Rad14 monomers bound to the DNA forming a dimer on DNA without direct contact of the monomers. Moreover, the DNA in both structures showed a distinct kink of 70° at the site of the lesion (Figure 128a) which is stabilised by the two independent Rad14 monomers. Both molecules create a 13mer recognition motif with the lesion at the centre. The most prominent binding feature is a -hairpin in Rad14 that intercalates at the DNA ends which we termed the "fingers" motif. Whereas the fingers hold the DNA, stabilisation of the kink is achieved by a thumb consisting of Arg294 in-helix 7. The thumb binds to the DNA backbone at the site of the lesion thereby creating the central hinge where the DNA is kinked. Directly after the hinge, Thr239 further stabilises the kink via backbone interactions. The above described interactions are accomplished by each Rad14 monomer with the lesion being located in the centre between the two protein molecules (Figure 128b). The validity of this recognition complex in solution was confirmed using mass spectrometry. In addition, the DNA binding mode observed in the structure perfectly matches biochemical data obtained with XPA and different DNA substrates [1]. The DNA damage analysed in our structures are known to support either pre-kinked structures or allow DNA kinking that is not observed in regular B-form DNA. Thus, Rad14 seems to bind and test the DNA for bendability in order to verify the presence of a lesion in a lesion unspecific manner through a novel mechanism. Other damage binding proteins involved in NER like DDB2 or XPC/HR23B have also been shown not to engage a specific damage directly but rather sense backbone anomalies [2].

Although XPA has not been directly implicated as a damage sensor, the structural and biochemical data obtained in our study may explain how NER might reach its high promiscuity towards different DNA lesions. The Rad14 crystal structures add another dimension to the mechanistic damage sensor portfolio revealing a mechanism for the specific recognition of kinked DNA structures in a sequence and lesion independent way.

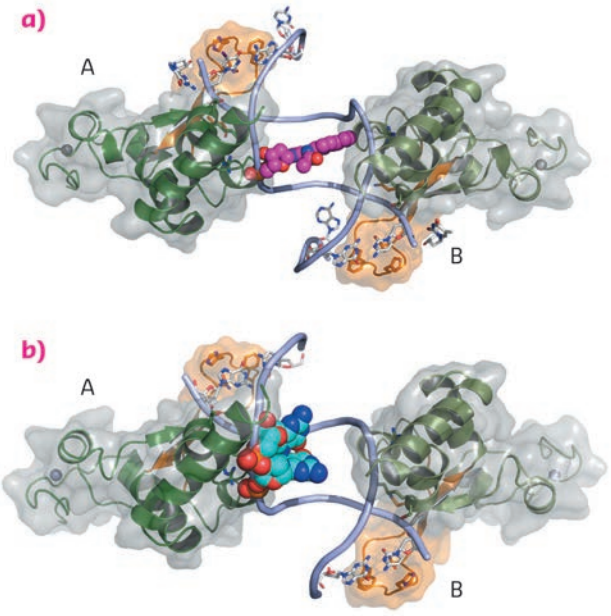

Fig. 127: The DNA binding domain of Rad14 bound to DNA. The different Rad14 monomers are labeled A and B. The finger motif is coloured in orange. For clarity only the DNA backbone is shown. The lesion is depicted in space-filling mode. (a) Rad14 bound to DNA containing a AAF-dG bulky adduct. (b) Rad14 bound to DNA containing a cisplatin 1,2-GG intrastrand crosslink.

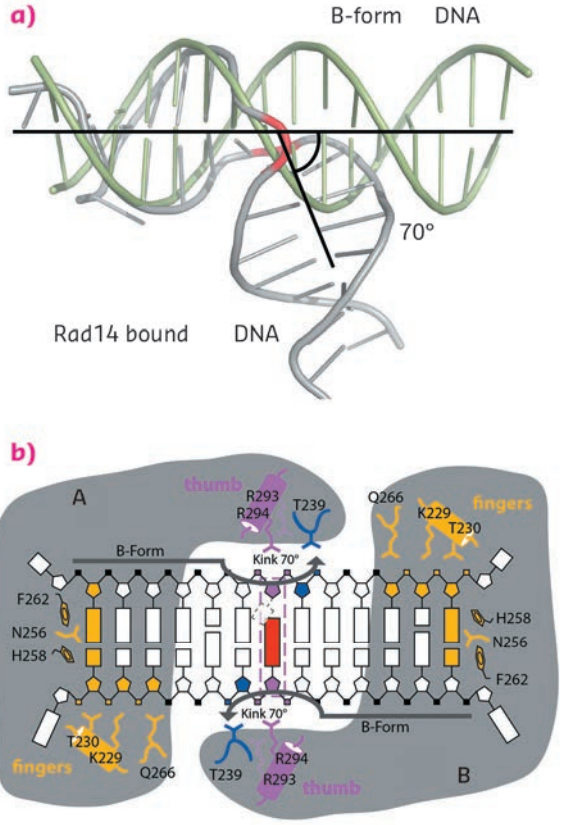

Fig. 128: Rad14 kinks DNA. (a) Superposition of regular B-form DNA with Rad14 bound DNA. The bend angle is indicated. (b) Schematic overview of the Rad14 DNA binding mode with kinked DNA.

PRINCIPAL PUBLICATION AND AUTHORS

Structural insights into the recognition of cisplatin and AAF-dG lesion by Rad14 (XPA), S.C. Koch (a), J. Kuper (b), K.L. Gasteiger (a), N. Simon (a), R. Strasser (a), D. Eisen (a), S. Geiger (a), S. Schneider (c), C. Kisker (b) and T. Carell (a),

PNAS **112**, 8272–8277 (2015); doi: 10.1073/pnas.1508509112.

(a) Center for Integrated Protein Science at the Department of Chemistry, Ludwig-Maximilians Universität München, Munich (Germany)
(b) Rudolf Virchow Center for Experimental Biomedicine, Institute for Structural Biology, University of Wuerzburg (Germany)
(c) Department of Chemistry, Technische Universität München, Garching (Germany)

REFERENCES

[1] U. Camenisch, *Nat Struct Mol Biol.* **13**, 278–284 (2006).
[2] J. Kuper, *Curr. Opin. Struct. Biol.* **22**, 88–93 (2012).

DECIPHERING ENZYME EVOLUTION IN ANTIBIOTIC BIOSYNTHESIS PATHWAYS

Soil bacteria *Streptomyces* are the source of many biologically active compounds. The molecular basis of the evolution of a classical methyltransferase into an unusual hydroxylase in the biosynthetic pathways of two anthracycline anticancer agents is the focus of this study.

Streptomyces soil bacteria are competent chemists that are able to produce thousands of chemically complex natural products. Key to the development of this rich source of metabolites appears to be an evolutionary pressure that promotes chemical diversity; new biosynthetic pathways are continuously being formed in these bacteria, which may result in the appearance of a novel bioactive compound that provides significant competitive advantage to the producing organism. This is reflected in the biosynthetic enzymes that have been able to evolve relatively freely and, as a consequence, have resulted in similar proteins having functions that may greatly differ. In recent years, our work has focused on understanding the details of this process [1, 2], in order to facilitate future protein engineering efforts for the generation of improved bioactive natural products.

Here we have elucidated the molecular basis of the evolution of a classical methyltransferase into an unusual hydroxylase in the biosynthetic pathways of two anthracycline anticancer agents. DnrK from the daunorubicin pathway [3] is a canonical 4-O-methyltransferase, whereas the closely related RdmB (52% sequence identity) from the rhodomycin pathway is an atypical 10-hydroxylase [4] that requires SAM, a thiol reducing agent, and molecular oxygen for activity (Figure 129).

In order to identify the regions responsible for the functional differentiation, we selected three regions (Figure 129, R1-R3) based on the crystal structures of the enzymes. We then created chimeric enzymes by interchanging these 10 to 12 amino acid segments both individually and in different combinations. Activity assays revealed that incorporation of the R1 region from RdmB into the DnrK scaffold was critical for introduction of the 10-hydroxylation activity. Further sequence analysis revealed that RdmB contained an insertion of one additional serine residue (S297) in this region in comparison to DnrK and, consequently, addition of this single residue was sufficient for the gain of monooxygenation activity in the DnrK-Ser mutant.

The crystal structure of DnrK-Ser in complex with aclacinomycin T and S-adenosyl-L-homocysteine was determined at beamline **ID23-1** and refined to 1.9 Å resolution. The data revealed that the inserted serine S297 resides in an α-helical segment adjacent to the substrate, but in a manner where the side chain points away from the active site (Figure 130). However, at the same time the preceding phenylalanine (F296) has rotated inward adjacent to the ligand near the site of monooxygenation. Comparison of the structures of DnrK-Ser and RdmB reveals that both enzymes have a phenylalanine, F296 and F300, respectively, next to the anthracycline ligand, in contrast to native DnrK, which contains glutamine Q295 at the equivalent position. The implication of these changes is that the glutamine in DnrK allows bulk solvent to access the active site cavity via an open channel, whereas the bulkier hydrophobic phenylalanine residues block this route to the surface of the protein in DnrK-Ser and RdmB (Figure 130).

In addition to 4-O-methylation activity, DnrK was shown to harbour a previously undetected moonlighting 10-decarboxylation activity, which we believe has been the key to the development of the 10-hydroxylation activity of RdmB.

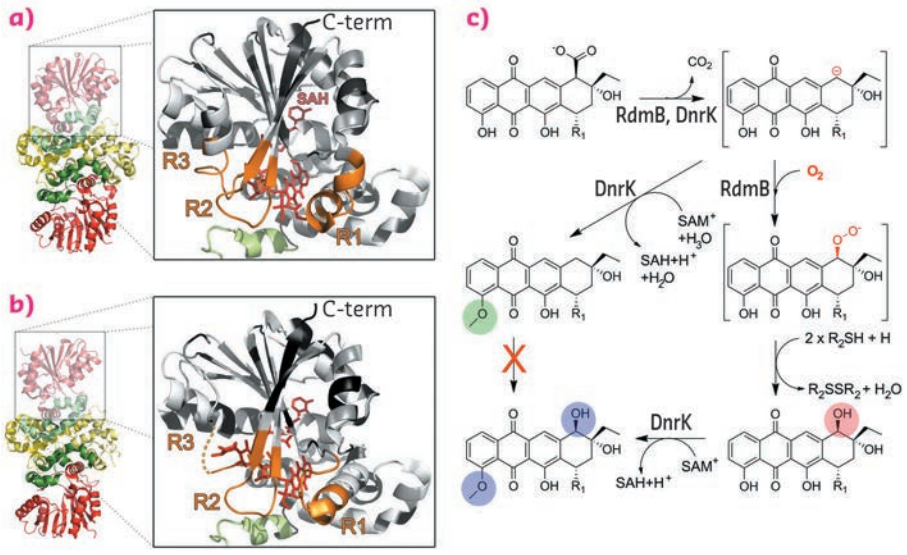

Fig. 129: Similar structures, distinct functions. Structures of (a) DnrK and (b) RdmB with regions investigated in this study highlighted in orange (R1, R2, R3). (c) Mechanistic proposal for the divergent reactions of DnrK and RdmB.

Our mechanistic proposal (Figure 129) suggests that 10-decarboxylation is a common initial step for both enzymes. In DnrK, the more open active site allows facile protonation of the carbanion by solvent molecules and results in the formation of a neutral 10-decarboxylated and 4-O-methylated anthracycline, which is unable to react further with oxygen. RdmB, on the other hand, avoids the protonation step by closing the channel to the surface of the protein and excluding solvent ions from the active site. The carbanion may be stabilised through distribution of the negative charge throughout the polyphenolic ring system and the adjacent positive charge of SAM. The delocalisation of electrons enables substrate-assisted activation of molecular oxygen and reaction of the substrate with dioxygen. Finally, the 10-peroxy anthracycline formed is reduced by a thiol reagent to generate the 10-hydroxylated end product.

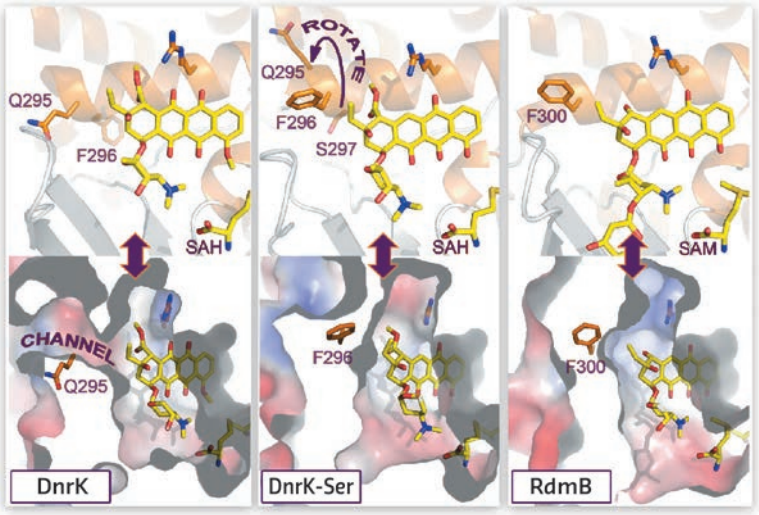

Fig. 130: Comparison of the active site architectures of DnrK, DnrK-Ser and RdmB.

Our work demonstrates that, in the evolution of antibiotic biosynthesis, addition of a single amino acid may result in the appearance of a new enzymatic reaction that leads to new bioactive products. Once this change occurred, a whole new subclass of 10-hydroxy anthracyclines became accessible to strains possessing enzymes such as RdmB in their biosynthetic repertoire.

PRINCIPAL PUBLICATION AND AUTHORS

Divergent evolution of an atypical S-adenosyl-l-methionine-dependent monooxygenase involved in anthracycline biosynthesis, T. Grocholski, P. Dinis, L. Niiranen, J. Niemi and M. Metsä-Ketelä, *PNAS* **112,** 9866–9871 (2015). doi: 10.1073/pnas.1501765112.

Department of Biochemistry, University of Turku (Finland)

REFERENCES

[1] P. Kallio *et al.*, *Biochemistry* **52**, 4507–4516 (2013).
[2] P. Patrikainen *et al.*, *Chem Biol* **21**, 1381–1391 (2014).
[3] A. Jansson *et al.*, *J Mol Biol* **334**, 269–280 (2003).
[4] A. Jansson *et al.*, *J Biol Chem* **280**, 3636–3644 (2005).

INJECTOR-BASED ROOM-TEMPERATURE SERIAL CRYSTALLOGRAPHY OF A MEMBRANE PROTEIN USING SYNCHROTRON RADIATION

To demonstrate how serial crystallography, developed in femtosecond timescales at X-ray free electron laser sources, can be implemented on a millisecond timescale at a synchrotron radiation source, membrane protein microcrystals in lipidic cubic phase have been injected into a X-ray microbeam. The resulting dataset allowed the structure to be solved at 2.4 Å resolution.

Serial femtosecond crystallography (SFX) as pursued at X-ray free electron laser (XFEL) sources relies mainly on injectors delivering the sample, such as protein microcrystals, in a fluid medium to pulsed X-rays. Simultaneously, vast datasets are recorded by fast area detectors specially designed for XFEL applications. A subset of these raw datasets contains the diffraction signal of the macromolecular sample (hits). Usually only a part of these hits can be matched to a single crystal lattice. These indexed frames are then merged to datasets suitable for macromolecular crystallographic structure solution methods.

The aim of this study was to adapt the SFX method for use with microfocused synchrotron radiation at the microbranch of beamline **ID13** (see Figure 131). Crystals of the membrane protein bacteriorhodopsin, grown in lipidic cubic phase (LCP) to be delivered by a LCP-injector [1], were chosen as a test case for realistic applications. LCP is a highly viscous

medium which allows the jet to be tuned for very low stream velocities. The LCP jet of 50 µm in diameter was aligned horizontally, perpendicular to an X-ray beam with a spot size of a few micrometres. The bacteriorhodopsin microcrystals with sizes ranging from 5 to 40 µm traversed the beam at a speed of around 100 µm/s while serial diffraction data were recorded using a fast CCD area-detector at a frame rate of more than 10 Hz and exposure times of 10 or 25 ms. Often, the same microcrystal was observed in several consecutive frames. However, most of the time, each of those frames was recorded in a slightly different crystal orientation and therefore contributed to the diversity of the data set.

Data reduction was carried out in a very similar way to SFX methods using the programs Cheetah [2] and CrystFEL [3]. Starting from 13000 hits (~ 1% hit rate) containing bacteriorhodopsin diffraction patterns, about 5700 frames could be indexed, producing a data set which was subsequently used for structure solution to a resolution of 2.4 Å. The result is very similar to crystal structures obtained in previous studies based on standard cryogenic data collection. Although this experiment was carried out at room temperature, the refined structure showed only very minor signs of radiation damage. Furthermore, less than a milligram of protein was used for the entire data collection. These results suggest that synchrotron based serial crystallography with fast and sensitive state-of-the-art detectors operating in the kHz range could well develop into a powerful method for macromolecular crystal structure determination that is complementary regarding timescales (*i.e.* femtoseconds vs. milliseconds) with SFX applications. Moreover, large-scale synchrotron upgrade programmes such as ESRF-EBS should provide sources delivering a photon flux enhanced by several orders of magnitude when compared to current installations. These improvements will further enable serial microsecond crystallography, offering interesting opportunities for room-temperature kinetics studies, *e.g.* via laser excitation.

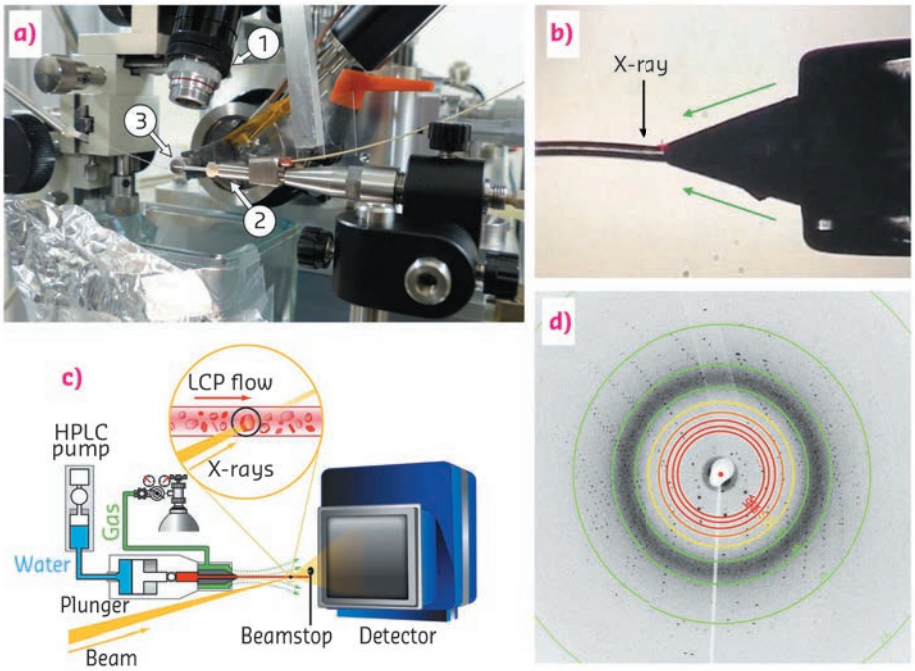

Fig. 131: (a) Experimental LCP-injector setup at ID13 showing: 1) the observation microscope, 2) the injector, 3) with its nozzle; (b) *In situ* microscope view of the LCP-jet during data collection; (c) schematic view of sample delivery and diffraction geometry; (d) diffraction pattern of bacteriorhodopsin with visible diffraction spots at up to 2.2 Å resolution.

PRINCIPAL PUBLICATION AND AUTHORS

Lipidic cubic phase serial millisecond crystallography using synchrotron radiation, P. Nogly (a), D. James (b), D. Wang (b), T.A. White (c) N. Zatsepin (c) A. Shilova (d), G. Nelson (b), H. Liu (b), L. Johansson (e), M. Heymann (c), K. Jaeger (a), M. Metz (c,f), C. Wickstrand (g), W. Wu (a), P. Bath (g), P. Berntsen (g), D. Oberthuer (c,f), V. Panneels (a), V. Cherezov (e), H. Chapman (c,h), G. Schertler (a,i), R. Neutze (g), J. Spence (b), I. Moraes (j,k,l), M. Burghammer (d,m), J. Standfuss (a) and U.Weierstall (b), *IUCrJ* **2**, 168-176 (2015); doi: 10.1107/S2052252514026487.

(a) Laboratory for Biomolecular Research, Paul Scherrer Institute (Switzerland)
(b) Department of Physics, Arizona State University (USA)
(c) Center for Free-Electron Laser Science, DESY (Germany)
(d) ESRF
(e) Department of Integrative Structural and Computational Biology, Scripps Research Institute (USA)
(f) Centre for Ultrafast Imaging, Hamburg (Germany)
(g) Department of Chemistry and Molecular Biology, University of Gothenburg (Sweden)
(h) Department of Physics, University of Hamburg (Germany)
(i) Deparment of Biology, ETH Zürich (Switzerland)
(j) Membrane Protein Laboratory, Diamond Light Source (UK)
(k) Department of Life Sciences, Imperial College London (UK)
(l) Research Complex at Harwell Rutherford, Appleton Laboratory (UK)
(m) Department of Analytical Chemistry, Ghent University (Belgium)

REFERENCES

[1] U. Weierstall *et al.*, *Nat. Commun.* **5**, 3309 (2014).
[2] A. Barty *et al.*, *J. Appl. Cryst.* **47**, 1118–1131 (2014).
[3] T.A. White *et al.*, *J. Appl. Cryst.* **45**, 335–341 (2012).

STRUCTURES OF ARCHAEAL TUBULIN-LIKE PROTEINS THAT CONTROL CELL SHAPE

Tubulin is an important protein in eukaryotes that assembles into filaments, controlling a cell's internal structure and movement. A family of tubulin-like proteins was found to also control cell shape and movement in a major group of prokaryotes called archaea. X-ray crystallography revealed the structures of independent protein subunits and polymerised filaments of these proteins, shedding light on their similarities with eukaryotic tubulins.

Tubulins make up microtubules, a key filament of the eukaryotic cytoskeleton responsible for DNA segregation during cell division, the maintenance of internal cellular order and morphological features involved in cell motility, including flagella and cilia. In contrast, the most widespread tubulin homolog in bacteria, FtsZ, forms filaments that establish the cytokinetic ring during cell division. Only a few other bacterial tubulins are known, and they perform specialised roles.

While many archaea produce FtsZ proteins involved in cell division, we set out to investigate a large uncharacterised group of archaeal FtsZ-like genes with sequence features similar to eukaryotic tubulins. Deletion of one of these genes (*cetZ1*) in the haloarchaeon *Haloferax volcanii* abolished motility. Remarkably, we also found that these cells could not develop from the common plate-shapes seen in liquid cultures into rod-shaped swimmer cells. Mutation of a predicted key residue in the CetZ1 GTPase active site directly affected changes in cell shape, blocking rod formation, even though an unaffected copy of *cetZ1* was also present. Interestingly, this mutant resulted in irregular cellular morphology and surface wrinkling, presumably due to hyperstability of CetZ1 polymers, since GTP hydrolysis is essential for polymer disassembly and turnover in tubulins. Our results therefore implied that CetZ1 polymerisation dynamics are required for its effect on cellular morphology.

Given the mix of FtsZ-like and tubulin-like sequence features of CetZ1, and its close relatives in archaea, it was of significant interest to determine the 3D structures of CetZs. High-resolution X-ray diffraction (1.9 to 2.1 Å) was recorded from crystals of three different CetZs at ESRF beamline **ID23-1** (two structures) and Diamond beamline I03 (one structure), and all three structures were solved by molecular replacement. We initially resolved the structure of a GDP-bound monomeric subunit of CetZ1, revealing that CetZs retain the canonical FtsZ / tubulin core fold (Figure 132a), with a C-terminal helical extension (H11) like tubulin, but without the N-terminal helical extension typically present in FtsZs. Given our anticipation of a cytoskeletal role for the CetZs, we attempted to visualise a CetZ polymer, screening CetZ1 extensively in the presence of GTP analogues, however no such crystals were obtained. A second CetZ homologue from the same species eventually yielded crystals containing tubulin-like protofilaments, showing that the polymerisation mechanism of CetZ proteins is consistent with archetypal tubulin and FtsZ protofilaments (Figure 132b and c). Finally, to confirm that CetZ orthologues were structurally consistent between archaeal species, we crystallised a divergent CetZ from *Methanosaeta thermophila*. The crystal structure of *Methanosaeta thermophila* CetZ revealed very similar morphology to both *Haloferax volcanii*

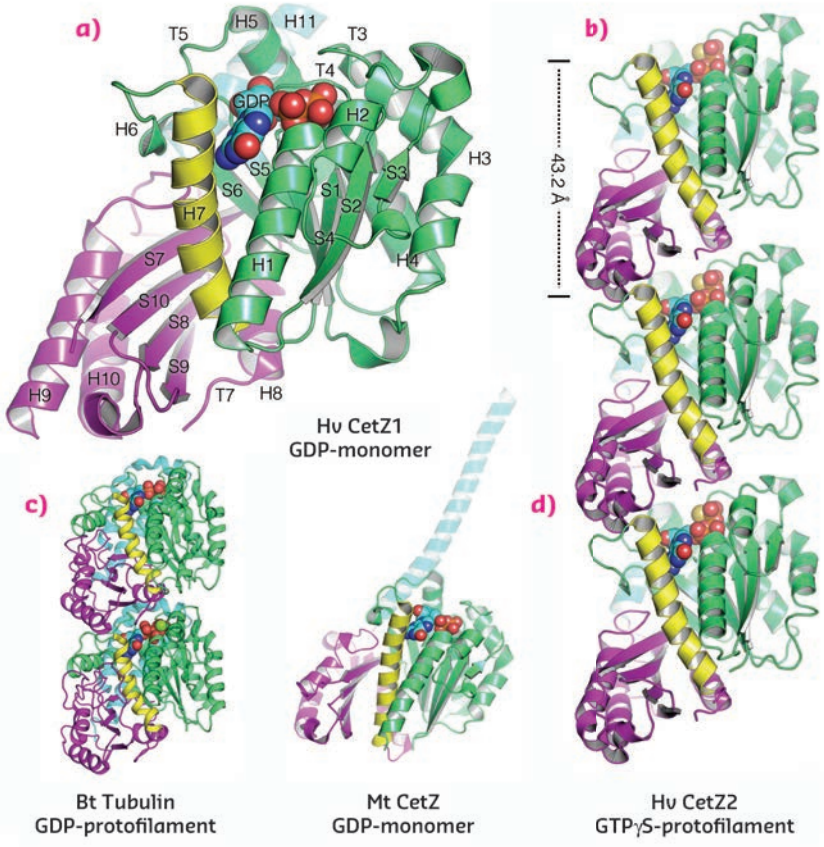

Fig. 132: Crystal structures of CetZs. (a) The crystal structure of *Haloferax volcanii* CetZ1 is shown with the secondary structural elements indicated according to the tubulin / FtsZ nomenclature. (b) The structure of a *Haloferax volcanii* CetZ2 protofilament. The tubulin dimer (c) is shown for the purposes of comparison. (d) The crystal structure of *Methanosaeta thermophila* CetZ. All full structures are shown from the same viewpoint in cartoon representation, with GTPase domains coloured green, activation domains coloured purple, H7 coloured yellow and the carboxy-terminal extension, H11, coloured blue.

homologues, most notably in the previously mentioned C-terminal H11 tail, implying conservation of the form, and presumably function, of the family.

In conclusion, our study identified a new and major group of the tubulin superfamily, confirmed, through structural and phylogenetic techniques, to be widespread in the Euryarchaeota, and provided the molecular and cell biological foundation for future studies of archaeal tubulins. Our study expands the known roles of the FtsZ/tubulin superfamily to include archaeal cell shape dynamics, implying that a cytoskeletal role for these proteins might have predated the evolution of the eukaryotic cell.

PRINCIPAL PUBLICATION AND AUTHORS

CetZ tubulin-like proteins control archaeal cell shape, I.G. Duggin (a, b), C.H.S. Aylett (a), J.C. Walsh (b, c), K.A. Michie (a), Q. Wang (a), L. Turnbull (b), E.M. Dawson (b), E.J. Harry (b), C.B. Whitchurch (b), L.A. Amos (a) and J. Löwe (a), *Nature* **519**, 362-365 (2015); doi: 10.1038/nature13983.
(a) Medical Research Council Laboratory of Molecular Biology, Cambridge (UK)
(b) The ithree institute, University of Technology Sydney (Australia)
(c) School of Physics, University of New South Wales, Sydney (Australia)

RNA VIRUS REPLICATION INTO RIBONUCLEOPROTEINS AND ITS REGULATION ELUCIDATED FROM BUNYAVIRUS POLYMERASE STRUCTURE

The structural characterisation of the La Crosse bunyavirus polymerase by X-ray crystallography and cryo-electron microscopy provides a detailed description of the polymerase's specific recognition of viral RNAs, the viral RNA genome's allosteric regulation of polymerase activity and RNA traffic inside the polymerase during RNA synthesis. These discoveries explain many biochemical observations accumulated over decades of bunyavirus research, providing a detailed mechanistic understanding of bunyavirus RNA synthesis.

In 1943, a new virus was isolated from *Aedes* mosquitoes during an investigation of yellow fever in the Semliki forest, Uganda. This virus, called Bunyamwera, was the first of a new family of segmented negative stranded viruses that took the name *Bunyaviridae*. Since then, more than 350 strains have been isolated around the globe. Among them, La Crosse virus (LACV) is a mosquito-transmitted human pathogen that causes 50–100 cases of encephalitis per year in the USA, mainly affecting children [1].

Bunyavirus, in common with *Arenavirus* (*e.g.* Lassa virus) and *Orthomixovirus* (*e.g.* nfluenza virus), have several genomic RNA segments coated by viral nucleoproteins that are assembled with their polymerase to form circular RNA structures called ribonucleoproteins (RNPs), functional units of replication and transcription [2]. Transcription is carried out by the polymerases through a unique mechanism known as "cap snatching" [3] These functional similarities contrast with the sequence

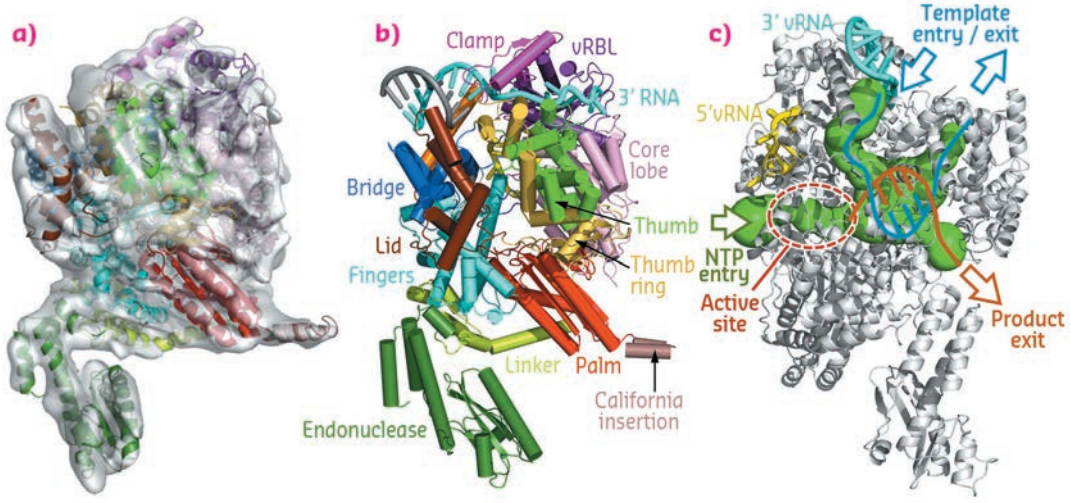

Fig. 133: (a) 3D reconstruction of the LACV polymerase apo-L1750 by cryo-EM at 8.3 Å resolution. (b) Crystal structure of L1750 in complex with the 3' (cyan) and 5' (yellow) vRNA. (c) RNA traffic within the LACV polymerase cavities (in green) where the template (blue) and product (orange) enter and exit as single strands.

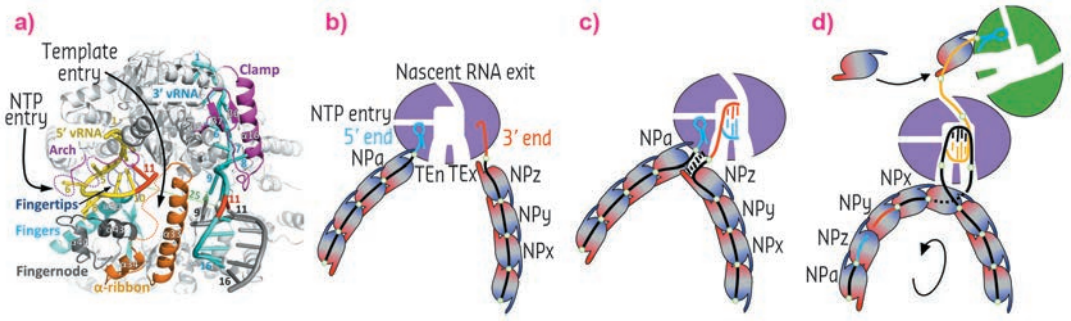

Fig. 134: (a) Representation of the LACV polymerase (grey) showing the disposition of key structural elements (labelled). The 5′ and 3′ vRNA ends are coloured in yellow and cyan, nucleotide 11 in each case is coloured in red to highlight their wide separation (>20 Å). (b) Schematic representation of panel (a), figure into the RNP. (c) With the 5′ end bound to the allosteric site for activation of RNA synthesis, a nascent cRNA begins to be synthesised. (d) Once the nascent c50 end emerges from the exit channel it can recruit an incoming apo-polymerase for encapsulating the progeny with incoming apo-NPs.

divergence between these viral polymerases. For example, the influenza virus polymerase is a heterotrimer [4] instead of a large monomeric polymerase (L protein) utilised by *Arenavirus* and *Bunyavirus*.

The structure of the LACV polymerase was obtained by protein crystallography using data collected at beamlines **ID23-1** and **ID29**, and cryo-electron microscopy (**Figure 133a,b**) revealing several domains extending from the universally conserved RdRpol core, sharing a striking structural similarity with the influenza polymerase [4].

The crystal structure of the L protein in complex with the viral RNAs clearly shows how the 3′ and 5′ RNA ends are bound at separate binding sites, and illustrates how the circularity of the RNP assembly is achieved (**Figures 133b** and **134a**). The high specificity for the self-viral RNA recognition is mediated by extensive sequence specific protein-RNA contacts in positively charged clefts outside the catalytic site and close to the template entrance channel. The binding of the 5′-vRNA end has an allosteric effect on the active site that activates the polymerase by ordering the important 'fingertips' structural element in an active conformation.

The internal cavity distribution allows for complete modelling of the RNA traffic inside the polymerase. This distribution implies that the template RNA to be read enters the polymerase and generates a double helix that after a few nucleotides is separated, the nascent RNA exits the polymerase near the cap-snatching machinery locus and the template RNA exits the polymerase proximal to the entry channel. The template RNA can then be reincorporated into the RNP with minimal disruption to the macro assembly structure (**Figure 133c**). This illustrates how the bunyavirus polymerase has adapted to work in the context of circular RNPs, maintaining their viral RNA as a single strand after duplication. Similar cavity distributions is found in the polymerase structures of influenza virus and vesicular stomatitis virus, therefore the conclusions revealed by the LACV polymerase structure can be extended to all NSV polymerases that work in an RNP context. We can thus propose a structure-based model of replication that might be extended to all sNSV and other related viruses such as VSV, Rabies or Ebola that also replicate in the RNP context [5] (**Figure 134**).

PRINCIPAL PUBLICATION AND AUTHORS

Structural insights into bunyavirus replication and its regulation by the vRNA promoter,
P. Gerlach (a,b), H. Malet (a,b), S. Cusack (a,b) and J. Reguera (a,b), *Cell* **161**, 1267–1279 (2015);
http://dx.doi.org/10.1016/j.cell.2015.05.006.

(a) European Molecular Biology Laboratory, Grenoble Outstation (France)
(b) Unit of Virus Host-Cell Interactions (UMI 3265), University Grenoble Alpes-EMBL-CNRS (France)

REFERENCES

[1] R.M. Elliott, *Nat Rev Microbiol* **12**, 673-685 (2014).
[2] J. Reguera *et al.*, *Curr Opin Virol* **5**, 7-15 (2014).
[3] J. Reguera *et al.*, *PLoS Pathog* **6**, e1001101 (2010).
[4] A. Pflug *et al.*, *Nature* **516**, 355-360 (2014).
[5] J. Reguera *et al.*, *PNAS* **110**, 7246-7251 (2013).

TRAPPING A SLIDING CLAMP IN ACTION: HOW MUTS ACTIVATES MUTL IN DNA MISMATCH REPAIR

DNA mismatch repair protects the genome from replication errors. In this process, the MutS protein activates MutL upon recognition of a mismatch and ATP binding. The crystal structure of the transient complex between MutS and the LN40 N-terminal domain of MutL was determined using a site-specifically cross-linked complex. This allowed analysis of the large conformational changes associated with sliding clamp formation. It showed why both mismatch and ATP are required for complex formation and how this step results in loading of MutL onto DNA. Validation by FRET, mutagenesis and stopped-flow kinetic analysis revealed the necessity of this step for DNA mismatch repair.

DNA mismatch repair (MMR) plays a crucial role in maintaining genome stability. Defects in the mismatch repair proteins in humans predispose them to Lynch syndrome (or hereditary non-polyposis colorectal cancer) and are associated with a variety of sporadic cancers. Upon replication, DNA mismatch repair is initiated by recognition of a mismatch or an unpaired base by MutS (in *Escherichia coli*) or its MSH homologues (in humans). Initial recognition of the mismatch is followed by an ATP-dependent conformational change of MutS into a sliding clamp state that can be recognised specifically by the next protein in the mismatch repair cascade, MutL (or its homologues). Intriguingly, both MutS and MutL are critical for correct repair and germline mutations in the human homologues of either of these proteins lead to cancer predisposition. How the transient sliding clamp of MutS promotes MutL homologue recruitment and activation of repair has long been unclear.

Here we have studied the sliding clamp state and the contribution of MutL to the mismatch repair initiation. The difficulty for structural analysis was the highly transient nature of the complex, requiring both mismatch and ATP, but causing a movement away from the mismatch. To trap this transient state we have made use of cysteine-free variants produced in the laboratory of P. Friedhoff in Giessen.

A highly specific cross-linked complex of MutS and MutL could be generated between specific single cysteines that would allow cross-linking of MutS to MutL only in the presence of a mismatch and ATP [1]. By scaling up the production of this cross-linked product and removal of flexible regions, we were able to obtain diffraction quality crystals of MutS (1-800) cross-linked to the LN40 domain of MutL. Data were collected at beamline **ID29** using a Pilatus 6M detector, resulting in a 4.7 Å dataset that allowed structure solution.

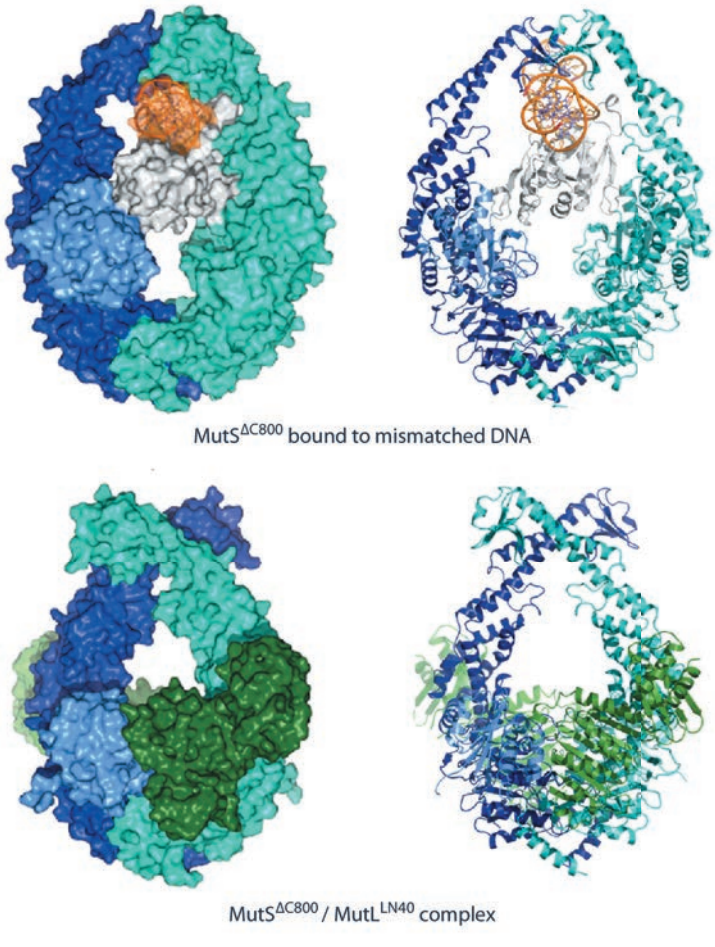

Fig. 135: Comparison of MutS DNA recognition and sliding clamp state. Top: Mismatch recognition state of MutS, shown in cyan and dark blue, N-terminal domain of subunit A, shown in light blue (connector domain) and white (mismatch recognition domain), DNA, shown in orange. Bottom: Crystal structure of MutS (colouring as above) complexed with the LN40 domain of MutL (dark green). Van der Waals surface and cartoon representations, left and right respectively.

In the structure of the complex, we observe that MutS has made large scissor-like movements relative to the mismatch bound state [2] (Figure 135), tilting about the ATPase domains. This pushes DNA down into a new channel, such that MutS can slide along the DNA. Meanwhile, the N-terminal connector domain has rotated to contribute to a compound MutL interface, together with the ATPase domain of the other MutS subunit. We were able to validate the observed conformation as the sliding clamp by FRET analysis of fluorophores linked at different sites using the single cysteine variants of MutS and MutL. The observed interfaces could be validated by mutagenesis using MMR complementation and SPR binding studies. The data showed that both MutS subunits were required for stable interaction with MutL explaining why MutL requires the sliding clamp for binding.

The new structure explains how the MutS sliding clamp promotes loading of MutL onto DNA, to activate downstream effectors. Using stopped-flow analysis, we could show that this was a slow step, after the fast recognition of the DNA. Using *in vitro* nuclease assays as well as *in vivo* complementation assays, we could show that this loading is essential for DNA mismatch repair. We thus elucidate a crucial mechanism that ensures that MMR is initiated only after detection of a DNA mismatch.

PRINCIPAL PUBLICATION AND AUTHORS

MutS/MutL crystal structure reveals that the MutS sliding clamp loads MutL onto DNA, F.S. Groothuizen (a), I. Winkler (b), M. Cristóvão (b), A. Fish (a), H.H.K. Winterwerp (a), A. Reumer (a), A.D. Marx (b), N. Hermans (c), R.A. Nicholls (d), G.N. Murshudov (d), J.H.G. Lebbink (c), P. Friedhoff (b) and T.K. Sixma (a), *eLIFE* **4**, e06744 (2015); doi: 10.7554/eLife.06744.
(a) Division of Biochemistry, Netherlands Cancer Institute, Amsterdam (The Netherlands)
(b) Institute for Biochemistry, Justus-Liebig-University, Giessen (Germany)
(c) Department of Genetics, Erasmus Medical Center, Rotterdam (The Netherlands)
(d) Structural Studies, MRC-LMB, Cambridge (UK)

REFERENCES

[1] I Winkler *et al.*, *J. Biol Chem.* **286,** 17326-37 (2011).
[2] M.H. Lamers *et al.*, *Nature* **407,** 711-717 (2000).

EXPOSING THE 'ACHILLES HEEL' OF DENGUE VIRUS SEROTYPES

Candidate Dengue disease vaccines have yet to offer protection against all four serotypes of dengue virus. Recently, human antibodies that neutralise all four serotypes have been isolated. Subsequent structural investigations show that these bind to a serotype-invariant site on the surface of the virus, revealing an 'Achilles heel' of dengue virus and potentially paving the way for the development of vaccines giving protection against all dengue virus serotypes.

Dengue disease is spread to humans by mosquito bites and is caused by four serotypes of the dengue virus (DENV). Of the nearly 400 million people per year infected with the virus, 75% exhibit no symptoms and recover quickly. However, for a small percentage, symptoms include bleeding from the nose or gums, severe abdominal pain, persistent vomiting and breathing difficulties. Although Phase III trials of potential vaccines have recently been carried out, current candidate vaccines show only partial protection with none providing protection against serotype 2 [1, 2]. Recently a series of human antibodies (bnAbs) that neutralise all four serotypes has been isolated [3] and structural studies of several of these bnAbs in complex with the envelope glycoprotein E ('protein E') from DENV serotype 2 were carried out using diffraction data collected at ESRF beamlines **ID23-2** and **ID29** and at SOLEIL. Protein E, relatively conserved among different serotypes, contains two conserved N-linked glycosylation sites (N67, N153) and is the only target of antibodies which neutralise dengue virus. In the mature dengue virus, 90 protein E dimers, arranged in an icosahedral configuration, completely coat the surface of the virus. Once the virus enters into cells, an irreversible conformational change leads to the fusion of viral and endosomal membranes.

The crystal structures of four bnAbs/Protein E dimer complexes were obtained, showing that all four bnAbs (B7, C8, C10 and A11) straddle

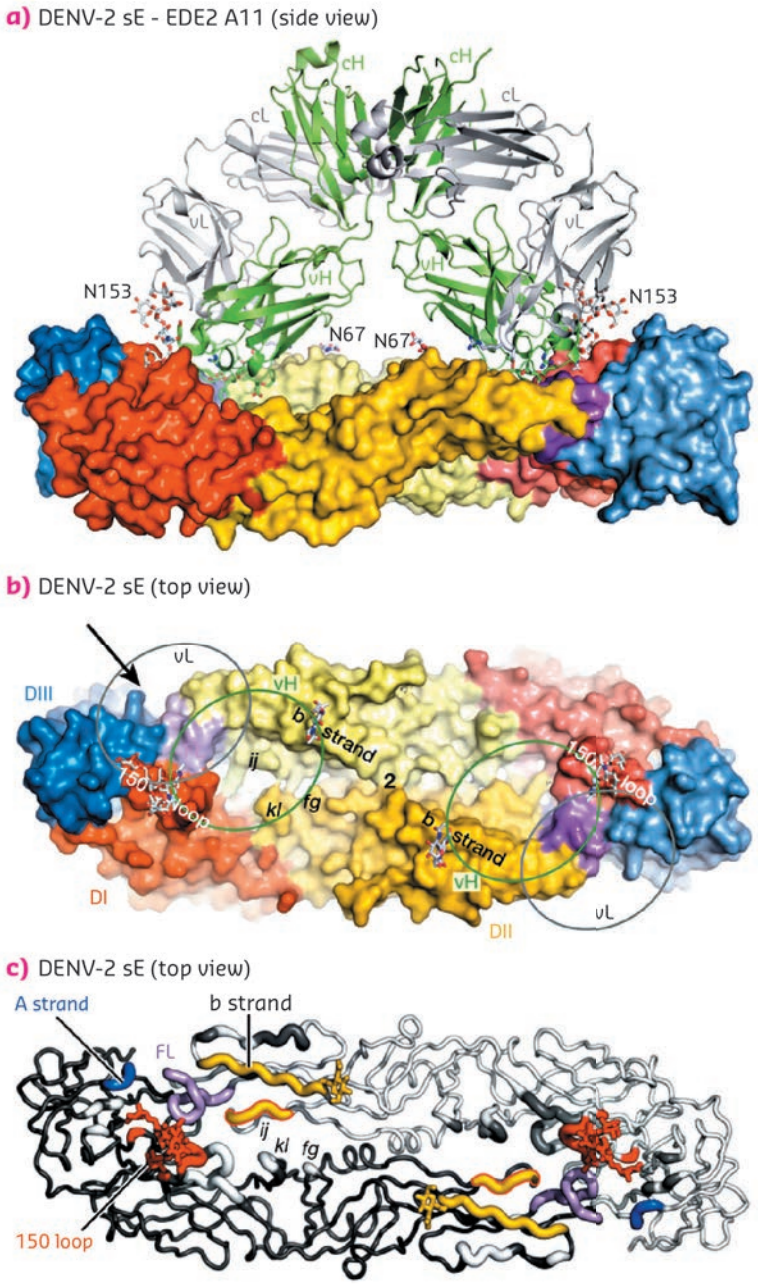

the protein E dimer interface and interact with protein E dimers in very similar regions, conserved in all four serotypes of dengue virus (Figure 136). On one subunit of the dimer, these regions include the N67 glycan bearing *b* strand, the *ij* loop and the domain II fusion loop. On the opposing subunit, the 150 loop is either directly targeted or rendered disordered by interaction of the antibody with domains I and III of protein E.

The major basis of the action of the bnAbs studied here seems to be interaction, in the specific context of an intact protein E dimer, with the domain II fusion loop and its surrounding area. This latter observation is important. In infected cells, immature DENV virions containing 180 copies of a heterodimer of protein E with the precursor membrane glycoprotein prM bound at their surface bud into the endoplasmic reticulum lumen, where the pH is neutral. Upon transportation to the acidic external medium, prM protects protein E from undergoing a premature acid-induced fusogenic conformational change and remains

Fig. 136: Interactions between the bnAbs and dengue virus protein E dimers. (a) Complex with bnAbs A11. The protein E dimer (side view) is shown in a surface mode representation coloured according to the domain structure shown in (b). The two N-linked glycans are shown as ball-and stick. A11 is shown in ribbon representation (heavy and light chains in green and grey respectively). (b) The unliganded Protein E dimer (2-fold axis labelled '2'). The ovals vH and vL show the contact sites of heavy and light chains of A11 respectively. (c) 'Worm' representation of the regions of the protein E dimer targeted by all four bnAbs. The main segments of the epitope are coloured and labelled. Reprinted by permission from Macmillan Publishers Ltd: *Nature* **520**, 109-113 (2015), copyright 2015.

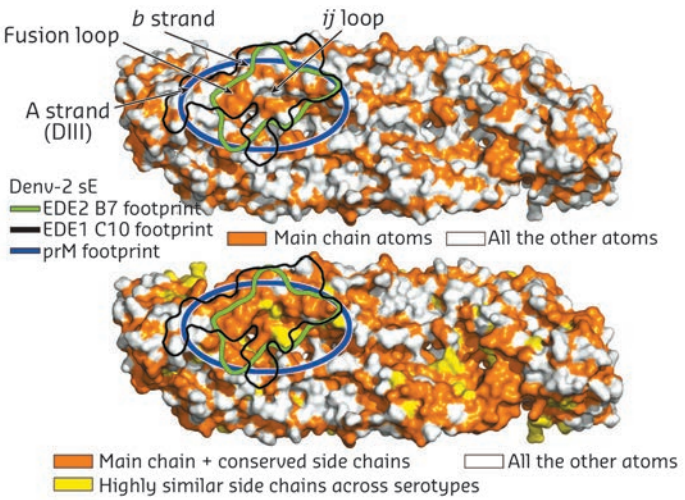

Fig. 137: The bnAbs protein E dimer epitope. The epitopes of bnAbs C10 (black line) B7 (green line) are indicated. The interaction area of the precursor membrane glycoprotein prM is shown as a blue oval. Reprinted by permission from Macmillan Publishers Ltd: *Nature* **520**, 109-113 (2015), copyright 2015.

bound to protein E dimers until the immature virions reach the exterior of the cell where the pH is neutral. Here, prM is released allowing the pre-fusion protein E dimers to become fusogenic upon encountering a new cell. The protein E dimer epitope (EDE) recognised by the bnAbs studied here maps extremely well with the binding site of prM on the protein E dimers (Figure 137), which thus represents an 'Achilles heel' of DENV as it is conserved across all four serotypes. A possible strategy for the development of vaccines against DENV might therefore be based on the presentation of DENV pre-fusion E dimers to the immune system with the aim of producing a response to the E dimer epitope identified here.

PRINCIPAL PUBLICATION AND AUTHORS

Recognition determinants of broadly neutralizing human antibodies against dengue viruses.
A. Rouvinski (a,b), P. Guardado-Calvo (a,b), G. Barba-Spaeth (a,b,c), S. Duquerroy (a,b,c), M-C. Vaney (a,b), C.M. Kikuti (a,b), M.E. Navarro Sanchez (a,b), W. Dejnirattisai (d), W. Wongwiwat (d), A. Haouz (e), C. Girard-Blanc (e), S. Petres (e), W.E. Shepard (f), P. Desprès (a), F. Arenzana-Seisdedos (a), P. Dussart (g), J. Mongkolsapaya (d,h), G.R. Screaton (d) and F.A. Rey (a,b,e), *Nature* **520**, 109-113 (2015); doi: 10.1038/nature14130.
(a) Institut Pasteur, Paris (France)
(b) CNRS UMR 3569, Paris (France)
(c) Université Paris-Sud, Faculté des Sciences, Orsay (France)
(d) Division of Immunology and Inflammation, Department of Medicine, Imperial College, London (UK)
(e) CNRS UMR 3528, Paris (France)
(f) Synchrotron SOLEIL, Gif-sur-Yvette (France)
(g) Institut Pasteur de Guyane, Cayenne (French Guiana)
(h) Dengue Hemorrhagic Fever Research Unit, Siriraj Hospital, University, Bangkok (Thailand)

REFERENCES

[1] M.R. Capeding *et al.*, *Lancet* **384**, 1358–1365 (2014).
[2] D. Normile, *Science* **345**, 367–368 (2014).
[3] W. Dejnirattisai *et al.*, *Nature Immunol.* **16**, 170–177 (2015).

Industrial research

Industry brings challenges to light sources, challenges coming from businesses' research and innovation needs. Challenges to our instrumentation and software, and sample environments and setups. But also fundamental challenges to the way light sources operate and serve users and clients from the worlds of academia and industry.

Over the last few years, the ESRF's commercial activities, operated through the Business Development Office, have generated over 2 MEuros annually. About 75% comes from beam time services, supplied on the basis of costs recovery, with the remainder from a growing technology transfer and instrumentation commercial programme exploiting the ESRF's intellectual property and singular pool of light source engineering know-how.

It is interesting to look at how this has changed over the years – in 1995, a pharma company was paying some 10,000 Euros for a day of beam time during which they might collect data on two or three protein crystal samples. The new "MASSIF" station, jointly created by ESRF and EMBL, allows us to offer a professional mail-in service at a price of 125 Euros per sample – an almost two orders of magnitude decrease in price, opening the door to any pharma or biotech, large or small, to benefit from our facilities. The ESRF is now building with its partners, from the EPN Campus and from private enterprises, research offers for industry with more than just X-rays, encompassing, for example, protein-to-structure or even gene-to-structure options. This builds on the local expertise and technological platforms, opening them for industry needs.

However, industry is still a largely immature user and client of light sources (and research infrastructures more widely) – there is potential for much more activity across large swathes of Europe's manufacturing, processing and technology-based industry. But a strong brake holding back further work is awareness and training of industry scientists and engineers as to the opportunities offered by modern synchrotrons. More and appropriate resources are needed at the facilities to support a "naïve" client such as industry with a service from translation of the R&I problem into the synchrotron experiment, to the experiment itself and analysis of the raw data to a finding that industry can understand and make use of.

Industry is often also confused by the academic processes and terminology which spillover into the commercial access. Whilst we are simplifying this as much as possible to make it cleaner for the clients, it remains a challenge. Facilitating access, and helping industry to cross this barrier, is a role increasingly played by small, nimble businesses bridging the gap between light sources and industry. An example in Grenoble is "Novitom", a strongly growing company focussing on providing industry with an efficient tomography access and analysis.

Working with industry is indeed a challenge and one the ESRF gladly takes on. Protein crystallography for drug discovery is largely assimilated across the world by the pharma industry. This has been enabled by a continual investment in the relationship with pharma, by technology developments at the light sources driven by industry needs, and by industry scientists valuing the light source data. Included in this chapter is an article by scientists at Genentech Inc. who studied the interaction between drug candidates and the binding site on a receptor linked with pain and other diseases.

Protein crystallography remains the mainstay of most light source industry programmes, although this is diversifying as techniques such as microtomography and SAXS mature towards high-throughput and cost-effectiveness for industry and carve out similar levels of work with industry thanks to the efforts of ESRF experts. In the last few years, the members of the ESRF, the European Commission and the ESFRI roadmaps have started to emphasise the need for European research infrastructures to be more active with industry and for industry to be able to more effectively exploit the investments made in these central research infrastructures. Light sources have a leading role to play in this with the application of X-rays for characterisation, going far beyond conventional techniques, of the advanced materials required for modern high performance and recyclable products.

In Grenoble, the IRT "NanoElec", a French public-private-partnership, is investing some 6 MEuros in a characterisation programme to pave the way for the local micro and nano-electronics industries to work with the ESRF, ILL and CEA-LETI, building a modern Rosetta Stone for us to understand the industry partners and industry to understand us, crafting dedicated instruments at the facilities for those needs, and testing business models on a larger scale beyond Grenoble. The budget is small in the overall context of the NanoElec programme,

but highly significant for the partners of the characterisation programme. The work is planned for nine years, completing as the new ESRF-EBS storage ring is installed, and potentially allowing a transition from effectively a non-existent interaction, to a dynamic and durable relationship with this industry sector. The work of the IRT is highlighted here by the description of the long-term innovation-led project on critical defects in integrated circuits.

Working with industry is not just about paid-for access. Equally important, perhaps even more so, is industry access via the ESRF's public beam time programme – to which industry is very welcome to apply for publishable work, as well as via collaborations with academic/industry partnerships, funded PhD students and post-doctoral fellows, and European and national grant programmes. These are important routes to generate industry impact using our facilities for pre-competitive research, which of course are also a very effective awareness and training mechanism. We also provide industry-dedicated training and education workshops and even tailored training at the ESRF or at company sites.

Looking to 2016 and further ahead with the incredible and fully unique materials analysis opportunities to be afforded by the ESRF-EBS in 2020, our efforts, as the ESRF and as a network of European light sources, with industry both large and small will grow, reinforcing the links between the facilities and industry to the benefit of European competitiveness.

We are available to discuss industry's future needs and we look forward to helping industry get the most out of the ESRF today and in the future.

So come on industry – we are ready, talk to us!

E. MITCHELL
mitchell@esrf.fr

INNOVATION-LED LONG-TERM PROJECT TO IDENTIFY CRITICAL DEFECTS IN INTEGRATED CIRCUITS

With a density of integration continuously increasing, driven by the need for better power efficiency and performance, 3D integration represents today the most promising strategy to adopt for next generation integrated circuit packaging.

Irrespective of the technology, all 3D-integrated circuits share the same challenge: to find critical defects and to verify the compliance of structural elements embedded within the bulk.

X-rays are a powerful tool for this analysis, in particular because they allow a non-destructive approach, *i.e.* 3D characterisation of the device, whilst the device functionality is maintained. However, nano-electronics is very demanding in terms of resolution. For this reason the use of synchrotron radiation is highly suitable to address the needs of this specific sector.

In the context of the ambitious French public-private partnership IRT "Nanoelec", in January 2015, ST Microelectronics engaged in a three-year innovation-led long-term project (iLTP) at the ESRF, with the support of the CEA-LETI and a PhD student dedicated to the project. This collaboration focuses on

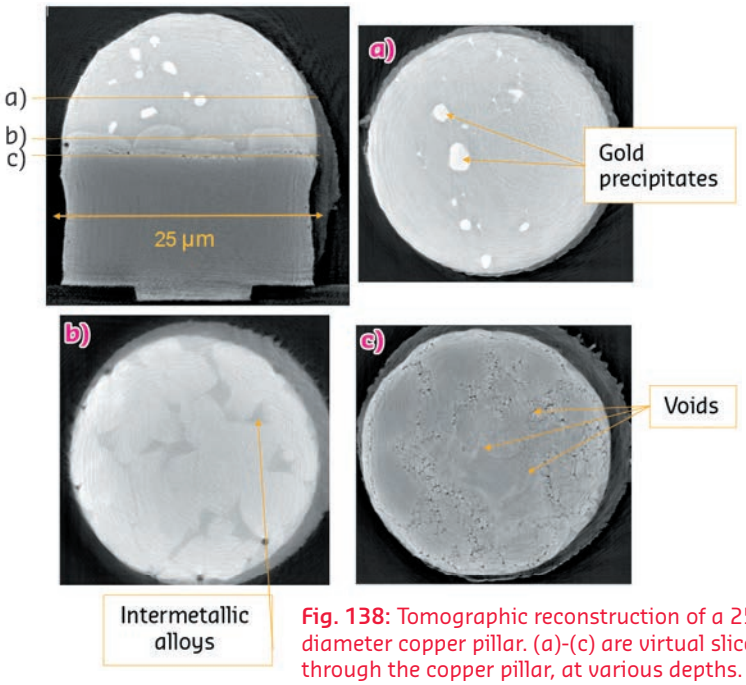

Fig. 138: Tomographic reconstruction of a 25 µm diameter copper pillar. (a)-(c) are virtual slices through the copper pillar, at various depths. Image courtesy of A. Fraczkiewicz, CEA/LETI.

advanced material characterisation, including statistical analyses, of the key interconnect and packaging technologies required in the coming generation of 3D integrated circuits. The iLTP beam time involves several of the ESRF's nanocharacterisation beamlines, ID16A, ID01 and ID19.

In this first year of experiments, an intense campaign of nanotomography characterisation has been carried out at ID16A, with the objective to identify the potential of the nanotomographic setup and also to build up ESRF expertise and facilities (with capital contribution from the IRT Nanoelec) to effectively respond to pre-competitive and competitive applications in nano-electronics.

Particular emphasis has been given to the investigation of copper pillars, some fundamental elements of the 3D-integrated circuits manufacturing technology. Copper pillars are cylinders of copper with a diameter spanning between 10 and 70 µm on which a soldering ball (Ag, Cu, Ni eutectic alloy) is deposed. One of the main results of this first year iLTP has been the tomographic acquisition of a 25 µm diameter copper pillar at the exceptional resolution of 32 nm (see Figure 138). This technique permits the main structural components of the copper pillar to be distingushed, and, in particular, the intermetallic, the control of which is one of the main concerns in the manufacturing process of these objects.

These studies result from a fruitful collaboration between A. Fraczkiewicz and P. Bleuet, CEA/LETI, F. Lorut, STMicroelectronics, and P. Cloetens and J.C. Da Silva at beamline ID16A.

AUTHORS

E. Capria
IRT-NANOELEC, ESRF

VISUALISING INHIBITION OF THE Nav1.7 PAIN CHANNEL

Voltage-gated sodium (Nav) channels are therapeutic targets for many diseases but isoform-selective blockers are not clinically available. We devised a new crystallisation strategy to determine structures of a previously unknown drug-binding site in the Nav1.7 channel. These results may accelerate the development of new treatments for pain and other diseases.

The opening of voltage-gated sodium (Nav) channels underlies the generation of action potentials in neurons and muscle cells. Nine Nav channel isoforms are differentially expressed throughout the human body and mutations are associated with migraine (Nav1.1), epilepsy (Nav1.1-Nav1.3, Nav1.6), pain (Nav1.7-Nav1.9), cardiac (Nav1.5), and muscle paralysis (Nav1.4) syndromes. The Nav1.7 channel is expressed primarily in sensory neurons, where gain-of-function mutations are associated with extreme pain disorders, and loss-of-function mutations cause an inability to feel pain. These contrasting phenotypes have identified Nav1.7 as a promising target in the pain perception pathway and have motivated efforts to develop selective inhibitors.

Human Nav channels are large membrane proteins (~2,000 residues) that contain a central pore module surrounded by four peripheral voltage-sensing domains (VSDs). Nav channel blockers used for the treatment of neurological and cardiovascular disorders lack isoform selectivity because they bind within the highly conserved central pore module, which limits their therapeutic utility. A recent breakthrough study identified a new class of antagonist that presumably targets a unique binding site on the fourth voltage-sensor domain (VSD4), raising hopes that an isoform-selective inhibitor can be found. Unfortunately, the inherent complexity of human Nav channels limits our ability to pursue high-resolution crystallographic studies because these proteins undergo extensive post-translational modification and associate with auxiliary subunits. To overcome the technical complexities of working with full-length human channels, we exploited a simpler homotetrameric bacterial sodium channel, called NavAb, by fusing portions of Nav1.7 VSD4 onto it. The antagonist binding-site was preserved within this VSD4-NavAb chimeric channel, and we subsequently found that this chimeric construct allowed purification, crystallisation, and structure determination of potent aryl sulfonamide inhibitors in complex with the human Nav1.7 VSD4 receptor site (Figure 139).

Functional studies using patch-clamp electrophysiology revealed that the inhibitors bind to an isoform-selective and extracellularly accessible site on VSD4. These inhibitors show a high level of state-dependence, potently blocking human Nav1.7 only when VSD4 is in its activated conformation. Remarkably, these inhibitors were 100,000-fold more selective for Nav1.7 over the cardiac isoform Nav1.5, a level of selectivity previously unseen among Nav channel blockers.

To understand the mechanism of Nav1.7 inhibition by this novel class of antagonist, we pursued high-resolution structural studies. After painstaking efforts to grow crystals, we contacted the ESRF for provision of synchrotron radiation facilities. With the aid of a dedicated staff, high-quality diffraction data were collected at beamline **ID29**. With access to these data, our crystallographic studies revealed that the anionic warhead from the inhibitors directly engages the fourth arginine "gating charge" on the S4 helix, which effectively traps VSD4 in its activated state. We subsequently demonstrated that isoform selectivity is achieved by inhibitor interactions with non-conserved residues found on the S2 and S3 transmembrane helices of VSD4. Remarkably, the drug receptor site is partially submerged within the membrane (**Figure 140**) and a peripherally bound phospholipid was observed to form a tripartite complex with the antagonist and channel.

In summary, we utilised a new crystallisation strategy and the ESRF to enable the structure determination of VSD4 from human Nav1.7 in complex with potent, state-dependent, isoform-selective small molecule antagonists. Mechanistically, inhibitor binding immobilises VSD4, stabilising a non-conductive state of the channel. An exposed inhibitor binding-site expands the importance of the membrane bilayer in ion channel biology. We hope that these structures will accelerate the development of new treatments for pain that target Nav1.7 and aid drug design efforts aimed at other voltage-gated ion channels.

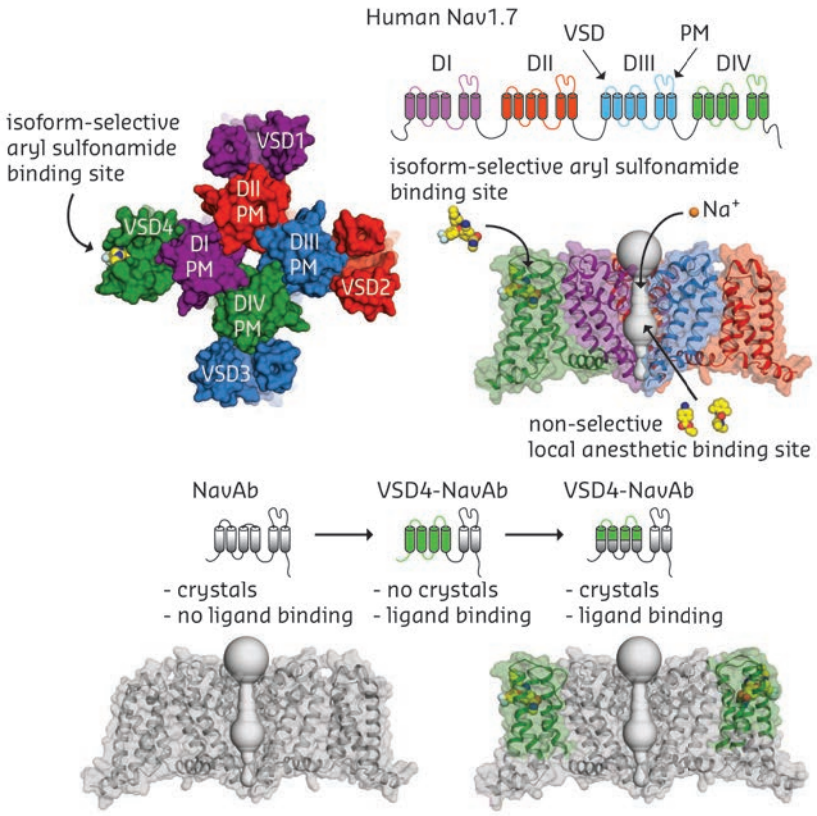

Fig. 139: Overview of Nav1.7 VSD4 crystallisation strategy highlighting domain structures, 3D models, and drug binding sites in Nav channels.

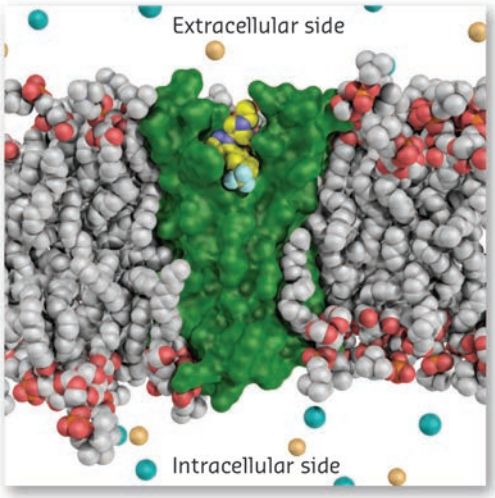

Fig. 140: Crystal structure of the Nav1.7 VSD4-antagonist complex viewed in a model membrane.

PRINCIPAL PUBLICATION AND AUTHORS

Structural basis of Nav1.7 inhibition by an isoform-selective small molecule antagonist, S. Ahuja (a), S. Mukund (a), L. Deng (b), K. Khakh (c), E. Chang (c), H. Ho (a), S. Shriver (a), C. Young (c), S. Lin (c), J.P. Johnson Jr. (c), P Wu (a), J. Li (d), M. Coons (a), C. Tam (a), B. Brillantes (a), H. Sampang (a), K. Mortara (a), K.K. Bowman (a), K.R. Clark (e), A. Estevez (a), Z. Xie (c), H. Verschoof (c), M. Grimwood (f), C. Dehnhardt (f), J. Andrez (f), T. Focken (f), D.P. Sutherlin (d), B.S. Safina (d), M.A. Starovasnik (a), D.F. Ortwine (d), Y. Franke (a), C.J. Cohen (c), D.H. Hackos (b), C.M. Koth (a) and J. Payandeh (a), *Science* **350,** 6267 (2015); doi: 10.1126/science.aac5464.

(a) Department of Structural Biology, Genentech Inc., South San Francisco (USA)
(b) Department of Neuroscience, Genentech Inc., South San Francisco (USA)
(c) Department of Biology, Xenon Pharmaceuticals Inc., Burnaby (Canada)
(d) Department of Discovery Chemistry, Genentech Inc., South San Francisco (USA)
(e) Department of Biochemical and Cellular Pharmacology, Genentech Inc., South San Francisco (USA)
(f) Department of Chemistry, Xenon Pharmaceuticals Inc., Burnaby (Canada)

Enabling technologies

Technical developments provide the backbone and basis for every aspect of the ESRF's scientific activity. They enable and facilitate advancements in science, and play a central role within the ESRF-EBS project. 2015 saw an increasing number of upgraded and refurbished beamlines becoming fully operational, and witnessed an accelerated migration of technical infrastructure and instrumentation development resources from the experimental facilities to the accelerator and source. While the ESRF User Community will profit from the largely improved performance of the new stations in the years up to the shutdown, the design and procurement of the new machine is in full swing, and R&D work has started to tackle the various challenges related to the increased brilliance of the X-ray source.

As in past years, the 2015 highlight contributions provide a representative slice through the diverse R&D activities, and reveal at the same time some trends. The first four contributions deal with instrumentation developments either originating from Upgrade Phase I (sub-30 nm focusing at ID16A) or in anticipation of future requirements such as the need for high-quality diamonds as monochromators, the characterisation of the X-ray wave front, or the prototype of an X-ray microscope for material science applications. The following three contributions deal with the development of algorithms and automation procedures, emphasising the increasing complexity of data analysis and the requirement for effective data collection and digestion. Finally, the last contribution on the prototype girder is representative of the numerous developments for the new storage ring and provides the natural link to the *Accelerator and X-ray Source* chapter.

In addition to the results presented in the Highlights articles, 2015 has witnessed other important accomplishments in different technological areas. In the context of detector and electronics development, various new photon counting pixel detectors were successfully built and tested, including CdTe Maxipix modules (within the FP7 CALIPSO project) and a prototype of a Smartpix pixel detector for high-frame rate applications above 1 kHz. The release of new IcePAP firmware offered advanced features such as linked axes and parametric trajectories, and a new position encoder processing Unit (PEPU) was developed as part of the DAnCE platform.

To enable top-up operation in user mode from 2016 onwards, important modifications of the building infrastructure and electricity supply were implemented and front-end boards for the ramping injector power supplies (RIPS) and the associated sequencer control have been delivered and validated.

For the accelerator complex, the HDB++ Cassandra cluster now acquires storage ring data in parallel with the former archive database, and for the booster upgrade, new SY BPM software based on Libera spark is now operational.

The migration of the NAS systems to the much faster GPFS disk storage systems has continued and provides a boost in performance for I/O intensive experiments.

Finally, the in-house production of aluminium compact refractive lenses has borne first fruit and a set of 2D paraboloidal lenses was delivered to the new powder diffraction beamline ID22.

The instrumentation beamline, BM05, continued to be a strategic tool for developments such as the characterisation of detectors, scintillators, and X-ray optical components. With the delivery of a new diffractometer for the new IRT NanoElec station for X-ray diffraction, reflectivity, and topography, its commissioning is almost completed, and its operation can start in spring 2016. This station opens up new perspectives for BM05 to provide new services for proprietary research, especially for customers from the semiconductor industry.

Besides the development and implementation of instrumentation for the experimental facilities and the accelerator and source, and joint efforts with other facilities such as the IcePAP, TANGO, LImA, and mxCuBE collaborations, the ESRF has provided technology and know-how in the delivery of a FReloN camera based on the EDXAS detector to the Diamond Light Source and the engineering design of the Materials Imaging and Dynamics station for the European XFEL.

M. KRISCH
and R. DIMPER

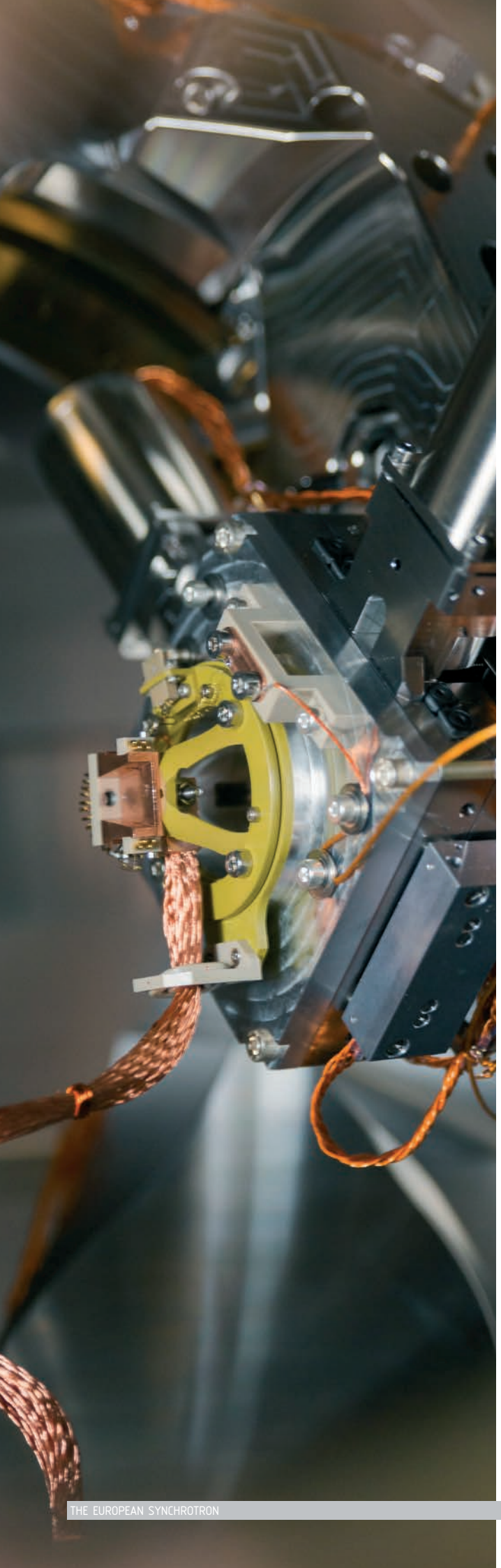

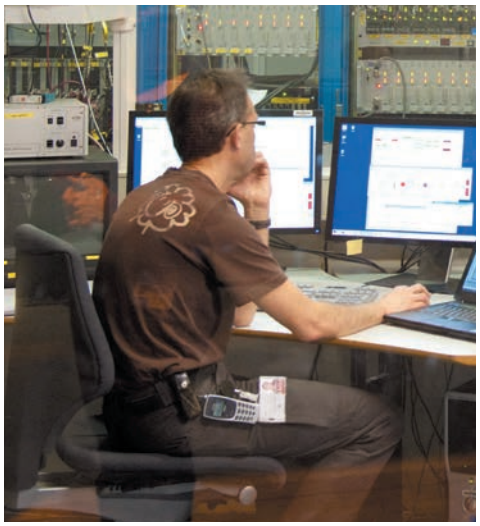

DIFFRACTION TOPOGRAPHY AS AN INDUSTRIAL TOOL FOR THE CHARACTERISATION OF THE CRYSTALLINE QUALITY OF DIAMOND

Beamline BM05 provides powerful tools for the characterisation of the crystalline quality of synthetic single crystal diamonds. White beam "topography" imaging is a fast and straightforward technique that is capable of identifying all the extended crystal defects. Using this method, we detected differences in the crystal quality such as dislocation densities and growth sectors between commercially available diamond plates from various suppliers. A quantitative extension of this diffraction imaging technique is rocking curve imaging using a monochromatic beam. This allows determination of the lattice parameter variations and the local lattice tilts. This can be related to the presence of specific defects and also the lattice deformation induced by impurity incorporation, for example due to boron doping, which is differentiated according to the local growth conditions.

Synchrotron techniques have been used for both academic and industrial studies to characterise silicon and diamond. X-ray Bragg diffraction imaging ("X-ray topography") is a well-known technique for characterising crystalline quality. The various Bragg diffraction imaging techniques (white beam topography, rocking curve imaging and others) have been implemented at beamline **BM05**, where they are used for research and as standard techniques to characterise the quality of crystals for industrial applications. This method is sensitive to defects such as dislocations, stacking faults, surface imperfections, even weak simple impurity concentration gradients and inclusions via the distortion they induce in the crystal lattice and allows their spatial structure to be investigated with a resolution down to the micrometre scale.

Interest in single crystal diamond for electronic applications is increasing because of its many attractive physical and electronic properties, in particular its wide band gap, high mobility of both charge carriers, high electric field breakdown strength, low X-ray absorption coefficient, low thermal expansion and extremely high thermal conductivity. Our interests are the application of diamond in the related fields of electronics and detectors, and diffractive and refractive optics, where many of the previously mentioned properties are particularly relevant. Boron and phosphorus doped diamond devices have already been shown to allow the fabrication of excellent high voltage diodes and FET switches. These are expected to efficiently commute high power at high frequency. The Horizon2020 European project Green Diamond [1] is a four year 4.5 M€ project that aims to develop all-diamond high power electronic devices, with the goal of substantially reducing the huge energy losses associated with electrical power transmission and transport. The ESRF is one of the 14 institutes participating in Green Diamond, playing a vital role in characterising the diamond material: hundreds of the [100] orientation plates needed by the project have already been measured at BM05. High quality diamond plates are also needed at modern synchrotrons for X-ray optical applications. Another potential application relies on the creation of a diamond superlattice by the periodic concentration variation of boron-doping during synthesis. A controlled periodic variation of the lattice parameter can be achieved while maintaining coherent lattice quality. Using high energy charged particle beams, diamond crystal undulators fabricated in this manner could theoretically generate powerful monochromatic radiation reaching up to γ-ray energies.

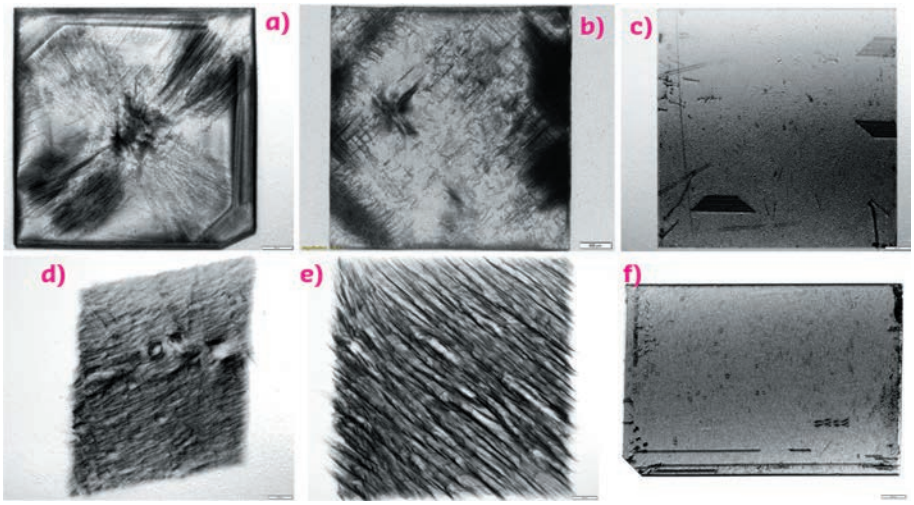

Fig. 141: White beam topography of different single diamond plates characterised at BM05: (a) HPHT, (b) CVD E6, (c) HPHT NDT, (d) CVD EDP, (e) Diam2tech, (f) IIa.

Such applications all require defect free (surface and bulk) diamond plates with high quality polished surfaces of well controlled (~ 0.1°) miscuts. The commercial availability of single crystal diamond substrates from various suppliers covers a large variety of crystalline qualities and prices. Examples of topography measurements made at BM05 are shown in **Figure 141**: The high

quality type-IIa diamond samples (Figure 141c and f) show areas that are almost dislocation free in the large 100 growth sector, with only a few stacking-faults and surface scratches visible.

The other 'low grade' commercial diamond plates shown present dislocations with densities of 10^3 to $10^4 cm^{-3}$. Figure 142 shows a quantitative measurement of the crystalline quality (assessed via the rocking curve width) of a boron doped layer grown on a diamond plate. The image suggests a correlation between the boron doped layer with distortion of the diamond surface: the rocking curve (FWHM > $3.5° \times 10^{-3}$) is much higher at the boron doped border than at the sample centre bulk region (FWHM $2.4° \times 10^{-3}$).

Particular attention must be paid not only to the quality of overgrown doped diamond layers, but also to the diamond substrate itself, including all the defects that exist in the bulk such as dislocations, stacking faults, growth sectors, and (sub) surface damage from polishing processes. In the case of electronic devices, all of these defects contribute to the final performance.

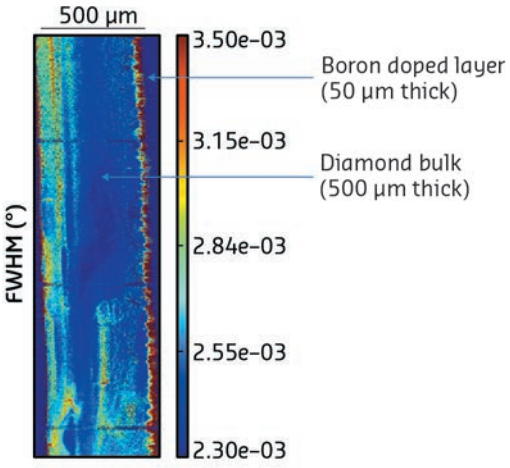

Fig. 142: Diamond 400 reflection FWHM maps obtained using section topography rocking curve imaging. The scale is in degrees and shows the variation in crystalline quality in a virtual cross-section through a 500 µm thick diamond plate overgrown with a 50 µm thick Boron doped diamond layer. The face with the Boron doped layer is on the right.

AUTHORS

T.N. Tran Caliste (a), J. Hartwig (a), J. Morse (a), E. Ziegler (a), R. Barret (a) and S. Connell (b).
(a) ESRF
(b) University of Johannesburg (South Africa)

REFERENCES

[1] GreenDiamond: www.greendiamond-project.eu

X-RAY WAVEFRONT METROLOGY OF PULSED BEAMS USING SPECKLE TRACKING

A new way of measuring the beam wavefront has been created by observing the granular pattern from a piece of abrasive paper illuminated with a laser-like X-ray beam. A "transparent" detector permits images of the granular pattern to be captured simultaneously by two distinct detectors. A computer algorithm has been developed to interpret the beam wavefront from these images.

At-wavelength metrology is gaining in importance at large-scale X-ray facilities in order to take full advantage of the beams delivered by high-brilliance sources. Its applications are the optimisation of adaptive optics, monitoring and limiting thermal effects on X-ray optical elements, and the determination of the X-ray beam wavefront itself, the latter being a crucial input for the analysis of coherent scattering experiments.

Using the experimental facilities at **BM05** and **ID22NI**, we have successfully commissioned a new instrument based on the X-ray speckle tracking (XST) principle to enable the recovery of an X-ray wavefront from two images acquired simultaneously [1]. The schematic experimental setup is depicted in Figure 143. The incident X-ray beam passes through a thin phase object and, due to the partial coherence of the X-ray beam, the waves scattered from such an object interfere with the transmitted X-rays to generate speckles, *i.e.* random contrast features. When a 2D detector is then inserted along the beam trajectory within the so-called near-field region, the recorded image shows a granular pattern with high frequency features whose shapes vary little with the detector's distance from the object. In this domain, the distortion of the interference pattern is only ruled by the wavefront transformation upon propagation in the Fresnel region. Therefore, when two images are recorded at different distances, it is possible by numerical processing to infer the trajectory of the X-rays from one image to the next and eventually deduce the exact shape of the wavefront.

The XST principle is based on computer cross-correlation algorithms capable of searching and identifying small subsets of pixels from one image

to the other in an accurate and robust manner. In practice, a first assumption of rigid subset displacement allows the determination, with sub-pixel accuracy, of the vector field. The latter can then be used as an initial guess for a Newton-Gauss minimisation enabling the consideration of subset distortion (local curvature) that pushes the evaluation of the displacement vector to an accuracy close to 0.01 pixel. The simultaneous recording of two distant images avoids any contribution due to synchrotron beam instability and more importantly is ready to be used for pulse-to-pulse metrology at free electron lasers (FEL) where each bunch could present a slight wavefront difference from the others.

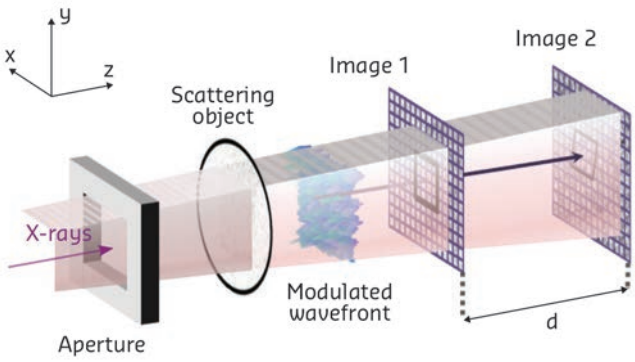

Fig. 143: Schema of the experimental setup for X-ray speckle tracking.

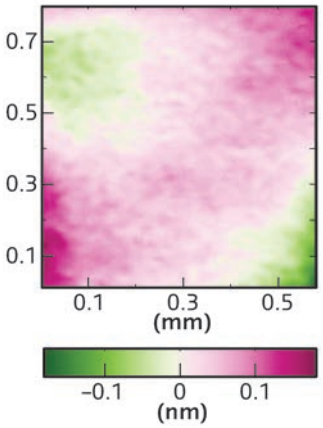

Fig. 144: X-ray beam wavefront errors determined experimentally with a distance of 510 mm between the two detectors. One can notice the scale amplitude in the order of the angstrom.

XST requires 2 detectors and the beam has to pass through either the first detector (as described here) or through both detectors (future development). For the first case, our approach was to use indirect illumination of CCD FreLoN cameras [2]. Most of the X-rays go through a thin garnet scintillator and a glassy carbon mirror (low absorption) orientated at 45° with respect to the incoming beam direction and continue their way to the second detector operating on the same principle. The image of the scintillator emitting visible light by luminescence is reflected at 90° by the mirror and transported by a microscope objective to the CCD chip. Numerical treatments are used to minimise the background noise and to correct the raw images for the inhomogeneous response of the scintillators and for the detector distortion.

The online metrology setup was tested at the former ID22NI beamline to characterise a 29 keV energy beam focused down to a spot size of ~ 50 nm x 50 nm using multilayer-coated mirrors set in a Kirkpatrick-Baez arrangement. After data processing, two-dimensional images of the wavefront gradient were obtained with a spatial resolution as low as a few micrometres, impossible to reach with previous methods. The wavefront was then recovered by two-dimensional numerical integration of the phase gradient. The wavefront errors were derived by subtraction of the best fitting ellipsoid from the reconstructed wavefront. **Figure 144** shows the results of such a reconstruction. The observed wavefront error is equivalent to a 45° astigmatism, which may be due to small sagittal focusing effects or orthogonal misalignment of the two mirrors of the upstream KB optical system.

In the present experiment, the horizontal and vertical wavefront gradient errors were in the order of 0.4 µrad and 0.7 µrad, respectively. The angular sensitivity could be improved to below 100 nrad by increasing, for instance, the propagation distance between detectors. This speckle-based instrument is expected to find future applications at FEL sources for the single-shot analysis of the X-ray pulses, provided further development of specific fast scintillators and semi-transparent mirrors with minimal degradation of the beam coherence and of the speckle pattern is undertaken [3].

PRINCIPAL PUBLICATION AND AUTHORS

X-ray pulse wavefront metrology using speckle tracking, S. Berujon, E. Ziegler and P. Cloetens, *Journal of Synchrotron Radiation* **22**, 886-94 (2015); doi: 10.1107/S1600577515005433.

ESRF

REFERENCES

[1] See references included in the principal publication.
[2] J-Cl. Labiche *et al.*, *Review of Scientific Instruments* **78**, 091301 (2007).
[3] Project funded by the European Union's Horizon 2020 research and innovation programme under grant agreement No 654220 (www.eucall.com).

Sub-30 nm FOCUSING WITH FIGURED MULTILAYER KIRKPATRICK-BAEZ MIRRORS

The upgraded ID16A nano-imaging end station was recently equipped with two new Kirkpatrick-Baez focusing systems based on figured mirrors and in-house coated graded multilayers. They consist of W/B_4C with d-spacings down to 2 nm and possess steep longitudinal thickness gradients to comply with Bragg's law along the full beam footprint. They operate at 17 keV and 33.6 keV, respectively. Users now have access to beam sizes down to 27 x 21 nm^2 (H x V) with a photon flux up to 10^{12} ph/s.

The Kirkpatrick-Baez (KB) configuration is commonly used to produce a focused X-ray beam. In this scheme, one mirror focuses the beam vertically and a second mirror horizontally. Contrary to previous setups [1], the new systems on ID16A use mirrors that were polished to their elliptical cylinder figures, thus obtaining lower figure errors with higher curvature than achievable with dynamically bent mirrors.

Often KB systems are used in combination with multilayer coatings. This allows the mirrors to be used at larger incidence angles and is therefore beneficial to increase the acceptance for a given mirror length. Multilayers reflect an energy band pass of 1-5% at an angle given by Bragg's law. Consequently, due to the strong variation in the local incidence angle on the mirror, the multilayer d-spacing must be graded to reflect along the full beam footprint on each mirror.

The new ID16A beamline is 185 m long and operates at fixed photon energies that are selected by a horizontally focusing multilayer. The multilayer generates a 50 µm wide secondary source in the horizontal direction at 40 m from the undulator. Since the source shape is strongly elliptical, this layout is required to obtain an approximately circular focal spot at the sample. Consequently, the source distances with respect to the KB are 183.5 m in the vertical and 144.6 m in the horizontal direction. By choosing the respective image distances to 0.1 m and 0.043 m, a circular focal spot can indeed be generated.

Two independent nano-focusing KB setups are installed in the experimental hutch to operate the end station either at 17 keV or at 33.6 keV. The total mirror lengths are only 70 mm (vertical) and 36 mm (horizontal). The respective mirror pairs differ in curvature and grazing angle but they were designed in such a way as to provide the same focal spot size at both photon energies. Assuming perfect optics, one would expect a diffraction limited spot size of 7-8 nm FWHM, as confirmed by wave optical simulations [2]. Including the measured figure errors of the mirrors, the expected spot size may increase slightly. The source size contribution should also blur the focal spot to at least 15 nm FWHM.

The multilayer coatings consist of W/B_4C with d-spacings down to 2 nm. The multilayers were deposited at the ESRF Multilayer Laboratory in dynamic mode where the substrates are moved in front of each cathode. Steep longitudinal gradients were achieved by varying the speed during each duty cycle. Based on X-ray reflectivity measurements at 8048 eV, the estimated total KB efficiency is about 45% at 17 keV and 75% at 33.6 keV, and the total bandwidth is 1.5% FWHM in both cases. **Figure 145** shows theoretical and experimental d-spacing profiles for both the horizontally and the vertically focusing multilayer of the 17 keV KB system. The total offset errors are close to 0.3% and the variations are below 0.5%. Taking into account both the involved energy bandwidths and the gradient accuracy, the full source intensity can be transmitted by the optical system to the experiment.

Both KB systems were installed and commissioned at ID16A. The size of the focal spot was measured using knife edge scans along both the horizontal and the vertical directions. The resulting FWHM spot size is 23 nm (hor) x 37 nm (ver) at 17 keV and 27 nm (hor) x 21 nm (ver) at 33.6 keV (**Figure 146**, left). The respective photon fluxes are 7x10^{11} ph/s

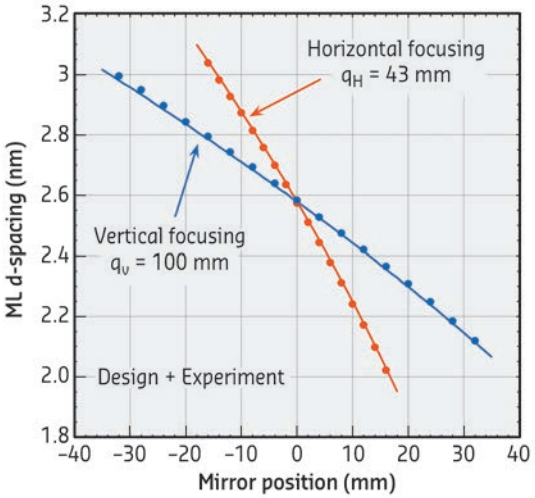

Fig. 145: D-spacing profiles of the horizontally focusing (red) and the vertically focusing (blue) multilayers (ML). Solid lines indicate theoretical curves, dots show experimental data.

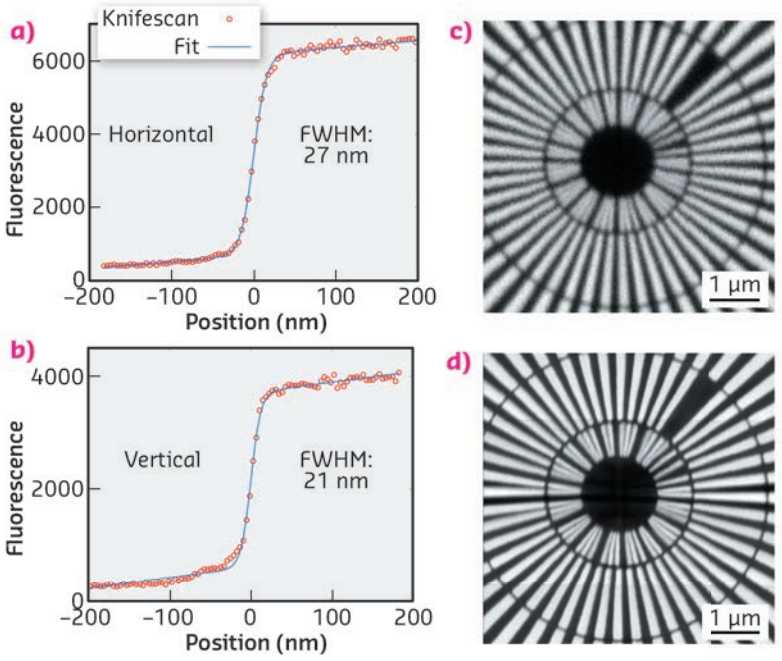

and $6x10^{10}$ ph/s. Discrepancies between the measured and expected spot sizes have not yet been explained but may be due to the physical extent of the knife edge or artefacts from the opto-mechanical assembly.

Fluorescence imaging was carried out to study image quality and resolution and to compare them with data from the previous KB system used on ID22NI. The pictures in **Figure 146** (right) show Siemens star images taken at ID22NI (c) and ID16A (d) and clearly demonstrate the improved spatial resolution with the new system.

Fig. 146: Left: Knife edge scans at 33.6 keV through the focal spot in fluorescence mode: (a) horizontal scan; (b) vertical scan. The blue lines are error functions fitted to the experimental data. Right: X-ray fluorescence imaging at 17 keV: (c) previous setup at ID22NI using a dynamically bent KB; (d) new setup at ID16A using a figured KB.

PRINCIPAL PUBLICATION AND AUTHORS

C. Morawe, R. Barrett, P. Cloetens, B. Lantelme, J.-C. Peffen and A. Vivo, *Proc. SPIE* **9588**, 958803 (2015); doi: 10.1117/12.2189279, with additional contributions from A. Pacureanu, Y. Yang, J.C. da Silva and R. Baker.
ESRF

REFERENCES

[1] R. Barrett *et al.*, *Proc. SPIE* **8139**, 813904 (2011); doi: 10.1117/12.894735.
[2] M. Osterhoff, C. Morawe, *Proc. SPIE* **8502**, 850208 (2012); doi: 10.1117.12.928938.

DIFFRACTION BASED TRANSMISSION X-RAY MICROSCOPY

Dark field X-ray microscopy is a new type of microscopy that enables the user to zoom in on internal parts of mm-sized crystalline samples and provides 3D maps of the local structure. By varying the degree of the zoom one can visualise the entire specimen, grains, domains or even individual defects. With ample space around the sample, the method is capable of acquiring 3D movies of changes inside components while they are processed by real-life sample environments.

Most materials and minerals are comprised of hierarchical crystalline structures and sub-structures such as grains, domains and atomic-scale defect networks. For both materials and geological sciences, it would be highly beneficial to be able to understand and model the interplay of physical phenomena and structural dynamics at and between many different length scales. With this capability, the final macroscopic properties of a material could be predicted from the initial microstructure and processing conditions, and materials could be designed and optimised using computer simulations rather than experimental trial-and-error. To guide such efforts, experimental techniques are needed that can rapidly swap between the different length scales and make *in situ*, three-dimensional (3D) movies of the local changes to the crystalline lattice: structure, strain and orientation.

To facilitate such studies, a prototype diffraction based transmission X-ray microscope is being developed at the Technique and Instrumentation Test Beamline, **ID06**. It operates in the 15-30 keV range. At the coarse end of the scale, 3D grain mapping techniques such as 3-dimensional X-ray diffraction (3DXRD) [1] and diffraction contrast tomography (DCT) are implemented for fast overviews of mm-sized specimens. Once a particular grain of interest has been selected, detailed studies are performed by dark-field X-ray microscopy, a new full-field imaging technique for non-destructive mapping (**Figure 147**). By placing an X-ray objective lens in the diffracted beam, users can intuitively 'zoom'

between different length scales by changing the objective focal length, overcoming the spatial bandwidth limitations of other techniques. The objective also filters stray diffraction signals, suppressing unwanted overlap and isolating the individual structural element of interest. The sample-to-detector distance is typically 2-6 m, enabling magnification ratios of up to 50 while still maintaining sufficient space around the sample for *in situ* apparatus. Like the electron microscope, the dark-field microscope can be operated in a variety of modes. Maps of the axial strain can be measured by scanning the objective and detector through 2θ, while the local misorientation can be similarly mapped by stepping the sample through two orthogonal tilt directions, (α,β).

3D measurements of axial strain and orientation can be obtained in two ways. Firstly, by using a one-dimensionally-focusing condenser to create a narrow line-beam which illuminates a 'slice' of the material, which is then imaged at an oblique angle. A 3D volume is then obtained layer-by-layer. A second, faster, method involves illuminating the entire grain and recording projections from different viewing angles while rotating the sample around the scattering-vector, $\vec{G}$. 3D reconstruction can then be accomplished by tomographic type algorithms [2].

This concept of multiscale mapping was used for an annealing study of a plastically deformed Al sample. Shown in **Figure 148** left is part of a DCT mapping of all grains in the specimen. Zooming in on one embedded grain, the intrinsic variation in orientation was then mapped. A vertical section through the grain is shown in **Figure 148** middle. Finally by zooming once more, individual sub-grains were mapped in 3D (**Figure 148** right). From left to right in the figure, the spatial resolution is 3.5 µm, 1.5 µm and 300 nm, and the angular resolution 0.5°, 0.15° and 0.03°, respectively.

Next the subgrain dynamics was tracked as function of time during annealing. The results are consistent with conjectures in the literature of subgrain growth by subgrain boundary motion, but this is the first time the processes have been directly verified and quantified.

Based on the principle illustrated above, a dedicated transmission X-ray microscope will be commissioned at beamline ID06 in 2016 with a target resolution of 50 nm.

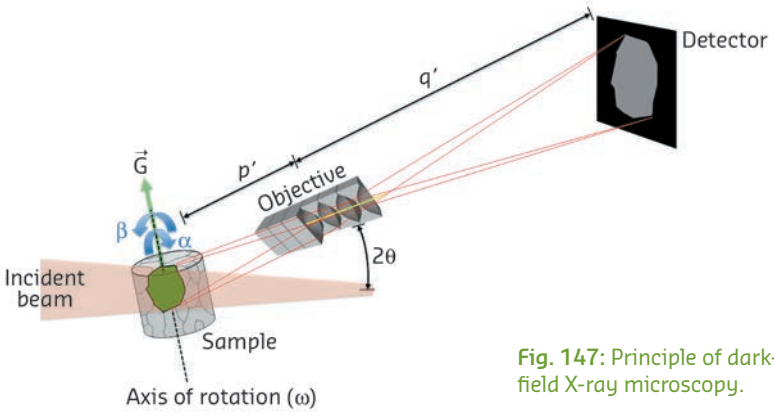

Fig. 147: Principle of dark-field X-ray microscopy.

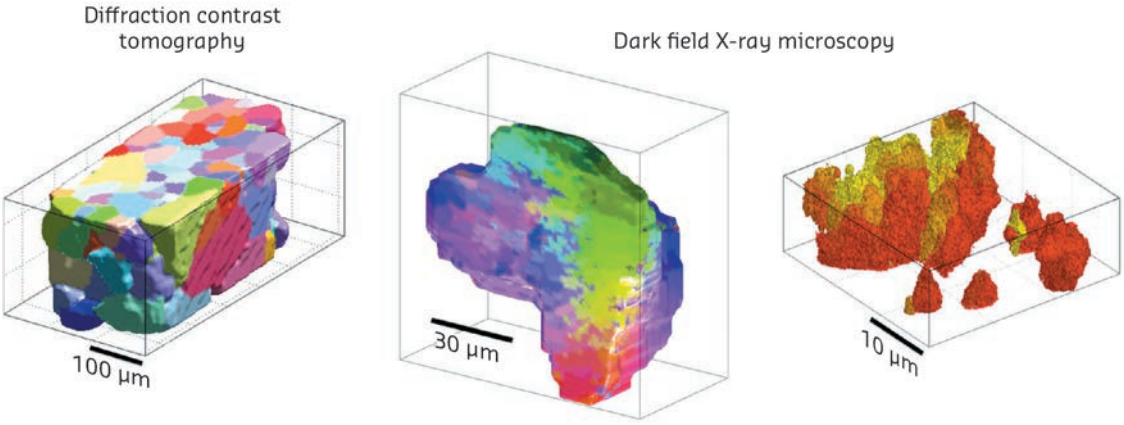

Fig 148: Multiscale mapping of 10% tensile deformed aluminium. The colours symbolise orientations.

PRINCIPAL PUBLICATION AND AUTHORS

Dark-field X-ray microscopy for multiscale structural characterization, H. Simons (a,b), A. King (b), W. Ludwig (c), C. Detlefs (b), W. Pantleon, (d), S. Schmidt (a), F. Stöhr (e), I. Snigireva (b), A. Snigirev (b) and H.F. Poulsen (a). *Nature Communications* **6**, 6098 (2015); doi: 10.1038/ncomms7098.
(a) Department of Physics, DTU, Lyngby (Denmark)
(b) ESRF
(c) MATEIS, INSA-Lyon (France)
(d) Department of Mechanical Engineering, DTU, Lyngby (Denmark)
(e) DTU Danchip, Lyngby (Denmark)

REFERENCES

[1] H.F. Poulsen, *Three-dimensional x-ray diffraction microscopy* (Springer, 2004).
[2] W. Ludwig *et al., J. Appl. Cryst.* **34**, 602–607 (2001).

ADVANCED ALGORITHMS FOR COMPUTED TOMOGRAPHY

Computed tomography (CT) numerical tools at third generation synchrotrons must sustain very high data rates in order to keep pace with the continuous improvement of the X-ray source and instrumentation of the experimental stations. The ESRF tomography reconstruction code PyHST2 now implements a powerful hybrid architecture (using CPUs and GPUs), parallel processing, pipelining, and new modern algorithms based on iterative techniques.

Tomography, having a high number of parallel projections at constant angular step and high signal to noise ratio, approaches an ideal case that is easily treatable without iterative methods and can be solved with a filtered back projection (FBP) algorithm. However, experimental constraints may take us away from the ideal situation. Users may ask for higher time resolution, improved signal to noise ratio for a given number of projections and reduced radiation damage. As an example, reducing the deposed dose requires either shortening the exposure time per projection, leading to a poorer statistics, or reducing the number of projections. This can lead to situations where the recorded information is not sufficient for a good quality reconstruction using standard methods.

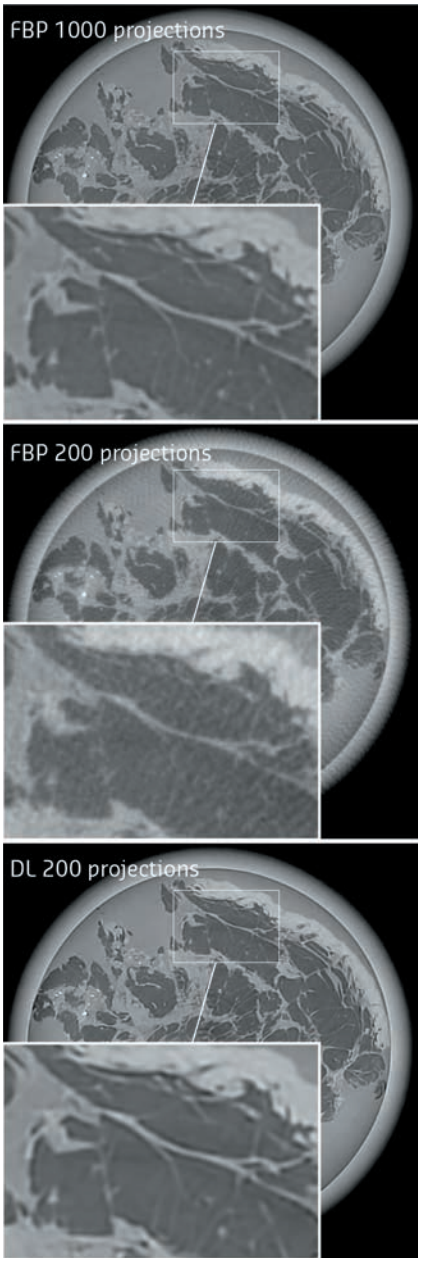

A solution to this problem consists in filling in the gap left by the missing information with *a priori* knowledge of the solution. This can be done without altering too strongly the final result if certain conditions are met. When the image, which is a point in an R^N space (N being the number of pixels) has a non uniform probability of being found across this space, a fundamental theorem of information theory tells us that the signal has a lower entropy than a random R^N image, and less information is required to retrieve it.

Fig. 149: Section of a reconstructed tomography of a human breast mastectomy specimen recorded at the biomedical beamline ID17 by filtered back projection (FBP) and Dictionary Learning (DL) techniques.

Signals occurring in nature, when noise has been removed, present most of the time an intrinsic sparsity. An image is intrinsically sparse when it can be expressed as a linear combination of a small number of basis functions. This means that, expressed on this basis, the image is represented by a point in a R^M space (M being the number of basis function, of the order of N) with only few of the M components different from zero (hence sparse from latin *sparsus*: scattered, having large empty intervals). This strong non-uniformity in the signal represents a drastic decrease in entropy and opens the door to reconstruction from a limited dataset.

The *a priori* knowledge methods implemented in PyHST2 find the optimal solution in a landscape of probability where the valleys represent high probability solutions and the mountains low ones. The landscape function is the sum of two terms: the quadratic distance from the measured (limited) data and a complementing function which takes low values for sparse solutions. The choice of the basis functions is of paramount importance because it implements our knowledge about the class of studied objects.

Figure 149 shows a human breast mastectomy specimen studied at the biomedical beamline ID17 with the analyser based phase contrast imaging (PCI) technique (which measure a phase gradient [1]). The sparsifying basis used was obtained with the dictionary learning (DL) technique that exploits the statistical correlations between different points of small patches obtained from images of other samples. It can be seen that the iterative dictionary learning technique can sustain a five-fold reduction in the number of projections with respect to the optimal one. This method goes well beyond the effect of reducing the noise and is able to recover details which were completely lost in the filtered back projection reconstruction. The patches (*i.e.* the basis functions) were made of two 8x8 components: one for each of the two measured phase gradient components. The use of the proper basis which implements the intrinsic correlations within different points of a patch and between gradient components was very effective in this case.

PyHST2 can also deal with 3D patches, where the correlation between adjacent slices is exploited. Besides dictionary-based methods, PyHST2 is also equipped with the total variation regularisation using the gradient representation which is sparse for piecewise constant objects. Another advantage of using iterative techniques is that more faithful representations of the experiments can be obtained, including otherwise neglected physical effects or technical imperfections that would be otherwise impossible to treat analytically. As an example, the removal of ring artefacts, which are due to miscalibration or failure of one or more detector elements, is shown in Figure 150, whereby the appropriate detector-pixel defect variables were optimised together with the image variables [2]. The sparsifying term, used with low strength, has the effect of pushing away from the images those features present in the data that can be easily fitted by varying the detector-defect variables.

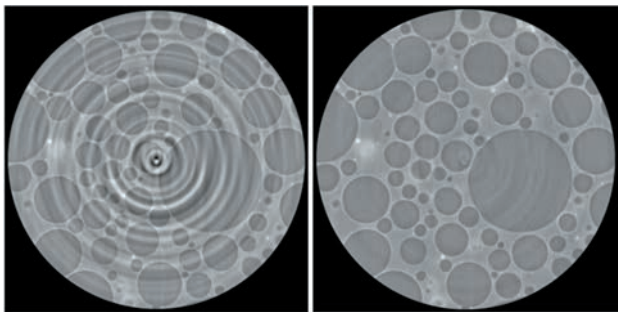

Fig. 150: Example of ring artefact removal from a tomographic slice of a syntactic foam, recorded at ID19.

All the PyHST2 features presented here, and many more, are available on the ESRF cluster and also in the source distribution of PyHST2 [3].

PRINCIPAL PUBLICATION AND AUTHORS

A dictionary learning approach with overlap for the low dose computed tomography reconstruction and its vectorial application to differential phase tomography, A. Mirone (a), E. Brun (a,b) and P. Coan (b,c), *PLOS ONE* (2014); doi:10.1371/journal.pone.0114325.
(a) ESRF
(b) Ludwig Maximilians University, Physics Department, Garching (Germany)
(c) Institute for Clinical Radiology, Ludwig-Maximilians-University Hospital Munich (Germany)

REFERENCES

[1] S.Gasilov *et al.*, *Opt. Express* **22**, 5216-27 (2014).
[2] P. Paleo, A. Mirone, *Journal of Synchrotron Radiation* **22**, 1268-1278 (2015).
[3] PyHST2 source: https://forge.epn-campus.eu/html/pyhst2/

6-DIMENSIONAL DIFFRACTION CONTRAST TOMOGRAPHY AND INDEXING BY BLIND RECONSTRUCTION

Structural materials like metals commonly exhibit a crystalline microstructure, characterised by the presence of domains with distinct crystallographic orientation called *grains*. Depending on the thermo-mechanical process history of the material, these grains may be further divided into sub-structures created by the arrangement of lattice defects and giving rise to measurable distortion of the crystalline lattice. Diffraction contrast tomography (DCT) is an X-ray diffraction imaging technique that enables the non-destructive three-dimensional analysis of undeformed polycrystalline microstructures. A recently developed six-dimensional framework extended the applicability of DCT to the study of moderately deformed materials exhibiting intragranular misorientation of several degrees. Thanks to its fast acquisition protocol, the technique enables time-lapse observations of processes like plastic deformation and grain coarsening in metallic or ceramic samples.

During acquisition of a diffraction contrast tomography (DCT) scan, a poly-crystalline sample mounted on a rotation stage is illuminated with a beam of monochromatic X-rays. Upon rotation, the various crystalline regions (grains) in the sample will repeatedly reach diffraction condition, and give rise to diffraction spots which are recorded on the detector positioned downstream of the sample. These diffraction spots, which represent geometrical projections of the grain volumes, will then be isolated (segmented), and used to identify and reconstruct the originating grains [1].

Due to the assumption of absent or negligible local misorientation, DCT has traditionally only been used for the structure determination of undeformed materials. However, many interesting problems in material science are linked to deformed microstructures. When materials present a non-negligible level of deformation, the diffraction spots are distorted, and tend to stay longer on the detector, transforming into diffraction blob volumes. Both their distorted nature, and the higher tendency to overlap, quickly degrade the quality of the traditional DCT reconstruction with increasing levels of grain deformation.

A new six-dimensional framework has extended the domain of applicability of DCT to include materials with moderate intragranular orientation spread by enabling the combined reconstruction of the shape and the local orientation inside each single grain. The six-dimensional nature of the method lies in the addition of three more degrees of freedom describing the local orientation for each spatial point and the simultaneous sampling of both position-space and orientation-space. The reconstruction is then formulated as a minimisation problem where additional *prior* terms that model the physical properties of the grains are used to cope with the increased complexity of the six-dimensional space.

In a more recent work [2], it was shown that the newly introduced framework is not only able to perform single grain reconstructions but it also enables the reconstruction of wider regions with similar orientation inside the analysed samples, along with the possibility to use raw images for the reconstruction of those regions. This means that previously difficult conditions will now be more approachable by DCT. Some examples include highly textured or moderately deformed materials where the diffraction spots have a much higher tendency to overlap and suffer from higher levels of distortion.

Figure 151a shows the surface a NaCl sample as observed by electron backscatter diffraction (EBSD), representing the surface crystalline structure, and its comparison with different approaches by DCT. Figure 151b is a dilated volume of a traditional 3D-DCT reconstruction and Figure 151c is an undilated 6D-DCT reconstruction.

Figure 151b and 151c are missing a few of the sub-grains that were successfully identified in the EBSD measurement. Figure 151d shows an extension of the 6D-DCT reconstruction where the adjacent grains with similar orientations and belonging to a cluster of grains have been reconstructed together in a larger region of the orientation-space. Including wider regions with similar orientations in the same reconstruction has enabled the reconstruction and identification of the regions that could not be indexed by a traditional DCT analysis.

More powerful computers would permit the analysis of even more deformed materials using DCT. Materials that exhibit higher degrees of overlap and distortion of the diffraction spots, could be analysed by simply extending the sampling to the full position and orientation spaces, thereby skipping the steps of image segmentation and grain indexing, and reconstructing the full sample at the same time. These developments, together with the fast acquisition speed of DCT and the experimental compatibility with other techniques such as phase contrast tomography, open up the possibility to perform time-lapse observations of plastic deformation, coarsening, phase transformation and crack propagation in polycrystalline structural materials.

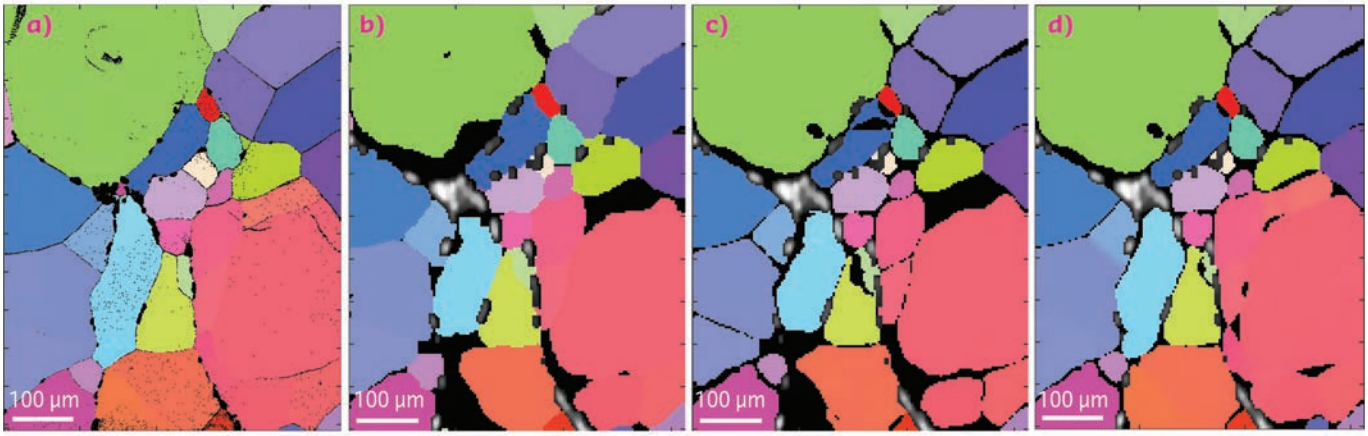

Fig. 151: Comparison of the reconstructions obtained with different approaches for the surface of a polycrystalline sample of rock salt (NaCl): (a) EBSD, (b) traditional DCT with a 2 voxels dilation, (c) 6D-DCT, (d) 6D-DCT with cluster reconstruction.

PRINCIPAL PUBLICATION AND AUTHORS

Reconstruction of local orientation in grains using a discrete representation of orientation space, N. Viganò (a,b,c), W. Ludwig (a,b) and K.J. Batenburg (d,c,e), *J. Appl. Cryst.* **47**, 1826–1840 (2014); doi: 10.1107/S1600576714020147.

(a) MATEIS, INSA Lyon (France)
(b) ESRF
(c) iMinds-Vision Lab, University of Antwerp (Belgium)
(d) CWI, Amsterdam (The Netherlands)
(e) Universiteit Leiden (The Netherland)

REFERENCES

[1] P. Reischig *et al.*, *J. Appl. Crystallogr.* **46**, 297 (2013).
[2] N. Viganò *et al.*, *Sci. Rep. accepted* (2015).

FULLY AUTOMATIC DATA COLLECTION: A NEW TOOL FOR STRUCTURAL BIOLOGISTS

Protein crystallography is essential in the understanding of fundamental biological processes and the design of new drugs. The process involves characterising hundreds of crystals and collecting optimised data sets, a laborious task performed non-stop day and night. A fully automated system that will mount, screen and collect the best possible data from hundreds of crystals without human intervention, 24 hours a day, has now been developed.

Considerable human effort is dedicated to evaluating protein crystals at synchrotron sources in order to find the few crystals that diffract well or to find the one crystal that contains a potential new drug candidate. Much of this work is repetitive and the time spent could be better invested in the interpretation of results. MASSIF-1 is a unique facility for the high throughput, fully automatic characterisation and data collection of crystals of macromolecules [1]. The combination of ESRF developed robotic sample handling (RoboDiff) and advanced software protocols [2] has provided a new tool to structural biologists. The beamline is not designed to replace user visits to the synchrotron but rather to do the hard work of screening crystals or collecting data sets through the night, freeing researchers to spend time on more challenging data collection problems and study the underlying biology.

At the core of the beamline is a fully automatic system to mount, locate, centre to the optimal diffraction volume, characterise and collect data, if possible, from multiple cryocooled crystals. Using the capabilities of pixel array detectors, the system operates at about the same speed as a human operator, taking an average of 6 minutes per sample, but performing far more than is possible with a user present, without getting tired. In the first step, the sample mount is analysed in order to determine the area to be scanned (Figure 152). A fast X-ray based routine is then launched to locate crystals and centre them to the beam systematically at the position of highest diffraction signal. The routine is often able to locate crystals more effectively than the human eye, either as they are mounted in opaque medium or a large excess of liquid causes lens effects. In many cases, diffraction data have been obtained when centring a crystal was not possible manually. Once centred, the samples are characterised (assessed for quality, diffraction limit, crystallographic symmetry) and important parameters, such as flux, beam size and crystal volume, are automatically taken into account, ensuring calculation of optimal data collection strategies. Optimised data sets are then collected and automatically processed [3] before the next sample is mounted.

Automation necessarily involves standardisation; however, for an automatic data collection service to be successful for a range of projects, considerable flexibility in data collection parameters must be allowed. This has been implemented by allowing user preferences (such as type of data collection, resolution required, beam size, etc.) to be entered at the sample level in the beamline database ISPyB [4] that also displays the results for each sample (Figure 153). An online booking system adds to the flexibility: rather than the rigid system in place at other beamlines, users can book time on the MASSIF-1 calendar with very short notice and samples then enter a queuing system.

Over 15,000 samples have now been processed with no human intervention allowing the accumulation and comparison of a large amount of information that was previously unknown, including the exact dimensions of crystals and further information about their quality. This has been fed back into the software in order to improve data collection. For example, the most commonly observed crystal length is 50 µm – this led to the selection of a default beam size that best reflects the samples. The latest developments now include options to allow the collection of data sets from multiple crystals on the same sample support (Figure 152) and more advanced data collection strategies such as helical data collection.

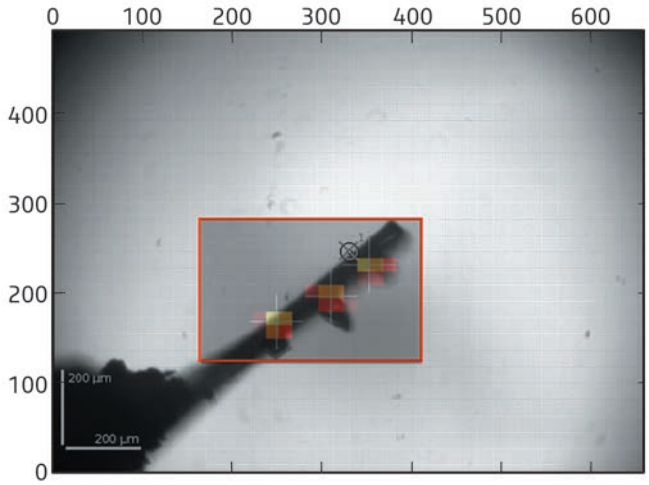

Fig. 152: Sample mounts are analysed and an area chosen to scan through the X-ray beam (red box). Analysis of the diffraction images obtained yields a heat map defining the location and diffraction quality of crystals. Optimum points are then selected for data collection (crosses), in this case, three separate crystals.

The new level of automation should decrease project lifecycles and, in partnership with developments being made in the automatic mounting of crystals [5], a fully automatic pipeline from protein to structure can now be envisioned.

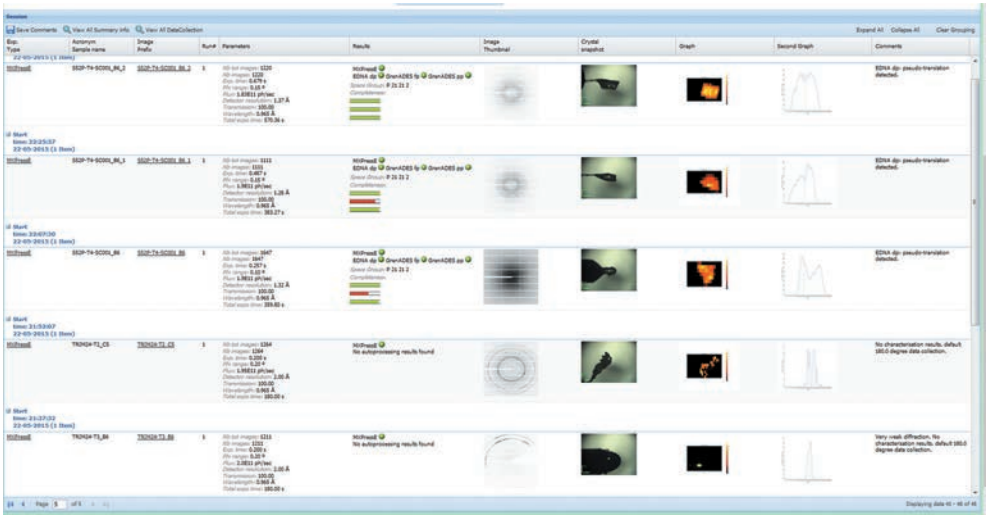

Fig. 153: A screenshot showing the display in ISPyB of results, such as diffraction maps and autoprocessing, for a series of samples processed at MASSIF-1. Comments are automatically written (far right column) to inform users on various stages of the process such as 'weak diffraction', default 180° data collection', etc.

PRINCIPAL PUBLICATION AND AUTHORS

Fully automatic characterization and data collection from crystals of biological macromolecules, O. Svensson (a), S. Monaco (a), A.N. Popov (a), D. Nurizzo (a) and M.W. Bowler (b), *Acta Cryst. D* **71**, 1757-1767 (2015).
(a) ESRF
(b) European Molecular Biology Laboratory, Grenoble Outstation (France)

REFERENCES

[1] M.W. Bowler *et al.*, *J. Synch. Rad.* **22**, 1540-1547 (2015).
[2] S. Brockhauser *et al. Acta Cryst. D* **68**, 975-984 (2012).
[3] S. Monaco *et al. J. App. Cryst.* **46**, 804-810 (2013).
[4] S. Delagenière *et al. Bioinformatics* **27**, 3186-3192 (2011).
[5] F. Cipriani *et al. Acta Cryst. D* **68**, 1393-1399 (2012).

DESIGN AND CHARACTERISATION OF THE PROTOTYPE GIRDER FOR THE ESRF-EBS STORAGE RING

One of the many challenges confronting the designers of the new storage ring is to significantly improve the vibration performance of the magnet assemblies whilst at the same time providing high-performance positioning systems which allow the alignment of one magnet to another with a precision of better than 50 µm.

In each of the 32 cells of the new storage ring there will be four identical girders to support the magnets arranged along the electron beam trajectory. The magnet arrangement of girders one and two are symmetric about the centre of the cell to the third and fourth girders.

The girder has been designed to optimise rigidity in order to minimise the effects of vibration and also to maintain the long term alignment of the magnets with respect to one another in the machine, and with respect to the beamlines. Almost as important is the possibility to align the girders with a precision of ± 50 µm with a resolution of 5 µm in the directions perpendicular to the electron beam. The vertical motion is motorised to correct ground movements quickly and without significantly interrupting the machine operation. The alignment tolerance between adjacent magnets is 70 µm. This means that all errors combined in the alignment of a single magnet must not exceed 50 µm. Electron beam position monitors (BPMs), vacuum chambers and other components installed on the girders have similarly demanding alignment tolerances.

A prototype girder was delivered to the ESRF in April 2015. It has been used to test and improve the EBS girder design and the alignment and support systems installed on it. Although many of the girder parameters are now fixed, work continues and will only be finalised in 2016.

The girder is a steel box beam 5.1 m long (**Figure 154**). It weighs 3.1 tons empty and is

supported by 4 commercially available Airloc wedges that have been motorised. Preloaded springs improve the stiffness of these components. They are used for vertical adjustment and the rotations about the longitudinal and radial girder axes. Because the system is statically indeterminate, very careful control of the wedges is required. Gliding surfaces under the wedges allow girder movements in the horizontal plane. Radial alignment movements including the rotation about the vertical axis are made using Nivell wedges preloaded with springs. Less demanding precision movements in the longitudinal direction are made through a simpler system of screws. The top surface and two longitudinal grooves are machined with a planarity of ± 50 µm over the length of the girder. They permit a precise pre-alignment of the magnets. The deformation of the girder under its full complement of the magnets is less than 40 µm.

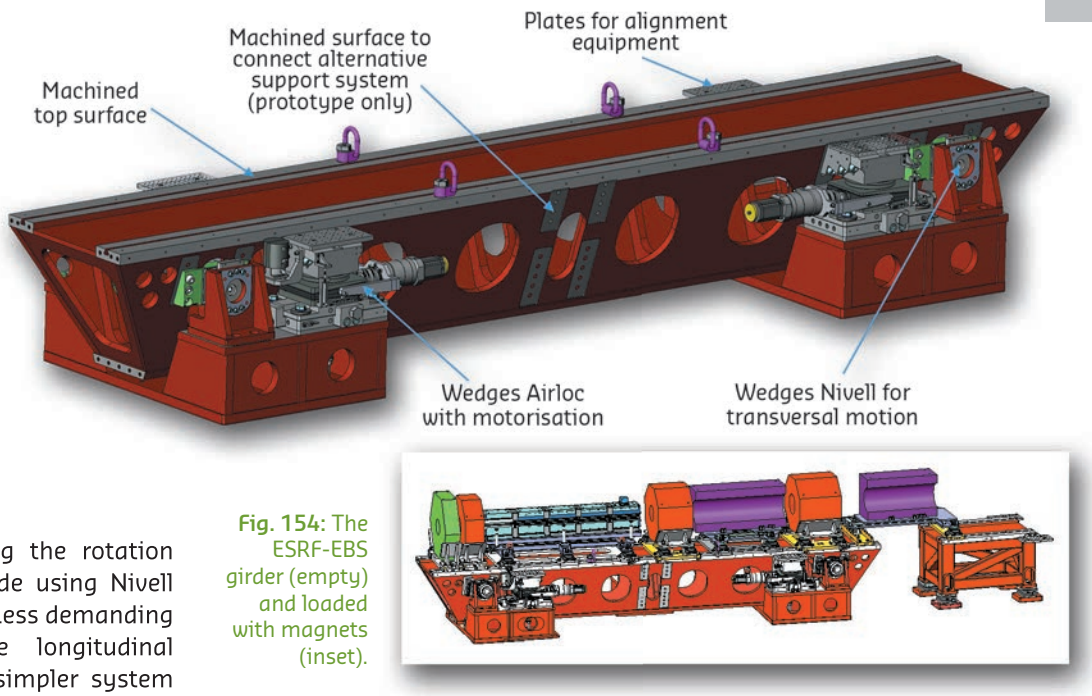

Fig. 154: The ESRF-EBS girder (empty) and loaded with magnets (inset).

A complete modal analysis of the equipped girder was made to ensure the first resonance frequency was above 50 Hz. This analysis included the floor and wedge stiffness. The wedge stiffness was determined in a dedicated laboratory experiment. The results of the test on the prototype confirmed the calculations without ambiguity.

High rigidity is required in order to limit the effects of vibration on the girder. Indeed, floor motion is the main excitation source and decreases proportionally to ~ $1/freq^2$. Therefore, the 1st vibration mode of the whole structure was designed to be in the 50 Hz region. The initial vibration measurements performed on the girder without dummy magnets revealed that this challenging target was accessible with a 1st mode at a remarkable 80 Hz. With the full set of dummy magnets installed the 1st vibration mode dropped to 42 Hz. This is a local mode of the so-called dipole-quadropole-2 magnet. The 2nd mode is also a local mode at 46 Hz for the sextupole magnet. A global girder mode occurs at 51 Hz. The displacement levels on the magnets are less than 1 µm peak to peak with weak amplification with respect to the floor.

Dummy magnets were installed on the girder to test fine alignment. A jig was successfully tested to facilitate the magnet installation to within 0.5 mm of their nominal positions. After installation, the magnets are fine-aligned. This has been tested several times. The uncertainty in the alignment of the magnets with respect their nominal positions (and one-another) was determined to be: 47 µm in the X direction along the electron beam direction; 25 µm in the Y direction perpendicular the electron beam in the horizontal plane; and, 37 µm in the Z direction perpendicular to the beam. The most critical alignment is in Y and Z directions.

An important number of tests have been performed on the prototype girder for a fine characterisation of all axis, X, Y and Z. These tests have simplified the original design on X and Y axis with a very good result. A fine Z characterisation showed us the possibility to move 10 tons within some few micrometres.

An extensive and redundant system of sensors (Hydrostatic Levelling System (HLS), Wire Positioning System (WPS) and inclinometers) are installed on the prototype girder. This installation serves two purposes: first it provides highly redundant information on how the girder moves and deforms; and, second it provides information that will be used to select the most appropriate system to equip the girders of the new machine.

Tests are ongoing to optimise girder performance. However the design of the girder is finished and production will commence soon.

AUTHORS

T. Brochard, F. Cianciosi, L. Eybert, M. Lesourd and D. Martin.
ESRF

Accelerator and Source

The Accelerator and Source Division (ASD) is in charge of the production of synchrotron light from the ESRF's 6 GeV storage ring and has continued its efforts to ensure reliable operation during 2015. Although the previous year's all-time record of 99.11% accelerator availability was not beaten in 2015, a total of 5401 hours of beam was delivered out of 5524 scheduled hours, representing a very respectable figure of 98.53% availability. There was a significantly low rate of failure, only 21 events during the last six months of 2015, including a period of 17 days in November without a single failure.

In addition to ensuring excellent operating conditions, 2015 also marked the completion of the Phase I Upgrade Programme. Staff came together to celebrate the division's successful completion of major upgrades to several subsystems of the accelerator complex, which included the upgrade of the RF system with solid state amplifiers and new HOM-damped cavities, the planned extensions of several straight sections and the development of improved systems for electron beam position monitoring and fast orbit feedback.

Following hot on the heels of Phase I, the year was especially important for the ASD as 1st January 2015 marked the start of the execution phase of the ESRF–EBS project. The project, approved by the ESRF Council in June 2014, will see the implementation of a new lattice for the storage ring to reduce the natural horizontal emittance from 4 nm to about 134 pm, thus greatly increasing the brilliance and coherence of the beam. The year saw a frenzy of activity in the division and great progress has been made. The project management team has grown with the addition of a new project assistant, procurement coordinator and installation officer, and a project planner is in the process of being recruited. Two 'Accelerator Project Workshop' events (see **Figure 155**) were held in July and November in order to review progress in the project, discuss future milestones and address any issues and actions to be taken. Discussion sessions spanned topics such as planning, risk analysis, safety aspects and resource requirements.

All efforts were put into a continuation of the intensive design work begun in 2014 and to start sending over 100 contracts out for tender, commencing with the most critical components or those longest to manufacture. Calls for tender have already been sent out for all of the magnets, including the sextupoles, octupoles, high-gradient and moderate-gradient quadrupoles, the dipole-quadrupoles and the permanent magnet blocks for the dipoles with longitudinal gradients and the correctors and mechanical parts for the longitudinal-gradient dipoles. In addition, a call went out for the stretched wire benches to take magnetic measurements. Calls for the girders for the storage ring were sent out in mid-December, with a delivery requested for the end of 2016. Concerning the vacuum chambers, calls were sent out for the high-profile stainless steel chambers and for the low-profile stainless steel chambers and the

Fig. 155: Accelerator physicist Dieter Einfeld discusses the assembly process with the accelerator project team during the first Accelerator Project Workshop.

aluminium vacuum chambers. The execution phase will continue until October 2018, when the installation stage will begin. It will be overlapped by the pre-assembly of components, which will start in autumn 2017.

The work on the ESRF–EBS project was presented for review to the new Machine Advisory Committee on two occasions during 2015. The Machine Advisory Committee, or MAC, now chaired by Richard Walker of Diamond Light Source, replaced the Accelerator Project Advisory Committee, or APAC, after APAC chairman Dieter Einfeld's appointment as accelerator physicist at the ESRF.

The first MAC meeting was held at the ESRF in April 2015. Over two days, work package leaders and other ESRF staff presented the progress of their work and, in particular, addressed the specific points raised at the last APAC. Following the event, the chairman complimented the project team on the significant technical progress made as well as the establishment of the definitive project organisation.

The second MAC meeting, in September, saw the panel of experts consider everything from the planning to the technical implementation and commissioning. The MAC was pleased to hear that the procurement of significant elements of the project such as the magnets and vacuum chambers was underway, and noted that a lot of work had been accomplished thanks to the strong support and motivation from all the ESRF divisions. Chairman Richard Walker emphasised that the project had made "great progress with no evident showstoppers foreseen!"

The ESRF also hosted the fifth Low Emittance Rings (LER) Workshop in September 2015, supported by the EuCARD-2* project (Enhanced European Coordination for Accelerator Research and Development). The goal of the workshop was to gather experts from the field of light sources, damping rings and colliders, to exchange their ideas, their results, and their future projects, demonstrating a remarkable example of open and friendly collaboration. The theme this year was beam dynamics and technological challenges for producing and controlling ultra-low emittance beams, and talks were given by individuals who have designed, commissioned and operated such rings. This was more than pertinent in view of the ESRF–EBS project!

P. RAIMONDI

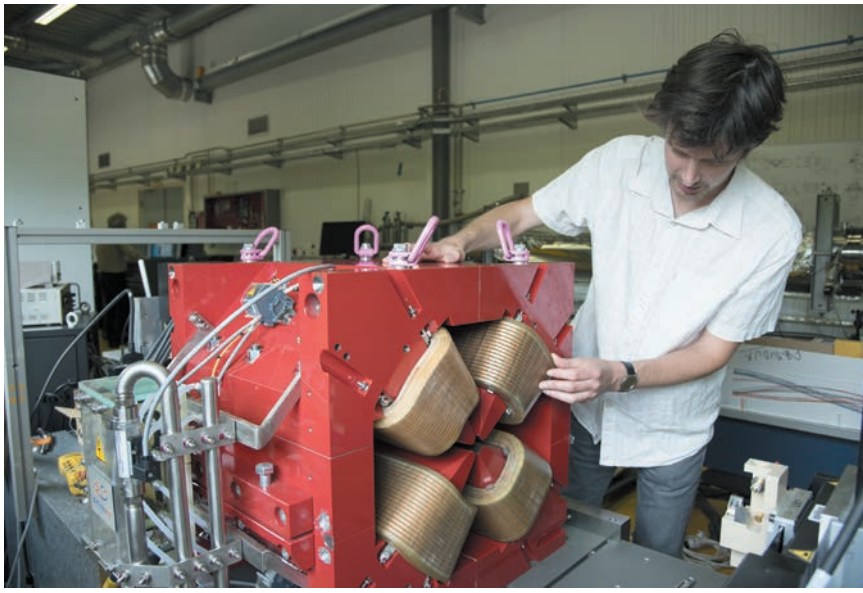

BEAM PARAMETERS OF THE STORAGE RING

Table 1 presents a summary of the characteristics of the storage ring electron beam.

Energy	[GeV]	6.04
Maximum current	[mA]	200
Horizontal emittance	[nm]	4
Vertical emittance	[pm]	4
Revolution frequency	[kHz]	355
Number of bunches		1 to 992
Time between bunches	[ns]	2.82 to 2816

Table 1: Principal characteristics of the electron beam.

Table 2 gives the main optic functions, electron beam sizes and divergences at various source points. For insertion device source points, the beta functions, dispersion, sizes and divergences are calculated in the middle of the straight section. For bending magnets, two representative source points have been selected for each type of magnet (even or odd cell number), corresponding to magnetic fields of 0.4 T and 0.85 T. These points differ by the observation angles, of respectively 3 and 9 mrad from the entrance of the magnet.

		Even ID (ID2, ID6...)	Odd ID (ID1, ID3...)	Even BM (ID2, ID6...) 3 mrad	Even BM (ID2, ID6...) 9 mrad	Odd BM (ID1, ID3...) 3 mrad	Odd BM (ID1, ID3...) 9 mrad
Magnetic field	[T]	Variable	Variable	0.4	0.85	0.4	0.85
Horiz. Beta function	[m]	37.6	0.35	1.33	1.06	2.12	1.61
Horiz. Dispersion	[m]	0.134	0.031	0.062	0.051	0.089	0.075
Horiz. rms e- beam size	[μm]	413	50	99	85	132	113
Horiz. rms e- divergence	[μrad]	10	107	116	114	104	99
Vert. Beta function	[m]	2.95	2.97	41.7	42.0	32.1	32.2
Vert. rms e- beam size	[μm]	3.4	3.4	12.9	13.0	11.3	11.4
Vert. rms e- divergence	[μrad]	1.17	1.16	0.50	0.50	0.36	0.36

Table 2: Beta functions, dispersion, rms beam size and divergence at the various source points.

Electron beam profiles are Gaussian and the size and divergence are presented in terms of rms values. The associated full width at half maximum sizes and divergences are 2.35 times higher. Horizontal electron beam sizes and divergences are given for the multibunch filling modes and apply to almost all filling patterns, except when the current per bunch is larger than 4.5 mA, for which a slightly larger size and divergence are attained because of the increased energy spread of the electron beam.

Vertical electron beam sizes and divergences are given for a vertical emittance of 4 pm, which is now the standard for 2 x 1/3 and 7/8+1 filling modes. The vertical sizes and divergences are about 1.4 times larger in uniform filling mode (due to ion effects, which are partially corrected by the use of a vertical bunch-by-bunch feedback). To increase the lifetime of the stored beam, the vertical beam sizes and divergences are deliberately increased by about a factor of 4 in the 16-bunch, 4-bunch and hybrid filling patterns.

The lifetime, bunch length and energy spread mainly depend on the filling pattern. These are given in **Table 3** for a few representative patterns. Note that in 16-bunch and 4-bunch filling patterns, the energy spread and bunch length decay with the current (the value indicated in the table corresponds to the maximum current). The bunch lengths are given for the usual radiofrequency accelerating voltage of 9 MV (8 MV for 16-bunch and 4-bunch).

Filling pattern		Uniform	7/8 + 1	Hybrid	16-bunch	4-bunch
Number of bunches		992	870+1	24x8+1	16	4
Maximum current	[mA]	200	200	200	90	40
Lifetime	[h]	50	45	30	16	9
Rms energy spread	[%]	0.11	0.11	0.11	0.12	0.16
Rms bunch length	[ps]	20	20	25	48	55

Table 3: Current, lifetime, bunch length and energy spread for a selection of filling modes.

SUMMARY OF ACCELERATOR OPERATION

With 5401 hours of beam delivered out of 5524 scheduled hours, the overall availability reached 98.53% compared to 99.11% in 2014. The lower availability is explained by four long failures that occurred in the first four runs of 2015: a problem with the master source, linked to ageing material and contamination of the network; a power supply fire, linked to ageing material and degradation of the insulation; leaking water hoses due to ageing; and dust particles clogging up the flowmeters and water filters in the cooling network. Also, in the first half of 2015, there was a higher than average number of arcs in the RF distribution system, solved by replacing a misplaced RF finger shield. For all these failures, proper corrective actions were taken in order to restart operation as soon as possible and avoid similar problems in the future.

The mean time between failures in 2015 reached 94 hours. The rate of failure was especially low during the last three runs, with only 21 failures over the last six months.

Failures aside, there were many excellent periods of unperturbed delivery in 2015, for example during November when beam was delivered without disturbance for 17 days (see Figure 156).

A summary of storage ring operation for the year is presented in Table 4.

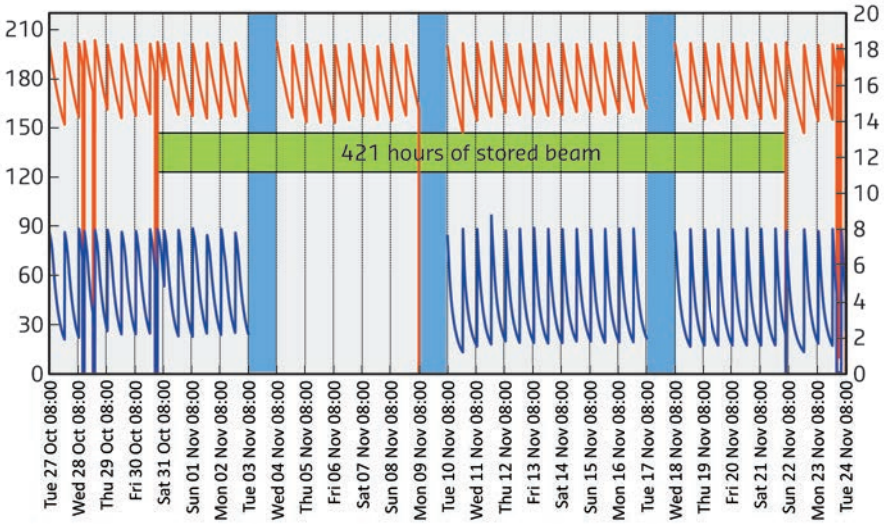

Fig. 156: Uninterrupted beam delivery for 17 days (421 hours) in 7/8+1 and uniform filling modes during the run 2015-05.

Table 4: Overview of storage ring operation in 2015.

RUN NUMBER	2015-01	2015-02	2015-03	2015-04	2015-05	TOTAL 2015
Start	16/01/2015	27/03/2015	05/06/2015	21/08/2015	23/10/2015	
End	18/03/2015	27/05/2015	29/07/2015	14/10/2015	16/12/2015	
Number of USM shifts	146.63	150	131.69	131.63	130.56	**690.50**
Beam available for users (h)	1123.70	1175.80	1039.60	1030.81	1031	**5400.91**
Availability	**96.39%**	**98.80%**	**99.36%**	**98.91%**	**99.41%**	**98.53%**
Dead time for failures	3.6%	1.2%	0.6%	1.1%	0.6%	**1.47%**
Number of failures	18	20	7	8	6	**59**
Mean time between failures (h)	65.2	60	150.5	131.6	174.1	**93.6**
Mean duration of a failure (h)	2.4	0.7	1	1.4	1	**1.37**

FILLING PATTERNS

In 2015, a greater number of shifts were delivered in uniform mode (to the detriment of the 7/8 mode): 13% in 2015 compared with 5% in 2014. This represents five weeks of delivery for uniform mode compared to two weeks in 2014 (Figure 157). The distribution of delivery modes between 16-bunch, 4*10 mA and hybrid modes remains the same as in previous years.

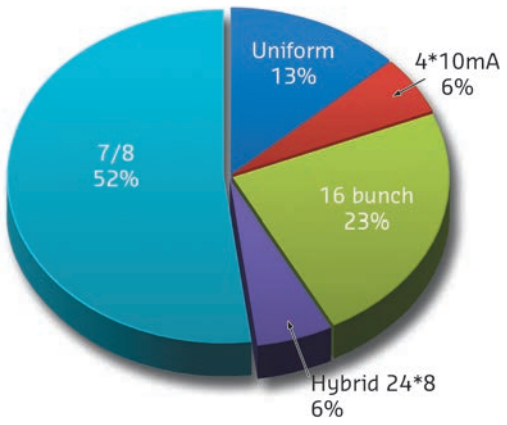

Fig. 157: Distribution of the various filling modes in 2015.

A noticeable improvement was made during the third run of 2015 when the single bunch intensity of the 7/8+1 mode was increased from 4 mA to 8 mA without any deterioration of other beam quality parameters such as emittance or lifetime (**Figure 158**). This was made possible thanks to the increase of the beam chromaticity coupled to a new optimisation algorithm of the lifetime. A similar increase of single bunch intensity was also done successfully during the delivery of the hybrid mode at the end of 2015.

Fig. 158: Increase of the single bunch intensity to 8 mA in the 7/8 + 1 mode.

PROGRESS OF THE TOP-UP PROJECT

In order to reduce the heat load variation of the beamline optics, the implementation of top-up has been under way over the past few years. This mode of operation will be initially beneficial for 16-bunch mode, and later for other filling patterns, by reducing the current variation and also by allowing delivery with low vertical emittance. The implementation of top-up has required development and modification of the machine in the following ways:

- Improving the reliability of the injector. Upgrades of the injector are close to being finalised (details below).
- Reducing or removing the vertical blow-up during the bunch cleaning process.
- Minimising the position stability disturbance during injection.

A feed-forward correction has been developed to limit the stability disturbance during injection and is now routinely used. Another correction system is used to minimise the effects of the septum field leakage.

Beam losses are being managed in order to allow injection with closed gaps. The gaps of the in-vacuum undulators are slightly open during the existing injection scheme to limit the beam losses and to avoid demagnetisation of the permanent magnets. In contrast, for top-up operation, the in-vacuum undulators will remain in their closed position. Simulations and experimental work was performed during 2015 to localise the losses on the scrapers.

An injection sequencer has been developed in order to automatically manage the equipment and to optimise electrical consumption. Using this tool, injection is now done in top-up in less than 30 seconds, including cleaning in the storage ring. The occurrence of the injection is communicated to the users using a software countdown system. It should be sufficient for most beamlines. An electrical signal could be provided to those who require a more precise gating of the data acquisition system.

User mode operation with the new hardware and a 'top-up-like' scheme is foreseen for the second run of 2016. In this run, the injection will continue with the standard sequence, but using the new hardware, timing sequence and bunch cleaning in the booster. User mode operation in top-up mode, starting with 16-bunch and 4-bunch modes, will commence thereafter, most likely during the third of run 2016.

RF UPGRADE OF THE BOOSTER

Two additional five-cell cavities were installed in the booster in 2015 (see **Figure 159**). Instead of powering two cavities via two couplers per cavity, the four solid state amplifiers in the booster will now power one cavity each through a single power coupler. This will provide redundancy and therefore increase the reliability for top-up operation, as nominal operation parameters can already be achieved with just three units in operation. With all four systems in operation, only half the power is required to obtain the same acceleration as compared to the former two-cavity system, and at maximum power, a 40% higher peak RF voltage is generated.

Fig. 159: Members of the RF group manage the tricky installation of two five-cell cavities in the booster.

LINAC UPGRADE

The refurbishment of the Linac, undertaken within Phase I of the ESRF Upgrade, has reached completion. In 2015 a new buncher cavity was installed and commissioned in the Linac and the initial buncher will now serve as a spare. In parallel, a third klystron modulator was built in house and commissioned to serve as a hot spare and safeguard operation in case of a major modulator failure. Today, some problems of arcing in the klystron output waveguide still need to be solved before this modulator becomes operational for the start of top-up operation in 2016.

BUNCH CLEANING IN THE INJECTOR

Currently, for the various filling patterns, the unwanted electrons in nominally empty buckets of the storage ring are systematically removed after each injection by means of a selective resonant excitation that also slightly perturbs the stored beam. To avoid this disturbance for the planned top-up operation, the bunch purity will be established first in the injector.

For this purpose, two approaches have been envisaged. A prototype fast stripline kicker has been successfully implemented, allowing the injection of only one bunch from the Linac and without a single spurious electron that could pollute adjacent buckets. The booster extraction still needs to be optimised to avoid tiny portions of the bunch tails being extracted before the fast extraction kicker is fired, when the slower extraction bumps are already being raised.

The second possibility is to perform bunch cleaning in the booster and the necessary hardware for this was installed during the 2015 winter shutdown. Many tests have been carried out showing the potential of this system. Nevertheless, the present stability and reproducibility of the booster power supply does not allow this system to be used in routine operation. Once operational, the new booster power supply should provide the required stability.

NEW BEAM POSITION MONITOR ELECTRONICS IN BOOSTER AND TL2

In March 2015, the 75 BPMs in the booster were all equipped with new Libera Spark electronics that have a greatly improved performance and functionality range. The tests and commissioning after the installation went very smoothly. In addition to X and Z position measurements, the system offers the possibility of monitoring the booster beam current with a high level of sensitivity and reproducibility. This in itself allows sensitive measurements to be made of the transfer efficiency of the booster current to the storage ring. Results of the first tests look very promising and a complete and routine application for serving this purpose is in progress.

In addition, the Spark electronics have been further developed and enhanced in collaboration with the manufacturer to serve other purposes such as position measurements and relative charge measurements in Transfer Line 2 (TL2) and seven BPMs are now in place. Concerning the extra BPMs for the EBS project, further improvements on resolution, precision and reproducibility of the Spark device have been tested on prototypes that carry adapted firmware versions. The tests performed so far confirm their full compatibility with the defined requirements.

NEW BOOSTER POWER SUPPLIES

A new booster ramped injection power supply (RIPS) operating at 4 Hz has been developed and is now under procurement and testing. Two dipole inverters will be delivered in March 2016 after successful factory acceptance tests. Tests of the dipole inverters and rectifiers, then of the whole RIPS system will follow in early 2016. The full cabling scheme is nearly complete and full power tests will be carried out after installation. Tests of the User mode operation with the new RIPS is foreseen for the second run of 2016, with operation in top-up mode commencing shortly thereafter. New power supplies for the septum magnets have also been installed.

In 2015, the power for each magnet was optimised to have a minimum number of different power converter units and preparations are being made for hot-swapping capabilities. The characteristics of the DC common source network distribution are ready to be finalised following the evaluation of the DC-DC converter prototypes for the ESRF–EBS. The first estimation of the cross section of power cabling within the core of the girders has been proposed and will be refined during 2016.

ID STRAIGHT SECTIONS

ID32 was completed with the installation of a new 2.5 m-long helical undulator in the straight section in May 2015 (see **Figure 160**). A high-performance cryogenic

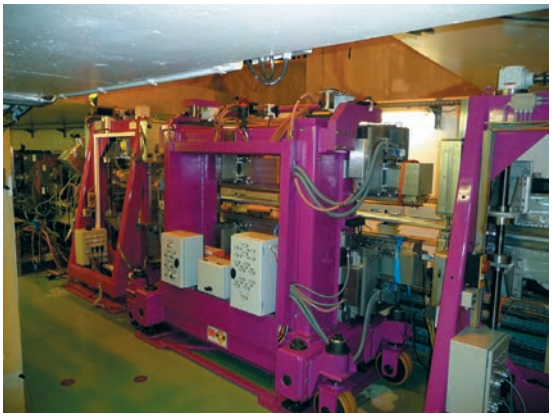

Fig. 160: The new 2.5 m-long helical undulator, installed on ID32, produces circular polarisation rather than only horizontal plane polarisation like most undulators.

permanent magnet undulator, due to be installed on ID31 at the end of 2015, will be postponed until summer 2016. Work to modify the ID15 straight section with a canting scheme has been carried out during the year. A required short, high-field wiggler has been designed and the associated components have been procured. The modification of the straight section and a new insertion device layout (a U22 in-vacuum device upstream and, later in summer 2016, an IVU-20 downstream) will be completed in 2016.

75 kW FROM A COMPACT IN-HOUSE RF SOLID STATE AMPLIFIER

The prototype radiofrequency solid state amplifier (see **Figure 161**) uses a cavity combiner to combine the power from 132 ESRF-developed fully planar 700W RF power modules. This SSA has now been tested successfully and in December 2015 the design RF power of 75 kW was reached with 61% DC-to-RF conversion efficiency. Further development should permit the total output power to be increased.

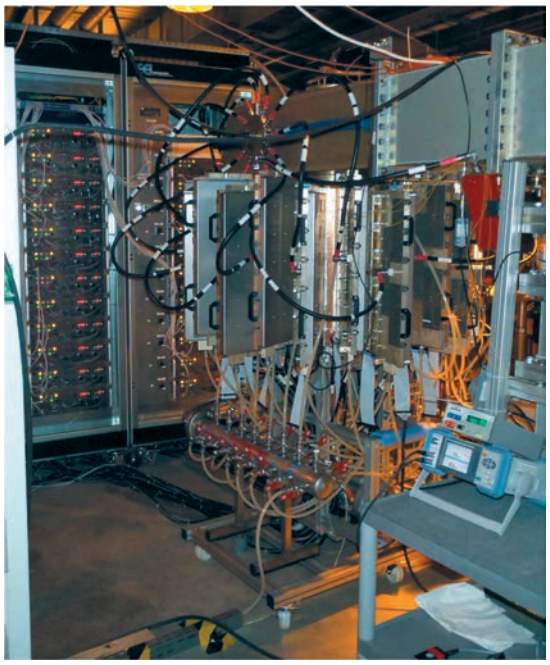

Fig. 161: The prototype solid state amplifier could eventually become the basis for a replacement of obsolete klystron transmitters.

Facts and Figures

MEMBERS AND ASSOCIATE COUNTRIES

(AS OF JANUARY 2016)

Member countries:		Associate countries:	
27.5%	France	1.5%	Israel
24%	Germany	1.3%	Austria
13.2%	Italy	1%	Poland
10.5%	United Kingdom	1%	Portugal
6%	Russia	1.05%	Centralsync (Czech Republic, Hungary, Slovakia)
5.8%	Benesync (Belgium, The Netherlands)	0.3%	South Africa
5%	Nordsync (Denmark, Finland, Norway, Sweden)		
4%	Spain		
4%	Switzerland		

THE BEAMLINES

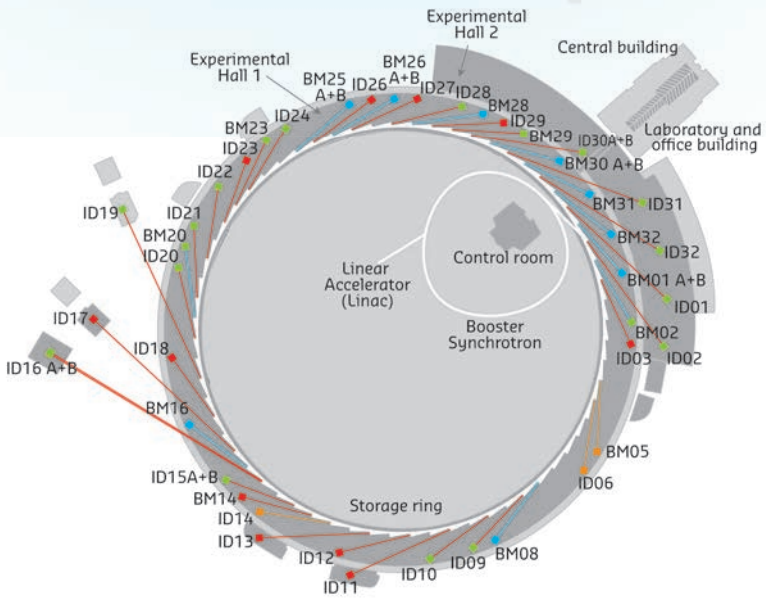

Details of the public ESRF beamlines as well as those operated by Collaborating Research Groups (CRG) are given in **Tables 5** and **6**. **Figure 162** shows the location of the beamlines in the experimental halls.

Fig. 162: Experimental hall showing location of the beamlines (public and CRG beamlines).

SOURCE POSITION	NUMBER OF INDEPENDENT END-STATIONS	BEAMLINE NAME	STATUS	
ID01	1	Microdiffraction imaging	Operational	since 12/14
ID02	1	Time-resolved ultra-small-angle X-ray scattering	Operational	since 07/14
ID03	1	Surface diffraction	Operational	since 09/94
ID06	0.3	Large volume press	Operational	since 10/13
ID09	1	White beam	Operational	since 09/94
ID10	1	Soft interfaces and coherent scattering	Operational	since 06/12
ID11	1	Materials science	Operational	since 09/94
ID12	1	Polarisation-dependent X-ray spectroscopy	Operational	since 01/95
ID13	1	Microfocus	Operational	since 09/94
ID16A	1	Nano-imaging	Operational	since 05/14
ID16B	1	Nano-analysis	Operational	since 04/14
ID17	1	Medical	Operational	since 05/97
ID18	1	Nuclear scattering	Operational	since 01/96
ID19	1	Microtomography	Operational	since 06/96
ID20	1	Inelastic X-ray scattering	Operational	since 06/13
ID21	1	X-ray microscopy / IR spectroscopy	Operational	since 12/97
ID22	1	High resolution powder diffraction	Operational	since 05/14
ID23	2	Macromolecular crystallography MAD	Operational	since 06/04
		Macromolecular crystallography microfocus	Operational	since 09/05
ID24	1	Dispersive EXAFS	Operational	since 02/96
ID26	1	X-ray absorption and emission	Operational	since 11/97
ID27	1	High pressure	Operational	since 02/05
ID28	1	X-ray scattering II	Operational	since 12/98
ID29	1	Multiwavelength anomalous diffraction	Operational	since 01/00
ID30A	2	Macromolecular crystallography	Operational	since 07/14
ID30B	1	Macromolecular crystallography	Operational	since 04/15
ID31	1	Interfaces and materials processing	Operational	since 11/15
ID32	1	Soft X-ray spectroscopy	Operational	since 11/14
BM14	1	Macromolecular crystallography (MAD)	Operational	since 01/10
BM23	1	X-ray absorption spectroscopy	Operational	since 03/11
BM29	1	Bio SAXS	Operational	since 06/12
Operational in 2016:				
ID09	1	Time-resolved structural dynamics	Operational	from 06/16
ID15A	1	Materials chemistry and engineering	Operational	from 09/16
ID15B	0.5	High-pressure diffraction	Operational	from 09/16

Table 5: List of the ESRF public beamlines.

SOURCE POSITION	NUMBER OF INDEPENDENT END-STATIONS	BEAMLINE NAME	FIELD OF RESEARCH	STATUS
BM01	2	Swiss-Norwegian BL	X-ray absorption and diffraction	Operational since 01/95
BM02	1	D2AM (French)	Materials science	Operational since 09/94
BM08	1	LISA (Italian)	X-ray absorption and diffraction	Operational since 09/94
BM20	1	ROBL (German)	Radiochemistry	Operational since 09/98
BM25	2	SPLINE (Spanish)	X-ray absorption and diffraction	Operational since 04/05
BM26	2	DUBBLE (Dutch/Belgian)	Small-angle scattering	Operational since 12/98
			EXAFS	Operational since 06/01
BM28	1	XMAS (British)	Magnetic scattering	Operational since 04/98
BM30	2	FIP (French)	Protein crystallography	Operational since 02/99
		FAME (French)	EXAFS	Operational since 08/02
BM32	1	IF (French)	Interfaces	Operational since 09/94
Operational in 2016:				
BM16	1	FAME-UHD (French)	XES from ultra high diluted samples	Operational from 09/16
BM31	1	SNBL II (Swiss-Norwegian)	X-ray absorption and diffraction	Operational from 09/16

Table 6: List of the Collaborating Research Group beamlines.

USER OPERATION

User operation at the ESRF during 2015 saw the successful culmination of Phase I of the Upgrade Programme, which began back in 2009, with all remaining upgrade beamlines except ID15 back in user operation by the end of the year. ID01 opened in December 2014, taking users for the whole of 2015; the MX beamline ID30B opened for users in April; beamline ID31 took its first user experiment at the end of November; and ID32, although only partially open in the first half of the year, returned to almost full user operation in the second half of 2015. Beamlines ID15A and ID15B were closed throughout the year, and ID09A took its last users in November before closing for its move to ID15B. From 2016, ID09B will become a full beamline (ID09) for time-resolved structural dynamics. In total, the equivalent of around 25 ESRF publicly funded beamlines (out of an optimum of 29.5 in the portfolio) and 9 CRG beamlines were available for users in 2015. **Figure 163** shows the number of applications for beamtime received since Phase I began in 2009. This has remained steadily around the 2000 mark throughout the duration of Phase I despite the heavy construction programme and unavailability of the different upgrade beamlines during this period. User interest in the ESRF therefore remains at a very healthy high.

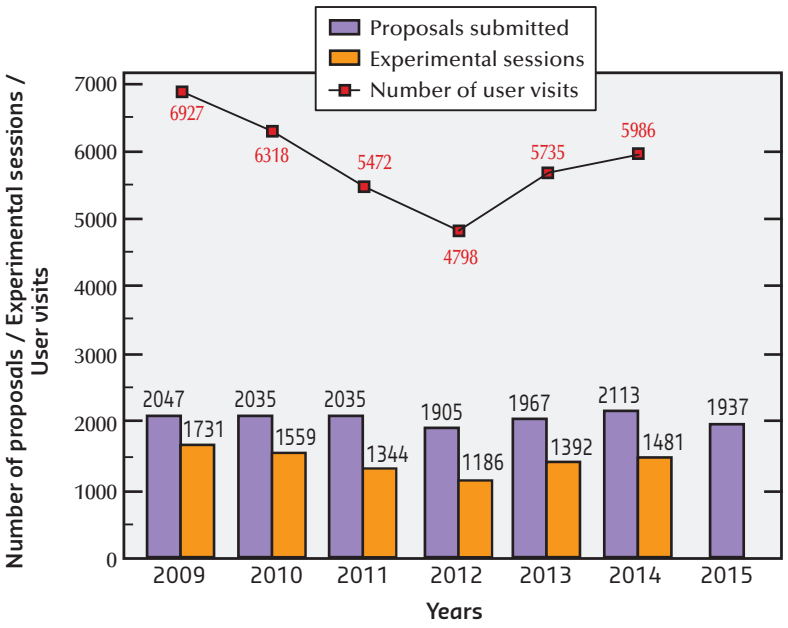

Fig. 163: Numbers of applications for beamtime, experimental sessions and user visits, 2009 to 2015. N.B. Final numbers of experimental sessions and user visits for 2015 were not available at the time of going to press.

Scientific field	Total shifts requested	Total shifts allocated
Chemistry	4 059	1 895
Earth Sciences	1 722	845
Environment	680	306
Hard Condensed Matter Science	8 395	3 360
Cultural Heritage	364	198
Life Sciences	1 029	465
Applied Materials Science	4 929	1 706
Medicine	927	553
Engineering	276	72
Methods & Instrumentation	259	174
Structural Biology	2 809	2 678
Soft Condensed Matter	2 445	959
Totals	**27 894**	**13 211**

Table 7: Shifts of beamtime requested and allocated for user experiments, year 2015.

Proposals for experiments are selected and beamtime allocations are made through peer review. As in previous years, beamtime for 2015 was allocated based on recommendations made by review committees of specialists, for the most part from European countries, Israel and South Africa. These beamline-based committees review all proposals received for a particular beamline. This gives the committees an overview of all the projects proposed for a single beamline, and allows them greater flexibility to optimise the selection of proposals awarded beamtime on each beamline. Proposals for experiments in 2015 were reviewed by 11 review committees grouping the following beamlines of similar techniques or activities:

- C01: ID01, ID03, BM25B, BM32
- C02: ID11, ID22, ID31
- C03: ID12, BM28, ID32
- C04: BM01B, BM08, BM20, BM23, BM25A, BM26A, BM30B
- C05: BM01A, ID06-LVP, ID09A, ID18, ID27, ID28
- C06: ID17, ID19
- C07: ID16A, ID16B, ID21
- C08: ID02, ID13, BM26B
- C09: BM02, ID09B, ID10
- C10: Structural biology beamlines
- C11: ID20, ID24, ID26

The scientific areas of the ESRF research activities reviewed by these eleven Committees are shown in **Table 7**.

The review committees met twice during the year, around six weeks after the deadlines for submission of proposals (1 September 2014 and 1 March 2015). They reviewed 1937 applications for beamtime in 2015 and selected 901 (46.5%) in total. This year, the September 2015 deadline date was modified from 1st to 10th September, in a bid to give proposers more time after the summer and conference season to prepare their beamtime proposals. This move was clearly a success as it resulted in a record number of 1135 proposals being submitted for the autumn deadline, the previous highest being 992 proposals back in September 2009.

Requests for beamtime in 2015, which is scheduled in shifts of 8 hours, totalled 27 894 shifts or 223 152 hours, of which 13 211 shifts or 105 688 hours (47.4%) were allocated. The distribution of shifts requested and allocated by scientific area for 2015 is shown in **Table 7**, while the number of shifts requested, allocated and delivered per year since 2009 is shown in **Figure 164**.

The breakdown of shifts delivered for experiments by scientific area in the first half of 2015 is shown in **Figure 165**. This same period saw 2933 visits by scientists to the ESRF under the user programme, to carry out 769 experiments. Overall, the number of users in each experimental team averaged just under 4 persons and the average duration of an experimental session was less than 9 shifts. This can be further broken down to show an average duration of less than 3 shifts for MX experiments and 13.5 shifts for non-MX experiments. The annual number of experimental sessions and user visits since 2009 is shown in **Figure 163**.

Based on beamtime delivered so far in 2015, the number of experiment sessions for the full year is expected to be well in excess of 1600, and the number of user visits is expected to surpass 6300. This brings these figures back to pre-Phase I values, despite the fact that not all beamlines were fully running in 2015. It is therefore expected that the ESRF will next year show a higher level of usage than ever before, despite the permanent closure of two beamlines during 2011.

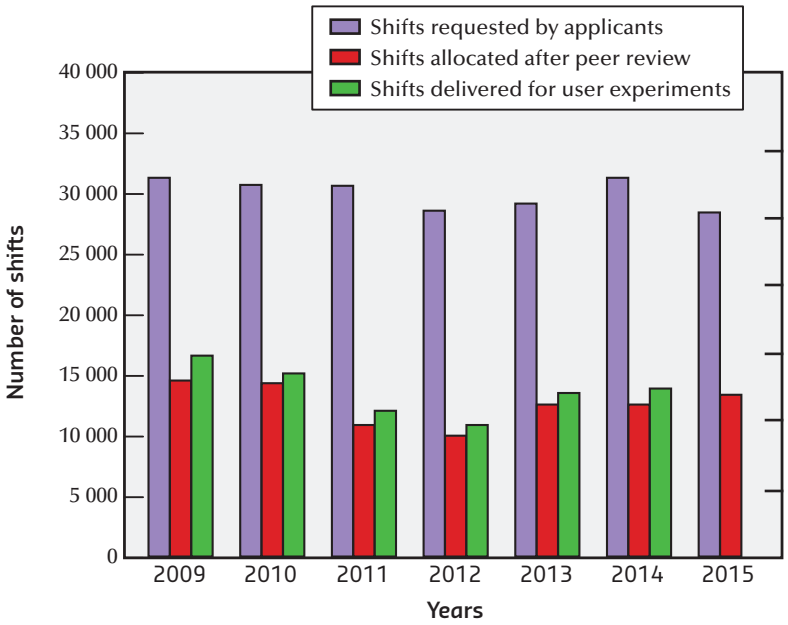

Fig. 164: Amount of beamtime requested, allocated and delivered, 2009 to 2015. N.B. The final number for beamtime delivered for 2015 was not available at the time of going to press.

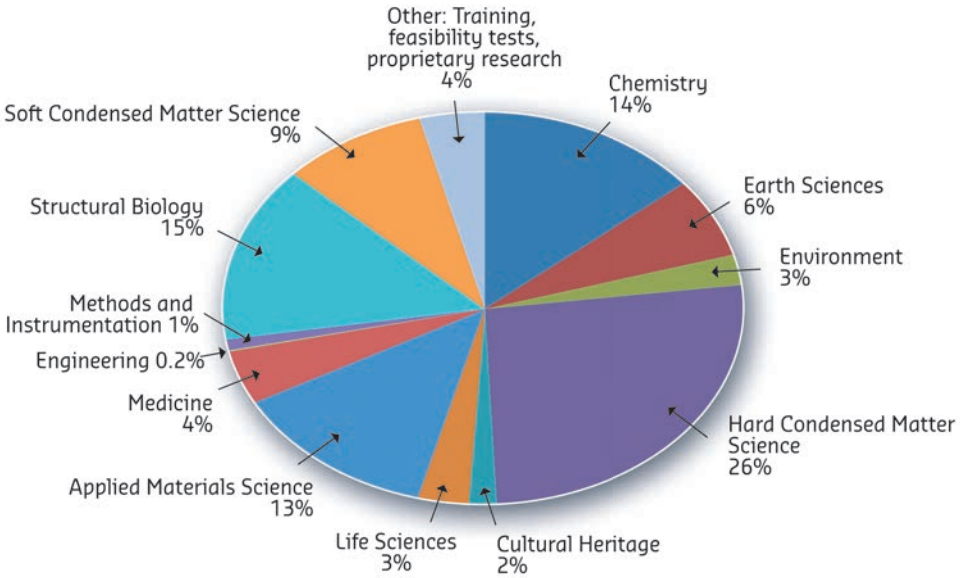

Fig. 165: Shifts delivered for experiments, March to July 2015, by scientific area, total 6714.

One of the principle measurable output parameters of the ESRF is the number and quality of publications accepted in peer-reviewed journals. The number of publications rose continuously for many years, eventually reaching a plateau of over 1800 publications per year over the period of the Phase I programme, as shown in **Figure 166**. These are excellent figures, showing research output maintained at a worldwide high despite a very busy and disruptive upgrade programme. The year 2015 may show the first signs of the expected small drop in output resulting from the 5-month general shutdown of the ESRF back in 2011-2012 and the various beamline closures over the duration of Phase I, with 1650 publications registered so far in the ILL/ESRF Library database which is slightly lower than the 2014 figure at this same time last year. Since the ESRF began user operation back in 1994, a total of 26881 publications have been accepted in peer-reviewed journals. Of these, around 300 every year are published in high impact factor journals.

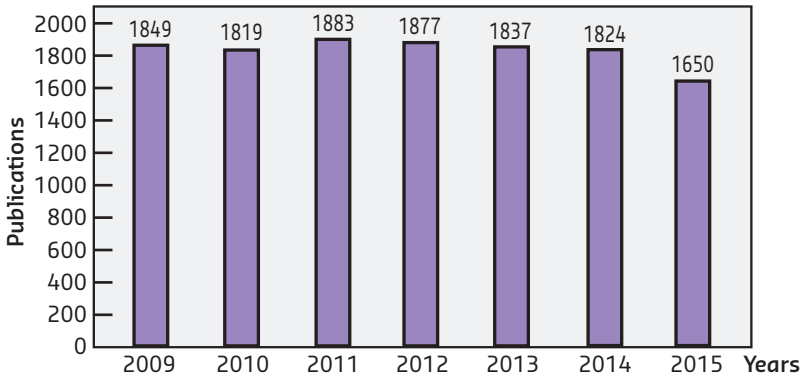

Fig. 166: Numbers of publications appearing in refereed journals reporting on data collected either partially or totally at the ESRF, 2009 to 2015.

User responses to questionnaires show once again that the ESRF continues to maintain its excellent reputation concerning the assistance and service given by scientists and support staff at the beamlines, and travel and administrative arrangements, in addition to the quality both of the beam and of the experimental stations. Facilities on site, such as preparation laboratories and collaborative platforms offering complementary techniques and support, the Guesthouse and a canteen open 7 days a week, also make an important contribution to the quality of user support.

ADMINISTRATION AND FINANCE

Expenditure and income 2014

Expenditure		kEuro
Accelerator and Source		
Personnel		6 430.9
Recurrent		1 669.6
Operating costs	*1 532.8*	
Other recurrent costs	*136.8*	
Capital		5 114.0
Accelerator and Source developments	*5 114.0*	
Beamlines, experiments and in-house research		
Personnel		18 415.1
Recurrent		5 002.0
Operating costs	*1 146.8*	
Other Recurrent costs	*3 855.2*	
Capital		14 596.0
Beamline developments	*14 596.0*	
Beamline refurbishment		
Technical and administrative supports		
Personnel		29 355.4
Recurrent		12 581.1
Capital		7 511.2
Industrial and commercial activity		
Personnel		458.2
Recurrent		110.8
Unexpended committed funds		
Funds carried forward to 2015		999.0
Total		**102 243.0**

Income	kEuro
2014 Members' contributions	85 835.4
Funds carried forward from 2014	25.6
Building costs provision	315.0
Other income	
Scientific Associates	6 102.7
Sale of beamtime	1 677.6
Compensatory funds	3 912.0
Scientific collaboration and Special projects	3 810.9
Pre-financing	– 435.0
Pre-financing carried forward to 2015	999.0
Total	**102 243.0**

Revised expenditure and income budget for 2015

Expenditure		kEuro
Accelerator and Source		
Personnel		6 907
Recurrent		1 621
Operating costs	*1 501*	
Other recurrent costs	*120*	
Capital		12 382
Accelerator and Source developments	*12 382*	
Beamlines, experiments and in-house research		
Personnel		19 205
Recurrent		4 992
Operating costs	*1 086*	
Other Recurrent costs	*3 906*	
Capital		12 275
Beamline developments	*12 275*	
Technical and administrative supports		
Personnel		30 170
Recurrent		12 691
Capital		6 861
Industrial and commercial activity		
Personnel		492
Recurrent		196
Total		**107 792**

Income	kEuro
2015 Members' contributions	91 121
Funds carried forward from 2014	999
Other income	
Scientific Associates	6 158
Income from industrial co.activity	1 954
Russian Fed contribution to construction	10 000
Scientific collaboration and Special projects	6 400
Pre-financing	–8 840
Total	**107 792**

Expenditure 2014 by nature of expenditure

	kEuro
PERSONNEL	
ESRF staff	52 530.2
External temporary staff	21.4
Other personnel costs	2 107.9
RECURRENT	
Consumables	6 855.7
Services	10 108.4
Other recurrent costs	2 399.5
CAPITAL	
Buildings, infrastructure	4 101.0
Lab. and Workshops	1 998.5
Accelator and Source incl. ID's and FEs	5114.0
Beamlines, Experiments	14 596.0
Computing Infrastructure	1 362.6
Other Capital costs	49.1
Unexpended committed funds	
Funds carried forward to 2015	999.0
Total	**102 243.0**

Revised budget for 2015 by nature of expenditure

	kEuro
PERSONNEL	
ESRF staff	54 455
External temporary staff	70
Other personnel costs	2 249
RECURRENT	
Consumables	7 357
Services	9 778
Other recurrent costs	2 365
CAPITAL	
Buildings, infrastructure	1 324
Lab. and Workshops	3 235
Accelator and Source incl. ID's and FEs	12 382
Beamlines, Experiments	12 275
Computing Infrastructure	2 191
Other Capital costs	111
Total	**107 792**

The budget for 2015 includes additional contributions from Members and Scientific Associates of 16 176 kEUR dedicated to the Upgrade Programme. The Upgrade expenditure budget amounts to a total of 25 041 kEUR including 13 020 kEUR of ESRF operating budget. 2015 is also the first year of the ESRF-EBS project.

2015 manpower *(posts filled on 31/12/2015)*

	Scientists, Engineers, Senior Administrators	Technicians and Administrative Staff	PhD Students	Total
Staff on regular positions				
Accelerator and Source*	38	45		83
Beamlines, instruments and experiments*	236	91	27	354
General technical services	32	54		86
Directorate, administration and central services	42	55		97
Sub-total	*348*	*245*	*27*	*620*
Other positions				
Short term contracts	7	9		16
Staff under "contrats de professionnalisation"		35		35
Total	**355**	**289**	**27**	**671**
Scientific collaborators and consultants	*8*			*8*

** Including scientific staff on time limited contracts.*

ORGANISATION CHART OF THE ESRF

(AS OF JANUARY 2016)

Administrative and Finance Committee
Chairperson: J. Scratcher

Council
Chairperson: B. Girard
up to 3 delegates per Contracting Party

Science Advisory Committee
Chairperson: D. McMorrow

Machine Advisory Committee
Chairperson: R. Walker

Director General
F. Sette

DG's Services:
- Head of DG's Office/Secretary of Council: I. Echeverria
- Communication Group
- Business Development Office
- Internal Auditor
- Safety Group

ACCELERATOR AND SOURCE
Director: P. Raimondi

- Beam dynamics and applications
- Power supplies
- Insertion devices
- Front-ends
- Radio frequency and linac
- Diagnostics
- Operation
- Secretariat

ADMINISTRATION
Director: L-J. Sánchez Ortiz

- Personnel
- Finance
- Purchasing

- Joint ILL/ESRF Medical service
- Joint ILL/ESRF Library

EXPERIMENTS

Director: J. Susini

Beamline groups:
- Complex systems and biomedical sciences
- Structural biology
- X-ray nanoprobe

Director: H. Reichert

Beamline groups:
- Electronic structure, magnetism and dynamics
- Matter at extremes
- Structure of materials

Scientific infrastructure
- Theory
- User office
- CRG liaison
- Secretariat

Beam Time Allocation Panels
- **C01** (ID01, ID03, BM25B, BM32) Chairperson: E. Lundgren
- **C02** (ID11, ID22, ID31) Chairperson: A. Tsirlin
- **C03** (ID12, ID32, BM28) Chairperson: P. Gambardella
- **C04** (BM01B, BM08, BM20, BM23, BM25A, BM26A, BM30B) Chairperson: F. Boscherini
- **C05** (ID06-LVP, ID09A, ID18, ID27, ID28, BM01A) Chairperson: U. Schwarz
- **C06** (ID17, ID19) Chairperson: B. Mueller
- **C07** (ID16A, ID16B, ID21) Chairperson: B. Kanngiesser
- **C08** (ID02, ID13, BM26B) Chairperson: H. Lichtenegger
- **C09** (ID09B, ID10, BM02) Chairperson: A. Gibaud
- **C10** (Structural Biology Beamlines) Chairperson: B.M. Hallberg
- **C11** (ID20, ID24, ID26) Chairperson: M. Wilke

INSTRUMENTATION SERVICES AND DEVELOPMENT DIVISION
Head: M. Krisch

- Advanced analysis and modeling
- Detector and electronics
- Software
- X-ray optics
- Mechanical engineering

TECHNICAL INFRASTRUCTURE DIVISION
Head: R. Dimper

- Management information systems and web
- Systems and communication
- Buildings and infrastructure
- EX2/CPER project team
- Survey and alignment
- Vacuum

We gratefully acknowledge the help of:

C. Argoud, T. Baudoin, J.C. Biasci, J.F. Bouteille, B. Boulanger, J. Chavanne, D. Chenevier, K. Colvin, K. Clugnet, E. Dancer, R. Dimper, I. Echeverría, L. Farvacque, S. Gerlier, P. Glatzel, L. Hardy, V. Honkimaki, J. Jacob, A. Joly, A. Kaprolat, M. Krisch, G. Leonard, S. Lombardo, C. Mueller-Dieckmann, J. McCarthy, S. Pascarelli, E. Plouviez, P. Raimondi, H. Reichert, J.L. Revol, S. Rio, K. Scheidt, T. Schülli, F. Sette, J. Susini, M. Wulff and all the users and staff who have contributed to this edition of the Highlights.

Cover
Cover design by S. Lombardo featuring the image "3D surface illustration of typical real-time SAXS data" by A. Sauter from the article *Two-step nucleation in protein crystallisation revealed by real-time SAXS*, A. Sauter *et al.*, p 82.

Photo credits:
M. Alexander, C. Argoud, S. Claisse, I. Ginzburg, P. Jayet, D. McBride, Molyneux Associates.

Editor
G. Admans
Layout
Pixel Project
Printing
Imprimerie du Pont de Claix

Communication Group
ESRF
CS40220
38043 Grenoble Cedex 9 • France
Tel. +33 (0)4 76 88 20 56
Fax. +33 (0)4 76 88 25 42
http://www.esrf.eu